Fault-Tolerant Operation of Three-Phase Squirrel Cage Induction Machine Drives after Inverter Open Circuit Faults

DISSERTATION

in fulfillment of the requirements for the degree
"Doktor der technischen Wissenschaften"

by

Heinrich Tore Eickhoff

submitted to

Graz University of Technology

Supervisor:
Univ.-Prof. Dr.-Ing. Annette Mütze
Electric Drives and Machines Institute
Graz University of Technology, Austria

External Examiner:
Prof. Elias G. Strangas
Department of Electrical and Computer Engineering
Michigan State University, USA

2020

Contents

Abstract

Inverter Open Circuit Faults (IOCFs) in three-phase Squirrel Cage Induction Machine (SCIM) drives may lead to a number of undesired effects and risks, which might even result in the drives' shutdown. Therefore, fast and unambiguous detection methods as well as post-fault operation strategies for such faults are desirable. Since the operation in the common zero-sequence stator current based post-fault strategies is performed with only two of three healthy phases, the power and the torque quality are reduced. Due to the atypical stator current distribution and the additionally occurring space harmonics, the maximum permissible continuous torque during the post-fault operations is typically not known.

This thesis proposes a fast detection method for IOCFs in stator current controlled drives. It is based on the observation of the current control deviation and a subsequent voltage testing procedure. The method can be implemented in the control algorithm, does not need additional hardware, and detects the fault within a few switching periods during steady state and transient operation.

Another major part of this thesis is dedicated to the thermal management of SCIMs during zero-sequence stator current based post-fault operations. The investigations include the calculation of and methods for the reduction of the power losses and temperatures. Thereby, a better utilization of the drives is enabled. Moreover, the thermally defined maximum continuous torque of different post-fault operations is analyzed. The analysis yields possibilities to significantly increase the permissible continuous torque as compared to a previously estimated torque limit.

Within the context of SCIM drives, the space harmonics and a saturation interaction are discussed that affects the machine parameters during the post-fault operations. The effects of this saturation interaction on the torque is investigated for a rotor flux-oriented SCIM drive.

Additionally, this thesis focuses on high alternating torques occurring during the start up and low speed post-fault operations. It proposes a model-based method for the reduction of these torques.

Kurzfassung (in German)

Unterbrechungsfehler in Pulswechselrichtern in dreiphasigen Käfigläufer-Asynchronmaschinenantrieben können zu unerwünschten Effekten und Risiken führen, welche sogar die Notabschaltung des Antriebs erfordern können. Daher sind schnelle und eindeutige Detektionsmethoden, sowie Strategien für den Betrieb nach dem Auftritt solcher Fehler, wünschenswert. Da Post-Fehler-Betriebsarten üblicherweise den Betrieb mit nur zwei von drei gesunden Phasen vollführen, sind die Leistung und die Qualität des Drehmoments reduziert. Durch die atypische Statorstromverteilung in diesen nullstrombasierten Betriebsarten und die auftretenden Oberwellen ist das zulässige dauerhafte Drehmoment ungewiss.

Diese Arbeit untersucht eine schnelle Detektionsmethode für Unterbrechungsfehler der aktiven Schalter in Pulswechselrichtern. Sie basiert auf der Beobachtung der Regelabweichung des Statorstromes und einer anschließenden Spannungstestung. Die Methode kann innerhalb der Regelung implementiert werden, braucht keine zusätzliche Hardware und detektiert den Fehler innerhalb weniger Schaltperioden sowohl während des stationären, als auch während des transienten Betriebs.

Ein weiterer Hauptteil dieser Arbeit ist dem thermischen Management von Käfigläufer-Asynchronmaschinen im nullstrombasierten Post-Fehler-Betrieb gewidmet. Die Untersuchungen beinhalten Berechnungsverfahren und Methoden für die Reduktion der Leistungsverluste und der Temperaturen, was eine bessere thermische Ausnutzung der Maschinen ermöglicht. Zusätzlich wird das thermisch definierte dauerhafte zulässige Drehmoment im Post-Fehler-Betrieb untersucht. Die Analyse zeigt Möglichkeiten zur deutlichen Erhöhung der zulässigen Drehmomente im Vergleich zu der bisher angenommenen Drehmomentgrenze auf.

Im Zusammenhang mit Käfigläufer-Asynchronmaschinen tritt eine Sättigungswechselwirkung auf, welche die Parameter der Maschine im Post-Fehler-Betrieb beeinflussen. Die beteiligten Oberwellen und die Effekte der Sättigungswechselwirkung werden im Zusammenhang mit einem rotorflussorientieren Antrieb diskutiert.

Abschließend beschäftigt sich diese Arbeit mit hohen Wechselmomenten im Post-

Fehler-Betrieb, welche speziell beim Anfahren und bei niedrigen Drehzahlen auftreten. Hierzu wird eine modellbasierte Kompensationsmethode für die Reduktionen dieser Wechselmomente untersucht.

Eidesstattliche Erklärung (in German)

Affidavit

Ich erkläre an Eides statt, dass ich die vorliegende Arbeit selbstständig verfasst, andere als die angegebenen Quellen/Hilfsmittel nicht benutzt, und die den benutzten Quellen wörtlich und inhaltlich entnommenen Stellen als solche kenntlich gemacht habe. Das in TUGRAZonline hochgeladene Textdokument ist mit der vorliegenden Dissertation identisch.

I declare that I have authored this thesis independently, that I have not used other than the declared sources/resources, and that I have explicitly indicated all material which has been quoted either literally or by content from the sources used. The text document uploaded to TUGRAZonline is identical to the present doctoral thesis.

Datum (*Date*)	Unterschrift (*Signature*)

Acknowledgements

This thesis was carried out during my employment at the Electric Drives and Machines Institute (EAM) at Graz University of Technology, Austria from 2014 to 2020 and my visit of the Electric Machines & Drives Laboratory (EM&DL) at Michigan State University, USA in autumn and winter 2016/2017.

I would like to thank the head of the EAM, Professor Annette Mütze, not only for the opportunity to carry out this thesis, but also for her great supervision and her professional guidance. Furthermore, I would like to express my sincere gratitude to the head of the EM&DL, Professor Elias Strangas, for taking the role as 2nd examiner and for the warm welcome and supervision during my stay in the United States. Also, I would like to express my thanks to Dr. Roland Seebacher for his great support and the arrangement of setups and controls at the test stands at the EAM. My special thanks go to Dr. Klaus Krischan, Ewald Seelmeister, Armin Jenni and Arno Huber for the reflections and the manufacturing in connection with induction machine 2 and the related test stand. Furthermore, I would like to express my gratitude to the Austrian Marshall Plan Foundation for the support of my research stay in the United States. Last but not least, I would like to thank my lovely wife and son for their personal support and for their accompanying me to the United States without any hesitation.

Motivation

Induction motors are nowadays the major electric motor type used in the medium power range between 0.75 kW to 375 kW worldwide [1]. Due to the availability of affordable inverters, such motors are increasingly used in variable speed drives and they have been widely replacing the less efficient DC machine drives [1] which require higher maintenance effort. In terms of efficiency, inverter operated induction motor drives show a high potential in applications where grid operated machines are currently used. This is the case if the drive is frequently operated at partial load or if devices such as gears, transmissions or throttles can be avoided [1]. Although other machine drives such as (reluctance assisted) permanent magnet synchronous machine drives potentially show a higher efficiency and power density, induction machine drives are still a plausible option, if the acquisition cost, the robustness, and the availability of the required materials are in the focus of the decision making. The occurrence, diagnosis, and the handling of faults in engineered systems appear to be as old as engineering itself. Research and development in the industrial era lead to highly developed systems. However, faults still occur, and every engineered system has, sooner or later, an end of life. In contrast to faults in electric machines, the faults in the combined systems of electric drives are a rather young research area. The research activities comprise fault statistics, the investigation of physical backgrounds, the detection and prediction of faults, as well as the mitigation and reconfiguration in order to keep the drives operating after the fault occurrence (see Chapter 1). The latest research activities are not only stimulated by scientific interests, since the industry and the energy sector demand a low failure risk of the drives [2]. Additionally, the electrification of the transportation sector has increased the importance of robust and fault-tolerant drives [2].

This thesis contributes to the understanding of the characteristics of squirrel cage induction machine drives during the occurrence of inverter open circuit faults and the detection of such faults. Furthermore, it contributes to the thermal exploitation and the improvement of the torque quality with zero-sequence stator current based post-fault operations of such machines.

Organization

Chapter 1 provides an overview of inverter faults in SCIM drives and the state-of-the-art of detection methods for IOCFs. Furthermore, common fault-tolerant inverter topologies and post-fault operation strategies for three-phase drives are discussed.

Chapter 2 investigates the behavior and characteristics of inverter fed three-phase AC-machine drives during IOCFs. It presents a knowledge-based detection method for such faults that features a particularly low detection time.

In Chapter 3, a zero-sequence stator current based post-fault operation strategy is presented that applies alternative stator current wave forms. An experimental investigation verifies a significant power loss reduction when compared to common post-fault operation strategies which enables a better utilization of the drives.

Chapter 4 discusses the development and the possible reduction of space harmonics that occur with zero-sequence stator current based post-fault operations. Furthermore, experimental studies with two example case SCIMs investigate a saturation interaction between these harmonics and the waves introduced by the balanced three-phase currents. The modeled magnetization surfaces are applied to illustrate the effects of the saturation interaction in the context of a rotor flux-oriented drive.

Chapters 5-7 investigate the power losses and temperature modeling of SCIMs for the zero-sequence stator current based post-fault operations: Chapter 5 discusses analytic approaches to model power losses during the post-fault operations. Chapter 6 shows the state-of-the-art of temperature models for SCIMs and summarizes the heat transfer phenomena in such machines. In Chapter 7, temperature models are developed that consider asymmetric loss and temperature distributions in the machine stators.

In Chapter 8, the thermally defined continuous torque of zero-sequence stator current based post-fault operations is investigated. Experiments with an example case SCIM and the results obtained with a proposed investigation program illustrate significant torque increases when compared to a previously estimated torque limit of such post-fault operations.

Finally, Chapter 9 discusses alternating torques that occur during the zero-sequence

stator current based post-fault operations of SCIMs. Furthermore, it provides an investigation of a reduction method for these torques. Experimental investigations show the speed dependence of the alternating torques as well as the performance of the proposed reduction method for different post-fault operations.

Chapter 1

Introduction

1.1 Faults in Squirrel Cage Induction Machine (SCIM) Drives

1.1.1 Faults, Failures, and Reliability

A *fault* is an "*immediate cause of failure*" [3]. Fig. 1.1 shows an overview of faults in Squirrel Cage Induction Machine (SCIM) drives as discussed and investigated in the literature. The faults differ in the *root causes* and in the appearing *symptoms*:

- Root causes can occur during the design, manufacturing, transportation, installation, operation, or maintenance phase [4]. During the operation, faults can be caused by a non-compliance of the specified voltage, current, speed, torque, ambient temperature, humidity, dust, dirt, shocks, vibrations, dielectric stress, electrostatic discharge, radiation etc., or degradation and fatigue [4, 5]. Different root causes can lead to the same fault [4]. E.g., overloads as well as an excess of the rated ambient temperature can accelerate the degradation of the insulation system and thereby the occurrence of a short circuit fault in the stator windings.
- Typical symptoms for faults are an unbalance or harmonics in the currents and voltages, torque oscillations, noise, vibrations, decreased average torque, increased power losses, excessive heating and temperature [4–6].

In contrast to a fault, a *failure* "*...is when the electrical machine fails to perform its energy conversion function. Failure is complete and does not imply partial functionality.*" [7]. The *failure rates* are typically assumed to show a bathtub characteristic in reliability engineering [4, 8, 9] as shown in Fig. 1.2. These failure rate curves are

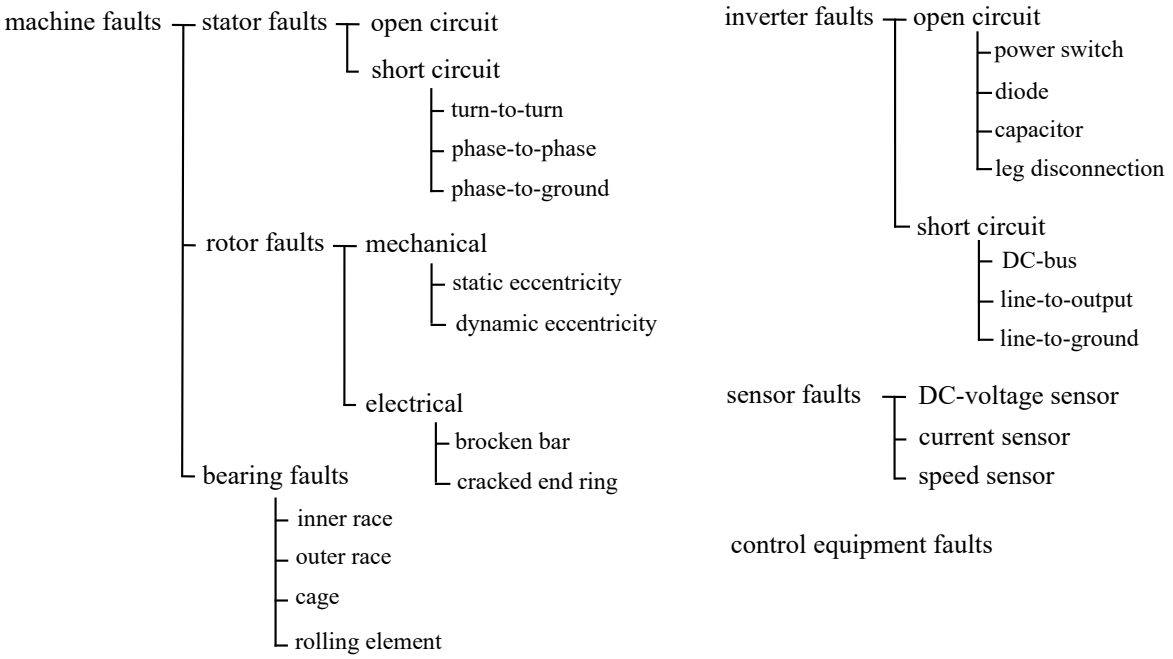

Fig. 1.1: Classification of faults in SCIM drives, summarized from [4–6, 36, 43].

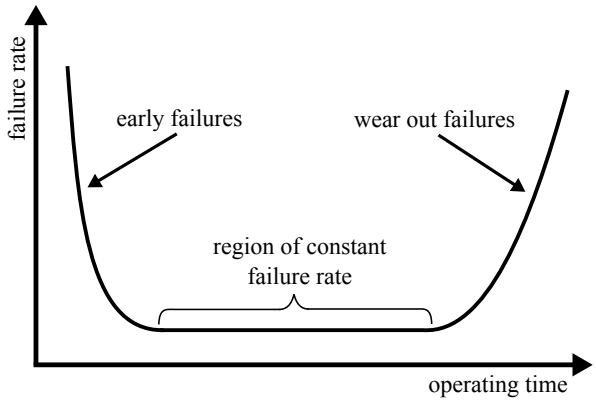

Fig. 1.2: Illustration of a bathtub characteristic of failure rates based on [4, 8, 9].

divided into three regions where all of them can mathematically be described by the Weibull function [4]. In the region of early failures, the failure rate starts at a high level and monotonically decreases to the value of the region with a constant failure rate. In the latter region, the failure rate is assumed to be related to the occurrence of "random" failures [8, 9]. It is assumed that after an (un)certain point in time, the failure increases due to wear out failures. Although the concept of bathtub shaped failure rates is widespread in the reliability literature and appears to be valuable for the description and understanding, some authors disagree in their general applicability, because of the inability to describe multiple early failure population modes [10].

If the failure rate is known, the *reliability* can be calculated as the probability that an item can be operated without a failure under stated conditions for a specified time [3,9]. A similar definition can be found in [11]: "*Reliability is the ability of an item to perform a required function under stated conditions for a stated period of time.*" According to the definitions, the presence of a failure and the reliability depend on the specification of the item.

For the evaluation, reliability indicators such as the *mean time to failure* (MTTF) and the *mean time between failures* (MTBF) can be used which are typically derived for the region with a constant failure rate [4, 9, 12]. However, according to [8, 12] they do not necessarily represent the actual life or repair time. Recently, a paradigm shift from empirical data based reliability prediction as applied in the military handbook MIL-HDB-217F [13] to the *physics-of-failure* based *design-for-reliability* has been performed [8, 12, 14]. In the physics-of-failure approach, failure mechanisms are analyzed and modeled, whereas the design-for-reliability uses such models to improve and prognosticate the reliability during the design phase [8, 12, 14].

Prognosis is the ability to accurately and precisely predict the *remaining useful life* of a failing item or subsystem, and it is based on empirical or physical lifetime models [8,14–16]. The prognosis research is supported by *accelerated aging* in which the time to failure of the investigated items is decreased [17–20]. In contrast to prognosis, *diagnosis* is the detection and isolation of a fault [15] based on symptoms. The associated terms *condition monitoring* and *fault detection* are related to the physics-of-failure approach. However, they aim to measure the condition of the item online [6, 7, 21–23]. Condition monitoring enables *condition-based maintenance* that aims to repair the item before the fault occurrence. Fault detection methods enable a safety shutdown of the item or the transition to a *post-fault operation* if the item is designed to be *fault-tolerant* [81].

1.1.2 Inverter Failures and Faults

In the past 15 years, several surveys with reliability data from the power electronic related industries have been published. According to a survey published in 2007 which was based on answers from 80 companies, most failures in inverters occur due to capacitor (30 %), PCB (26 %), semiconductor (21 %), and soldering failures (13 %) [2,24]. A survey, published in 2011, with 56 participating companies from the power electronic industries, indicates that the most fragile components in power electronic converters are the power devices (31 %), capacitors (18 %), gate drivers (15 %), and connectors (12 %) [25]. A more recent survey published in 2018 based on 51 participating com-

panies, also indicates that power semiconductors and capacitors are the most critical components [26]. The main stress sources reported in these surveys are high temperatures and temperature cycles, vibration, shock, and high humidity [16, 25, 26], where the temperature related stresses appear to be dominant.

An industry case study performed by a German manufacturer of power semiconductor components [27] offers a different view on possible root causes. The study is based on 25 000 wind power modules operating for 5 years and 90 000 wind power modules operating for 2 years. It indicates that 50 % of the failures appeared within the first 120 days of operation, and therefore are classified as early failures. The manufacturer states that the root causes for these failures happened during the manufacturing, shipment or installation. If the defects occurred during the manufacturing, they had not been detected in the performed end tests. The main reported root causes are weak connections, wiring mistakes, electrostatic discharge, vibration, shock, pollution, humidity, rain, and condensation. The manufacturer excludes classical wear out failures, an exceedance of the permissible voltage, current, or temperature and cosmic rays as possible root causes of the observed failures [27].

Inverter faults can basically be separated into two main categories [28]:

- *Inverter short circuit faults* lead to a low-resistance connection of the DC-link potentials and high fault currents [28]. Root causes considered by academia are an abnormal gate-voltage, overvoltage, latch-up, energy shocks, or a thermal-break down due to an overcurrent [28, 35]. Because of the high currents, such faults are critical for the inverter. For the protection, fast hardware circuits have been proposed to detect and mitigate such faults, and to avoid serious damage [16, 35].

- *Inverter open circuit faults* (IOCFs) occur when a galvanic connection in the inverter gets lost or if the turn on of a switch is hindered [16, 28]. Typical root causes considered by academia are damages of the bond wires that are used to connect the terminals in semiconductor devices [23, 28–33]: Bond wire lift offs or cracks are caused by different thermal expansion coefficients of the connected materials and thermal cycling. The lift off is especially expected at the connections of the aluminum bond wires and the silicon [32]. In [23, 29–31], physics-of-failure and life time models for bond wire damages are discussed. Another considered root causes, for IOCFs is a failure in the gate driver circuit [28]. IOCFs can occur at different locations in the inverter. If they occur in the freewheeling path of the inverter, for example at one of the diodes, the high

derivative of the current during the switch's turn off event in connection with the inductance of the load can lead to a high overvoltage. IOCFs at a power switch or due to a fault of the gate driver are not necessarily considered to be critical for the inverter, but potentially for the connected devices [28, 35]. Especially with electric drive applications, such faults can lead to a deviation from the desired torque, high alternating torque components, the loss of flux-orientation, increased power losses, and an exceedance of the maximum permissible temperature of the machine and/or the inverter [36, 37, 43, 69]. Furthermore, IOCFs can lead to secondary faults of other components after some time [28].

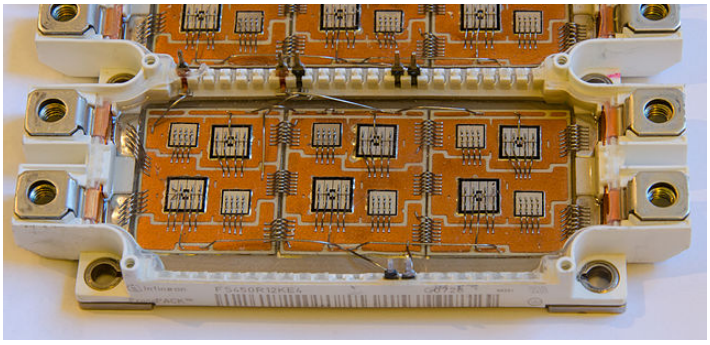

Fig. 1.3: Insulated Gate Bipolar Transistor (IGBT) module with bond wires [34].

To summarize, different root causes for IOCFs have been discussed. Physics-of-failure based models and design as well as accelerated testing might reduce failure rates. However, the expense of reliability engineering is also an economic decision, early failures are not necessarily covered by the physics-of-failure approach and the occurrence of failures will never be fully eliminated. Therefore, the occurrence of IOCFs in electric drives cannot be excluded and the detection of such faults and post-fault operations should be considered and investigated from a drive engineering point of view. Especially in safety relevant applications and applications with high downtime cost, the consideration of such faults is important. The following section reviews detection methods for IOCFs in electric drives.

1.2 Detection of Inverter Open Circuit Faults (IOCFs)

This thesis focuses on the widely-spread drive topology of a three-phase machine fed by a two-level voltage source inverter, as illustrated in Fig. 1.4. Many detection methods have been proposed to identify IOCFs in such a topology. Overviews of such methods

and corresponding performance evaluations are provided in [35, 40]. The methods differ in the detection time, the implementation effort and cost, the ability to correctly identify the faulty switch, the ability to identify multiple faults, and the sensitivity to set point and load changes [35, 50, 55]. Many of these methods have the ability to detect the fault independently of the root cause. Typically, it is assumed that the fault is complete and not intermitting.

IOCFs directly affect the currents and voltages of the drive, and thus most of the detection methods extract features from these quantities. If, for example, an IOCF of switch S_1 occurs, the inverter leg a cannot provide a positive terminal voltage v_{ta} when the current of this leg is $i_{\mathrm{a}} > 0$. This leads to an unbalanced current distribution after the fault occurrence, as illustrated in Fig. 1.5.

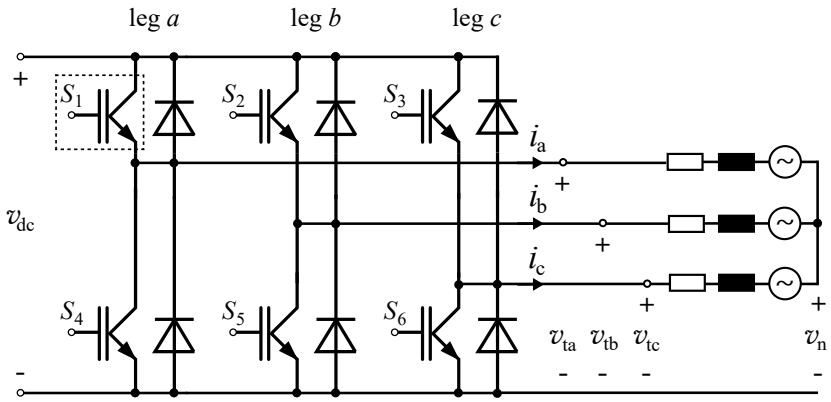

Fig. 1.4: Electric drive consisting of a three-phase voltage source inverter connected to a three-phase machine.

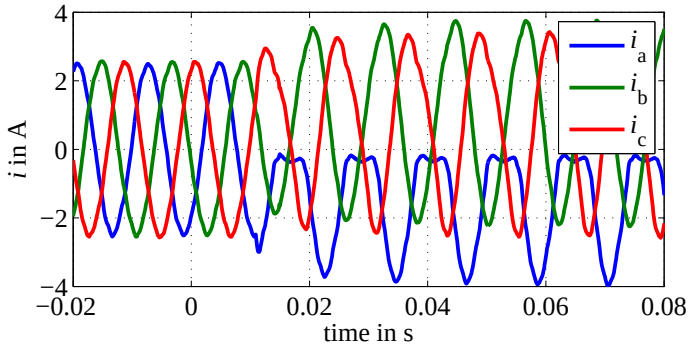

Fig. 1.5: Measured phase currents during a single switch IOCF of switch S_1.

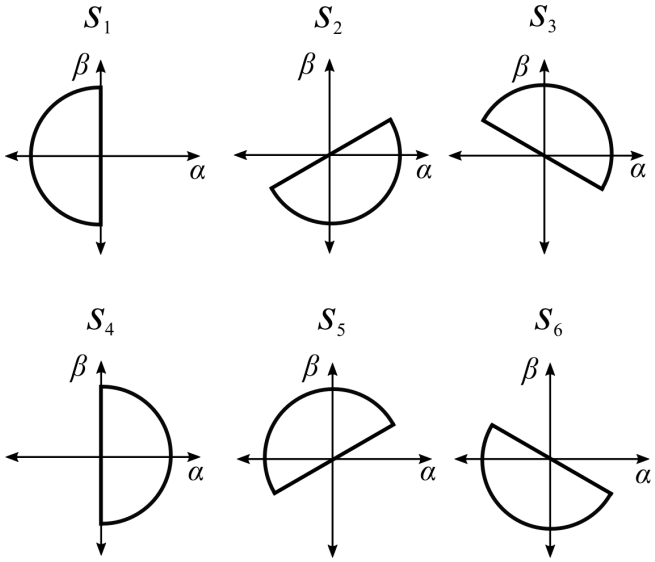

Fig. 1.6: Ideal trajectories of the stator current space vector in the stator reference frame during steady state operation and single switch IOCFs of the different switches assigned in Fig. 1.4, reproduced from [43].

The average current methods (e.g., [35, 38–40]) take advantage of this unbalance by detecting the fault from the mean value of the currents over one fundamental period. They either use the phase currents or the current space vector in the stator frame, applying the Clarke Transformation [41]. Ideal trajectories of this space vector for single switch IOCFs are shown in Fig. 1.6. The space vector based methods use the magnitude and the angle of the average current space vector over one fundamental period to detect the faulty switch. To improve the performance at low currents, a normalization has been suggested in [39]. The averaging over one fundemental period intrinsically restricts the detection time of the average current methods.

In the slope method (e.g., [35, 40, 43]), the slope of the trajectory of the current space vector in the stator frame is observed. It is assumed that the slope is rather constant during the fault for at least a quarter of a period, which is also the method's intrinstic detection time. The slope depends on the inverter leg that experiences the fault. Further current based detection methods that apply signal processing, fuzzy logic, artificial intelligence, and observers and with detection times greater than a fundamental period have been proposed, e.g., in [44–48]. More recently, a further developed average current method [49] and a further developed slope method [50] have been proposed which both feature increased robustness and the ability to detect multiple IOCFs.

Current based methods have the advantage that they typically do not require additional hardware, since the currents are already measured for the control of the drive. Faster detection times than with the current based methods mentioned above, are reported with voltage based methods. However, such methods require additional voltage sensing hardware. The methods proposed in [52] are based on analytic inverter models and the comparison of the actual and desired values of the inverter voltages, the machine phase voltages, or the voltage of the machine's neutral point with respect to the ground. The reported detection times of these methods are less than a quater of a fundamental period. Another voltage based method, with a reported detection time of approximately 2.5 ms, was proposed in [53], where the measured voltages across the lower switches are compared to the desired voltages.

More recently, methods with shorter detection times (less than 1 ms) have been proposed. The approach in [54] is a current based method that applies a model reference adaptive system technique. Voltage distortions introduced by the fault in the rotor reference are estimated by a machine model based voltage distortion observer. This observer is fed by the difference of the measured currents and the reference currents. The method presented in [55] is based on the calculation of the average values of the control deviation of the phase currents and the observation of identifiers. The method is also suitable for the detection of multiple faults.

As reported in [56–58] even faster detection speeds ($\leq 10\,\mu$s) are reported by the application of fast hardware circuits. In [56], the monitoring of the gate-emitter voltages of the IGBT is proposed. The fault causes a change in the miller plateau during the turn on event of the transistor that can be detected. In [58], a method is proposed by measuring the inverter output voltage. However, for those methods, additional hardware is required.

In the last few years, further methods, e.g., based on the dwelling time of the current space vector [59], the phase currents and a current zero-cross detection [60], the calculated bridge arm pole-to-pole voltages [61], a state observer [62], and allelic points [63] have been proposed.

1.3 Post-Fault Operations after IOCFs

Post-fault operations of AC-machines after IOCFs are based on adapted and redundant drive topologies and the application of alternative stator currents. To enhance the reliability, multiphase machines [64, 65] and machines with alternative design [66] as

well as the application of fault-tolerant inverters with three-phase SCIMs [67–73] and three-phase Permanent Magnet Synchronous Machines (PMSMs) [74–80] have been proposed. In such fault-tolerant inverters, the standard topology (Fig. 1.4) is expanded by additional switches, diodes and fuses to enable alternative current paths after the fault occurrence. Reviews of the fault-tolerant three-phase drive topologies can be found in [81] and [82].

The main goal of the post-fault operation strategies is to obtain rotating fundamental waves. To achieve such waves in three-phase machines after IOCFs, many of the proposed post-fault operation strategies apply a zero-sequence stator current [68–79]. This current can be calculated from the phase currents i_a, i_b, and i_c as follows:

$$i_{\mathrm{s0}} = \frac{1}{3}(i_\mathrm{a} + i_\mathrm{b} + i_\mathrm{c}). \tag{1.1}$$

A sinusoidal zero-sequence stator current enables the application of two sinusoidal stator currents in the healthy phases with a phase shift of 60 electrical degrees to achieve rotating fundamental waves [69–71, 73–78], as shown in Fig. 1.7. The standard topology (Fig. 1.4) does not allow the flow of such currents. Therefore, the machine's neutral point is typically connected to the DC-link's midpoint [69–71] or a forth inverter leg [73–78], as illustrated in Fig. 1.8.

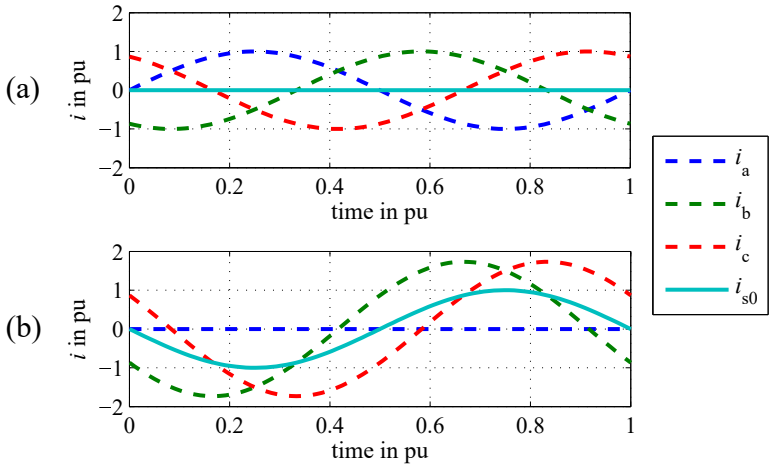

Fig. 1.7: Phase currents and zero-sequence stator current during the standard three-phase operation (a) and during continuous two-phase post-fault operation in the case of an IOCF of switch S_1 [69–71, 73–78] where a fundamental rotating wave is obtained with two stator currents with a phase shift of 60 electrical degrees (b).

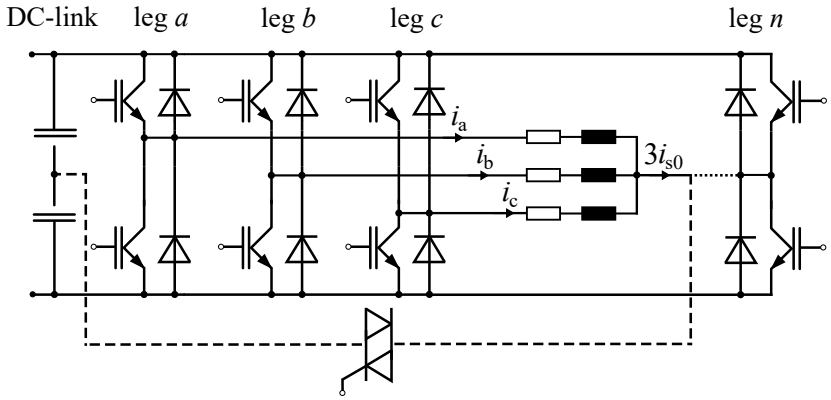

Fig. 1.8: Fault-tolerant topologies that enable the flow of a zero-sequence stator current. The current flows from the neutral point of the machine to the midpoint of the DC-link (dashed line) or to a forth inverter leg (dotted line).

To obtain the same amplitude of the fundamental wave of the stator magnetomotive force, and hence similar torque, the phase currents in the healthy two phases need to be increased by a factor of $\sqrt{3}$ compared to the three-phase operation [69]. This leads to increased power losses in the healthy inverter legs. The neutral current $i_\mathrm{n} = 3i_{\mathrm{s}0}$ is by a factor of $\sqrt{3}$ greater than the phase currents, and the components in the neutral path need to be designed accordingly [81]. If the standard inverter legs are rated for the nominal machine current and the neutral path is rated for $\sqrt{3}$ of the nominal machine current, the output power capability is approximately $\frac{1}{\sqrt{3}} \cdot \frac{\sqrt{3}}{2} = 0.5\,\mathrm{pu}$ for the topology with the DC-link midpoint connection and $\frac{1}{\sqrt{3}} \approx 0.58\,\mathrm{pu}$ for the topology with the neutral inverter leg [81]. If a higher inverter output power is necessary, the components must be rated accordingly. Special care must also be taken for the rating of the DC-link capacitors to avoid a drift of the midpoint voltage with the topology with the DC-link connection [69]. Apart from the limited inverter power, the zero-sequence stator current based strategies show several machine related drawbacks that are addressed in this thesis.

Fault-tolerant topologies that allow the application of the standard three-phase currents and unchanged output power have been proposed in [74, 83]. However, these topologies require a higher number of semiconductor devices which leads to significantly higher component costs [81]. The fuses applied in [74] increase the commutating inductance and are considered as further possible sources of failure [81]. Standard three-phase currents are also enabled with the connection of the faulty phase's terminal to the midpoint of the DC-link. However, in this case, the output power and voltage are limited to approximately 0.5 pu [81]. This reduces the speed capability in the case

of PMSMs [84] and requires flux weakening starting from half of the rated speed in the case of SCIMs [81].

The post-fault operations in this thesis avoid higher component cost and fuse related drawbacks of standard three-phase currents based strategies by applying the four-leg inverter topology (Fig. 1.8) and zero-sequence stator current based post-fault operation strategies. This thesis improves machine related shortcomings introduced by such currents in SCIM drives by thermal exploitation, the increase of the continuous torque capability and the enhancement of the torque quality.

Chapter 2

Fast Detection of Single Switch IOCFs (SSFs)

This chapter discusses the behavior of two-level inverter fed three-phase AC-drives during a Single Switch inverter open circuit Fault (SSF). The provided analysis illustrates the disturbed voltage space vector and the reduced controller dynamics during an SSF. Based on the analysis, a method is investigated that enables the fast detection of SSFs during steady state and transient operation. Finally, simulated and experimental results are provided which show the performance of the detection method.

2.1 Behavior of AC-Drives during an SSF

This section provides a detailed analysis of three-phase AC-drives during an SSF for motor and generator operation. The analysis is performed for a fault of switch S_1 (see Fig. 1.4). However, it is also valid for the other switches and can be transferred by rotating the reference frame by a constant angle (cf., Table 2.1 in Section 2.2.2). The analysis is initially developed for a Permanent Magnet Synchronous Machine (PMSM) drive and is subsequently transferred to an SCIM drive. The analysis illustrates that the disturbed voltage space vector and the reduced controller dynamics after the occurrence of an SSF lead to a rapid change of the derivative of a switch specific current space vector component (i_α, in the case of switch S_1). Additionally, the space vector of the machine's back ElectroMotive Force (EMF) and the occurring disturbance voltage determine if the component is established again. The design of the proposed detection method builds on these mechanisms.

Section 2.1.1 discusses trajectories of the space vectors of the stator current and the current control deviation during an SSF. Section 2.1.2 shows the realized voltage space

vectors after the fault occurrence. In Section 2.1.3, the fault dynamic is illustrated. Sections 2.1.4 and 2.1.5 provide a discussion of zero crossings of the switch specific current space vector component. Finally, the similarities between SCIM drives and PMSM drives with regard to SSFs are discussed in Section 2.1.6.

2.1.1 Current Trajectories during SSFs

A surface PMSM drive is used as the first example case drive. The data of the example case machine SM1 is summarized in Appendix G. The inverter is operated with space vector modulation, a DC-link voltage of 500 V, and a switching frequency of 10 kHz. As already discussed, Fig. 1.4 shows a sketch of inverter-fed three-phase machines with the assignment of the switch numbers. For the discussion of an SSF, the gate signal to the upper switch of the inverter leg a (S_1) is interrupted.

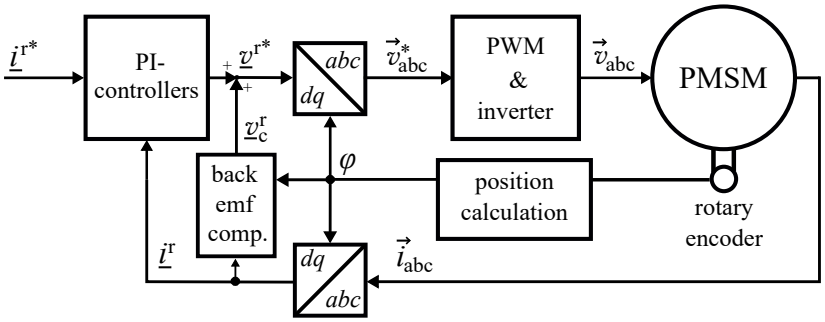

Fig. 2.1: Current control loop of the flux-oriented PMSM drive.

Fig. 2.1 illustrates the inner current control loop of the flux-oriented PMSM drive. It consists of two Proportional-Integral (PI-)controllers for the components of the current space vector in the rotor reference frame, transformations between the rotor and the phase quantities, a three-phase inverter, a PMSM, a rotor angle calculation, and a compensation of the back EMF of the machine. The electrical rotor angle φ is calculated by scaling and integrating the incremental rotary encoder signal, whereas the compensation voltage $\underline{v}_\mathrm{c}^\mathrm{r}$ is generated based on a machine model ((2.1) and (2.2)).

Figs. 2.2a)-c) show simulated trajectories of the current space vector of the PMSM example case drive in the stator reference frame at different operating points. In a healthy condition and at a steady state, the extremity of the current space vector rotates on a circle with the radius of the desired current. However, when the SSF occurs, the trajectory changes to a figure which resembles a semicircle plus a nearly straight line along the diameter (cf., also ideal trajectories Fig. 1.6). After a fault

occurs, the radius exceeds the desired value in the healthy half-plane: During the fault, the integral components of the PI-controllers experience a windup, which leads to a permanent current control deviation, as can be seen in Fig. 2.2d).

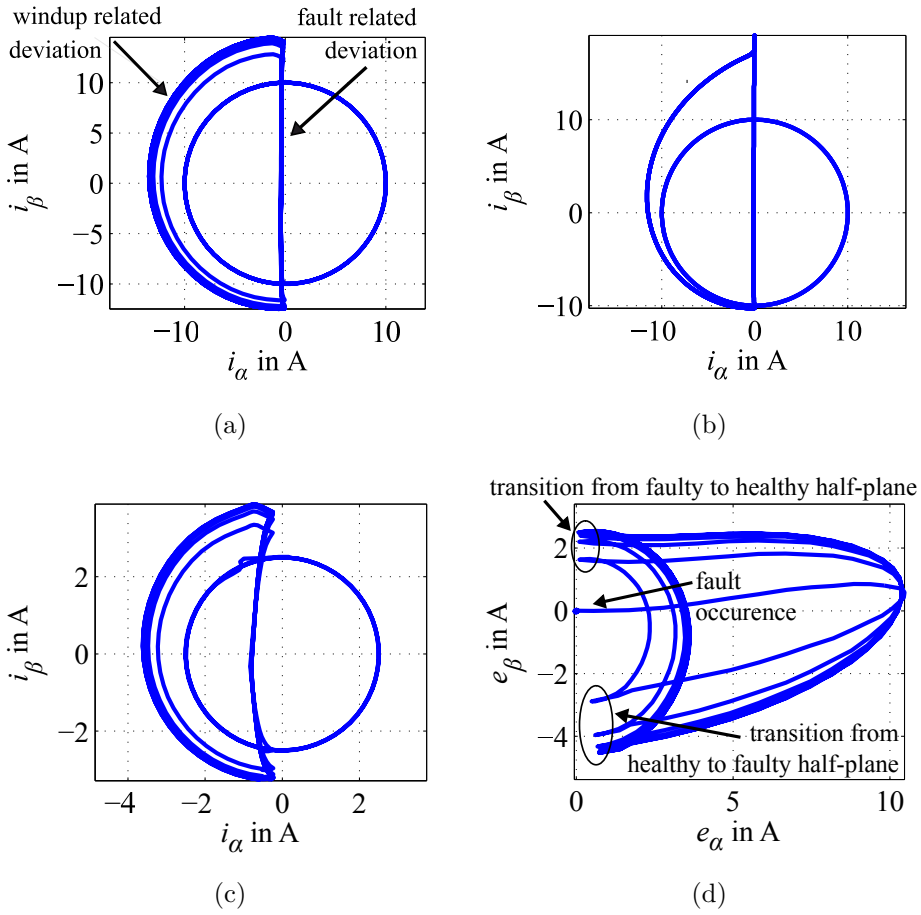

Fig. 2.2: Simulated trajectories of the current space vector in the stator reference frame before and after the SSF (S_1) occurrence at different operating points of the PMSM drive: (a) 1000 r/min and $i_\mathrm{q}^* = 10$ A, (b) 200 r/min and $i_\mathrm{q}^* = 10$ A, (c) 1000 r/min and $i_\mathrm{q}^* = 2.5$ A, and (d) trajectories of the control deviation space vector after the fault occurrence of the operating point of case (a) 1000 r/min and $i_\mathrm{q}^* = 10$ A. Note the different scaling of the α-axis and the β-axis in (d). The data of the example case machine SM1 is summarized in Appendix G.

At low speed and low current, the trajectories tend to differ from an ideal semicircle, as can be seen in Figs. 2.2b) and 2.2c). The lower the stator frequency, the more time the integrators have to reduce the deviation in the healthy half-plane. This leads to a non-symmetric current trajectory with respect to the α-axis at low speed, as shown in Fig. 2.2b). The non-symmetry at low speed was also reported in [40]. At the low

current operating point, see Fig. 2.2c), the current trajectory does not follow the axis at a right angle to the projection axis of the faulty leg; rather, it shows a curvature. This behavior occurs due to the current ripple and the desired low current amplitude.

2.1.2 Realized Voltage Space Vectors in the State $i_\alpha > 0$

The surface PMSM is modeled using the well-known voltage equations in the stator reference frame [85]:

$$v_\alpha = R_\mathrm{s} i_\alpha + L_\mathrm{s}\dot{i}_\alpha \underbrace{-\dot{\varphi}\Psi_\mathrm{PM}\sin\varphi}_{\dot{\psi}_\alpha}, \tag{2.1}$$

$$v_\beta = R_\mathrm{s} i_\beta + L_\mathrm{s}\dot{i}_\beta \underbrace{+\dot{\varphi}\Psi_\mathrm{PM}\cos\varphi}_{\dot{\psi}_\beta}, \tag{2.2}$$

with the stator resistance R_s, the stator inductance L_s (no saliency, $L_\mathrm{s} = L_\mathrm{d} = L_\mathrm{q}$), the flux linkage caused by the permanent magnets Ψ_PM, the electrical rotor angle in the stator reference frame φ (d-axis), and the derivatives of the components of the flux linkage space vector $\dot{\psi}_\alpha$ and $\dot{\psi}_\beta$. Similar equations can be found for an SCIM drive, see Section 2.1.6. As evident from (2.1) and (2.2), the components of the current space vector in the stator reference frame, i_α and i_β, can be controlled via the components of the voltage space vector, v_α and v_β. Modulation based voltage generation methods such as space vector and pulse width modulation assume that the components of the voltage space vector for a given switching period t_s can be generated by an average space vector over discrete inverter switching states. The components of this average voltage space vector in the stator reference frame can be calculated from:

$$\overline{v}_\alpha = \frac{1}{t_\mathrm{s}}\int_0^{t_\mathrm{s}} \left(\frac{2}{3}v_\mathrm{ta} - \frac{1}{3}(v_\mathrm{tb} + v_\mathrm{tc})\right) dt, \tag{2.3}$$

$$\overline{v}_\beta = \frac{1}{t_\mathrm{s}}\int_0^{t_\mathrm{s}} \left(\frac{1}{\sqrt{3}}v_\mathrm{tb} - \frac{1}{\sqrt{3}}v_\mathrm{tc}\right) dt, \tag{2.4}$$

where $v_\mathrm{ta}, v_\mathrm{tb}$, and v_tc are the terminal voltages (cf., Fig. 1.4). During an SSF, the voltage space vector is disturbed (the component $\overline{v}_\alpha$ in the case of an SSF of switch S_1) as discussed in the following. For simplicity, voltage drops across the semiconductor devices and dead times are neglected, without significant loss of accuracy.

During an SSF of switch S_1, only the lower free-wheeling diode of the faulty leg a can conduct a positive i_α current. As a result, the terminal voltage of phase a is

clamped to $v_{\mathrm{ta}} = 0$ if $i_\alpha > 0$ (cf., discussions in [36, 43, 53]). Due to this clamping, only four of eight switching states can be realized. Moreover, states that cannot be realized are turned into other states (cf., also [51]), as illustrated in Fig. 2.3. Due to the replacement of non-realizable switching states, the realized α-component of the voltage space vector during these states is $\frac{2}{3}v_{\mathrm{dc}}$ lower than its desired value. As a result, also the α-component of the average voltage space vector (2.3) is generally significantly lower than the desired value $\overline{v}^*_\alpha$.

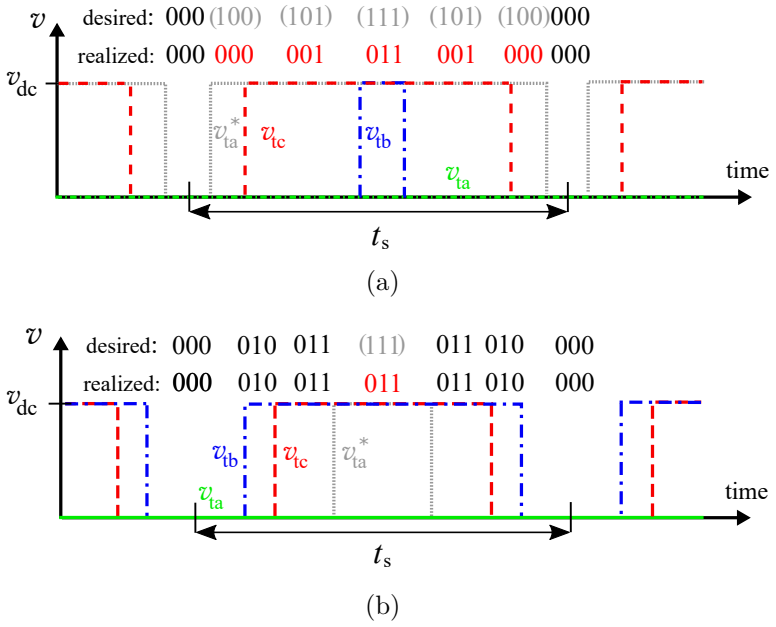

Fig. 2.3: Terminal voltages during the space vector modulation if $i_\alpha > 0$ applies to the whole switching period t_{s}: (a) modulation of space vector $\underline{v}_{\mathrm{I}}$ and (b) modulation of space vector $\underline{v}_{\mathrm{II}}$ of Fig. 2.4. v^*_{ta} is the commanded terminal voltage of leg a. The digits of the three-digit numbers indicate the terminal voltage in pu of the phases a, b and c, respectively. 1 pu corresponds to v_{dc}. Non-realizable switching states are indicated in gray, with parentheses.

Fig. 2.4 shows the transformation of a desired average voltage space vector into the average voltage space vector realized during space vector modulation. The transformation for sinusoidal pulse width modulation is similar and is discussed in Appendix A. During healthy operation, the components of the average voltage space vector $\overline{v}_\alpha$ and $\overline{v}_\beta$ are equal to the desired values $\overline{v}^*_\alpha$ and $\overline{v}^*_\beta$, see Figs. 2.4a) and b). However, during an SSF of switch S_1, $\overline{v}_\alpha$ is disturbed if $i_\alpha > 0$, whereas the orthogonal component $\overline{v}_\beta$ remains unaffected, see Figs. 2.4c) and d). The desired average space vectors are transformed into the negative α-region, and the realizable average space vectors are

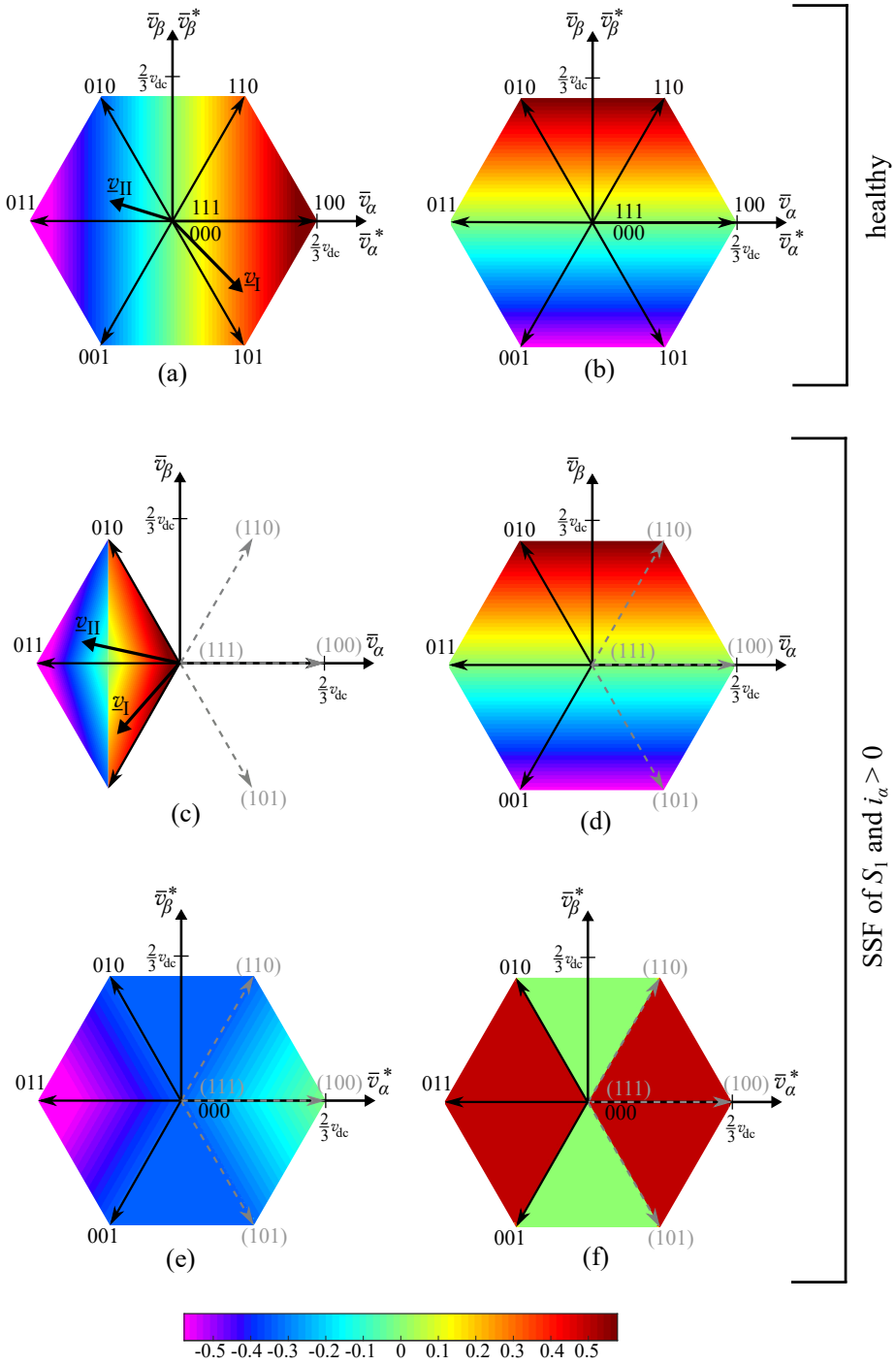

Fig. 2.4: Transformation during space vector modulation of desired voltage space vectors into realized voltage space vectors during healthy operation (a) and (b), and under an SSF of switch S_1, if $i_\alpha > 0$ (c)-(f). The switching states that can be realized and that cannot be realized are indicated in black, without parentheses, and in gray, with parentheses, respectively. The colors show the following: The desired average space vector components in one switching period $\overline{v}_\alpha^*$ in (a) and (c) and $\overline{v}_\beta^*$ in (b) and (d). The realized component $\overline{v}_\alpha$ is shown in (e), whereas (f) shows the derivative $\frac{\delta \overline{v}_\alpha^*}{\delta \overline{v}_\alpha}$. Additionally, the transformation of two example space vectors v_I and v_II is illustrated.

restricted significantly due to the limited number of switching states that are realized (Fig. 2.4c). The deviation (the difference of the realized and desired α-components of Figs. 2.4a) and e)) depends on the position of the desired voltage space vector.

Fig. 2.4f) illustrates the slope $\frac{\delta v_\alpha^*}{\delta v_\alpha}$. If $v_\beta^* = 0$, the realized α-component increases steadily with increasing v_α^*. However, it does so with half of the slope of the desired value. This reduced slope occurs due to the replacement of the switching states 100 and 111 by the states 000 and 011, respectively, and the desired time in the state 111 is $\frac{t_s}{2}\left(1 - \frac{|v_\alpha^*|}{\frac{2}{3}v_{\mathrm{dc}}}\right)$. If $v_\beta^* \neq 0$, positions occur in which an increase of the desired α-component does not affect the realized component v_α (green areas in Fig. 2.4f)). This happens due to the replacement of the switching states 110 and 101 by the states 010 and 001, respectively, and the constant time in the passive states 000 and 111 for constant v_β^*.

2.1.3 Fault Dynamics for $i_\alpha > 0$

When the voltage drop at the stator resistance R_s is neglected, the derivative of the current space vector component i_α is given by:

$$\dot{i}_\alpha = \frac{1}{L_\mathrm{s}}\left(v_\alpha - \dot{\psi}_\alpha\right) = \frac{1}{L_\mathrm{s}}\left(v_\alpha + \dot{\varphi}\Psi_\mathrm{PM}\sin\varphi\right). \tag{2.5}$$

As per (2.5), the derivative $\dot{i}_\alpha$ depends on the difference of the α-component of the voltage space vector v_α and the α-component of the back EMF of the machine. When the SSF of switch S_1 occurs and $i_\alpha > 0$, the realized v_α is immediately significantly lower than desired, which leads to a rapid decrease of $\dot{i}_\alpha$. The controllers try to counteract the resulting current deviation by increasing the desired α-component of the voltage space vector. This dynamic process can be approximately described by a disturbance transfer function which models the time continuous counterpart of the disturbance loop. If the controllers are designed as discussed in Section 2.2.2, the disturbance transfer function is given by:

$$\underline{D}(\underline{s}) = \frac{\underline{I}_\alpha(\underline{s})}{\underline{V}_{\mathrm{d}\alpha}(\underline{s})} = \frac{\underline{s}}{\underline{s}^2 L_\mathrm{s} + (R_\mathrm{s} + WG)\underline{s} + \frac{WGR_\mathrm{s}}{L_\mathrm{s}}}, \tag{2.6}$$

where $\underline{V}_{\mathrm{d}\alpha}(\underline{s})$ is the disturbance voltage and G is the controller gain of the PI-controllers (cf., (2.14)). Due to the fault, the increase of v_α, which is forced by the controllers, is disturbed. As per Fig. 2.4f), the slope of the realized α-component of the voltage space vector with respect to its desired value is less than 1. This has the same effect as a reduced controller gain and is considered in (2.6) by the weakening factor $W = \frac{\delta v_\alpha^*}{\delta v_\alpha}$.

The weakening factor as well as controllers with a lower selected gain lead to a faster decrease of $\dot{i}_\alpha$. If $W = 0$, an increase of the desired α-component does not lead to an increase of the realized component v_α, and the controllers cannot influence the dynamic process after the fault occurrence.

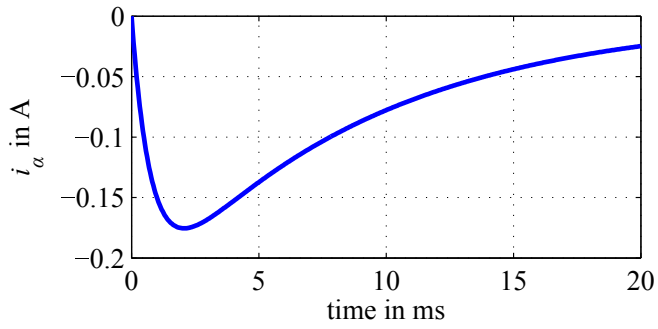

Fig. 2.5: Step response of the disturbance transfer function of the example case drive ($W = \frac{1}{2}$) for a step of the disturbance voltage $V_{\mathrm{d}\alpha}$ from 0 V to -1 V.

Fig. 2.5 shows the step response of (2.6) with $\underline{V}_{\mathrm{d}\alpha}(\underline{s}) = \frac{v_\alpha^* - v_\alpha}{\underline{s}} = -\frac{1}{\underline{s}}$. In the state $i_\alpha > 0$, the occurrence of an SSF of S_1 leads to a rapid decrease of the current component i_α (cf., also simulations and experimental results in Section 2.3). The disturbance voltage depends on the location of the voltage space vector when the fault occurs, as can be seen from Fig. 2.4. The disturbance voltage decreases with decreasing v_α^*, and thus the disturbance voltage tends to be lowest during the generator operation at high speed. The dynamic response of the current controllers to voltage disturbance is typically slower than the response to set point changes defined by (2.15). The weakening factor additionally slows down the controller dynamics.

Due to the fact that the PI-controllers of the current control loop operate in the rotor reference frame, and thus the disturbance voltage differs from a step, the actual response may deviate with progressing time from Fig. 2.5. Nonetheless, it can be assumed that the controllers are increasingly hampered. When the current component i_α reaches 0 after the fault occurrence, the conditions change as discussed in the next sections.

2.1.4 Condition for $i_\alpha > 0$

If i_α is negative, the space vector of the machine's back EMF determines whether a positive i_α is established. For $i_\alpha = 0$ and the case that the switch S_4 is off, the inverter leg a shows a high resistance. The terminal voltage of the phase a is defined in this

state by the α-component of the back EMF and the terminal voltages of the healthy inverter legs (see derivation in Appendix B). In the case of a PMSM, the terminal voltage of the phase a in this state is defined by:

$$v_{\mathrm{ta}} = -\frac{3}{2}\dot{\varphi}\Psi_{\mathrm{PM}}\sin\varphi + \frac{1}{2}(v_{\mathrm{tb}} + v_{\mathrm{tc}}). \tag{2.7}$$

Starting from $i_\alpha = 0$, $i_\alpha > 0$ can only be reached if $v_{\mathrm{ta}} < 0$. Since $\frac{1}{2}(v_{\mathrm{tb}} + v_{\mathrm{tc}}) \geq 0$ and $\dot{\varphi} > 0$, this is only possible if $0 < \varphi < \pi$. A special case arises if the flux building component of the current space vector i_{d} is $i_{\mathrm{d}} = 0$ and the controller windup discussed above has not occurred yet. In this case, the current space vector and the space vector of the back EMF are in phase (motor operation) or show a phase shift of π (generator operation). Thus, when the desired current space vector enters the faulty half-plane during motor operation, the rotor angle is $\pi \leq \varphi \leq 2\pi$ which prevents the state $i_\alpha > 0$.

2.1.5 Zero Crossing of i_α

When the rotor angle is $0 < \varphi < \pi$ (which leads to $\dot{\psi}_\alpha < 0$), the back EMF can cause positive values of i_α in the desired states 000 and 100. The current ripple and the related changes between the states $i_\alpha < 0$, $i_\alpha = 0$, and $i_\alpha > 0$ prevent a closed mathematical description of the zero crossing. Therefore, experiments at standstill of the drive were performed for the investigation. The necessary negative α-component of the back EMF is emulated by means of a DC voltage source in phase a. Fig. 2.6 shows the topology used for the experiments.

The experiments showed significantly decelerated current step responses. Fig. 2.7 illustrates the observed response for a step of the desired current i_α^*. Already at standstill, without the rotor reference frame rotating, the controllers need significant time to achieve a positive current component i_α. In comparison, the step response time constant of the current control loop of the example case drive during healthy operation is 0.4 ms.

Immediately after the step of the desired current, the measured current is still located in the healthy half-plane, and it increases with the time constant of the healthy drive (0.4 ms). When the current i_α reaches 0, $\dot{i}_\alpha$ is reduced significantly. During the zero crossing in the experiment, the disturbance voltage does not occur abruptly; rather, it increases steadily with the average value of i_α. The current ripple leads to $i_\alpha = 0$ during a switching period, and the current remains zero if the switching state 111 is desired. During this time, the terminal voltage is defined by (2.7). The time in the

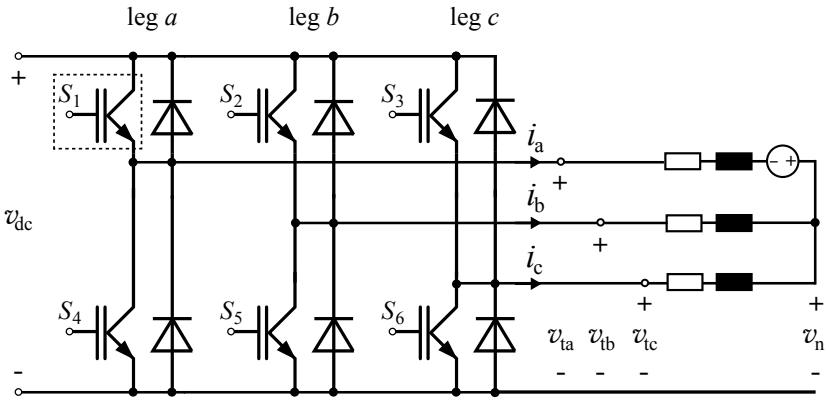

Fig. 2.6: Topology used for the zero crossing experiments including a DC voltage source in phase a.

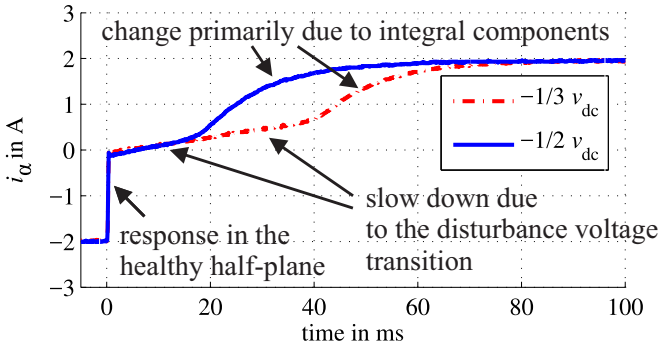

Fig. 2.7: Measured zero crossings of the current component i_α at standstill of the drive at different simulated back EMFs of the machine in α-direction and resulting current ripples. The step of the desired current from -2 A to 2 A appears at $t = 0$ s.

state $i_\alpha = 0$ and the α-component of the voltage space vector both decrease with increasing average i_α. This leads to a smooth transition to the disturbed voltage space vectors after the fault occurrence for $i_\alpha > 0$ shown in Section 2.1.2. The controllers must increase the desired voltage to compensate the disturbance voltage which leads to a significant slowdown of the current step response.

2.1.6 SCIM Drive Behavior

The analysis above was initially performed for a PMSM drive. In this section, the similarity between PMSM and SCIM drives with regard to SSFs is discussed. The current control loop of a flux-oriented SCIM drive is shown in Fig. 3.4. Simulated trajectories of stator current space vector trajectories in the stator reference frame for such a drive are illustrated in Fig. 2.8. Also in the case of an SCIM drive, the SSF

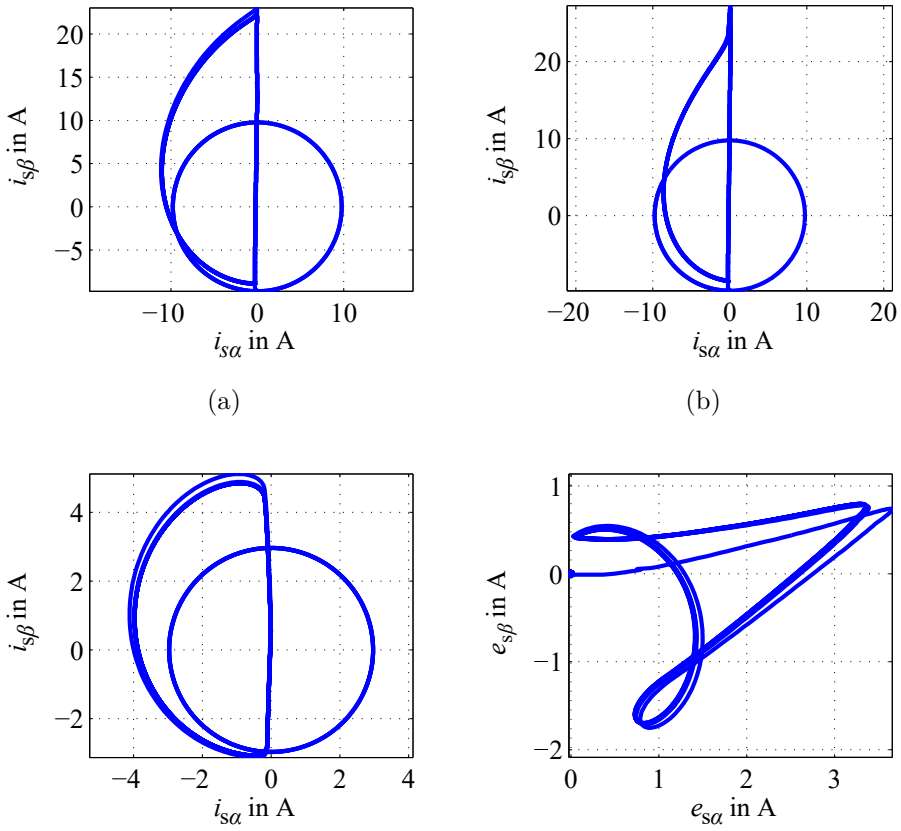

Fig. 2.8: Simulated trajectories of the stator current space vector in the stator reference frame before and after the SSF (S_1) occurrence at different operating points of the SCIM drive: (a) 1000 r/min and $i^*_{\mathrm{sq}} = 7\,\mathrm{A}$, (b) 750 r/min and $i^*_{\mathrm{sq}} = 7\,\mathrm{A}$, (c) 2000 r/min and $i^*_{\mathrm{sq}} = 2\,\mathrm{A}$, and (d) trajectory of the stator current control deviation space vector after the fault occurrence of the operating point of case (c). The data of the example case machine IM1 is summarized in Appendix G.

leads to a deviation between the desired and the realized voltage space vector. The disturbed inverter voltages discussed in Section 2.1.2, as well as the condition for the zero crossing discussed in Section 2.1.4 and Appendix B are also valid for an SCIM drive, without any changes. Differences between the PMSM drive and the SCIM drive can be observed inherently in the machine equations. The components of an SCIM's stator voltage space vector in the stator reference frame can be described as follows [85]:

$$v_{\mathrm{s}\alpha} = R_{\mathrm{s}} i_{\mathrm{s}\alpha} + L_{\sigma\mathrm{s}} \dot{i}_{\mathrm{s}\alpha} + \dot{\psi}_{\mathrm{m}\alpha}, \tag{2.8}$$

$$v_{\mathrm{s}\beta} = R_{\mathrm{s}} i_{\mathrm{s}\beta} + L_{\sigma\mathrm{s}} \dot{i}_{\mathrm{s}\beta} + \dot{\psi}_{\mathrm{m}\beta}, \tag{2.9}$$

with the stator resistance R_s, the stator leakage inductance $L_{\sigma\mathrm{s}}$, and the derivatives of the components of the magnetization flux linkage $\dot{\psi}_{\mathrm{m}\alpha}$ and $\dot{\psi}_{\mathrm{m}\beta}$. The comparison of (2.8) and (2.9) with the equations for the PMSM (2.1) and (2.2) shows a structural similarity. However, the main difference lies in the back EMF generation which is caused by the rotating permanent magnets in the case of the PMSM and by the flux excited by the rotating stator and rotor current space vectors in the case of the SCIM. The behavior of the rotor current's space vector in the rotor reference frame can be described by the following differential equation (cf., SCIM model in Section 3.1.3):

$$\dot{\underline{i}}_\mathrm{r}^\mathrm{r} = -\frac{R_\mathrm{r}}{L_{\sigma\mathrm{r}} + L_\mathrm{m}} \underline{i}_\mathrm{r}^\mathrm{r} - \frac{L_\mathrm{m}}{L_{\sigma\mathrm{r}} + L_\mathrm{m}} \dot{\underline{i}}_\mathrm{s}^\mathrm{r}, \tag{2.10}$$

where R_r is the rotor resistance, L_m is the magnetization inductance, $L_{\sigma\mathrm{r}}$ is the rotor leakage inductance, and $\underline{i}_\mathrm{s}^\mathrm{r}$ is the stator current space vector in the rotor reference frame. The magnetization flux linkage (3.7) is supported by the rotor currents in case the stator current space vector in the rotor reference frame $\underline{i}_\mathrm{s}^\mathrm{r}$ changes. The time of the support is defined by the rotor time constant. Due to the support, the rotating SCIM produces a considerable back EMF even if the stator currents are disturbed after the occurrence of an SSF. Hence, the SCIM drive shows similar fault dynamics and zero crossing behavior as a PMSM drive (cf., Sections 2.1.3 and 2.1.5).

2.2 Proposed Fast SSF Detection Method

2.2.1 Overview

Fig. 2.9 shows an overview of the proposed detection method. The findings from the previous section are applied to monitor the impact on the current control deviation. In the proposed method, the current control deviation space vector in the stator reference frame $\underline{e}^\mathrm{s}$ is monitored and used as a fault indicator. Immediately after the fault occurs, the deviation increases, and the deviation space vector's angle indicates the faulty switch. If the trigger criterion is met, an additional voltage test is enabled to further validate. This test increases the desired voltage depending on the deviation space vector's angle to counteract the said deviation, and to increase the level of confidence. If the additional voltage $\underline{v}_+^\mathrm{s}$ does not reduce the current control deviation as expected under healthy conditions, a fault flag occurs. The method is designed to repeat the additional voltage test if the trigger criterion for a full-leg open circuit fault (i.e., an open circuit fault of both switches of the same leg) is satisfied, so as to detect this

fault. The proposed method does not require additional sensors apart from the current sensors which are already provided for the current control.

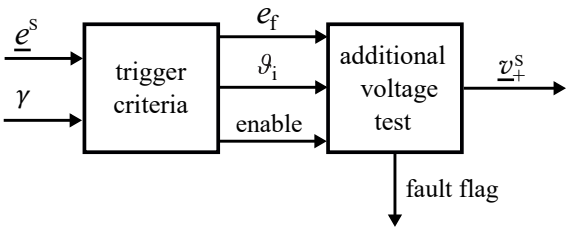

Fig. 2.9: Signal flow diagram of the detection method.

2.2.2 Monitoring of the Current Control Deviation

In the context of a current controlled machine, the findings from the previous section are applied to monitor the impact on the current control deviation space vector components in the stator reference frame $e_\alpha = (i_\alpha^* - i_\alpha)$ and $e_\beta = (i_\beta^* - i_\beta)$, where i_α^* and i_β^* are the desired values. The disturbed voltage space vector and the reduced controller dynamics after the fault occurrence rapidly increase the control deviation. Due to the fact, that the disturbed component depends on the faulty switch, the control deviation space vector's angle indicates the faulty switch. Therefore, this space vector is monitored and used as a fault indicator in the proposed method, as will be detailed in the following.

Current Control Deviation

The components of the current control deviation space vector in the stator reference frame can be calculated from the current space vector components in the rotor reference frame as follows (cf., also Appendix I):

$$e_\alpha = (i_{\mathrm{d}}^* - i_{\mathrm{d}})\cos\varphi - (i_{\mathrm{q}}^* - i_{\mathrm{q}})\sin\varphi, \tag{2.11}$$

$$e_\beta = (i_{\mathrm{d}}^* - i_{\mathrm{d}})\sin\varphi + (i_{\mathrm{q}}^* - i_{\mathrm{q}})\cos\varphi, \tag{2.12}$$

where i_{d} and i_{q} are the normalized direct and quadrature currents in the rotor reference frame, i_{d}^* and i_{q}^* are the normalized desired direct and quadrature currents in the rotor reference frame, and φ is the electrical rotor angle (direct axis). The angle of the space vector $\vartheta = \mathrm{atan2}(e_\beta, e_\alpha)$ is used as an indicator for the faulty switch immediately after the fault occurs. The ideal angles are summarized in Table 2.1.

Table 2.1: Ideal angles of the control deviation space vector in the stator reference frame.

faulty switch	S_1	S_2	S_3	S_4	S_5	S_6
ϑ_i	0°	120°	−120°	180°	−60°	60°

Sectors of Fault Occurrence

The control deviation space vector's magnitude differs depending on the angle of the current space vector at which the fault occurs. For the analysis, the trajectory of the desired current is divided into four sectors, as shown in Fig. 2.10 for the example case of an SSF of switch S_1.

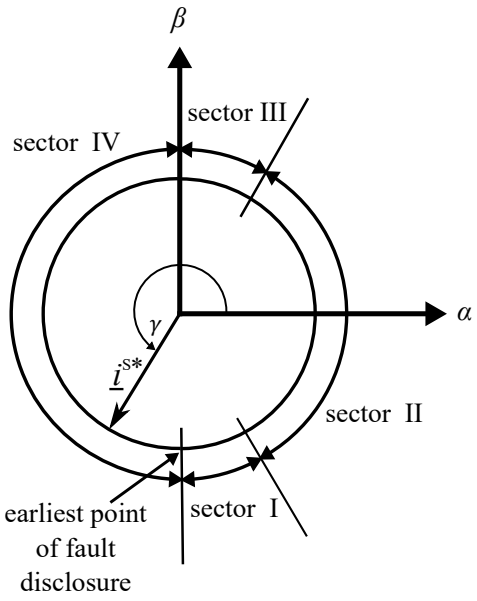

Fig. 2.10: Current trajectory of the desired current space vector in the stator reference frame and definition of the sectors for an SSF of S_1.

- Sector I contains the first 30 ° of the circle, starting at the earliest point of fault disclosure. In this sector, it is expected that i_α does not enter the faulty half-plane as discussed in Sections 2.1.4 and 2.1.5. Due to the fact that i_α^* increases, the deviation also increases continuously.

- If an SSF occurs in sector II, it is expected that the deviation is greater than $\sin(30°) = 0.5\,\mathrm{pu}$ immediately after the fault occurs, due to the rapid decrease of $\dot{i}_\alpha$ as discussed in Section 2.1.3.

- In sector III, it can be assumed that the deviation's immediate increase is smaller than $\sin(30°) = 0.5\,\text{pu}$ and that the deviation decreases rapidly due to the fact that i_α^* decreases.

- If an SSF occurs in sector IV, it is assumed that the fault does not cause a deviation.

The detection method uses the angle $\gamma = \text{atan2}(i_\beta^*, i_\alpha^*)$ to determine the desired current space vector's location in the stator reference frame (see Fig. 2.10).

Trigger Criteria

The normalized control deviation must meet specific trigger criteria to enable the additional voltage test. 1 pu corresponds to the momentary magnitude of the current space vector. The criteria in the simulations and experiments of the example case drive are set as follows:

- In sector I, the magnitude of the deviation space vector $\underline{e}^{\text{s}}$ must be greater than 0.2 pu.

- In sector II, the magnitude of the deviation space vector must be greater than 0.4 pu.

- If the magnitude of $\underline{e}^{\text{s}}$ is greater than 0.2 pu in sector III, the additional voltage test is not activated immediately due to the fact that the deviation decreases autonomously and rapidly. The test is enabled in the following period in sector I. (Note: In this case, the windup in the healthy half-plane is usually negligible and does not interfere with the fault detection.)

- If the control deviation leaves the faulty half-plane in sector IV, the additional voltage test is triggered once again in the direction of the faulty inverter legs second switch, to confirm a full-leg open circuit fault.

To decrease the proposed detection method's sensitivity towards noise, it is suggested to observe the absolute values of the control deviation when the desired current amplitude is lower than a specific value.

Dynamic Response Model

The control deviation is calculated from the difference between the desired and the measured currents. To ensure the detection method's robustness with regard to rapid set point changes, it is necessary to model the dynamic response of the drive's current control loop. A simple way to describe this response is possible in the common case that the PI-controllers' reset time t_r for the stator current components i_d and i_q is chosen equal to the stator time constant, i.e.,:

$$t_\mathrm{r} = \frac{L_\mathrm{s}}{R_\mathrm{s}}. \tag{2.13}$$

The current control loop's open loop transfer function is given by [85]:

$$\underline{O}(\underline{s}) = \underbrace{G\frac{\underline{s}t_\mathrm{r}+1}{\underline{s}t_\mathrm{r}}}_{\text{PI-controller}} \underbrace{\frac{1}{R_\mathrm{s}+\underline{s}L_\mathrm{s}}}_{\text{plant}}, \tag{2.14}$$

where G is the controller gain. For $t_\mathrm{r} = \frac{L_\mathrm{s}}{R_\mathrm{s}}$, the closed loop transfer function becomes a low pass filter of order 1 (PT1 element):

$$\underline{C}(\underline{s}) = \frac{\underline{I}_\mathrm{d}(\underline{s})}{\underline{I}^*_\mathrm{d}(\underline{s})} = \frac{\underline{I}_\mathrm{q}(\underline{s})}{\underline{I}^*_\mathrm{q}(\underline{s})} = \frac{\underline{O}(\underline{s})}{1+\underline{O}(\underline{s})} = \frac{1}{\underline{s}\frac{L_\mathrm{s}}{G}+1}. \tag{2.15}$$

Eq. (2.15) shows that the drive's dynamic response can be modeled by filtering the desired currents i^*_d and i^*_q with PT1 elements with the time constant $t_\mathrm{PT1} = \frac{L_\mathrm{s}}{G}$. For the implementation in the the detection method, (2.15) is discretized by means of the bilinear transform:

$$\underline{C}(\underline{z}) = \frac{\underline{z}+1}{(1+2t_\mathrm{PT1}f_\mathrm{d})\underline{z}+1-2t_\mathrm{PT1}f_\mathrm{d}}, \tag{2.16}$$

where f_d is the sampling frequency. The dynamic response model can be applied to the detection method by substituting the desired currents i^*_d and i^*_q with the modeled currents $\tilde{i}_\mathrm{d}$ and $\tilde{i}_\mathrm{q}$ in (2.11) and (2.12). The signal flow diagram for this case is illustrated in Fig. 2.11. Fig. 2.12 shows a measured step response of the investigated permanent magnet drive and a step response of $\underline{C}(\underline{z})$ for a step of the current i^*_q.

If the reset time is chosen differently (i.e., $t_\mathrm{r} \neq \frac{L_\mathrm{s}}{R_\mathrm{s}}$), the drives dynamic response can be described by a filter of higher order. However, if the desired currents change slowly, it can be sufficient to use a low order filter or no filter at all. In the latter case, the threshold values in the trigger criteria should be greater than the expected permanent

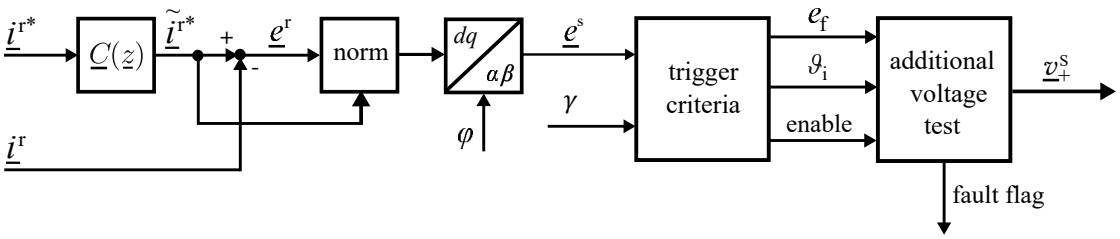

Fig. 2.11: Detailed signal flow diagram of the detection method including the dynamic response model.

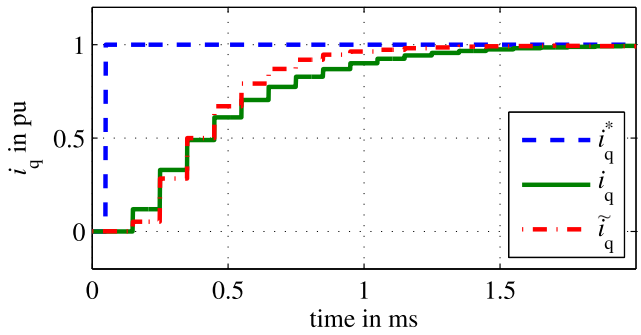

Fig. 2.12: Measured step response: desired current i_q^*, measured current i_q, and modeled current $\tilde{i}_q$.

control deviation [86] in the case of a ramp $e_{\infty,1/s^2} = \frac{L_s}{G}\frac{\Delta i^*}{\Delta t}$, where $\frac{\Delta i^*}{\Delta t}$ is the maximum slope of the desired current ramp.

2.2.3 Testing with an Additional Voltage

This test increases the desired voltage with the aim of eliminating the control deviation within one switching period. The magnitude is chosen as a function of the machines' inductance, the switching period of the inverter, and the control deviation space vector's components. In the common case that $\dot{\varphi}\Psi_{PM}$ is compensated and that the voltage drop at R_s is negligible, the components of the additional voltage space vector that eliminates the control deviation in the case of a healthy switch can be calculated from:

$$v_{\alpha+} = \frac{L_s}{t_s} e_f \cos\vartheta_i, \tag{2.17}$$

$$v_{\beta+} = \frac{L_s}{t_s} e_f \sin\vartheta_i, \tag{2.18}$$

where t_s is the switching period, ϑ_i is the control deviation space vector's ideal angle in the stator reference frame given in Table 2.1, and e_f is the control deviation's component

in the fault direction:

$$e_\mathrm{f} = e_\alpha \cos\vartheta_\mathrm{i} + e_\beta \sin\vartheta_\mathrm{i}. \tag{2.19}$$

As discussed in Section 2.1.4, a zero crossing of the current space vector's component in fault direction is not expected when the back EMF space vector is suitably located. Additionally, the realized component of the average voltage space vector in fault direction is less than or equal to 0.5 pu of its desired value. Based on this information, the fault flag is chosen to occur, if the control deviation in fault direction is reduced to less than $0.5\,e_\mathrm{f}$ by the additional voltage. The additional voltage test can only be performed in one period if the voltage reserve in fault direction is sufficient. The voltage reserve is discussed below.

Relationship between Average and Sampled Currents

The phase currents are typically sampled at positions in the switching pattern, where the currents' momentary values are theoretically equal to the average values in the considered switching period. Due to the fact that the state $i_\alpha = 0$ remains, the switching pattern is no longer symmetrical at low currents, and the sampled currents can deviate from the average currents as illustrated in Fig. 2.13. The sampled currents' values after the additional voltage test depend both on the position at which the currents are sampled and on the faulty switch. This can result in the situation that a potential increase of the component i_α due to the additional voltage test might not be sampled (see $i_{\alpha s1}$ in Fig. 2.13). However, the fact that the actually decreased control deviation is not sampled can be seen as an attribute of the fault, and it does not interfere with the detection.

Voltage Reserve

The voltage reserve for the additional voltage test is defined by the DC-link voltage v_dc and the desired voltage space vector components. If the modulation index $m \leq 1$, the voltage reserve for testing an SSF of switch S_1 can be calculated from:

$$v_{\alpha,\mathrm{res}} = \frac{2}{3} v_\mathrm{dc} - \frac{1}{\sqrt{3}} v_\beta^* \,\mathrm{sign}(v_\beta^*) - v_\alpha^*. \tag{2.20}$$

Fig. 2.14 shows the relationship between the voltage reserve on the position of the desired voltage space vector in the stator reference frame. The voltage reserve decreases with increasing v_α^*, and thus the reserve tends to be lowest during motor operation at high speed.

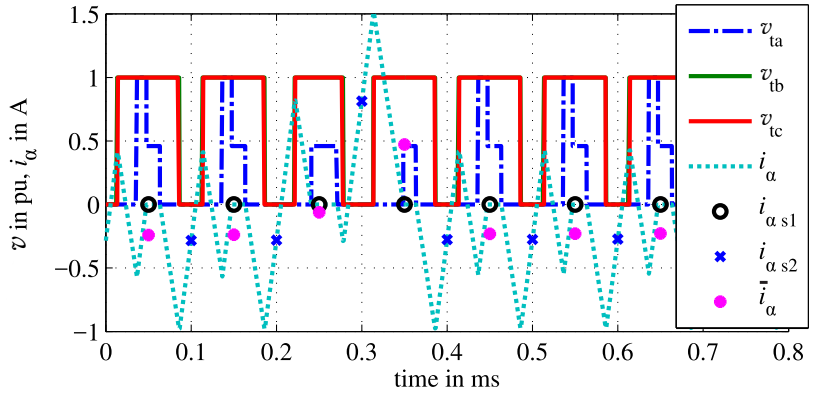

Fig. 2.13: Simulation of sampled and average currents at low i_α. The additional voltage test is activated at $t = 0.2\,\text{ms}$ with the goal to achieve $i_\alpha = 3\,\text{A}$. $i_{\alpha s1}$ and $i_{\alpha s2}$ are the sampled currents in the middle of the switching states 111 and 000, respectively. $\bar{i}_\alpha$ is the average value of i_α in one switching period.

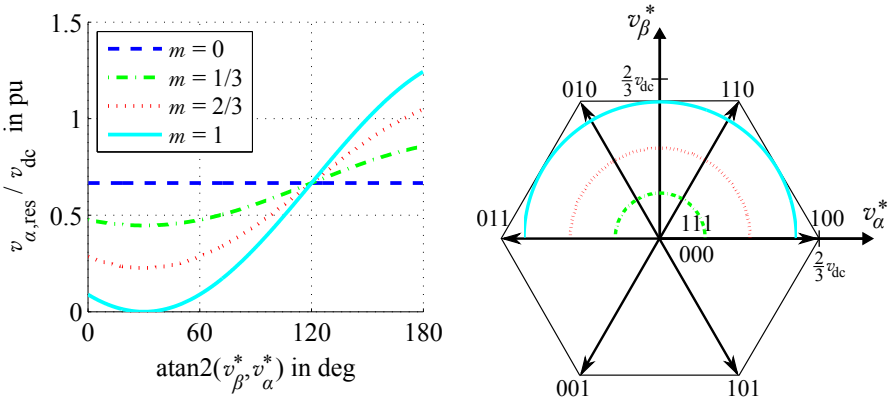

(a) (b)

Fig. 2.14: Voltage reserve as a function of the desired voltage space vector's angle in the stator reference frame at different modulation indices $m = \sqrt{3}\sqrt{v_\alpha^2 + v_\beta^2}/v_{\text{dc}}$. The curves in (a) are symmetrical with respect to the α-axis.

2.3 Simulations and Experiments

2.3.1 Results PMSM

The setup consists of a three-phase surface PMSM (SM1 in Appendix G) connected to an inverter module (a SEMIKRON SKiiP 2) and a speed controlled load and driving machine (IM1 in Appendix G). The inverter operates with space vector modulation, a DC-link voltage of 500 V, and a switching frequency of 10 kHz. To simulate an SSF, the gate signal to the upper switch of the inverter leg a (S_1) is interrupted at the beginning of a switching period during state 000. The desired direct current is set to $i_\mathrm{d}^* = 0$. The control and the detection method are implemented in the experiments on a digital signal processing system (dSPACE DS1005). Inputs of the signal processing system are all three phase currents, the DC-link voltage, and the rotary encoder signal. The phase currents are sampled in the middle of a switching period during state 111. The current control loop of the example case drive is designed to achieve a fast dynamic response during healthy operation. A Norma 5000 power analyzer measures the three phase currents and the inverter output voltages. Note: An overview of the measurement setups is provided in Appendix F.

Fig. 2.15 shows simulation results of an SSF (S_1) occurring at different angles of the current space vector. If the fault occurs in the healthy half-plane or at the beginning of sector I, the control deviation space vector's magnitude increases steadily. In the faulty half-plane, the deviation may increase rapidly depending on the angle at which the fault occurs in sector II. The initial angles ϑ of the control deviation space vector deviate less than 10° from the ideal angles of the deviation in the stator reference frame (0° cf., Table 2.1) in the simulated operating points.

Fig. 2.16 shows a simulation result for detecting an SSF (S_1). The stator current space vector is filtered by means of $\underline{C}(\underline{z})$. Therefore, the filtered control deviation is small during the rapid set point change at $t = -0.005\,\mathrm{s}$, and the additional voltage test is not triggered. However, the test is triggered after the fault occurrence at $t = 0\,\mathrm{s}$. The angle of the control deviation $\vartheta = 3°$ is close to the ideal angle 0°, and the desired voltage in this direction is increased. The additional voltage does not decrease the deviation as expected in the healthy condition, and a fault flag occurs eight switching periods (0.8 ms) after the fault occurrence.

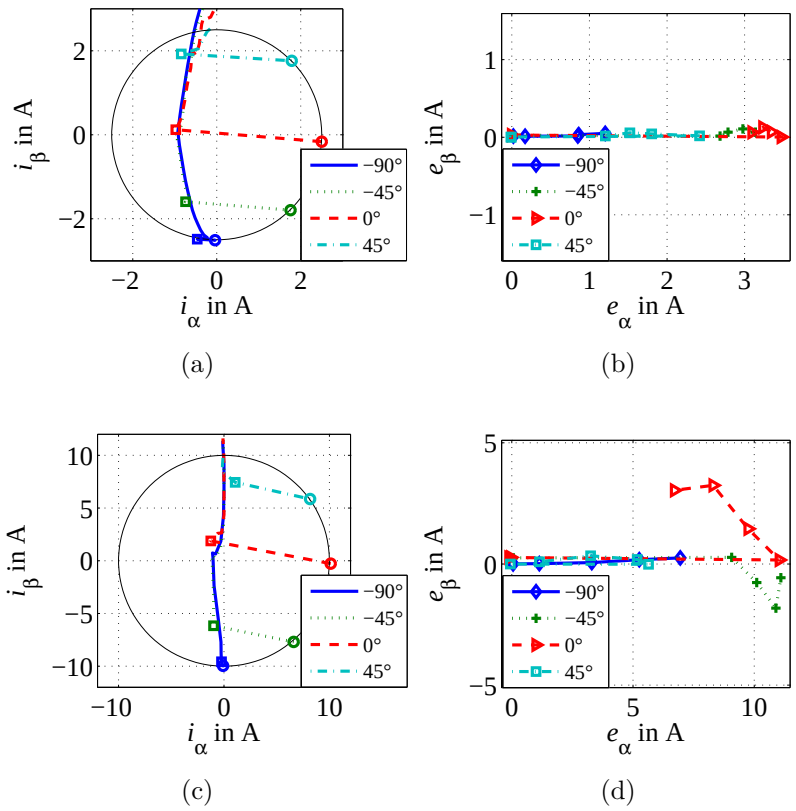

Fig. 2.15: Simulated trajectories of the current space vector in the stator reference frame before and after the SSF (S_1) and first four sampled control deviation space vectors after the fault occurrence in the stator frame at different angles γ of the current space vector and operating points of the PMSM drive: (a) and (b) 200 r/min and $i_\mathrm{q}^* = 2.5\,\mathrm{A}$, (c) and (d) 2000 r/min and $i_\mathrm{q}^* = 10\,\mathrm{A}$. The circles in (a) and (c) indicate the fault occurrence, whereas the rectangles indicate the fulfillment of the trigger criterion. The current space vector is located in sector I for $\gamma = -90°$ and in sector II for $\gamma = -45°$, 0° and 45° in case of an SSF of switch S_1.

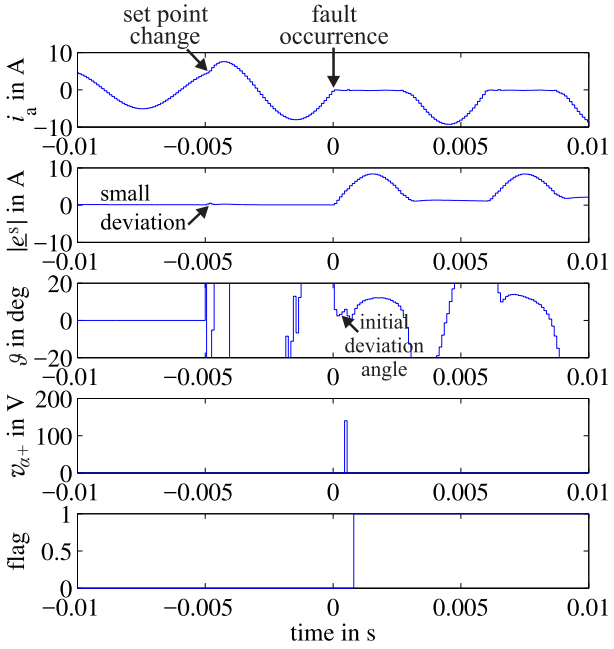

Fig. 2.16: Simulated drive characteristics of the PMSM drive after a set point change of i_q^* from 5 A to 8 A at 2000 r/min and fault occurrence at $\gamma = -90°$. 1: Current in phase a, 2: magnitude of the control deviation space vector, 3: angle of the control deviation space vector in the stator reference frame, 4: α-component of the additional voltage space vector, 5: fault flag. The angle ϑ before the fault occurrence is irrelevant.

Fig. 2.17 shows experimental results of an SSF (S_1) occurring at different angles of the current space vector. The experiments show the same characteristics as the simulation results. If the fault occurs in the healthy half-plane, the deviation increases steadily as soon as the desired current space vector enters the faulty half-plane. If the fault occurs in the faulty half-plane, the deviation increases instantaneously. In sector II, the step is greater than 0.5 pu and depends on the angle at which the fault occurs. If the fault occurs at the end of sector II, the deviation decreases rapidly due to the desired current's reduction in the direction of the fault. In the experiments, the initial deviation angles ϑ deviate less than 15° from the ideal angle in the stator reference frame (0°).

Fig. 2.18 shows experimental results for the detection of an SSF (S_1) during steady state and transient operation in the time domain. The control deviation increases rapidly, and the angles of the control deviation ϑ are close to the ideal angle of 0° (7° and 4° in Figs. 2.18a) and b), respectively). When the trigger criteria are fulfilled, the additional voltage test is enabled. The additional voltage does not decrease the deviation as expected under healthy conditions and the fault flag occurs at eight switching periods (0.8 ms) and seven switching periods (0.7 ms) after the fault occurrence in Figs. 2.18a) and b), respectively.

Fig. 2.19 illustrates experimental results which show the proposed detection method's performance during steady state and transient operation in the stator reference frame. Fig. 2.19a) shows the fault occurrence in sector III and the activation of the additional voltage test in sector I. Figs. 2.19b) and 2.19c) depicts the fault occurrence at the same desired current magnitude and speed during motor and generator operation, respectively, and the additional voltage test's different effects. Figs. 2.19d)-f) show the fault occurrence during transient operation during motor and generator operation, respectively. In this case, the fault occurs on a trajectory defined by the current control loop's transient response and the machine's rotational speed.

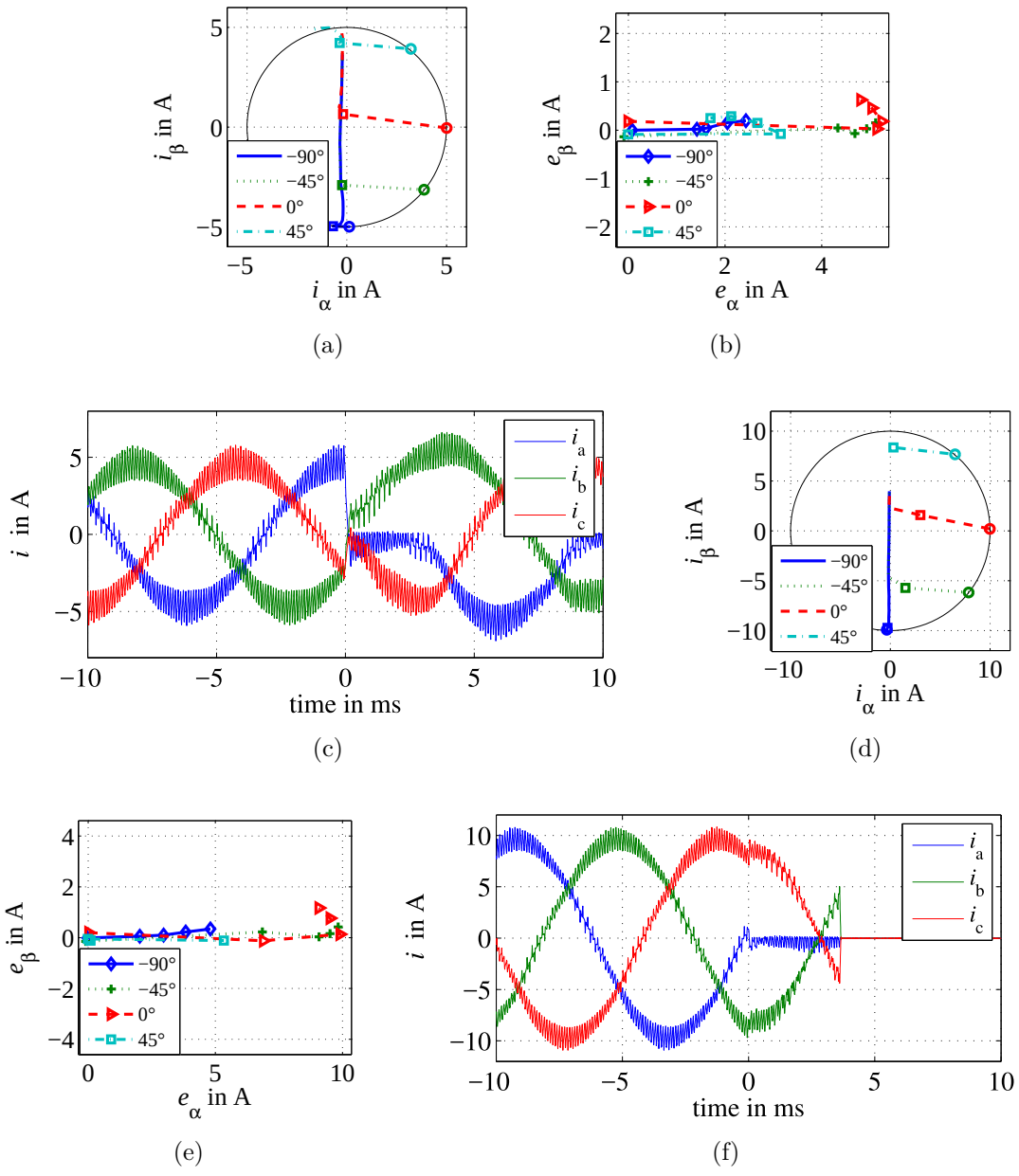

Fig. 2.17: The PMSM drive's measured current trajectories before and after the SSF (S_1) (a) and (d), sampled current control deviations after the fault occurrence in the stator reference frame at different angles γ of the current space vector (b) and (e) and measured phase currents (c) and (f). (a), (b) and (c) at 1000 r/min and $i_q^* = 5$ A and (d), (e) and (f) at 1000 r/min and $i_q^* = 10$ A. The circles in (a) and (d) indicate the fault occurrence, whereas the rectangles indicate the fulfillment of the trigger criterion. The current space vector is located in sector I for $\gamma = -90°$ and in sector II for $\gamma = -45°$, 0° and 45° in case of an SSF of switch S_1. The angles in (c) and (f) are $\gamma = 0°$ and $\gamma = -90°$, respectively. At the 10 A operating point, the inverter was turned off directly after the moment the fault occurred to avoid demagnetizing the example case machine.

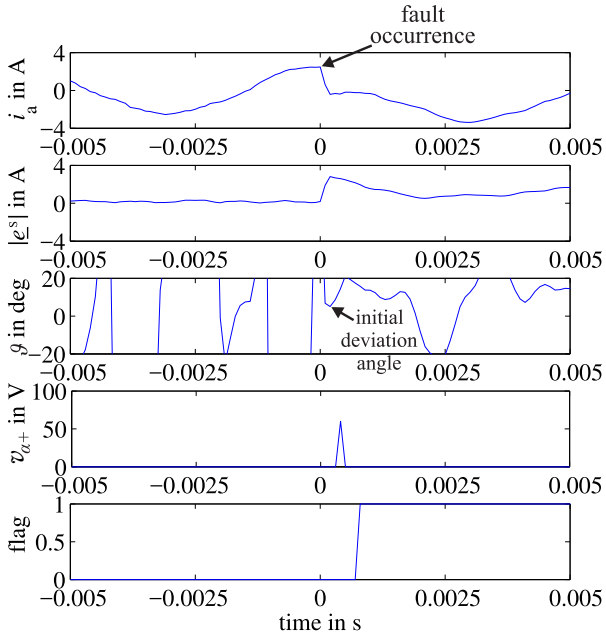

(a)

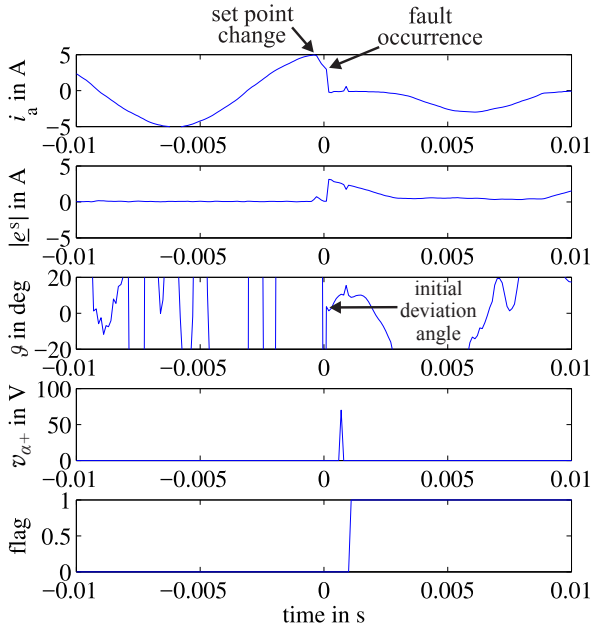

(b)

Fig. 2.18: Measured characteristics of the PMSM drive in the time domain at 2000 r/min and $i_q^* = 2.5\,\mathrm{A}$ (a) and set point step of i_q^* from 5 A to 2.5 A at 1000 r/min (b). 1: Current in phase a, 2: magnitude of the control deviation space vector, 3: angle of the control deviation space vector in the stator reference frame, 4: α-component of the additional voltage space vector, 5: fault flag. The angles γ at the fault occurrence in (a) and (b) are $\gamma = 0°$. The angle ϑ before the fault occurrence is irrelevant.

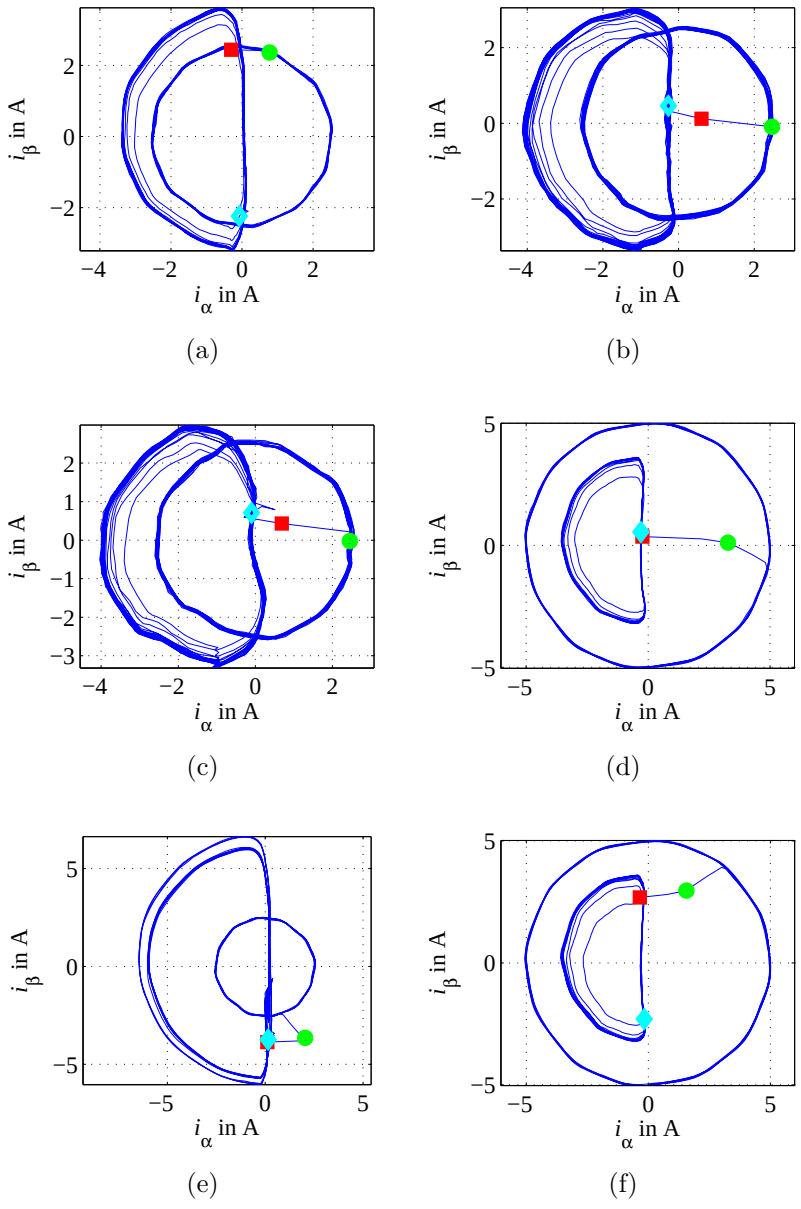

Fig. 2.19: Measured trajectories of the current space vector from the PMSM drive in the stator reference frame before and after the SSF (S_1): (a) 1000 r/min and $i_q^* = -2.5$ A, (b) 2000 r/min and $i_q^* = 2.5$ A, (c) 2000 r/min and $i_q^* = -2.5$ A, (d) 1000 r/min and step of i_q^* from 5 A to 2.5 A, (e) 1000 r/min and step of i_q^* from -2.5 A to -5 A and (f) 1000 r/min and step of i_q^* from 5 A to 2.5 A. The green circles indicate the fault occurrence, the red squares the fulfillment of a trigger criterion and the cyan diamonds the activation of the additional voltage test. The angles γ at the fault occurrence, the corresponding sectors and the detection speeds (including complementary validation) are as follows: (a) 70°, sector III, 62 switching periods (6.2 ms), (b) 0°, sector II, 6 switching periods (0.6 ms), (c) 0°, sector II, 6 switching periods (0.6 ms), (d) 0°, sector II, 8 switching periods (0.8 ms), (e) −60°, sector I, 7 switching periods (0.7 ms) and (f) 70°, sector III, 85 switching periods (8.5 ms).

2.3.2 Results SCIM

The SCIM drive is operated with the same inverter parameters as the PMSM drive above. To adapt the dynamic response model (Section 2.2.2) and the additional voltage test (Section 2.2.3) to the dynamic of the current control loop of the SCIM drive, the stator inductance L_s is replaced by the sum of the stator and rotor leakage inductance of the SCIM.

Fig. 2.20 shows simulation results of an SSF (S_1) occurring at different angles of the current space vector. As in the case of the PMSM drive, the magnitude of the stator current control deviation space vector increases rapidly, and the initial angle of this space vector in the stator reference frame ϑ is close to the ideal angle of 0°.

Fig. 2.21 shows simulation results for the detection of an SSF (S_1) in the time domain. The control deviation increases rapidly, and the angles of the control deviation ϑ are close to the ideal angle of 0°(4° and 5° in Figs. 2.21a) and b), respectively). When the trigger criteria are fulfilled, the additional voltage test is enabled. The additional voltage does not decrease the deviation as expected under healthy conditions, and the fault flag occurs 13 switching periods (1.3 ms) and 9 switching periods (0.9 ms) after the fault occurrence in Figs. 2.21a) and b), respectively. The set point change before the fault occurrence in the latter figure does not increase the control deviation filtered with the adapted dynamic response model for the SCIM drive, as desired.

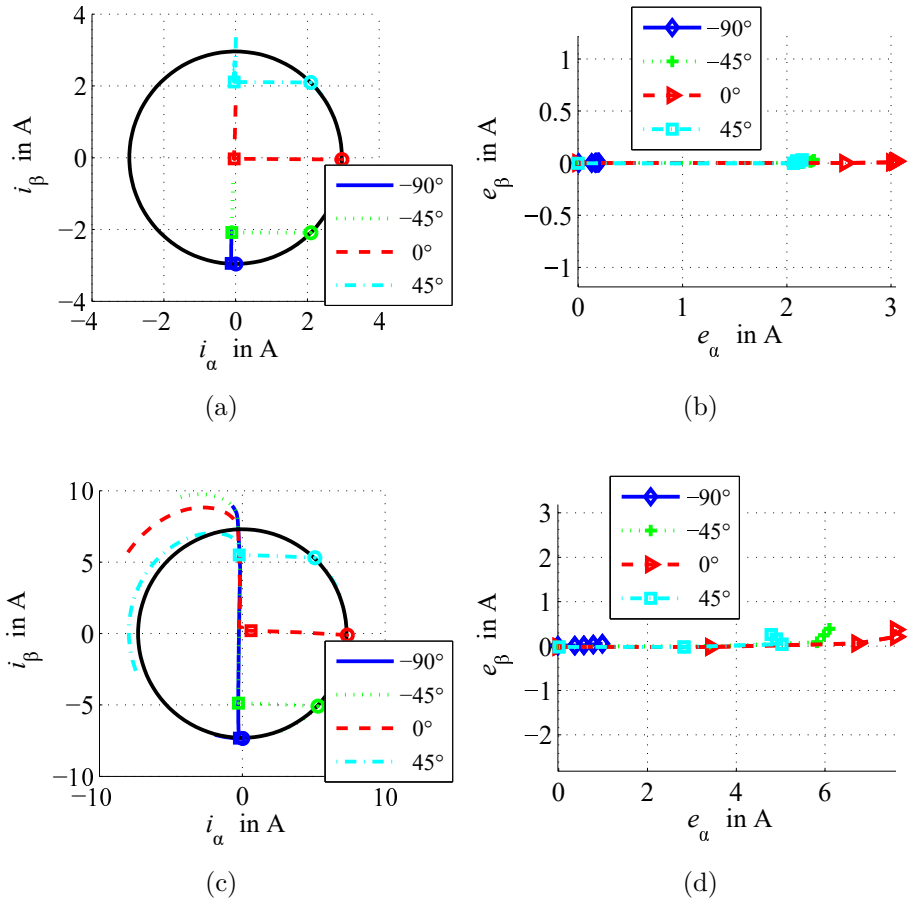

Fig. 2.20: Simulated trajectories of the stator current space vector in the stator reference frame before and after the SSF (S_1), and the first four sampled control deviations after the fault occurrence in the stator frame at different angles γ of the current space vector and operating points of the SCIM drive: (a) and (b) 500 r/min, $i_{sd}^* = 2.1$ A and $i_{sq}^* = 2$ A, (c) and (d) 2500 r/min, $i_{sd}^* = 2.1$ A and $i_{sq}^* = 7$ A. The circles in (a) and (c) indicate the fault occurrence, whereas the rectangles indicate the fulfillment of the trigger criterion. The current space vector is located in sector I for $\gamma = -90°$ and in sector II for $\gamma = -45°$, 0° and 45° in case of an SSF of switch S_1.

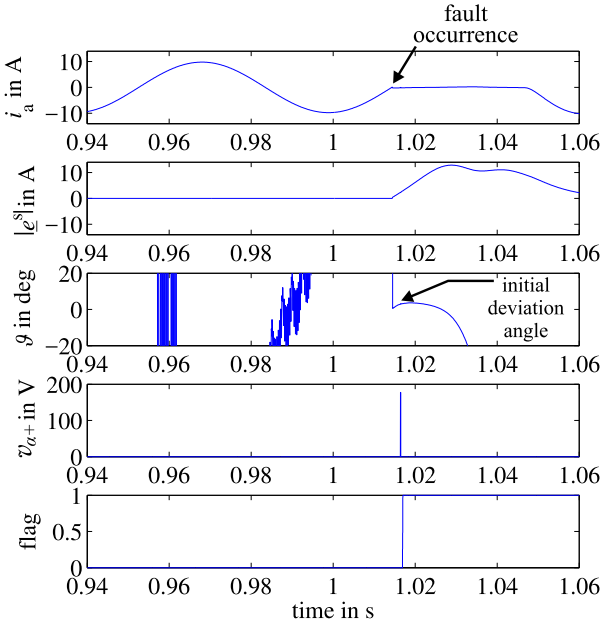

(a)

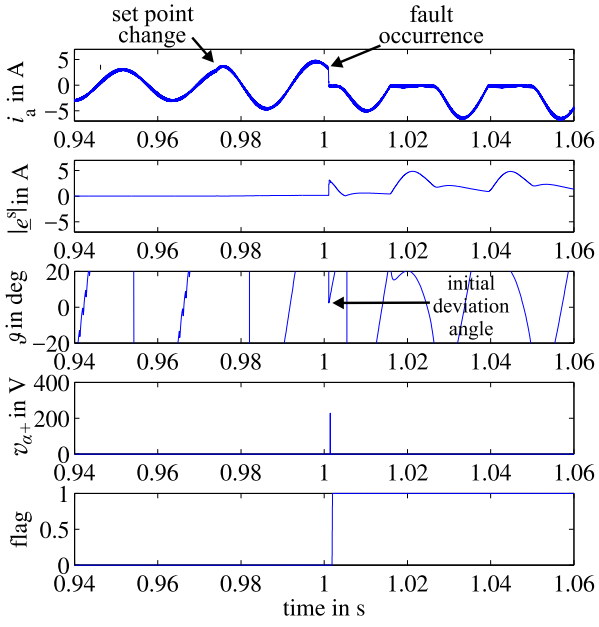

(b)

Fig. 2.21: Simulated characteristics of the SCIM drive in the time domain at 1000 r/min, i^*_{sd} = 6.8 A and i^*_{sq} = -7 A (a), and 2500 r/min, i^*_{sd} = 2.1 A and set point step of i^*_{sq} from 2 A to 4 A (b). 1: Current in phase a, 2: magnitude of the control deviation space vector, 3: angle of the control deviation space vector in the stator reference frame, 4: α-component of the additional voltage space vector, 5: fault flag. The angles γ at the fault occurrence in (a) and (b) are $\gamma = -90°$ and $\gamma = 45°$, respectively. The angle ϑ before the fault occurrence is irrelevant.

2.4 Conclusion

This chapter discusses the behavior of flux-oriented current controlled PMSM and SCIM drives during an SSF. Furthermore, it proposes a detection method for SSFs in such drives. The method quickly detects the fault so as to prevent a possible demagnetization or the tripping of overcurrent protections. The proposed method's detection times in the order of 1 ms are short when compared to the reported detection times of many other methods [35]. More recently, methods with similarly short detection times (less than 1 ms) were proposed in [54, 55] (see also the discussion in Section 1.2). As reported in [56–58], even faster detection speeds ($\leq 10\,\mu$s) are possible with additional hardware in the gate driver. The proposed method does not require additional hardware, however, it requires the knowledge of some drive parameters such as resistances and inductances. Especially when the method is used in dynamic drives that feature rapid changes of the controlled current space vector components, the dynamic current response must also be considered. As with many other detection methods, it is assumed that the fault is complete and not intermitting. If the occurrence of multiple IOCFs is likely in a specific application, the method is to be further investigated for such faults.

Chapter 3

Post-Fault Operation Strategy for an SCIM Drive

This chapter proposes a new post-fault operation strategy for Single Switch inverter open circuit Faults (SSFs). The strategy leads to a significant reduction of the power losses and thus heat development within SCIM drives in comparison to the conventional two-phase operation, which allows higher continuous torques during the post-fault operation (see Chapter 8). Simulated and experimental results are provided to show the performance of the proposed strategy.

3.1 Strategy for SSFs

Many post-fault operation strategies for IOCFs in three-phase drives based on a sinusoidal zero-sequence stator current have been proposed [69–71, 73–78] (see also Section 1.3). To obtain similar flux and torque with these conventional two-phase operation strategies, the phase currents in the two healthy phases have to be increased by a factor of $\sqrt{3}$ during the post-fault operation. It was estimated, apparently based on the increased local power losses in the stator phases, that with the proposed methods, the maximum continuous torque is limited to $\frac{1}{\sqrt{3}} \approx 0.58\,\text{pu}$ in the case of a PMSM drive [75, 81] and to $\frac{1}{3} \approx 0.33\,\text{pu}$ in the case of an SCIM drive [69].

This section proposes a new post-fault operation strategy that can be applied in the special case of an SSF. The strategy enables an increase of the post-fault operation torque in comparison to strategies that apply the conventional two-phase operation.

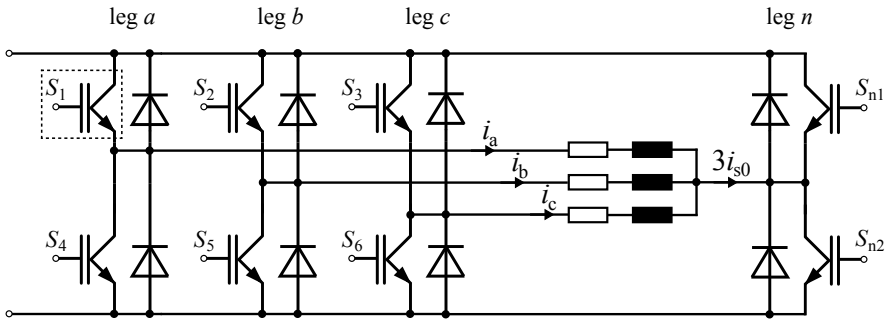

Fig. 3.1: Three-phase induction machine drive with neutral inverter leg.

3.1.1 Topology and Desired Phase Currents

The proposed strategy is based on a four-leg inverter topology [73–78] and the application of a zero-sequence stator current i_{s0}, as shown in Fig. 3.1. The strategy takes advantage of the fact that during an SSF, one switch of the faulty inverter leg remains controllable. If, for example, an SSF of switch S_1 occurs, the output voltage of the inverter leg a can be controlled via S_4 when $i_a < 0$. In contrast to the conventional zero-sequence stator current based operation strategies, the proposed strategy switches between two operation modes, depending on the angle γ of the reference stator current space vector in the stator reference frame, as shown in Fig. 3.2. In the faulty half-plane, two currents with a phase shift of 60 electrical degrees (and the resulting zero-sequence stator current i_{s0}) are applied, while in the healthy half-plane, balanced three-phase currents are applied, as illustrated in Fig. 3.3. In the latter mode, i_{s0} and the corresponding neutral current are zero. The proposed switched two-three-phase operation significantly reduces the power losses and thus heat development compared to conventional two-phase operation with a sinusoidal zero-sequence stator current (see Section 3.3.2).

3.1.2 Current Control Loop

Fig. 3.4 shows the current control structure of a rotor flux-oriented SCIM drive. It consists of standard PI-controllers for the direct and quadrature components of the stator current space vector in the rotor flux-oriented reference frame, a rotor flux observer, and a compensation for disturbance terms in the stator voltage equation. The rotor position and speed are calculated from a rotary encoder signal.

For the application of the proposed post-fault operation strategy, this control structure is extended by the block “zero-sequence controller.” This block is enabled after the

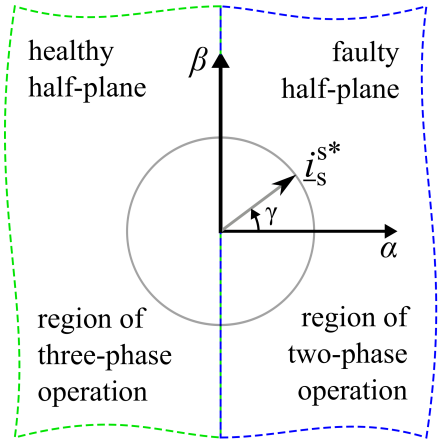

Fig. 3.2: Reference current space vector in the stator reference frame and regions of operation for the proposed switched two-three-phase operation after an SSF of switch S_1.

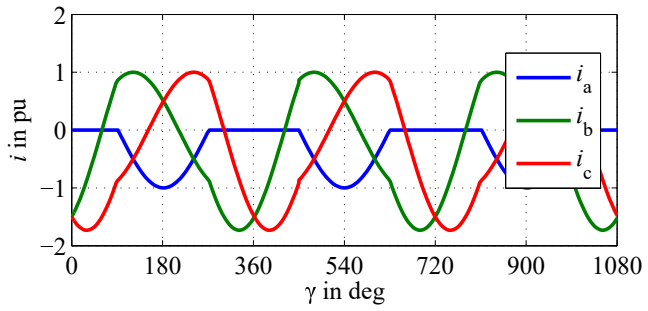

(a)

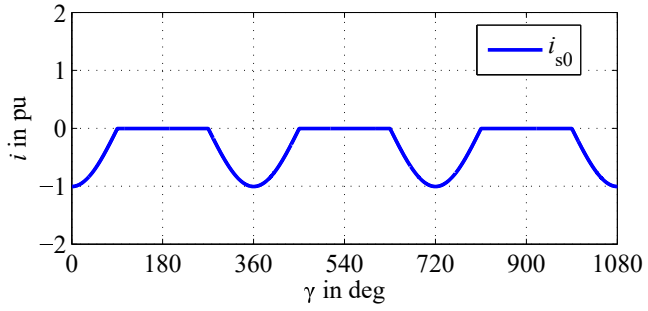

(b)

Fig. 3.3: Desired phase currents (a) and the resulting zero-sequence stator current (b) for the proposed switched two-three-phase operation in case of an SSF of switch S_1.

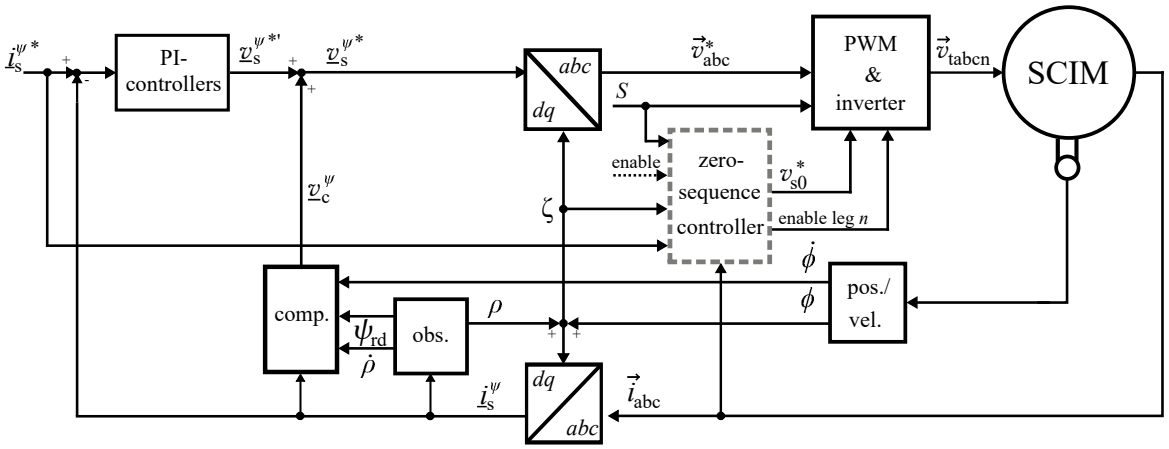

Fig. 3.4: Current control structure of a rotor flux-oriented SCIM drive that has been extended by a zero-sequence controller for the post-fault operation.

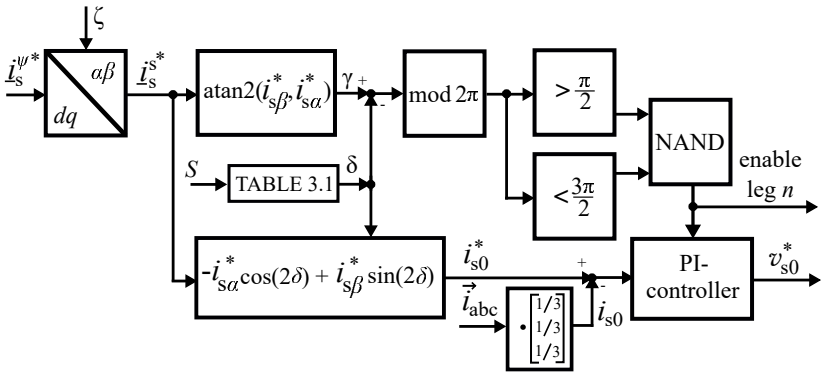

Fig. 3.5: Inner structure of the zero-sequence controller.

detection of an SSF of the faulty switch S. The activation signal of the block "enable" and the signal of the faulty switch S are provided by a fault detection algorithm.

Fig. 3.5 shows the inner structure of the proposed zero-sequence controller. The angle of the rotor flux space vector in the stator reference frame ζ is used for the transformation of the desired stator current space vector $\underline{i}_\mathrm{s}{}^*$ from the rotor flux-oriented into the stator reference frame. The angle of $\underline{i}_\mathrm{s}{}^*$ in the stator reference frame $\gamma = \mathrm{atan2}(i^*_{\mathrm{s}\beta}, i^*_{\mathrm{s}\alpha})$ is used for the determination of the half-plane where this space vector is located. The angle δ is subtracted from γ to consider the influence of the orientation of the half-planes on the faulty switch S. The values of δ are summarized in Table 3.1.

Table 3.1: Transformation angles for the rotation of the reference frame.

faulty switch S	S_1	S_2	S_3	S_4	S_5	S_6
δ	0	$\frac{2\pi}{3}$	$\frac{4\pi}{3}$	π	$-\frac{\pi}{3}$	$\frac{\pi}{3}$

When the space vector is located in the faulty half-plane, a PI-controller for the zero-sequence stator current and the switches of the neutral inverter leg n are enabled (enable leg $n = 1$). In the healthy half-plane, the current controller and the switches of the neutral inverter leg n are disabled (enable leg $n = 0$). The negated signal of enable leg n and the faulty switch S are also used in the inverter logic to enable ($\overline{\text{enable leg } n} = 1$) and disable ($\overline{\text{enable leg } n} = 0$) the healthy switch of the faulty inverter leg.

The zero-sequence stator current i_{s0} is controlled by a PI-controller. The open loop transfer function for the zero-sequence stator current is modeled by:

$$O(s) = \underbrace{G\frac{st_{\text{r}}+1}{st_{\text{r}}}}_{\text{PI-controller}}\underbrace{\frac{1}{R_0+sL_0}}_{\text{plant}}, \tag{3.1}$$

with the controller gain G and the plant from (3.15). The resetting time t_{r} of the PI-controller is chosen equal to the equivalent stator time constant of the zero-sequence system:

$$t_{\text{r}} = \frac{L_0}{R_0}. \tag{3.2}$$

Note: The parameters R_0 and L_0 are not necessarily constant and depend on the stator frequency, speed and saturation level (cf., Sections 3.1.3, 3.2, and 4.3.2.) Furthermore, causes other than a zero-sequence stator current can lead to zero-sequence voltages in the control loop, such as saturation space harmonics (cf., Section 4.3.2), space harmonics caused by the rotor magnetomotive force, and the inverter nonlinearity (dead time and the voltage drops of the semiconductors). The use of a PI-controller to control i_{s0} was chosen over a model based compensation based on (3.14) or (3.15), due to its ability to compensate some of the parameter deviations and disturbance voltages.

The output of the controller v^*_{s0} is solely injected via the voltage of the neutral inverter leg n. To avoid a windup when the switches of the neutral leg n are disabled, the integrator of the PI-controller is set to zero if enable leg $n = 0$. The desired zero-sequence current i^*_{s0} in the faulty half-plane can be obtained on the condition that the phase current of the faulty phase is zero [74], and it depends on the faulty inverter leg. As discussed in [74], the desired zero-sequence stator current is $i^*_{\text{s0}} = -i_{\text{s}\alpha}$, in case of an open circuit fault in leg a. The desired current for the faults in the different inverter legs can be calculated by means of δ, as shown in Fig. 3.5.

3.1.3 Model of an SCIM during the Post-Fault Operations

The main system (fundamental wave) of the induction machine is modeled by using the well-established relationships to describe the space vectors of the voltages, the currents, and the flux linkages, all in the stator reference frame [87]:

$$\underline{v}_{\mathrm{s}}^{\mathrm{s}} = R_{\mathrm{s}}\underline{i}_{\mathrm{s}}^{\mathrm{s}} + \dot{\underline{\psi}}_{\mathrm{s}}^{\mathrm{s}}, \tag{3.3}$$

$$0 = R_{\mathrm{r}}\underline{i}_{\mathrm{r}}^{\mathrm{s}} + \dot{\underline{\psi}}_{\mathrm{r}}^{\mathrm{s}} - j\dot{\phi}\underline{\psi}_{\mathrm{r}}^{\mathrm{s}}, \tag{3.4}$$

$$\underline{\psi}_{\mathrm{s}}^{\mathrm{s}} = L_{\sigma\mathrm{s}}\underline{i}_{\mathrm{s}}^{\mathrm{s}} + \underline{\psi}_{\mathrm{m}}^{\mathrm{s}}, \tag{3.5}$$

$$\underline{\psi}_{\mathrm{r}}^{\mathrm{s}} = L_{\sigma\mathrm{r}}\underline{i}_{\mathrm{r}}^{\mathrm{s}} + \underline{\psi}_{\mathrm{m}}^{\mathrm{s}}, \tag{3.6}$$

$$\underline{\psi}_{\mathrm{m}}^{\mathrm{s}} = L_{\mathrm{m}}(\underline{i}_{\mathrm{s}}^{\mathrm{s}} + \underline{i}_{\mathrm{r}}^{\mathrm{s}}), \tag{3.7}$$

where $\underline{v}_{\mathrm{s}}^{\mathrm{s}}$ is the stator voltage, $\underline{i}_{\mathrm{s}}^{\mathrm{s}}$ is the stator current, $\underline{i}_{\mathrm{r}}^{\mathrm{s}}$ is the rotor current, $\underline{\psi}_{\mathrm{m}}^{\mathrm{s}}$, $\underline{\psi}_{\mathrm{s}}^{\mathrm{s}}$ and $\underline{\psi}_{\mathrm{r}}^{\mathrm{s}}$ are the magnetization, stator and rotor flux linkage, respectively, R_{s} is the stator resistance, R_{r} is the rotor resistance, L_{m}, $L_{\sigma\mathrm{s}}$ and $L_{\sigma\mathrm{r}}$ are the magnetization, stator leakage and rotor leakage inductance, respectively, and ϕ is the electrical rotor angle.

When using a zero-sequence stator current, the zero-sequence system of the induction machine must also be considered. It is assumed that due to the symmetry of the three-phase winding, the zero-sequence system does not lead to a fundamental wave of the stator magnetomotive force. However, it causes space harmonics, with the third harmonic being the dominant one. The zero-sequence system is modeled in the stator reference frame [J2]:

$$v_{\mathrm{s0}} = R_{\mathrm{s0}}i_{\mathrm{s0}} + \dot{\psi}_{\mathrm{s0}}, \tag{3.8}$$

$$0 = R_{\mathrm{r3}}\underline{i}_{\mathrm{r3}}^{\mathrm{s}} + \dot{\underline{\psi}}_{\mathrm{r3}}^{\mathrm{s}} - j3\dot{\phi}\underline{\psi}_{\mathrm{r3}}^{\mathrm{s}}, \tag{3.9}$$

$$\psi_{\mathrm{s0}} = L_{\sigma\mathrm{s0}}i_{\mathrm{s0}} + \mathrm{Re}\{\underline{\psi}_{\mathrm{m3}}^{\mathrm{s}}\}, \tag{3.10}$$

$$\underline{\psi}_{\mathrm{r3}}^{\mathrm{s}} = L_{\sigma\mathrm{r3}}\underline{i}_{\mathrm{r3}}^{\mathrm{s}} + \underline{\psi}_{\mathrm{m3}}^{\mathrm{s}}, \tag{3.11}$$

$$\underline{\psi}_{\mathrm{m3}}^{\mathrm{s}} = L_{\mathrm{m3}}(i_{\mathrm{s0}} + \underline{i}_{\mathrm{r3}}^{\mathrm{s}}), \tag{3.12}$$

with the space vectors and parameters of the zero-sequence system: v_{s0} is the stator voltage, i_{s0} is the stator current, $\underline{i}_{\mathrm{r3}}^{\mathrm{s}}$ is the rotor current, $\underline{\psi}_{\mathrm{m3}}^{\mathrm{s}}$, ψ_{s0}, and $\underline{\psi}_{\mathrm{r3}}^{\mathrm{s}}$ are the magnetization, stator and rotor flux linkage, respectively, R_{s0} is the stator resistance, R_{r3} is the rotor resistance, and L_{m3}, $L_{\sigma\mathrm{s3}}$, and $L_{\sigma\mathrm{r3}}$ are the magnetization, stator leakage and rotor leakage inductance, respectively.

The electromagnetic torque is calculated from the sum of the torque of the main

system τ_f and the torque of the zero-sequence system τ_0. For the example case that the number of pole pairs is $p = 1$, the torque is calculated with:

$$\tau = \underbrace{-\frac{3}{2}\mathrm{Im}\{\underline{\psi}^\mathrm{s}_\mathrm{m}\overline{\underline{i}^\mathrm{s}_\mathrm{s}}\}}_{\tau_\mathrm{f}} \underbrace{-9\,\mathrm{Im}\{\underline{\psi}^\mathrm{s}_\mathrm{m3} i_\mathrm{s0}\}}_{\tau_0}, \tag{3.13}$$

where $\overline{\underline{i}^\mathrm{s}_\mathrm{s}}$ is the complex conjugate of $\underline{i}^\mathrm{s}_\mathrm{s}$. The voltage v_{s0} can be modeled by means of (3.8) and (3.10):

$$v_\mathrm{s0} = R_\mathrm{s0} i_\mathrm{s0} + L_{\sigma\mathrm{s0}} \dot{i}_\mathrm{s0} + \mathrm{Re}\{\dot{\underline{\psi}}^\mathrm{s}_\mathrm{m3}\}. \tag{3.14}$$

The authors of [73] suggested describing u_s0 by an RL network:

$$v_\mathrm{s0} = R_0 i_\mathrm{s0} + L_0 \dot{i}_\mathrm{s0}. \tag{3.15}$$

In [73], the following estimations are proposed that will examined below: $R_0 = R_\mathrm{s}$ and $L_0 = L_{\sigma\mathrm{s}}$.

3.2 Parameter Determination

The parameters of the example case machine (IM1 in Appendix G) used for the controller design were determined by means of different experiments. An overview of the measurement setups is provided in Appendix F. The parameters of the main system were determined from standard tests (no-load, locked-rotor, and load test). The tests for the determination of the parameters of the zero-sequence system were determined from tests with series-connected windings. The power source in these tests was an analog three-phase power amplifier. The stator resistance of the zero-sequence system R_s0 equals the phase resistance, and it was obtained by DC-measurements. The magnetization characteristic of the zero-sequence system was determined by means of voltage steps and the integration of the stator voltage (cf., also Section 4.3). Fig. 3.6a) shows the magnetization flux linkages of the main system and the stator flux linkage of the zero-sequence system as a function of the magnetizing current of the main system and the zero-sequence magnetizing current, respectively.

For the determination of further zero-sequence system parameters and the investigation of the torque characteristics, the results from tests with a sinusoidal zero-sequence stator voltage with a constant amplitude and frequency but variable rotational speed were compared with the parametrized model. The tests showed a nonzero torque of

the zero-sequence system of the example case machine and the domination of the third space harmonic. Fig. 3.6b) shows measured torque-speed curves of the zero-sequence system at a stator frequency of 5 Hz and 10 Hz and the modeled torque which was computed by the second term of (3.13).

Fig. 3.7 illustrates the variability of the control loop parameters R_0 and L_0 in the experiments. More constant values occur at higher relative speeds between the zero-sequence space harmonics and the rotor, which is obtained at higher rotational speeds in the experiments. However, in a rotor flux-oriented drive, such higher relative speeds occur at lower rotational speeds than the experiments discussed here. This is caused by the adaption of the stator frequency to the rotational speed, as illustrated in Appendix C. As is obvious from Fig. 3.7, the proposed equations $R_0 = R_\mathrm{s}$ and $L_0 = L_{\sigma\mathrm{s}}$ [73] provide suitable estimates at higher speeds in the case of IM1.

In the test performed here, the main system and the zero-sequence system were investigated independently. As discussed in Section 4.3.2, the magnetization of these systems changes due to saturation interaction when both systems are present simultaneously during the post-fault operations.

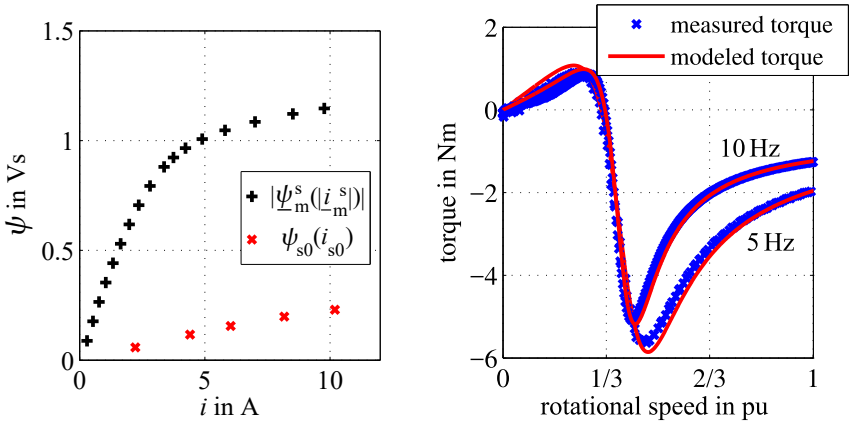

Fig. 3.6: Magnetization flux linkages as a function of the magnetizing current of the main system which was obtained by no-load tests and zero-sequence stator flux linkage as a function of the zero-sequence magnetizing current (a). The latter was obtained by means of voltage steps with series-connected windings. (b) shows the measured and modeled torque of the zero-sequence system at a stator frequency of 5 Hz and 10 Hz and a zero-sequence stator voltage of 15 V and 17 V, respectively. 1 pu corresponds to the synchronous rotational speed of the main system (300 r/min and 600 r/min, respectively).

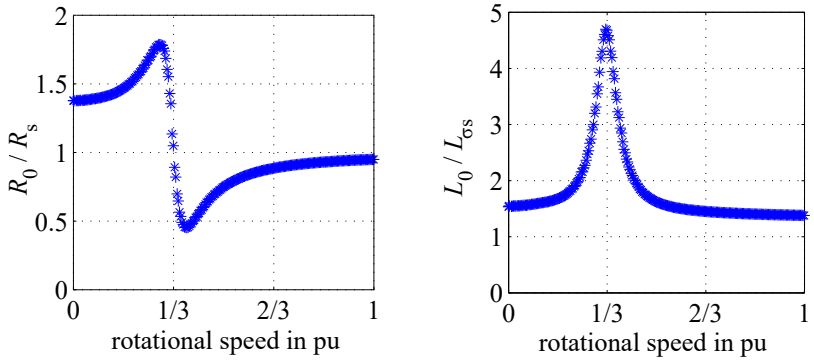

(a) (b)

Fig. 3.7: Control loop parameters R_0 and L_0 with a sinusoidal zero-sequence voltage of 17 V and 10 Hz. The parameters are normalized by the estimations proposed in [73].

3.3 Simulations and Experiments

The setup consists of a three-phase SCIM (IM1 in Appendix G) connected to an inverter module (a SEMIKRON SKiiP 2) and a speed-controlled PMSM as a load (SM1 in Appendix G). The inverter operates with symmetric sinusoidal pulse width modulation with a third harmonic injection, a DC-link voltage of 500 V and a switching frequency of 10 kHz. In the experiments, the control is implemented on a digital signal processing system (dSPACE DS1005). Inputs of the signal processing system are the three phase currents, the DC-link voltage, and the rotary encoder signal. A Norma 5000 power analyzer measures the three phase currents and the three phase voltages. The torque is measured by an HBM T12 torque sensor. In order to simulate an SSF, the gate signal to the upper switch of the first leg (S_1) of the inverter is interrupted.

During the proposed post-fault operation, the pulse width of the healthy switch of the faulty inverter leg is modulated as follows: If the reference current space vector is located in the healthy half-plane, it is modulated in the same manner as during healthy operation. Otherwise, if the space vector is located in the faulty half-plane, it is turned off.

A similar distinction is made for the modulation of the pulse width of the neutral leg: If the space vector is located in the faulty half-plane, it is modulated with sinusoidal pulse width modulation. Otherwise, if the space vector is located in the healthy half-plane, the switches of the neutral leg are turned off.

To extend the output voltage range, a third harmonic is added to the reference signals of all four inverter legs. The output of the PI-controller for the zero-sequence stator current is solely injected via the neutral inverter leg n.

3.3.1 Performance of the Proposed Post-Fault Operation Strategy

Figs. 3.8 - 3.10 show simulated and experimental results at different operating points of the machine. In the simulation depicted in Fig. 3.8, an SSF of switch S_1 occurs at $t = 1.088\,\mathrm{s}$. At $t = 1.137\,\mathrm{s}$, the zero-sequence controller is enabled which reconfigures the drive to the proposed post-fault operation strategy. After the reconfiguration, the components of the stator current space vector in the stator reference frame $i_{s\alpha}$ and $i_{s\beta}$ return to the desired trajectories. The neutral inverter leg n and the PI-controller for the zero-sequence stator current are only activated when the reference stator current space vector is located in the faulty half-plane. The activation enables the flow of the zero-sequence stator current during that time. Figs. 3.9 and 3.10 depict experimental results at 2400 r/min and 120 r/min in which the SSF occurs at $t = 0.274\,\mathrm{s}$ and $t = 0.1\,\mathrm{s}$, respectively. After the reconfiguration at $t = 0.316\,\mathrm{s}$ and $t = 0.4\,\mathrm{s}$, respectively, a rotating stator current space vector is achieved with the proposed strategy. In the results, the reconfiguration of the drive to the post-fault operation was delayed to show the characteristic current wave forms during an SSF. Faster reconfiguration can be required especially during high load or low inertia operating conditions.

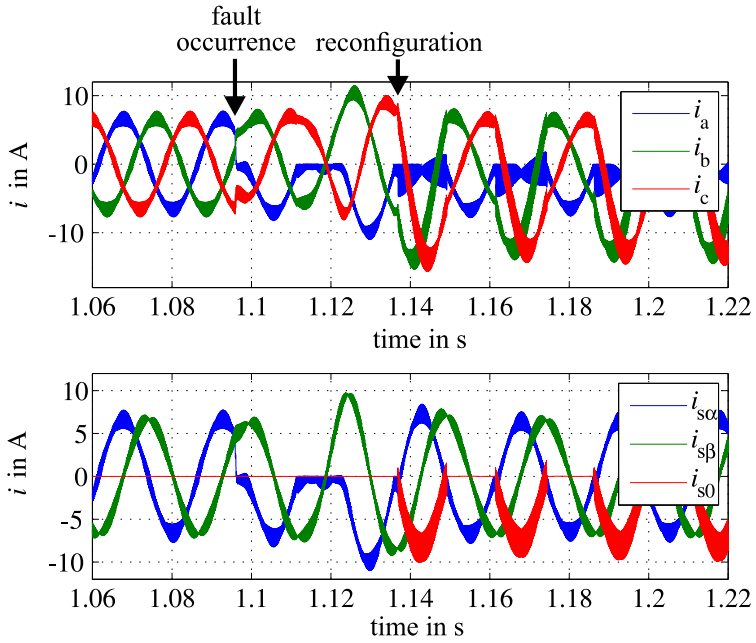

Fig. 3.8: Simulated currents at 2400 r/min and 6.5 A with an SSF of switch S_1 that occurs at $t = 1.088\,\mathrm{s}$ and the reconfiguration of the drive to the proposed post-fault operation strategy at $t = 1.137\,\mathrm{s}$.

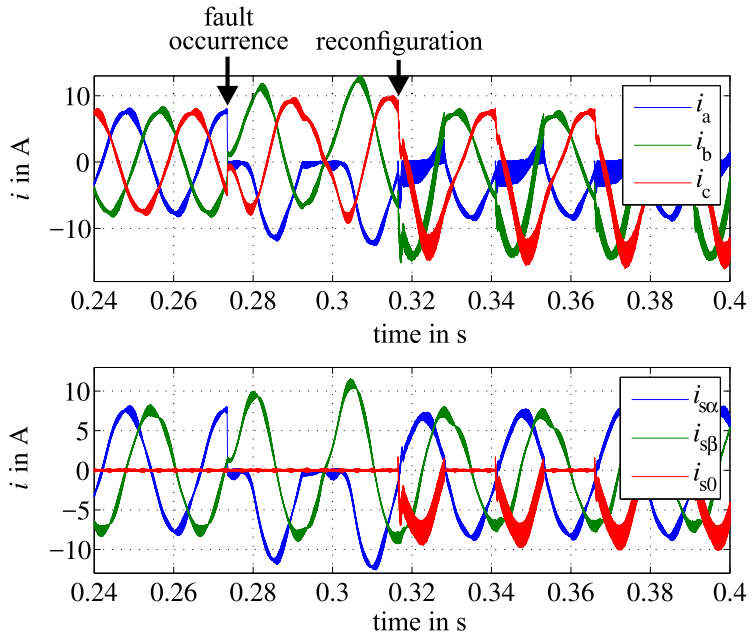

Fig. 3.9: Experimental result at 2400 r/min and 7.5 A obtained with IM1. The SSF of switch S_1 occurs at $t = 0.274\,\mathrm{s}$ and the drive is reconfigured to the proposed post-fault operation strategy at $t = 0.316\,\mathrm{s}$.

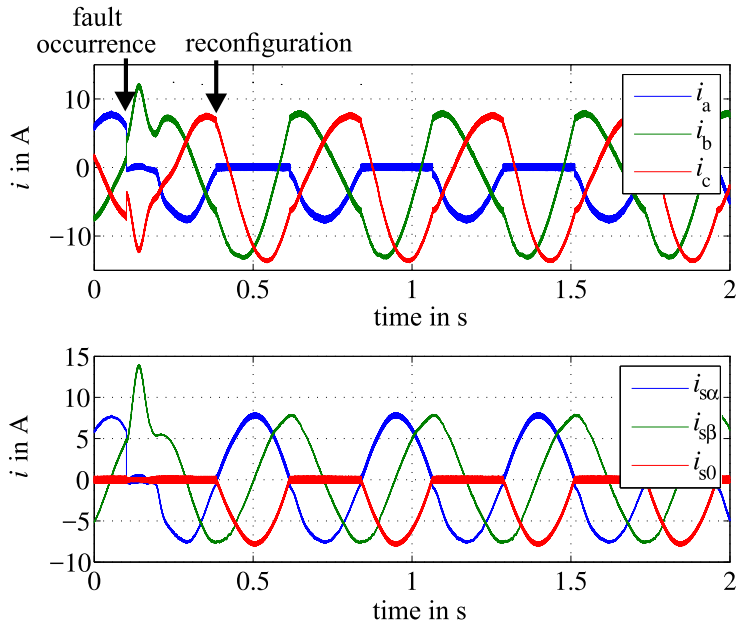

Fig. 3.10: Experimental result at 2400 r/min and 7.5 A obtained with IM1. The SSF of switch S_1 occurs at $t = 0.1\,\mathrm{s}$ and the drive is reconfigured to the proposed post-fault operation strategy at $t = 0.4\,\mathrm{s}$.

3.3.2 Analysis of the Power Losses

The power losses of IM1 are determined by means of electrical power and torque measurements at different operating points of the test drive. For the comparison of the losses, the drive is operated in the standard and two post-fault operation modes:

- three-phase operation (3ph)
- two-phase operation (2ph)
- switched two-three-phase operation (2/3ph)

Fig. 3.11 illustrates the current wave forms in these three operation modes. In both the two-phase and the proposed switched two-three-phase operation mode, the q-component of the stator current space vector i_{sq} is increased to obtain a similar average torque in all three operation modes. Table 3.2 illustrates the rotational speed and the torque at the operating points as well as the measured electrical power P_{el}, the mechanical power P_{mech}, and the derived total losses P_{loss}. Furthermore, it shows the per-unit total losses $P_{\mathrm{loss,pu}}$ with respect to the three-phase operation and the calculated power losses in the stator winding P_{Cu}. These losses are calculated based on the resistances of the stator phases measured immediately after measuring each operating point and the RMS-values of the corresponding phase currents. From the measurements, the following observations can be made:

- During the post-fault operations, the power losses increase significantly with respect to the standard three-phase operation. During the two-phase operation (2ph) the loss is approximately 1.70 - 1.90 pu (i.e., a factor of 1.7 - 1.9 greater than during the three-phase operation), whereas during the proposed switched two-three-phase operation (2/3ph), the ratio is significantly lower (approximately 1.35 - 1.45, i.e., a factor of 1.35 - 1.45 greater).
- During the post-fault operations, the stator winding losses significantly increase because of increased RMS-values of the stator currents (see Fig. 3.11). However, a comparison with the increase in the total losses shows that the increase of the stator winding losses is only responsible for approximately 40 % - 60 % of the total loss increase. This indicates, that other zero-sequence loss sources are present, such as rotor winding losses or iron losses. The presence of such losses could also be expected due to the non-zero torque of the zero-sequence system (see Section 3.2).

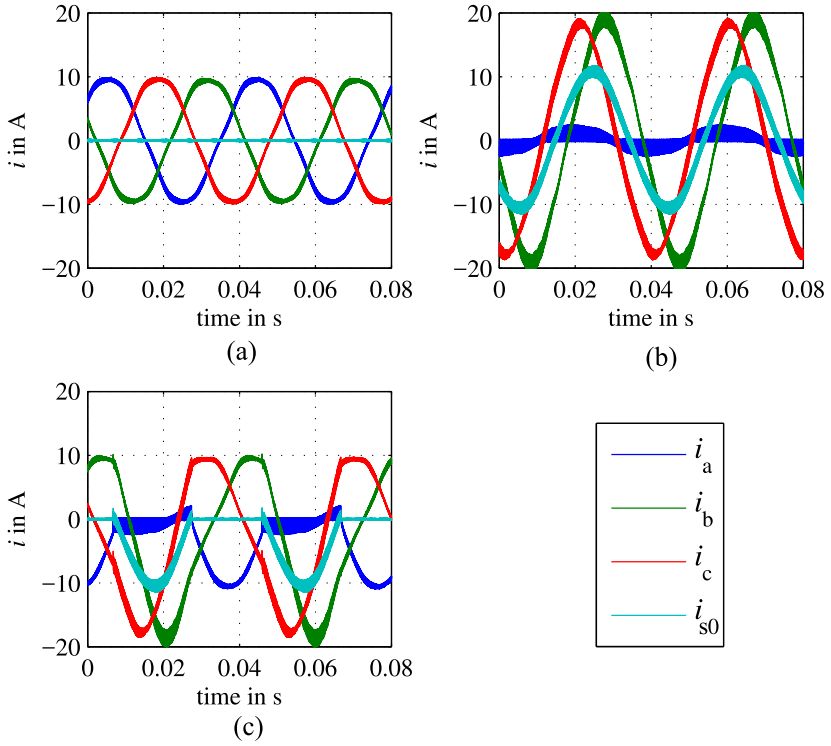

Fig. 3.11: Measured phase currents and zero-sequence stator current during the three operation modes at 1500 r/min: (a) three-phase operation, (b) two-phase operation, and (c) proposed switched two-three-phase operation.

Table 3.2: Measured power losses of IM1 during different operation modes.

Mode	Speed	Torque	P_{el}	P_{mech}	P_{loss}	$P_{\mathrm{loss,pu}}$	P_{Cu}
3ph	750 r/min	4.66 Nm	495 W	366 W	129 W	1.00	49 W
2ph	750 r/min	4.68 Nm	586 W	368 W	218 W	1.68	104 W
2/3ph	750 r/min	4.68 Nm	541 W	368 W	173 W	1.34	77 W
3ph	750 r/min	9.67 Nm	945 W	759 W	186 W	1.00	82 W
2ph	750 r/min	9.68 Nm	1113 W	760 W	353 W	1.90	181 W
2/3ph	750 r/min	9.70 Nm	1028 W	762 W	266 W	1.42	130 W
3ph	1500 r/min	4.61 Nm	921 W	724 W	197 W	1.00	51 W
2ph	1500 r/min	4.61 Nm	1056 W	724 W	332 W	1.80	108 W
2/3ph	1500 r/min	4.60 Nm	989 W	723 W	266 W	1.35	80 W
3ph	1500 r/min	9.59 Nm	1765 W	1506 W	259 W	1.00	80 W
2ph	1500 r/min	9.58 Nm	1985 W	1505 W	480 W	1.85	183 W
2/3ph	1500 r/min	9.57 Nm	1872 W	1503 W	369 W	1.42	132 W

3.4 Conclusion

This chapter proposes a new post-fault operation strategy for SSFs in SCIM drives. The experiments showed that both the conventional and the proposed post-fault strategy basically allow the same torque to be produced as during the standard three-phase operation. However, the experiments also showed increased power losses in the SCIM with the post-fault operation strategies. These power losses are mainly of interest with respect to the resulting heat. Energy savings are typically of secondary interest during the post-fault operations. The resulting increased heat development limits the maximum continuous torque during the post-fault operations. With the proposed strategy, the power losses are increased as compared to the three-phase operation; however, they are reduced by approximately 50 % when compared to conventional post-fault operation strategies with continuous two-phase operation. The proposed strategy thereby increases the maximum continuous torque during the post-fault operation. The experiments demonstrated that the operation strategies lead to significantly increased losses not only with respect to the copper losses in the stator winding. Therefore, the space harmonics of the zero-sequence system in the modeling of the fault-tolerant drive shall be considered, too. Chapters 5 - 8 discuss the heat development, machine temperatures, and maximum continuous torque during the post-fault operations, respectively, with consideration of these harmonics. Chapter 9 discusses alternating torque components occurring with the investigated post-fault operation strategies and proposes a method to reduce these components.

Chapter 4

MMF and Saturation Interaction due to a Zero-Sequence Stator Current

The application of a zero-sequence stator current leads to additional space harmonics that cause additional torques and heat in SCIMs. The joint iron core and the field strength dependent magnetic permeability of the iron lead to a saturation interaction between space harmonics of the balanced three-phase system and the zero-sequence system. In the context of post-fault operations based on zero-sequence stator currents, this interaction affects the machine parameters and torque. This chapter discusses the influence of the stator winding design on the space harmonics and exemplary studies of the saturation interaction at two SCIMs. Furthermore, it discusses the effects of the interaction in the context of the post-fault operations after an IOCF of a rotor flux-oriented drive.

4.1 Discussion of the Stator Magnetomotive Force

The operation of a three-phase machine with an ordinary stator winding with a non-zero zero-sequence stator current leads to additional space harmonics. These space harmonics are part of the MagnetoMotive Force (MMF) of every individual stator phase, and they are not canceled out. The consideration of these space harmonics in the modeling and control of zero-sequence stator current operated three-phase squirrel cage induction machines has been discussed previously in [73,89]. Fig. 4.1 shows the spectra of the stator MMF in the case of a symmetrical three-phase full-pitch winding during the standard three-phase and zero-sequence sator current based post-fault operations. To obtain the same amplitude of the fundamental wave, the phase currents in the

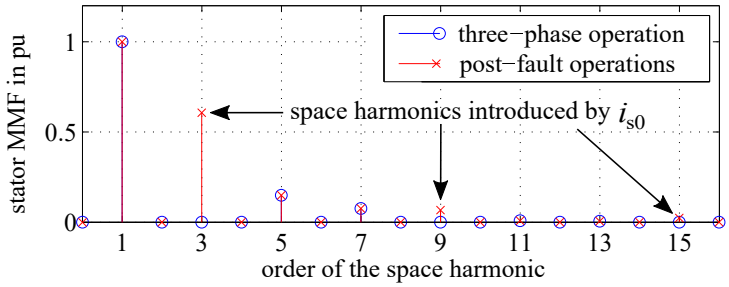

Fig. 4.1: Computed amplitude spectrum of the stator MMF during the three-phase operation and the zero-sequence sator current based post-fault operations when i_{s0} reaches its maximum. The spectrum is computed for a concentrated three-phase full-pitch winding (one slot per pole and phase).

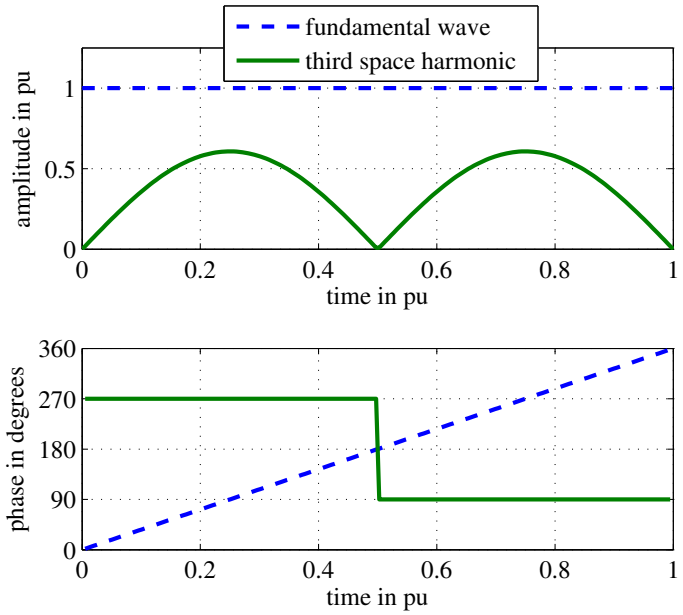

Fig. 4.2: Computed amplitude and phase of the stator MMF during the two-phase post-fault operation as shown in Fig. 1.7b) for one period of the stator currents.

two healthy phases are increased by a factor of $\sqrt{3}$ during the post-fault operations. The additional space harmonics introduced by the zero-sequence stator current have the order $\nu = 3(2\mu - 1)$, $\mu \in \mathbb{N}$, where the third space harmonic is the largest. The spectrum in Fig. 4.1 is calculated for the point in time when i_{s0} reaches its maximum. Fig. 4.2 illustrates the amplitude and the phase of the fundamental wave as well as the third harmonic of the stator MMF for one period of the stator currents during the two-phase operation. The fundamental wave rotates 360 electrical degrees. However, the sinusoidal wave form of the zero-sequence stator current causes a pulsation of the stator MMF's third harmonic.

The amplitudes of the space harmonics caused by the zero-sequence stator current and the related zero-sequence magnetization inductance (see Section 4.2 below) strongly depend on the type of stator winding. Fig. 4.1 shows the MMF spectrum for a winding with one slot per pole and phase. The zero-sequence space harmonics and inductance can be reduced by the same techniques as typically applied for the reduction of the fifth, seventh, eleventh and thirteenth space harmonic, e.g., by means of an increase in the number of stator slots per pole and phase and/or by short-pitching. The zero-sequence stator current's effects on the heat developed in the machine and torque depend on the related space harmonics. These space harmonics can be neglected during the standard three-phase operation as they cancel out. They are, on the contrary, a central element for the modeling of the magnetization behavior during the post-fault operations.

The basic theory of the winding design on the MMF space harmonics is discussed in [99, 100, 103]. [89] addresses the winding factors and the unsaturated zero-sequence magnetization inductance for a full-pitch winding. The results of [89, 99, 100, 103] are reviewed and expanded below for the context of the calculation and the analysis of the influence of the winding design of zero-sequence stator current operated three-phase machine drives.

4.1.1 Analytic Calculation of the MMF Space Harmonics

The instantaneous amplitude of the MMF harmonic with the order ν of a stator coil is given by [103]:

$$\hat{\Theta}_{\nu,\mathrm{ph}} = \frac{2Ni}{\pi}\frac{\xi_\nu}{\nu}, \tag{4.1}$$

where N is the number of turns, i is the instantaneous value of the coil current, and ξ_ν is the winding factor. The winding factor depends on the order of the harmonic, the number of slots per pole and phase, as well as the pitch. It can be calculated from the product of the group factor ξ_{gr} and the pitching factor ξ_{p} [99, 100, 103]:

$$\xi_\nu = \underbrace{\frac{\sin\left(q\nu\frac{\alpha_\mathrm{s}}{2}\right)}{q\sin\left(\nu\frac{\alpha_\mathrm{s}}{2}\right)}}_{\xi_{\mathrm{gr}}} \underbrace{\sin\left(\nu\frac{W_\mathrm{c}}{W_\mathrm{p}}\frac{\pi}{2}\right)}_{\xi_{\mathrm{p}}}, \tag{4.2}$$

where q is the number of slots per pole and phase, α_s is the displacement angle of the slots, W_c is the coil width, and W_p is the pole pitch. The space vectors of the MMF-harmonics can be calculated by the vectorial addition of the phase MMFs. In

the case of a symmetrical three-phase winding, the MMF space vector of the harmonic ν can be calculated from:

$$\underline{\Theta}_\nu = \hat{\Theta}_{\nu,\mathrm{pha}} + \hat{\Theta}_{\nu,\mathrm{phb}} e^{j\frac{2\pi}{3}\nu} + \hat{\Theta}_{\nu,\mathrm{phc}} e^{j\frac{4\pi}{3}}, \tag{4.3}$$

where the amplitudes of the MMFs of the three phases $\hat{\Theta}_{\nu,\mathrm{pha}}$, $\hat{\Theta}_{\nu,\mathrm{phb}}$, $\hat{\Theta}_{\nu,\mathrm{phc}}$ can be calculated by means of (4.1) with the corresponding phase currents. For the balanced three-phase operation, the following phase currents apply:

$$i_\mathrm{a} = \hat{I}\cos(\gamma), \tag{4.4}$$
$$i_\mathrm{b} = \hat{I}\cos(\gamma - 2\pi/3), \tag{4.5}$$
$$i_\mathrm{c} = \hat{I}\cos(\gamma - 4\pi/3), \tag{4.6}$$

whereas, for the continuous two-phase operation, assuming the current amplitude to be constant and the example case of a fault in phase a, the following phase currents apply (cf., also [69]):

$$i_\mathrm{a} = 0, \tag{4.7}$$
$$i_\mathrm{b} = \hat{I}\cos(\gamma - 5\pi/6), \tag{4.8}$$
$$i_\mathrm{c} = \hat{I}\cos(\gamma - 7\pi/6), \tag{4.9}$$

where $\hat{I}$ is the amplitude of the phase currents and γ is the instantaneous current angle. The instantaneous amplitude of the MMF with the order ν can be calculated from the absolute value of the complex space vector:

$$\hat{\Theta}_\nu = |\underline{\Theta}_\nu|. \tag{4.10}$$

By combining (4.1), (4.3), (4.4), (4.5), (4.6), and (4.10), it can be shown that during the three-phase operation, the amplitude of the MMF of the fundamental wave and the occurring space harmonics (fifth, seventh, eleventh, thirteenth,...) are independent of the current angle γ, and the relative amplitude can be calculated from (cf., also [100]):

$$\frac{\hat{\Theta}_\nu}{\hat{\Theta}_1} = \frac{\xi_\nu}{\nu\xi_1} \qquad \nu = 1, 5, 7, 11, 13, \ldots \tag{4.11}$$

During two-phase operation, the amplitudes of the fundamental wave and the space harmonics in (4.11) are lower by a factor of $\sqrt{3}$ during the three-phase operation with the same current amplitude $\hat{I}$, as can be shown by combining (4.1), (4.3), (4.7), (4.8),

(4.9) and (4.10). However, since both the fundamental wave and the space harmonics are affected, (4.11) can also be applied for the two-phase operation.

Space harmonics that are multiples of three are canceled out during the three-phase operation (cf., [89, 100, 103]), and their amplitudes are zero. However, the uneven of these space harmonics are non-zero when the machine is operated with a zero-sequence stator current (cf., [89, 103]). By combining (4.1), (4.3), (4.7), (4.8), (4.9), and (4.10) it can be shown that during the two-phase operation, the MMF space vectors related to the zero-sequence stator current (third, ninth, fifteenth,...) only have a real component, and they pulsate with $\cos(\gamma)$, as illustrated in Fig. 4.2 for the third harmonic. Furthermore, the ratio for the amplitudes of these harmonics due to a zero-sequence stator current doubles when compared to the ratio for the other harmonics (4.11):

$$\frac{\hat{\Theta}_\nu}{\hat{\Theta}_1} = 2\frac{\xi_\nu}{\nu\xi_1} \qquad \nu = 3, 9, 15, ... \tag{4.12}$$

Since the switched two-three-phase operation applies three-phase and two-phase operation for half a period, the relative amplitudes above also apply for this operation mode in the corresponding half-planes (cf., Section 3.1.1).

4.1.2 Discussion of Amplitude Reduction Possibilities

Figs. 4.3 and 4.4 illustrate the influence of the number of slots per pole and phase and the influence of pitching on the space harmonic amplitudes, respectively. The relative amplitudes were calculated by means of (4.11) and (4.12), respectively. The results have been validated by means of high resolution numerical conductor models that apply Ampere's law and the discrete Fourier transform. The results show that especially the third space harmonic has a high amplitude when compared to the other harmonics. For a full-pitch winding, the amplitude of the third space harmonic quickly converges from 0.66 pu (one slot per pole and phase) to 0.44 pu (infinite number of slots per pole and phase), as illustrated in Fig. 4.3. Further reduction can be achieved by pitching the stator winding, as illustrated in Fig. 4.4. A special case occurs with a pitching by 2/3. For such a winding, the third harmonic is zero (cf., [89, 100]). However, such a winding leads to poorly exploited machines, since the fundamental wave is also reduced significantly (down to 0.866 pu when compared to a full-pitch winding). Therefore, in the context of the design and selection of a machine for a fault-tolerant drive, again, a compromise between a good machine exploitation and low parasitic effects of zero-sequence system related harmonics is desirable.

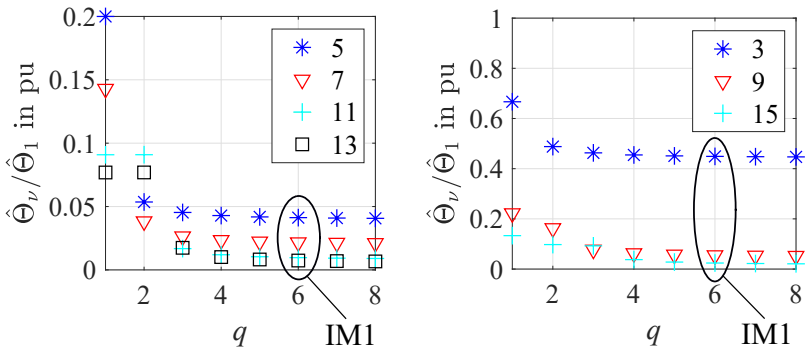

Fig. 4.3: Influence of the number of slots per pole and phase on the amplitudes of the space harmonics for a full-pitch winding. Visualization of the space harmonics of the stator MMF occurring during both the three-phase and the post-fault operations (left) and the space harmonics only occurring during the post-fault operations (right). The MMF harmonics for Induction Machine 1 (IM1) are also included.

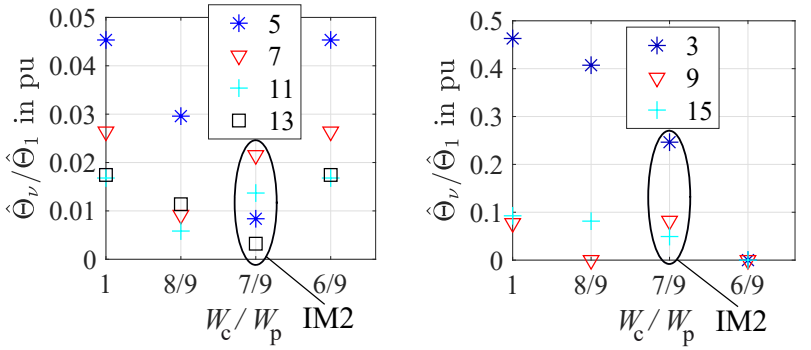

Fig. 4.4: Influence of pitching on the amplitudes of the space harmonics for a winding with 3 slots per pole and phase. Visualization of the space harmonics of the stator MMF occurring during both the three-phase and the post-fault operations (left) and the space harmonics only occurring during the post-fault operations (right). The MMF harmonics for Induction Machine 2 (IM2) are also included.

4.2 Zero-Sequence Magnetization Inductance

The space harmonics of (4.11) with the dominant fundamental wave are associated with the main system, whereas the space harmonics of (4.12) with the dominant third harmonic are associated with the zero-sequence system. [89] discusses a method for the calculation of the unsaturated ratio between the zero-sequence magnetization inductance and the main magnetization inductance based on the winding factors of the third harmonic and the fundamental wave. As shown in [89], for a full-pitch winding with an infinite number of slots per pole and phase, the magnetization inductance of the zero-sequence system for such a winding is approximately 0.1 pu of the magnetization inductance of the main system. Further special ratios can be calculated by applying the method from [89] on a full-pitch winding with one slot per pole and phase (approximately 0.2 pu) or on a winding pitched by 2/3 (0 pu).

Two three-phase squirrel cage induction machines are used as example case machines including experimental analysis (IM1 and IM2 in Appendix G). IM1 has a single layer full-pitch winding with six slots per pole and phase, IM2 has a dual layer winding with three slots per pole and phase and a pitching by 7/9. The corresponding MMF harmonics are indicated in Figs. 4.3 and 4.4. The measurements of the magnetic circuits discussed in the next section allow to calculate the ratios of the unsaturated magnetization inductances of the zero-sequence system and the unsaturated magnetization inductances of the main system. The measured ratio for IM1 is approximately 0.09 pu which is close to the ideal value (0.1 pu). The measured ratio for IM2 is approximately 0.035 pu which is consistent with the reduced space harmonic amplitudes due to the pitching. The ideal value for IM2 calculated based on the method described in [89] is 0.03 pu. These values are valid for the unsaturated case. However, as will be discussed in the next section, a saturation interaction between the main system and the zero-sequence system occurs that significantly affects the magnetization behavior.

4.3 Identification of the Saturation Interaction

4.3.1 Methodology

Due to the magnetization dependent permeability of the magnetic circuit, the flux distribution and the corresponding magnetizing currents do not linearly depend on each other. To analyze the magnetic circuit and the interaction between the main and the zero-sequence systems, experiments with IM1 and IM2 were performed. In

these experiments, stepped DC currents were applied with an analog three-phase power amplifier during the machines' standstill (see Fig. 4.5.) The measurement circuit is illustrated in Appendix F, Fig. F.4.

Different combinations of the magnetization currents of the main system I_{m} and zero-sequence system I_{m3} were chosen to excite these systems and to determine the saturation interaction of these systems. The phase flux linkages $\vec{\Psi}_{\mathrm{abc}}$ were calculated by integrating the stator phase voltages $\vec{v}_{\mathrm{abc}}$ while taking into consideration the voltage drop at the stator resistances:

$$\vec{\Psi}_{\mathrm{abc}} = \int_{t_0}^{t_1} (\vec{v}_{\mathrm{abc}} - \boldsymbol{R}_{\mathrm{abc}} \vec{i}_{\mathrm{abc}}) dt, \tag{4.13}$$

where $\boldsymbol{R}_{\mathrm{abc}}$ is the diagonal matrix of the stator resistances. The integration intervall $[t_0 \ t_1]$ was chosen from a point in time starting shortly before the current steps (t_0) until the integrated flux linkages remain constant after the current steps (t_1). Thereby, the SCIM's rotor currents are quasi zero at t_1, and the magnetizing currents of the main and zero-sequence systems equate to the corresponding stator currents. The circuit was demagnetized after the steps by applying a low frequency and slowly decreasing stator current space vector.

The integrated phase flux linkages were transformed into the stator flux linkage space vector $\underline{\Psi}_{\mathrm{s}}^{\mathrm{s}}$ (see Clarke Transformation in Appendix I) and the zero-sequence stator flux linkage Ψ_{s0}. The latter can be calculated analogously to the zero-sequence stator current (1). The magnitudes of the magnetization flux linkages of the main system

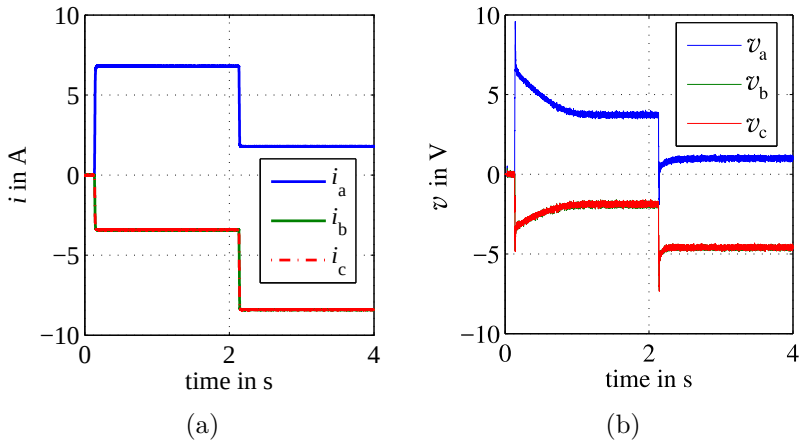

Fig. 4.5: Measured phase current wave forms (a) and phase voltage wave forms (b) both for $|\underline{i}_{\mathrm{s}}^{\mathrm{s}}| = 6.8\,\mathrm{A}$ and $i_{\mathrm{s0}} = 0\,\mathrm{A}$ as well as $|\underline{i}_{\mathrm{s}}^{\mathrm{s}}| = 6.8\,\mathrm{A}$ and $i_{\mathrm{s0}} = -5\,\mathrm{A}$ during the experiments with stepped DC currents with IM1.

Ψ_m and the zero-sequence system Ψ_m3 were calculated by subtracting the estimated stator leakage flux linkages. They were computed by means of leakage inductances that were determined by use of locked-rotor tests and load tests with series-connected stator windings, respectively (cf., Section 3.2).

The measurements with IM2 were performed by means of measurement coils (referred to as Flux Linkage Measurement Systems, FLMSs, see Appendix H.3). The coils are aligned to determine the α-component as well as the usually inaccessible β-component of the zero-sequence flux linkage. The application of the coils has the further advantage, that the voltage drop at the Ohmic resistance does not affect the flux linkage integration ($\vec{i}_\mathrm{abc}$ in (4.13) is zero).

4.3.2 Results

Figs. 4.6 and 4.7 show the measured magnetizing currents as a function of the magnetization flux linkages of the main and zero-sequence systems for IM1. The results show a significant saturation interaction between the main and the zero-sequence system. At non-zero zero-sequence flux linkage, the magnetizing current of the main system increases, due to saturation. Similarly, at non-zero magnetization flux linkage of the main system, the magnetizing current of the zero-sequence system increases, due to saturation. The main system's magnetization flux linkage's influence on the zero-sequence magnetizing current is significantly higher than the influence of the zero-sequence magnetization flux linkage on the magnetizing current of the main system. The magnetic circuit of IM2 exhibits the same behavior. The description of the relations between the magnetization flux linkages and magnetizing currents and the corresponding saturation interaction for both machines IM1 and IM2 and a comparison with the measurement results are provided in the following Section 4.4.

The results in Figs. 4.6 and 4.7 are obtained for a constant position of the main system's magnetizing current space vector in the stator reference frame. As shown in Fig. 4.8, the zero-sequence system's flux linkage of IM1 also depends on the angle of this current space vector. Such an angle dependent flux linkage can be caused by saturation space harmonics introduced by the main system currents. In contrast to the harmonics introduced by the zero-sequence magnetizing current, saturation space harmonics are excited by the balanced three-phase currents and occur due to a varying saturation of the parts of the magnetic circuit [100]. Note that during the experiments, a zero-sequence flux linkage was observed even when the zero-sequence magnetizing current was zero, which can be explained by such saturation space harmonics. The maximum

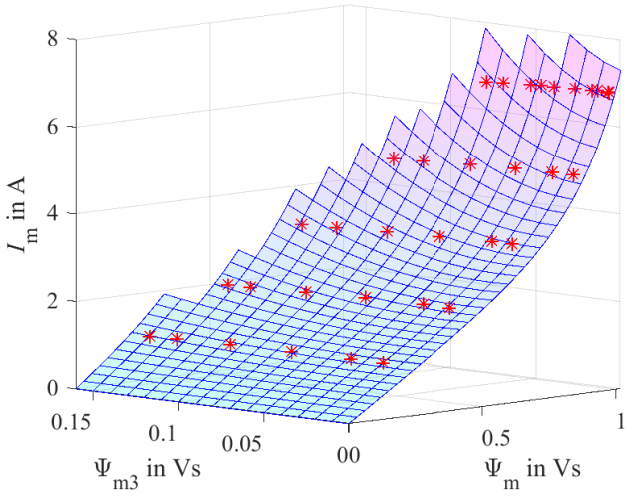

Fig. 4.6: Magnetizing current of the main system as a function of the magnetization flux linkages of the main and the zero-sequence systems of IM1. The measured data points are indicated with red stars. The visualized magnetization surface is calculated from (4.14), (4.15), and (4.16).

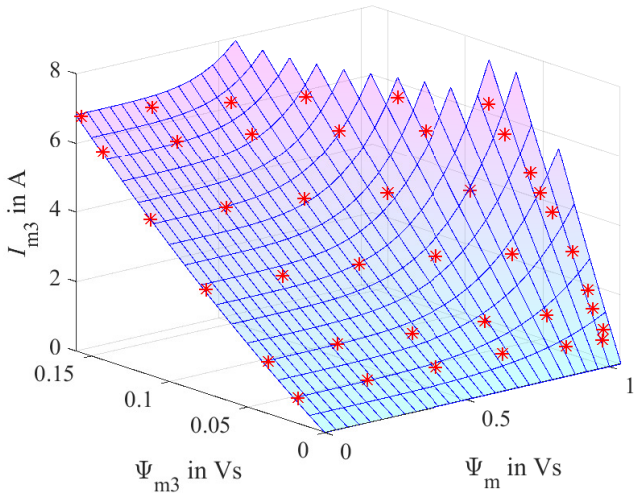

Fig. 4.7: Magnetizing current of the zero-sequence system as a function of the magnetization flux linkages of the zero-sequence and main systems of IM1. The measured data points are indicated with red stars. The visualized magnetization surface is calculated from (4.17), (4.18), and (4.19).

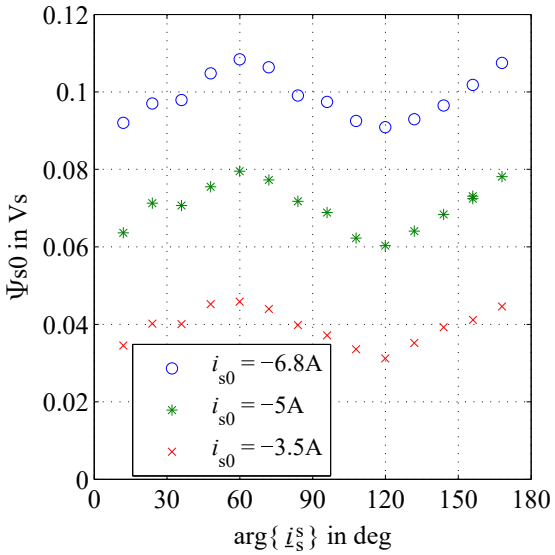

Fig. 4.8: Relationship between the zero-sequence system's stator flux linkage and the angle of the current space vector during the stepped DC experiments with IM1.

values of this flux linkage in the experiments were 0.005 Vs (IM1) and 0.015 Vs (IM2) and thereby lower than the zero-sequence flux linkages introduced by the zero-sequence magnetizing current.

Further investigations regarding the relationship between the angle of the magnetizing current space vector and the zero-sequence flux linkage were performed with IM2. Fig. 4.9a) shows the relationship when $i_{s0} = 0\,\mathrm{A}$. The 90 degrees phase shift between the α- and β-components obtained with the FLMSs and the three periods of the flux linkages for one electrical rotation of the magnetizing current space vector indicate the presence of a third saturation space harmonic. Fig. 4.9b) shows the relationship during the additional presence of a zero-sequence magnetizing current. This current shifts the α-component by a (more or less) constant value, whereas the β-component remains almost unchanged. This is also illustrated by the integration of the flux linkages of the second part of the two successively conducted experiments in Fig. 4.9c). Such a behavior indicates a minor coupling between the zero-sequence flux linkage introduced by the zero-sequence magnetizing current and the angle of the magnetizing current space vector. The proposed modeling of the saturation interaction discussed in the following section neglects the dependence of zero-sequence flux linkage on the angle of the current space vector and focuses on the relationships between the average flux linkages and currents.

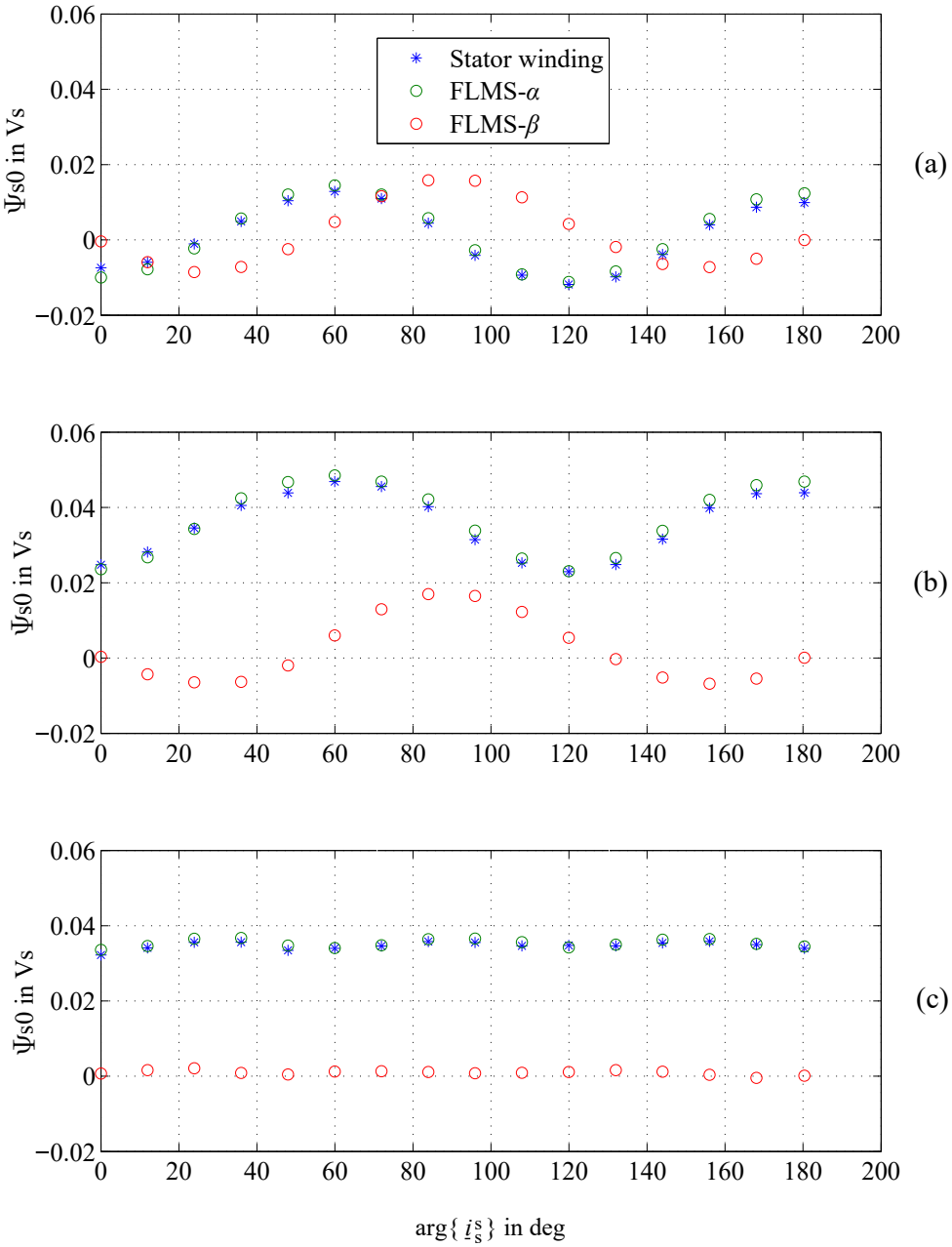

Fig. 4.9: Relationship between the measured zero-sequence system's stator flux linkage and the angle of the magnetizing current space vector during the stepped DC experiments with IM2. The figure illustrates the results obtained with the stator winding and the flux linkage measurement systems FLMCS-α and FLMCS-β. (a) $|\underline{i}_\mathrm{s}^\mathrm{s}| = 6\,\mathrm{A}$ and $i_{\mathrm{s}0} = 0\,\mathrm{A}$, (b) $|\underline{i}_\mathrm{s}^\mathrm{s}| = 6\,\mathrm{A}$ and $i_{\mathrm{s}0} = -6\,\mathrm{A}$. The flux linkage of (c) is obtained by integrating the voltages from the step of the zero-sequence current and a constant main system current. Note: The zero-sequence flux linkage of IM2 for the cases $|\underline{i}_\mathrm{s}^\mathrm{s}| = 0\,\mathrm{A}$ and $i_{\mathrm{s}0} = -6\,\mathrm{A}$ is approximately 0.07 Vs.

4.4 Saturation Interaction Model

To consider the saturation interaction during the post-fault operations of the example case machines in simulations, the measured data points are approximated by means of modeled surfaces. Figs. 4.6 and 4.7 also show these modeled surfaces of the magnetizing currents of the main and the zero-sequence systems for IM1. They are calculated by the empirical approach discussed below.

The unaffected magnetizing current of the main system (at $\Psi_{\mathrm{m3}} = 0$) is approximated by the monotonously increasing function

$$I_{\mathrm{mu}} = c_1 \Psi_{\mathrm{m}} + c_2 (e^{c_3 \Psi_{\mathrm{m}}} - 1), \tag{4.14}$$

where c_1, c_2, and c_3 are positive and constant fitting parameters. The magnetizing current in the presence of a zero-sequence system is modeled by

$$I_{\mathrm{m}} = I_{\mathrm{mu}} w. \tag{4.15}$$

The dimensionless weighting factor w is calculated as

$$w = 1 + c_{w1} \Psi_{\mathrm{m}} (\Psi_{\mathrm{m3}}^2 - 2 \Psi_{\mathrm{m3}} \Psi_{\mathrm{c3}}) + c_{w2} \Psi_{\mathrm{m3}} (\Psi_{\mathrm{m}} - \Psi_{\mathrm{c}})^2, \tag{4.16}$$

where c_{w1}, c_{w2}, Ψ_{c}, and Ψ_{c3} are constant fitting parameters. The value of w is 1 for $\Psi_{\mathrm{m3}} = 0$ and it increases with Ψ_{m3}.

The unaffected magnetizing current of the zero-sequence system (at $\Psi_{\mathrm{m}} = 0$) is modeled by

$$I_{\mathrm{m3u}} = d_1 \Psi_{\mathrm{m3}} + d_2 \Psi_{\mathrm{m3}}^2, \tag{4.17}$$

where d_1 and d_2 are constant fitting parameters. The magnetizing zero-sequence current in the presence of a main system is modeled by

$$I_{\mathrm{m3}} = I_{\mathrm{m3u}} w_0. \tag{4.18}$$

The dimensionless weighting factor for the zero-sequence system w_0 is calculated from

$$w_0 = 1 + d_{\mathrm{w1}} \Psi_{\mathrm{m}}^{d_{\mathrm{w2}}}, \tag{4.19}$$

where d_{w1}, d_{w2} are constant fitting parameters. The value of w_0 is 1 for $\Psi_{\mathrm{m}} = 0$, and it increases with Ψ_{m}.

Fig. 4.10 illustrates the measured and modeled magnetizing currents as a function of the flux linkages for IM1 and IM2. The main system's magnetization flux linkage's influence on the zero-sequence magnetizing current is significantly higher than the influence of the zero-sequence magnetization flux linkage. This also applies to the maxima of w and w_0 in the investigated regions. The maximum of w is approximately 1.35 for both machines, whereas the maximum of w_0 is greater than 2 for both machines.

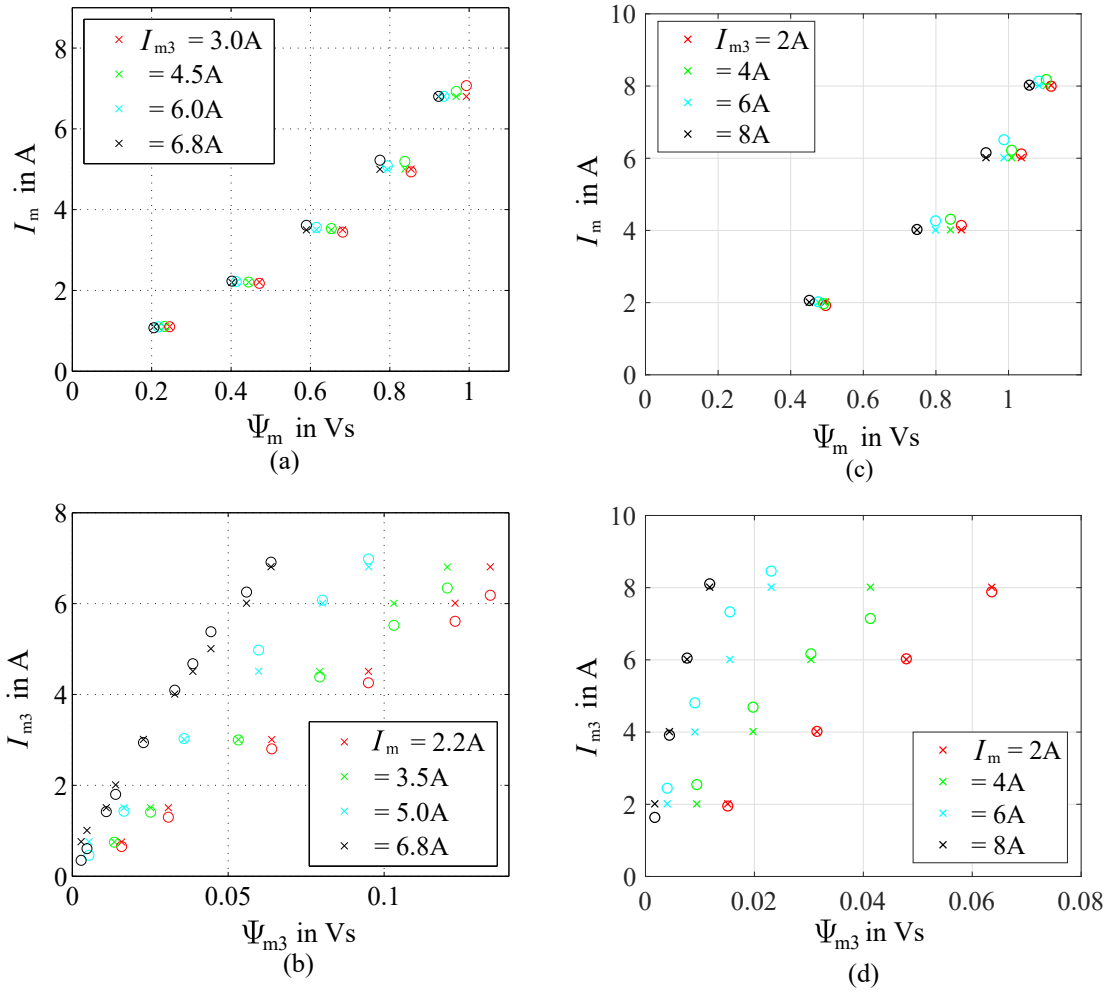

Fig. 4.10: Measured and modeled magnetizing currents as a function of the flux linkages for IM1 (a)-(b) and IM2 (c)-(d). The top figures show the main system with the parameter of the zeros-sequence magnetizing current. The bottom figures illustrate the zero-sequence system with the parameter of the main system magnetizing current. The stars indicate the measured data points, whereas the circles are the results obtained from the saturation interaction model.

Since the magnetization flux linkages are calculated by means of estimated leakage inductances, uncertainties of these inductances affect the calculated magnetization surfaces. Such uncertainties mainly affect the zero-sequence flux linkages, since the leakage and magnetization inductance of the zero-sequence system are in a similar range. Furthermore, Fig. 4.10 shows the intrinsic uncertainty of the description of the saturation interaction of the zero-sequence system by the simple equation of (4.19).

4.5 Discussion of the Saturation Interaction's Effects

During the post-fault operations, the stator MMF and the rotor MMF contribute to the machine's magnetization. Therefore, the magnetization state depends also on the stator frequency and speed. To investigate the magnetization states, simulations for a rotor flux-oriented drive during the standard three-phase operation and the two-phase operation were performed. The simulation model is based on the space vector model and the control structure discussed in Sections 3.1.2 and 3.1.3. The space vector model was extended by the saturation interaction model.

Fig. 4.11 illustrates trajectories of the main and zero-sequence systems on the magnetization surfaces during the steady state post-fault operation. The region of operation highly depends on the desired rotor flux linkage since it is linked with the main system's magnetization flux linkage. As discussed in Section 4.1, the sinusoidal zero-sequence stator current causes pulsations of the space harmonics that are related to the zero-sequence system. This leads to a continuous pulsation of the zero-sequence flux linkage. Since the flux linkage of the main system depends on the zero-sequence flux linkage, this also changes parameters of the main system. The pulsation reduces with increasing rotational speed.

Fig. 4.12 shows simulated inductances and torques for different speeds. The saturation interaction leads to a deviation from the unaffected value of the magnetization inductance of the main system. This leads to a deviation in the torque during start-up if the rotor flux observer is parametrized with the unaffected values. This is also illustrated by the simulation and experimental results provided in Fig. 4.13. Apparently, the reduction and the pulsation of the torque are associated with the torque of the main system, since it is assumed that the zero-sequence system cannot produce torque at standstill. Additional experimental results presented in Fig. 4.14 illustrate a pulsation and a reduction of the average value of the stator flux linkage space vector

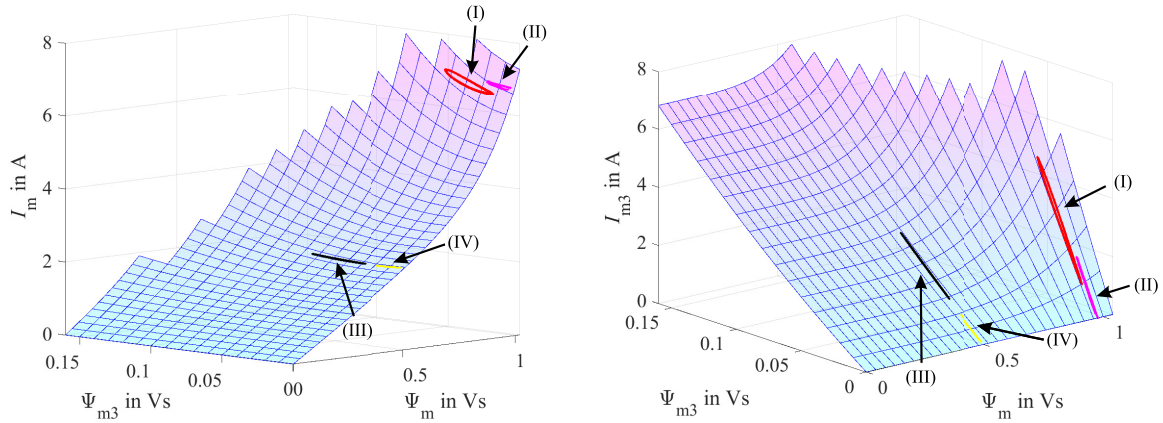

Fig. 4.11: Computed trajectories at different operating points on the surface of the main system's magnetizing current, and the magnetization flux linkages both of the main and zero-sequence systems (a) and on the surface of the magnetizing current of the zero-sequence system, and the main and zero-sequence system's magnetization flux linkages (b). The desired rotor flux linkages, torques, and rotational speeds are as follows: 1 Vs, 5 Nm and 100 r/min (I), 1 Vs, 5 Nm and 1000 r/min (II), 0.5 Vs, 5 Nm and 100 r/min (III), 0.5 Vs, 5 Nm and 1000 r/min (IV).

when a sinusoidal zero-sequence flux linkage is present.

The torque of the zero-sequence system comprises a steady component and alternating components (cf., Chapter 9). These torque components of the zero-sequence system are significant at low speed due to the low relative speed between the space harmonics of the zero-sequence system and the rotor (cf., Appendix C) as well as the corresponding comparatively high magnetizing currents of the zero-sequence system in this region. Fig. 4.11 shows the dependence of the corresponding inductance L_{m3} on the main system's flux level. Thereby, the torque is influenced by the desired rotor flux linkage. The method for the reduction of the alternating torques discussed in Chapter 9 applies the saturated magnetization inductance of the zero-sequence system to achieve a good performance in the low speed region.

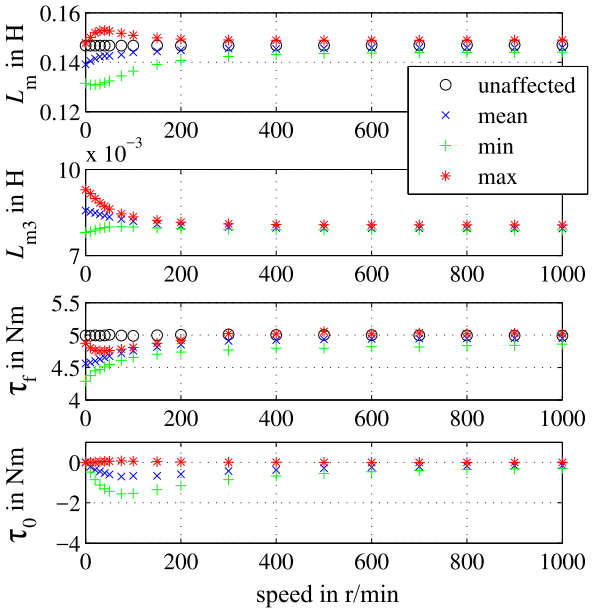

(a)

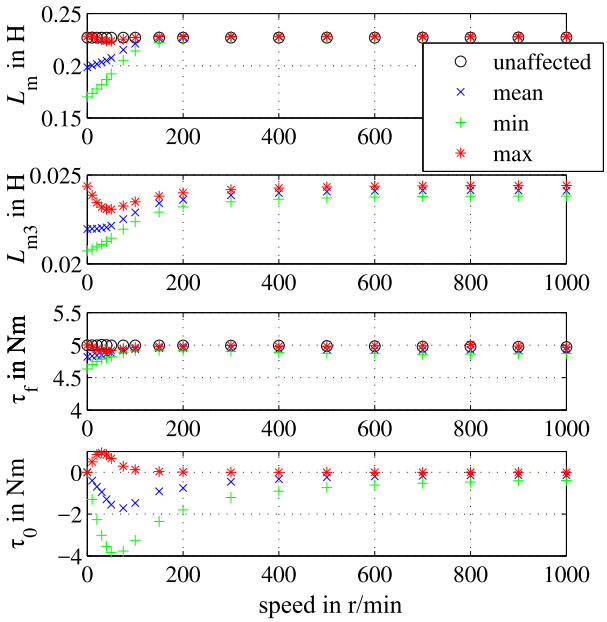

(b)

Fig. 4.12: Simulation results at different speeds. The desired rotor flux linkage and desired torque of the main system are as follows: (a) 1 Vs and 5 Nm, (b) 0.5 Vs and 5 Nm. 1: Magnetization inductance of the main system, 2: magnetization inductance of the zero-sequence system, 3: torque of the main system, 4: torque of the zero-sequence system. The results show unaffected values during the three-phase operation and the average (mean), maximum (max), and minimum value (min) in one stator current period during the steady state operation post-fault.

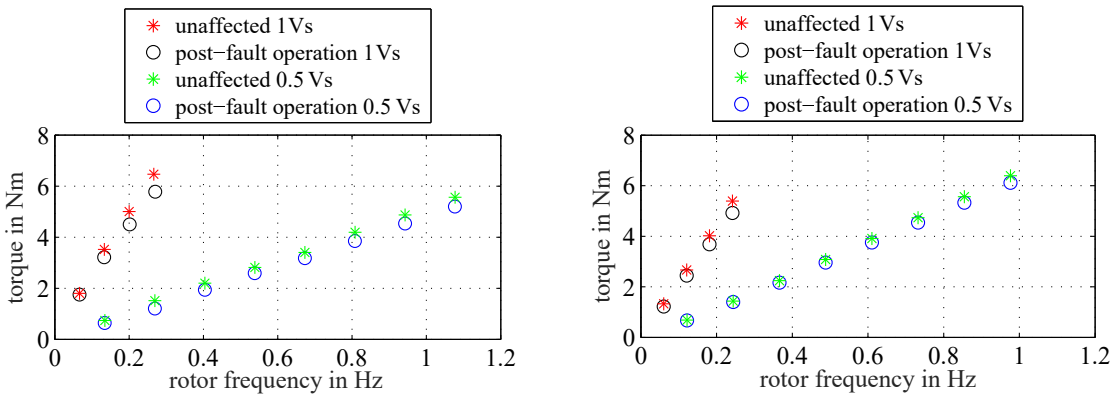

Fig. 4.13: Experimental (a) and simulation (b) results for the average torque at the standstill of IM1 during the three-phase operation (unaffected), and the two-phase operation for two different desired rotor flux linkages. The magnitude of the stator current space vector and the rotor frequency are the same for both operation modes. During the post-fault operation, the torque is reduced. The measurement setup is the same as in described in Section 3.3.

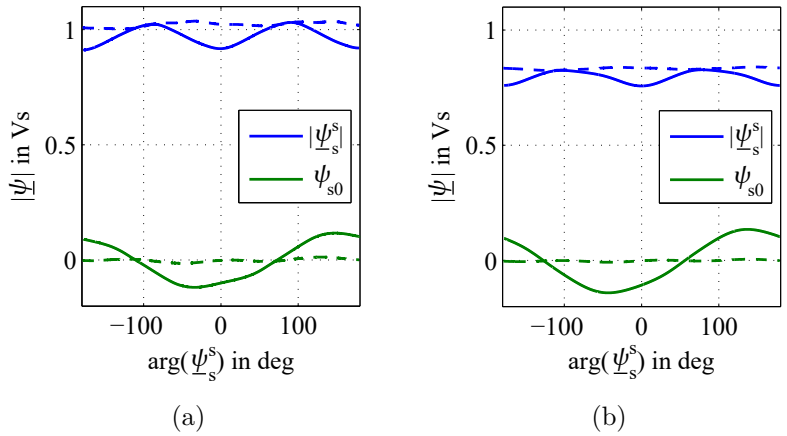

Fig. 4.14: Magnitude of the stator flux linkage space vector and zero-sequence stator flux linkage during AC experiments with IM1 at standstill: (a) $|\underline{i}_{\mathrm{s}}^{\mathrm{s}}| = 6.8\,\mathrm{A}$ and $f_{\mathrm{s}} = 0.1\,\mathrm{Hz}$, (b) $|\underline{i}_{\mathrm{s}}^{\mathrm{s}}| = 6.8\,\mathrm{A}$ and $f_{\mathrm{s}} = 0.4\,\mathrm{Hz}$. The dashed lines show the flux linkages without the presence of a zero-sequence stator current. The solid lines show the flux linkages during the two-phase operation which leads to $i_{\mathrm{s0}} = -i_{\mathrm{s}\alpha}$. The mean values of the measured torque with and without the presence of a zero-sequence stator current are 2.52 Nm and 2.39 Nm in (a) and 6.33 Nm and 5.86 Nm in (b), respectively. The measured alternating torque components at $2f_{\mathrm{s}}$ are 0.05 Nm in (a) and 0.1 Nm in (b). The measurement setup is the same as in described in Section 4.3.1.

4.6 Conclusion

The operation of a three-phase machine with an ordinary stator winding with a zero-sequence stator current leads to additional space harmonics. These space harmonics are part of the MMF of every individual stator phase, and they are not canceled out if the machine is operated with a zero-sequence stator current. The amplitudes of these space harmonics depend on the design of the stator winding.

During the post-fault operations, both, a symmetrical three-phase system stator current and a zero-sequence stator current are applied. Due to the field strength dependent magnetic permeability of the joint magnetic circuit, a saturation interaction between the flux introduced by the three-phase system stator current (the main system flux linkage with the dominant fundamental wave) and the flux introduced by the zero-sequence stator current (the zero-sequence flux linkage with the dominant third harmonic). The flux linkage of both systems is reduced if a magnetizing current of the other system is present which causes pulsations and changes the average inductance when both systems are present during the post-fault operations with a rotor flux-oriented SCIM drive. The effects of the interaction, which mainly occur in the low speed region, are illustrated with simulations based on a proposed saturation interaction model and experimental results in the context of a rotor flux-oriented drive.

Chapter 5

Power Losses in an SCIM during the Post-Fault Operations

During the post-fault operations with a zero-sequence stator current, the power losses and heat generation are increased in comparison to the standard three-phase operation. This is because of the increased RMS-values of the phase currents in the healthy phases and the space harmonics related to the zero-sequence system. This chapter discusses a steady state approach for the calculation of the power losses during the post-fault operations, including the symmetrical components used for the description of the fundamental and space harmonics related to the zero-sequence system (Section 5.1), the power loss calculation (Section 5.2), and the parameter studies for two example case machines (Section 5.3). The resulting loss models are applied in Chapter 8 for the calculation of the continuous torque during the post-fault operations.

5.1 Symmetrical Components

The method of the Symmetrical Components is well established for the analysis of unbalanced electric multiphase systems [88,89]. In contrast to the Clarke Transformation (cf., Appendix I), the method is applied to steady-state time vectors in order to transform an asymmetrical system into a set of symmetrical systems [89]. For a three-phase system, the complex time vectors of the phase quantities $\underline{Q}_{\mathrm{a}}$, $\underline{Q}_{\mathrm{b}}$, and $\underline{Q}_{\mathrm{c}}$ (this set of vectors represents the RMS-values and mutual phase shifts for one frequency) can be transformed into the complex symmetrical components (of phase a) as follows [89]:

$$\begin{pmatrix} \underline{Q}_{\mathrm{s1}} \\ \underline{Q}_{\mathrm{s2}} \\ \underline{Q}_{\mathrm{s0}} \end{pmatrix} = \underbrace{\frac{1}{3}\begin{pmatrix} 1 & \underline{a} & \underline{a}^2 \\ 1 & \underline{a}^2 & \underline{a} \\ 1 & 1 & 1 \end{pmatrix}}_{\boldsymbol{F}} \begin{pmatrix} \underline{Q}_{\mathrm{a}} \\ \underline{Q}_{\mathrm{b}} \\ \underline{Q}_{\mathrm{c}} \end{pmatrix}, \tag{5.1}$$

where $\underline{a} = e^{j\frac{2\pi}{3}}$, $\underline{Q}_{\mathrm{s1}}$ is the positive-sequence component, $\underline{Q}_{\mathrm{s2}}$ is the negative-sequence component, and $\underline{Q}_{\mathrm{s0}}$ is the zero-sequence component.

5.1.1 Components of the Stator Currents

For the description of the different operation modes, the time vectors of the phase currents are transformed by means of (5.1) into the symmetrical components. For a balanced three-phase operation, the symmetrical components of the stator currents are:

$$\begin{pmatrix} \underline{I}_{\mathrm{s1,3ph}} \\ \underline{I}_{\mathrm{s2,3ph}} \\ \underline{I}_{\mathrm{s0,3ph}} \end{pmatrix} = \boldsymbol{F} \begin{pmatrix} I \\ Ie^{-j\frac{2\pi}{3}} \\ Ie^{-j\frac{4\pi}{3}} \end{pmatrix} = \begin{pmatrix} I \\ 0 \\ 0 \end{pmatrix}, \tag{5.2}$$

where I is the RMS-value of the phase currents. In this case, only a positive-sequence component of the stator currents is present. For the two-phase post-fault operation with two phase currents with a phase shift of 60 electrical degrees, the symmetrical components of the stator currents are:

$$\begin{pmatrix} \underline{I}_{\mathrm{s1,2ph}} \\ \underline{I}_{\mathrm{s2,2ph}} \\ \underline{I}_{\mathrm{s0,2ph}} \end{pmatrix} = \boldsymbol{F} \begin{pmatrix} 0 \\ Ie^{j\frac{\pi}{6}} \\ Ie^{-j\frac{\pi}{6}} \end{pmatrix} = \begin{pmatrix} \frac{1}{\sqrt{3}} Ie^{j\pi} \\ 0 \\ \frac{1}{\sqrt{3}} Ie^{j0} \end{pmatrix}. \tag{5.3}$$

The comparison of (5.2) and (5.3) shows that if two phase currents with a phase shift of 60 degrees with the same value of I are applied, the magnitude of the positive-sequence component is lower by a factor of $\sqrt{3}$ (see also Section 1.3 and the discussion in Section 4.1.1 in the context of the fundamental wave of the stator MMF.) Additionally, (5.3) shows the occurring zero-sequence component during the two-phase operation that has the same magnitude as the positive-sequence component (a similar result is derived for the relationship between the amplitude of the zero-sequence stator current and the magnitude of the stator current *space vector*, see Section 3.1.2 and [74]). The negative-sequence component of the stator currents is not present in both operation modes and is therefore neglected in the further discussion.

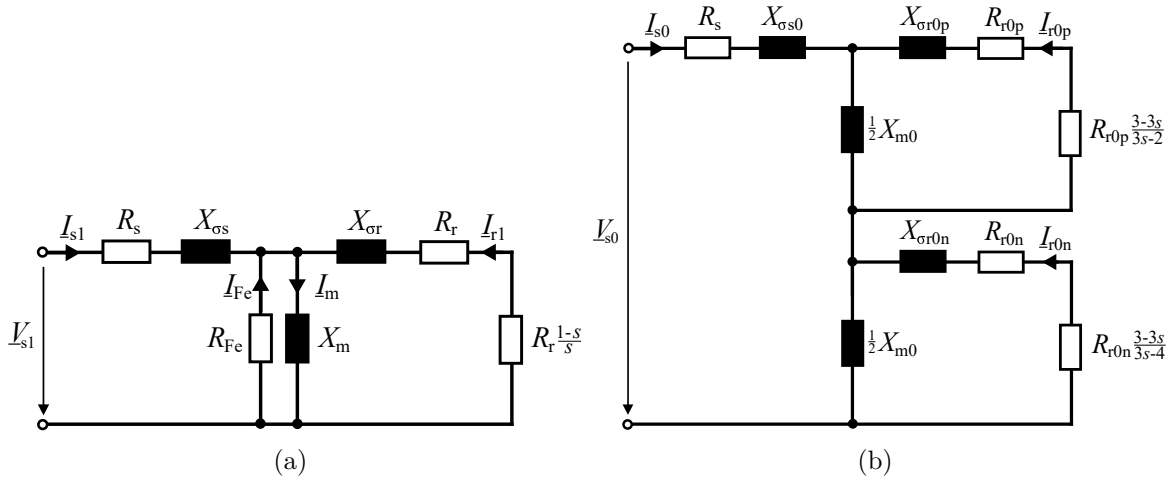

Fig. 5.1: Equivalent circuits of a SCIM's positive-sequence system (a) and zero-sequence system (b), based on [90, 91] and [89], respectively.

5.1.2 Equivalent Circuits of the Positive- and the Zero-Sequence System

The positive-sequence component of the stator currents represents a symmetrical three-phase system rotating in the positive direction of rotation with the stator frequency f_s. It leads to a dominating fundamental wave of the MMF, and its effects can be modeled by the standard single-phase equivalent circuit of an SCIM [90, 91], see Fig. 5.1a). The stator impedance of the positive-sequence system is given by:

$$\underline{Z}_{s1} = \frac{\underline{V}_{s1}}{\underline{I}_{s1}} = R_s + jX_{\sigma s} + \frac{\frac{jX_m R_{Fe}}{jX_m + R_{Fe}}\left(jX_{\sigma r} + \frac{R_r}{s}\right)}{\frac{jX_m R_{Fe}}{jX_m + R_{Fe}} + jX_{\sigma r} + \frac{R_r}{s}}, \tag{5.4}$$

where $\underline{V}_{s1}$ is the positive-sequence voltage, R_s is the stator resistance, R_r is the rotor resistance, R_{Fe} is the iron loss resistance, X_m is the magnetization reactance, $X_{\sigma s}$ is the stator leakage reactance, $X_{\sigma r}$ is the rotor leakage reactance, and s is the slip.

The zero-sequence component of the stator currents represents a sinusoidal current with the stator frequency f_s flowing in all three stator phases with the same amplitude and phase. It causes sinusoidally pulsating space harmonics of the stator MMF with the third space harmonic being the dominant one. This harmonic can be split into a third space harmonic rotating with $\frac{1}{3}f_s$ (positive direction of rotation), and a third space harmonic rotating with $-\frac{1}{3}f_s$ (negative direction of rotation), cf., [89]. The effects of these third space harmonics can be modeled with the equivalent circuit [89] shown in

Fig. 5.1b). The stator impedance of the zero-sequence system can be calculated from:

$$\underline{Z}_{\mathrm{s0}} = \frac{\underline{V}_{\mathrm{s0}}}{\underline{I}_{\mathrm{s0}}} = R_{\mathrm{s}} + jX_{\sigma\mathrm{s0}} + \frac{j\frac{1}{2}X_{\mathrm{m0}}(jX_{\sigma\mathrm{r0p}} + \frac{R_{\mathrm{r0p}}}{3s-2})}{j\frac{1}{2}X_{\mathrm{m0}} + jX_{\sigma\mathrm{r0p}} + \frac{R_{\mathrm{r0p}}}{3s-2}} + \frac{j\frac{1}{2}X_{\mathrm{m0}}(jX_{\sigma\mathrm{r0n}} + \frac{R_{\mathrm{r0n}}}{4-3s})}{j\frac{1}{2}X_{\mathrm{m0}} + jX_{\sigma\mathrm{r0n}} + \frac{R_{\mathrm{r0n}}}{4-3s}}, \tag{5.5}$$

where $\underline{V}_{\mathrm{s0}}$ is the zero-sequence voltage, X_{m0} is the zero-sequence magnetization reactance, $X_{\sigma\mathrm{s0}}$ is the zero-sequence stator leakage reactance, R_{r0p} and $X_{\sigma\mathrm{r0p}}$ are the zero-sequence rotor resistance and leakage reactance for the third space harmonic rotating in the positive direction of rotation, respectively, and R_{r0n} and $X_{\sigma\mathrm{r0n}}$ are the zero-sequence rotor resistance and leakage reactance for the third harmonic rotating in the negative direction of rotation, respectively.

In the context of the thermal calculation and with the consideration of different operating points, the mapping of the electromagnetic power losses on equivalent circuits is beneficial and was previously applied to the three-phase operation in [133–138]. The following sections discuss the power losses including the losses during the post-fault operations.

5.2 Power Losses

Methods for the determination and the separation of the power losses of rotating electric machines are summarized in [90–93]. The total power losses can be determined directly by measuring the machine's input and output power. For the standard operation, special tests for the separation of the total losses are proposed. The power losses of inverter driven SCIMs are typically separated into the following losses [90–93]:

- Stator winding losses
- Rotor winding losses
- Iron losses
- Friction and windage losses
- Additional load losses
- Additional high frequency losses

The modeling and determination of these losses, also with regard to the post-fault operations are discussed below in further detail.

5.2.1 Winding Losses

The equivalent circuit based determination of the I^2R-losses in the windings is based on the determination of the corresponding resistances. They can be determined by a combined evaluation of different tests (cf., [90–92] DC-test, no-load test, load or locked-rotor test.) For the calculation and comparison of the winding losses during the different operation modes, the losses are described as a function of the symmetrical components of the stator currents.

Three-Phase and Two-Phase Operation

The copper losses in the stator phases a, b, and c can be calculated from:

$$\begin{pmatrix} P_{\mathrm{Cu,a}} \\ P_{\mathrm{Cu,b}} \\ P_{\mathrm{Cu,c}} \end{pmatrix} = R_{\mathrm{s}} \begin{pmatrix} |\underline{I}_{\mathrm{a}}|^2 \\ |\underline{I}_{\mathrm{b}}|^2 \\ |\underline{I}_{\mathrm{c}}|^2 \end{pmatrix}. \tag{5.6}$$

The total copper losses in the stator winding are given by:

$$P_{\mathrm{Cu}} = R_{\mathrm{s}}(|\underline{I}_{\mathrm{a}}|^2 + |\underline{I}_{\mathrm{b}}|^2 + |\underline{I}_{\mathrm{c}}|^2) = 3R_{\mathrm{s}}(|\underline{I}_{\mathrm{s1}}|^2 + |\underline{I}_{\mathrm{s0}}|^2). \tag{5.7}$$

The total losses in the rotor cage are given by:

$$P_{\mathrm{Al}} = 3R_{\mathrm{r}}|\underline{I}_{\mathrm{r1}}|^2 + 3R_{\mathrm{r0p}}|\underline{I}_{\mathrm{r0p}}|^2 + 3R_{\mathrm{r0n}}|\underline{I}_{\mathrm{r0n}}|^2. \tag{5.8}$$

The positive-sequence rotor current can be calculated from (cf., Fig 5.1a):

$$\underline{I}_{\mathrm{r1}} = \frac{-j\underline{q}_{\mathrm{Fe}}X_{\mathrm{m}}}{j(\underline{q}_{\mathrm{Fe}}X_{\mathrm{m}} + X_{\sigma\mathrm{r}}) + \frac{R_{\mathrm{r}}}{s}}\underline{I}_{\mathrm{s1}}, \tag{5.9}$$

with the complex iron loss factor:

$$\underline{q}_{\mathrm{Fe}} = 1 - \frac{jX_{\mathrm{m}}}{R_{\mathrm{Fe}} + jX_{\mathrm{m}}}. \tag{5.10}$$

The rotor currents of the zero-sequence system for the third harmonic rotating in the positive and negative direction of rotation can be calculated from (cf., Fig 5.1b):

$$\underline{I}_{\mathrm{r0p}} = \frac{-j\frac{1}{2}X_{\mathrm{m0}}}{j(\frac{1}{2}X_{\mathrm{m0}} + X_{\sigma\mathrm{r0p}}) + \frac{R_{\mathrm{r0p}}}{3s-2}}\underline{I}_{\mathrm{s0}}, \tag{5.11}$$

$$\underline{I}_{\mathrm{r0n}} = \frac{-j\frac{1}{2}X_{\mathrm{m0}}}{j(\frac{1}{2}X_{\mathrm{m0}} + X_{\sigma\mathrm{r0n}}) + \frac{R_{\mathrm{r0n}}}{4-3s}}\underline{I}_{\mathrm{s0}}. \tag{5.12}$$

If the phase currents in the healthy phases are increased by a factor of $\sqrt{3}$ during the two-phase post-fault operation to obtain the same positive-sequence current and the influence of the temperature is neglected, the losses in the healthy phases increase by a factor of 3, whereas the total copper losses increase by a factor of 2, as can be derived from (5.2), (5.3), (5.6), and (5.7). The occurring zero-sequence system additionally leads to an increase of the losses in the rotor winding, as can be obtained from (5.8), (5.9), (5.11), and (5.12). (Note: All three stator phases of the machine are well. For simplicity, the terms “healthy phase” and “faulty phase” are also used to illustrate the power losses and temperatures of the machine phases connected to the healthy and faulty inverter leg during the post-fault operations of the drive.)

Switched Two-Three-Phase Operation

The phase currents during the switched two-three-phase operation lead to a rotating fundamental wave. Therefore, the positive-sequence system can be considered in analogy to the other operation modes with the corresponding currents $\underline{I}_{\mathrm{s1}}$ and $\underline{I}_{\mathrm{r1}}$ in (5.7), (5.8), and (5.9). However, the sinusoidal half wave of the zero-sequence stator current during the switched two-three-phase operation consists of various harmonic components, as shown in Fig. 5.2.

The harmonic composition of the zero-sequence stator current prevents the direct application of the equivalent circuit for the zero-sequence system shown in Fig. 5.1b). Each component of the zero-sequence stator current leads to a dominating third space harmonic pulsating with the frequency of the component. The DC-component leads to a stationary third space harmonic and each third space harmonic introduced by the other components can be divided into two waves rotating into the positive and negative direction with $\pm\frac{1}{3}f/f_{\mathrm{s}}$ of the speed of the fundamental wave. The analogous extension of the equivalent circuit theory would imply that each component be considered (or at least the dominating ones) with an equivalent circuit analog to the circuit shown in Fig. 5.1b). The dependences of the rotor impedances on the slips s (and the reac-

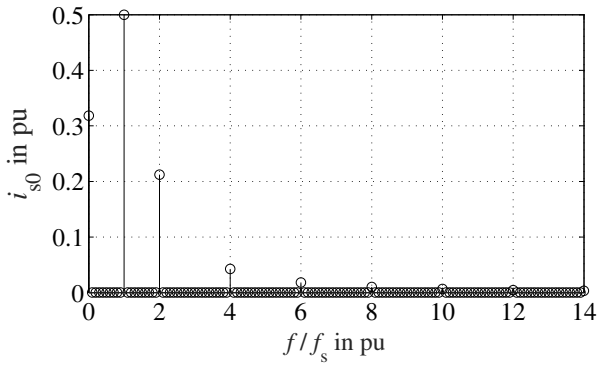

Fig. 5.2: Fourier spectrum of the zero-sequence stator current during the switched two-three-phase operation that comprises of a DC-component, a component at the stator frequency f_s and components that occur at even multiples of f_s. 1 pu corresponds to the extreme value of i_{s0} during the switched two-three-phase operation (cf., Fig. 3.3).

tances) in these circuits would have to be adapted according to the frequency of the component. However, in this work, a different approach was implemented that evades the application of multiple equivalent circuits of the zero-sequence system, and derives the losses from the results for the three-phase and two-phase operation.

From the RMS-values of the ideal stator current wave forms during the switched two-three-phase operation (Fig. 3.3) the total copper losses in the stator winding can be derived:

$$\begin{aligned} P_{\mathrm{Cu}} = P_{\mathrm{Cu,a}} + P_{\mathrm{Cu,b}} + P_{\mathrm{Cu,c}} = {} & \frac{1}{t_\mathrm{f}} \int_0^{t_\mathrm{f}/2} \left[\sqrt{2}|\underline{I}_{\mathrm{s1}}| \sin\left(\frac{2\pi}{t_\mathrm{f}} t\right)\right]^2 dt R_\mathrm{a} \\ & + \frac{1}{t_\mathrm{f}} \int_0^{t_\mathrm{f}/2} \left[\sqrt{2}|\underline{I}_{\mathrm{s1}}| \sin\left(\frac{2\pi}{t_\mathrm{f}} t - \frac{2\pi}{3}\right)\right]^2 dt R_\mathrm{b} \\ & + \frac{1}{t_\mathrm{f}} \int_{t_\mathrm{f}/2}^{t_\mathrm{f}} \left[\sqrt{3}\sqrt{2}|\underline{I}_{\mathrm{s1}}| \sin\left(\frac{2\pi}{t_\mathrm{f}} t - \frac{\pi}{6}\right)\right]^2 dt R_\mathrm{b} \\ & + \frac{1}{t_\mathrm{f}} \int_0^{t_\mathrm{f}/2} \left[\sqrt{2}|\underline{I}_{\mathrm{s1}}| \sin\left(\frac{2\pi}{t_\mathrm{f}} t - \frac{4\pi}{3}\right)\right]^2 dt R_\mathrm{c} \\ & + \frac{1}{t_\mathrm{f}} \int_{t_\mathrm{f}/2}^{t_\mathrm{f}} \left[\sqrt{3}\sqrt{2}|\underline{I}_{\mathrm{s1}}| \sin\left(\frac{2\pi}{t_\mathrm{f}} t + \frac{\pi}{6}\right)\right]^2 dt R_\mathrm{c}, \end{aligned} \tag{5.13}$$

where t_f is the fundamental period and R_a, R_b, and R_c are the phase resistances. By using the substitution [94]:

$$\sin(x)^2 = \frac{1}{2} - \frac{1}{2}\cos(2x), \tag{5.14}$$

the general form of the integrals in (5.13) can be calculated:

$$\frac{1}{t_\mathrm{f}}\int_{t_0}^{t_0+t_\mathrm{f}/2}\left[c\sin\left(\frac{2\pi}{t_\mathrm{f}}t+\phi_0\right)\right]^2 dt = \frac{c^2}{t_\mathrm{f}}\int_{t_0}^{t_0+t_\mathrm{f}/2}\left[\frac{1}{2}-\frac{1}{2}\cos\left(\frac{4\pi}{t_\mathrm{f}}t+2\phi_0\right)\right] dt =$$

$$= \frac{c^2}{t_\mathrm{f}}\left[\frac{1}{2}t-\frac{t_\mathrm{f}}{8\pi}\sin\left(\frac{4\pi}{t_\mathrm{f}}t+2\phi_0\right)\right]_{t_0}^{t_0+t_\mathrm{f}/2} = \frac{c^2}{4}. \tag{5.15}$$

Using the result of (5.15) and assuming the phase resistances equal $R_\mathrm{s} = R_\mathrm{a} = R_\mathrm{b} = R_\mathrm{c}$ allows the total stator winding losses to be calculated from:

$$P_\mathrm{Cu} = \underbrace{\frac{2}{4}R_\mathrm{a}|\underline{I}_\mathrm{s1}|^2}_{P_\mathrm{Cu,a}} + \underbrace{\left(\frac{2}{4}+\frac{6}{4}\right)R_\mathrm{b}|\underline{I}_\mathrm{s1}|^2}_{P_\mathrm{Cu,b}} + \underbrace{\left(\frac{2}{4}+\frac{6}{4}\right)R_\mathrm{c}|\underline{I}_\mathrm{s1}|^2}_{P_\mathrm{Cu,c}} = 4.5R_\mathrm{s}|\underline{I}_\mathrm{s1}|^2, \tag{5.16}$$

which equals the average value of the total stator winding losses during the three-phase operation $3R_\mathrm{s}|\underline{I}_\mathrm{s1}|^2$ and the two-phase operation $6R_\mathrm{s}|\underline{I}_\mathrm{s1}|^2$. (5.16) reveals that the total stator winding losses are increased by a factor of 1.5 when compared to the losses during the three-phase operation. Furthermore, the local losses in the faulty phase $P_\mathrm{Cu,a}$ and healthy phases $P_\mathrm{Cu,b}$= $P_\mathrm{Cu,c}$ during the switched two-three-phase operation are $\frac{1}{9}$ and $\frac{4}{9}$ of the total losses, respectively. Hence, for the same positive-sequence stator current, the local losses in the healthy phases are increased by a factor of 2 when compared to the three-phase operation.

The rotor winding losses during the switched two-three-phase operation are approximated by assuming an ideal coupling of the harmonic components of the zero-sequence stator currents (Fig. 5.2) and the corresponding rotor currents $\underline{I}_{\mathrm{r0p},\nu} = \underline{I}_{\mathrm{r0n},\nu} = -\underline{I}_{\mathrm{s},\nu}$. In such a case, the magnetization reactance is assumed infinite when compared to the rotor impedance for all harmonic components. The assumption above allows the rotor winding losses to be estimated from the sum of the squares of the RMS-values of the harmonic components:

$$P_\mathrm{Al} = 3R_\mathrm{r0p}\sum_{\nu=0}^{\infty}|\underline{I}_{\mathrm{r0p},\nu}|^2 + 3R_\mathrm{r0n}\sum_{\nu=0}^{\infty}|\underline{I}_{\mathrm{r0n},\nu}|^2 \approx 3(R_\mathrm{r0n}+R_\mathrm{r0p})\sum_{\nu=0}^{\infty}|\underline{I}_{\mathrm{s0},\nu}|^2. \tag{5.17}$$

The evaluation of the right-hand side for switched two-three-phase operation (harmonic components of Fig. 5.2) and the two-phase operation (one component at $\nu = f/f_\mathrm{s} = 1$ with an amplitude of 1 pu) yields zero-sequence rotor winding losses of 50 % during the switched two-three-phase operation when compared to the two-phase operation. This result can be applied to estimate the rotor winding losses during the switched two-three-

phase operation from the average value of the losses during two-phase and three-phase operation (5.8). For the calculation of (5.11) and (5.12), the zero-sequence stator current is chosen equal to the two-phase operation with the same positive-sequence current.

The influence of the temperature was neglected here, however, it is discussed in the following section.

Influence of the Temperature

The influence of the temperature on the winding resistances has not yet been considered. During the measurements, it is inherently taken into consideration, especially by waiting for the thermal steady-state (cf., [90–92] 2K/hour-criterion). From a modeling point of view, the influence of the temperature dependence can be considered by the linearization of the specific resistance with respect to the temperature change of the conductor material [101]:

$$r(T) = r_{\mathrm{ref}}[1 + \alpha_{\mathrm{ref}}(T - T_{\mathrm{ref}})], \tag{5.18}$$

where r_{ref} is the specific resistance and α_{ref} is the linear temperature coefficient, both at the reference temperature T_{ref}. This linearization is typically assumed to be sufficiently accurate in the temperature range within the electric machines are operated. The choice $T_{\mathrm{ref}} = 0°\mathrm{C}$ and the transition to the winding resistance yields [95]:

$$R(T_c) = R_{0°\mathrm{C}}[1 + \alpha_{0°\mathrm{C}} T_{\mathrm{c}}], \tag{5.19}$$

where $R_{0°\mathrm{C}}$ is the electric resistance and $\alpha_{0°\mathrm{C}}$ is the linear temperature coefficient both at 0°C, respectively, and T_{c} is the Celsius temperature. In [95] $\alpha_{0°\mathrm{C}}$ is specified as $\frac{1}{235}\,\frac{1}{\mathrm{K}}$ for copper and $\frac{1}{225}\,\frac{1}{\mathrm{K}}$ for aluminum. The application of (5.19) allows the consideration of the influence of the temperature on the resistances in (5.7), (5.8) and (5.16) by means of a temperature feedback from a temperature model, see Sections 7.3 and 8.2. The feedback from the model that separately considers the stator phases can be used to include the influence of a temperature asymmetry on the stator phase resistances. However, since the ideal current and copper losses in phase a are zero during the two-phase operation and $P_{\mathrm{Cu,a}}$ is a minor proportion of the total copper losses in (5.16) during the switched two-three-phase operation, R_{s} in (5.7) and (5.16) can be approximated by the phase resistances of the healthy phases.

5.2.2 Iron Losses

Iron losses correspond to the power converted into heat flow due to the alternation of the magnetic field in magnetic permeable materials. The iron loss density per volume is defined as the enclosed area of the close B-H-hysteresis curve per fundamental period t_f [96]:

$$p_\mathrm{Fe} = \frac{1}{t_\mathrm{f}} \oint H dB, \tag{5.20}$$

where H is the magnetic field strength and B is the magnetic flux density. The loss density increases with flux density and frequency. Several models for the calculation and the separation of the iron loss density have been proposed [96–98]:

$$p_\mathrm{Fe} = u_\mathrm{s} f^{o_\mathrm{sf}} \hat{B}^{o_\mathrm{sB}}, \qquad \text{(Steinmetz)} \tag{5.21}$$

$$p_\mathrm{Fe} = u_\mathrm{h} f \hat{B}^2 + u_\mathrm{e} f^2 \hat{B}^2, \qquad \text{(Jordan)} \tag{5.22}$$

$$p_\mathrm{Fe} = u_\mathrm{h} f \hat{B}^{o_\mathrm{h}} + u_\mathrm{e} f^2 \hat{B}^2 + u_\mathrm{a} f^{1.5} \hat{B}^{1.5}, \qquad \text{(Bertotti)} \tag{5.23}$$

where $\hat{B}$ is the amplitude of the flux density, f is the frequency, u_s is the coefficient as well as o_sf and o_sB are the exponents of the Steinmetz equation, o_h is the hysteresis loss coefficient, u_e is the eddy current loss coefficient, o_h is the hysteresis loss exponent, and u_a is the anomalous loss coefficient (also referred to as excess loss coefficient). Such models can be parameterized by means of manufacturer data and applied to the iron loss calculation from the results of electromagnetic finite element analyses. Also, the analytic iron loss calculation approaches in classic electric machine design handbooks [99–103] appear to be inspired by (5.21)-(5.23) or similar models. They apply a segmentation of the magnetic circuit and the calculation of the total iron losses from the sum of the local iron losses of the segment:

$$P_\mathrm{Fe,l} = p_\mathrm{Fe,l} M_\mathrm{l} = \left[u_\mathrm{h,add} u_\mathrm{h,ref} \left(\frac{f}{f_\mathrm{ref}} \right) \left(\frac{\hat{B}}{\hat{B}_\mathrm{ref}} \right)^2 + u_\mathrm{e,add} u_\mathrm{e,ref} \left(\frac{f}{f_\mathrm{ref}} \right)^2 \left(\frac{\hat{B}}{\hat{B}_\mathrm{ref}} \right)^2 \right] M_\mathrm{l}, \tag{5.24}$$

where $p_\mathrm{Fe,l}$ is the iron loss density of the segment (here, per mass), M_l is the mass of the segment, $u_{h,ref}$ and $u_{e,ref}$ are the hysteresis and eddy current loss per mass provided from the steel sheet manufacturer at the reference point defined by f_ref and $\hat{B}_\mathrm{ref}$ (e.g., 50 Hz or 60 Hz and 1.5 T). The models (5.21)-(5.23) assume a sinusoidal alternating flux density. The transition from a loss density to the losses in (5.24)

implies the assumption of a homogeneous material and a homogeneous flux density distribution in the considered segment. Since these assumptions are only partially valid with the material parameters and the flux distribution in an electric machine, supplementary factors such as $u_{\mathrm{h,add}}$ and $u_{\mathrm{e,add}}$ are applied to take the loss increase due to harmonics, rotational fields, material degradation caused by the manufacturing, and additional effects such as surface losses and losses caused by tooth pulsations into account [99–103].

The iron losses of the equivalent circuit in Fig. 5.1a) can be calculated from:

$$P_{\mathrm{Fe}} = \frac{3(2\pi f_{\mathrm{s}}\Psi_{\mathrm{m}})^2}{R_{\mathrm{Fe}}}. \tag{5.25}$$

Hence, in the context of the calculation of different operating points, a description of the iron loss resistance as a function of the other parameters, the iron losses P_{Fe}, the stator frequency f_{s} and the magnetization flux linkage Ψ_{m}:

$$R_{\mathrm{Fe}} = R_{\mathrm{Fe}}(P_{\mathrm{Fe}}, f_{\mathrm{s}}, \Psi_{\mathrm{m}}) \tag{5.26}$$

would be beneficial. The standard [95] provides a procedure for the determination of the total iron losses of SCIMs that can be obtained from no-load tests. The iron losses are determined as a function of the flux linkage and calculated by subtracting the stator winding, friction and windage losses from the input power. Assuming that the total magnetic circuit of the machine follows (5.22) and is mainly a function of the magnetization flux linkage (or at least can be approximated by the following equation):

$$P_{\mathrm{Fe}} = u_{\mathrm{h,t}} f_{\mathrm{s}} \hat{\Psi}_{\mathrm{m}}^2 + u_{\mathrm{e,t}} f_{\mathrm{s}}^2 \hat{\Psi}_{\mathrm{m}}^2, \tag{5.27}$$

with the constants $u_{\mathrm{h,t}}$ and $u_{\mathrm{e,t}}$, leads to a simple and convenient description of the iron loss resistance:

$$R_{\mathrm{Fe}} = \frac{6\pi^2}{\frac{u_{\mathrm{h,t}}}{f_s} + u_{\mathrm{e,t}}}. \tag{5.28}$$

The iron losses than can be calculated from:

$$P_{\mathrm{Fe}} = 3R_{\mathrm{Fe}} \left| \frac{(\underline{q}_{Fe} - 1)(jX_{\mathrm{r}\sigma} + \frac{R_{\mathrm{r}}}{s})}{j(\underline{q}_{\mathrm{Fe}} X_{\mathrm{m}} + X_{\mathrm{r}\sigma}) + \frac{R_{\mathrm{r}}}{s}} \underline{I}_{\mathrm{s1}} \right|^2. \tag{5.29}$$

5.2.3 Friction and Windage Losses

These losses comprise the losses due to the fluid and bearing friction as well as the power for a potentially mounted fan. The first two losses are discussed below.

Fluid Friction

The fluid friction in the air gap depends on the properties of the fluid, the geometry of the air gap and the rotational speed. A great contribution for the study of the kinetics and the heat transfer of a fluid between rotating concentric cylinders was performed by *G. I. Taylor* [104–107]. At low speed, the rotation leads to a laminar flow of the fluid. In this region, it can be assumed that the fluid friction is proportional to the square of the rotational velocity [106, 108]. However, it was observed that at a certain speed, vortices occur, that increase the fluid friction (and also the heat transfer between the cylinders cf., Section 6.3.4). If the inner cylinder rotates, and the ratio between the gap length and the radius is small, the critical speed can be calculated from the following instability criterion [104, 106]:

$$\frac{\pi^4 \nu^2}{\omega^2 r l_g^3} \leq 0.0571, \tag{5.30}$$

or in a different form with the Taylor number [166]:

$$Ta = \frac{\omega^2 r l_{\mathrm{g}}^3}{\nu^2} \geq 1706, \tag{5.31}$$

where ω is the angular frequency, r is the radius of the inner cylinder, l_g is the gap length, and ν is the kinematic viscosity of the liquid. Many publications use the square root of (5.31) for the definition of Ta. The frictional power can be calculated from [108]:

$$P_{\mathrm{w}} = \pi C_{\mathrm{d}} d r^4 \omega^3 l, \tag{5.32}$$

where C_{d} is the skin friction coefficient and d is the density of the fluid. As discussed in [108–110] the coefficient C_{d} for the turbulent flow can be calculated from the Reynolds number:

$$Re = \frac{\omega r l_{\mathrm{g}} d}{\eta}. \tag{5.33}$$

where η is the dynamic viscosity. The proposed relationship between the Reynolds number and the skin friction coefficient from [108] is shown in Fig. 5.3a).

Bearing Friction

The calculation of the friction of mechanical bearings is complex. The friction depends on many aspects such as the type and dimensions of the bearing, the properties of the lubricant, the load, and the speed. The paragraph below briefly summarizes a model for the calculation of the bearing friction published by the Swedish bearing manufacturer SKF [111]:

The frictional power of a grease lubricated bearing is modeled by [111]:

$$P_{\mathrm{fr}} = \tau_{\mathrm{fr}}\omega = (\tau_{\mathrm{rr}} + \tau_{\mathrm{sl}} + \tau_{\mathrm{seal}})\omega, \tag{5.34}$$

where τ_{rr} is the rolling frictional torque, τ_{sl} is the sliding frictional torque, and τ_{seal} is the frictional torque of the seals. The rolling frictional torque models the shearing, and the starvation of the lubricant as well as the effect of loads. It is calculated from [111]:

$$\tau_{\mathrm{rr}} = c_{\mathrm{ish}} c_{\mathrm{rs}} c_{\mathrm{rr}} (\nu n)^{0.6}, \tag{5.35}$$

where c_{ish} is the inlet shear heating reduction factor, c_{rs} is the kinematic replenishment/starvation reduction factor, c_{rr} is a load variable, ν is the kinematic viscosity of the base oil of the grease, and n is the rotational speed. The factors c_{ish} and c_{rs} depend on the lubricant and dimensions and both decrease with the speed and viscosity. The variable c_{rr} depends on the bearing type and diameter and increases with both the axial and radial forces. The sliding frictional torque models the contact between asperities [111]:

$$\tau_{\mathrm{sl}} = c_{\mathrm{sl}} c_{\mathrm{sll}}, \tag{5.36}$$

where c_{sl} is the sliding friction coefficient, and $\mathrm{c_{sll}}$ is a load variable. c_{sl} depends on the bearing type and diameter as well as the lubricant and decreases with the speed and viscosity. The variable c_{sl} depends on the bearing type and diameter and increases with both the axial and radial forces. The frictional torque due to seals τ_{seal} is assumed to be a constant value depending on the seal type and the bearing type and size. It has been stated in [111], that τ_{sl} may exceed the other torque components in (5.34). Fig. 5.3b) qualitatively illustrates the torque of a grease lubricated roller bearing as a function of speed.

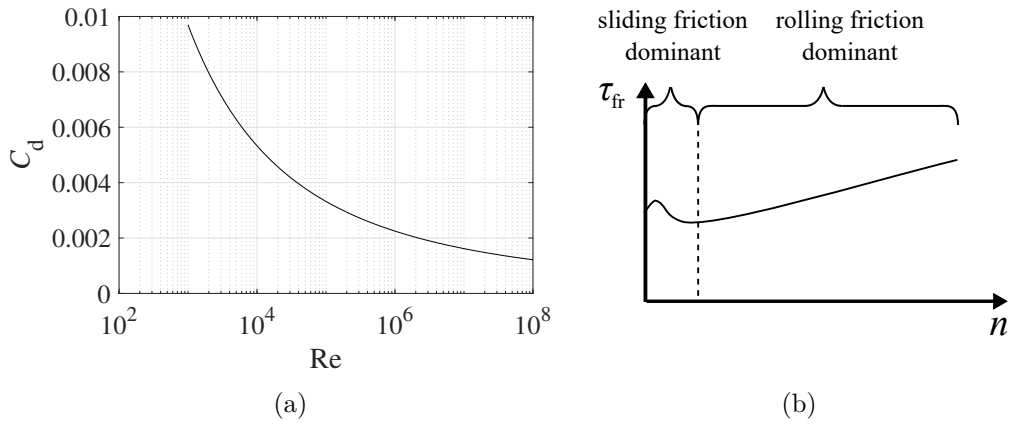

(a) (b)

Fig. 5.3: (a) Skin friction coefficient as a function of the the Reynolds number [108], and (b) qualitative progression of the friction torque of a grease lubricated roller bearing as a function of speed, based on [112].

5.2.4 Additional Load Losses

The *additional losses* of SCIMs can be defined as losses caused by permanence variations, harmonics of the MMF and leakage fluxes [101, 103, 113–115]. Some of these losses occur during no-load and they are measured during no-load tests [115], e.g., surface and tooth pulsation losses introduced by the magnetization flux as well as rotor losses introduced by rotor tooth pulsations and stator MMF harmonics are considered to occur at no-load [101, 115]. Furthermore, some of the additional losses are load dependent. Especially the leakage flux related additional losses and the losses due to harmonics of the stator MMF are considered to increase with the load and therefore to contribute to the *additional load losses* [101, 113–115].

In [90], a method for the determination of additional load losses by means of a combined evaluation of no-load and load tests is proposed. The additional load losses are determined by subtracting the mechanical power and expected winding losses (both from the load tests) as well as the iron, friction, and windage losses (all from the no-load tests) from the input power during the load tests [90]. This difference, called the residual losses, is evaluated over the second power of the torque. The linear part of this residual loss curve is defined as the additional load losses. [90] also provides estimated values for additional load losses if load tests cannot be performed (e.g., no torque measuring device is available). The estimated values for the additional load losses in the nominal point are 2.5 % of the input power for machines < 1 kW, and they decrease logarithmically to 0.5 % of the input power for machines > 10000 kW. The

uncertainty of using these values is classified as medium to high; however, the values are given as the upper limit of the investigation results of a large number of induction machines [90].

5.2.5 Additional High Frequency Losses

Additional high frequency losses occur due to the high frequency components in the inverter output voltages [93, 96, 116–118]. These components lead to high frequency currents that cause increased stator and rotor winding losses [93, 116, 117] and potentially also to increased iron losses [96]. The losses can be determined by a comparison of investigations with both a sinusoidal and inverter voltage supply [93]. The losses depend on the modulation index and the switching frequency [96, 116]. The influence of the load dependence is considered negligible [93]. In [116, 117], equivalent circuits for the determination of the high frequency winding losses are proposed. Due to the high relative speed between the high frequency traveling fundamental waves and the rotor, the slip is approximately 1 which allows to neglect the magnetization inductance (considered infinite) as compared to the low rotor impedance [116].

5.3 Loss and Parameter Studies

An initial investigation of the stator winding losses and the total losses during the different operation modes was performed with the example case machine IM1 when the performance of the proposed switched two-three-phase operation mode was investigated (cf., Section 3.3.2). It illustrated the increased stator winding losses due to the zero-sequence stator current and further power losses that are attributed to the zero-sequence system.

This present section further investigates the power losses with two additional example case induction machines IM3 and IM2. These machines have a different nominal power and stator winding design: 5.5 kW and single layer winding versus 3.7 kW and dual layer winding, respectively (see Appendix G for more detailed information on and an overview of the involved machines). Numerical results with IM3 and experimental results with IM2 are compared to results obtained from analytic power loss models discussed in Sections 5.1 and 5.2.

5.3.1 Investigations with IM3

The investigations with IM3 were performed with a 2D-finite element model. These investigations included the power losses and the rotor currents during the different operation modes and the determination of the parameters of the equivalent circuits of the positive-sequence and the zero-sequence system (cf., Section 5.1.2). All Finite Element Analysis (FEA) calculations were performed until steady state was reached.

The stator resistance R_s was calculated from the thermal conductivity, the cross section, and the length of the wires. The other parameters of the positive-sequence system were determined by standard tests in the FEA with balanced three-phase currents applied. The parameters $L_{\sigma\mathrm{s}}$, $L_{\sigma\mathrm{r}}$, and R_r were determined by locked-rotor tests. The magnetization inductance L_m was determined as a function of the magnetizing current by no-load tests (Fig. 5.4a). The iron losses were determined by the post-processing of loss calculations obtained from the no-load tests at different stator frequencies. The iron losses and the approximations by means of (5.27) are shown in Fig. 5.4b).

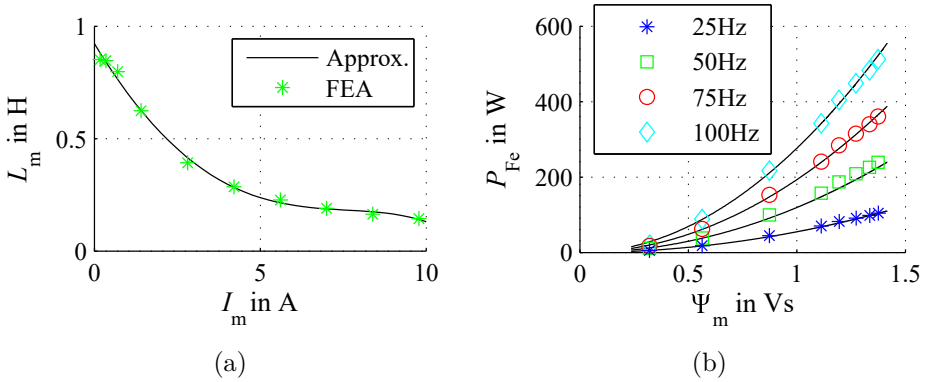

Fig. 5.4: Simulated results from the no-load tests with IM3: (a) magnetization inductance as a function of the magnetizing current, and (b) iron losses as a function of the magnetization flux linkage at different stator frequencies as well as approximations by means of (5.27).

The space harmonics of the zero-sequence system cause harmonic rotor currents during the post-fault operations. Fig. 5.5a) shows the occurring time harmonics in the Fourier spectra of a bar current at a load operating point during the three-phase-operation (3ph), the two-phase operation (2ph) and the switched two-three-phase operation (2/3ph). The occurring time harmonics are assigned to different orders and directions of rotation of the space harmonics. Furthermore, the frequencies of the exciting zero-sequence stator current components during the switched two-three-phase

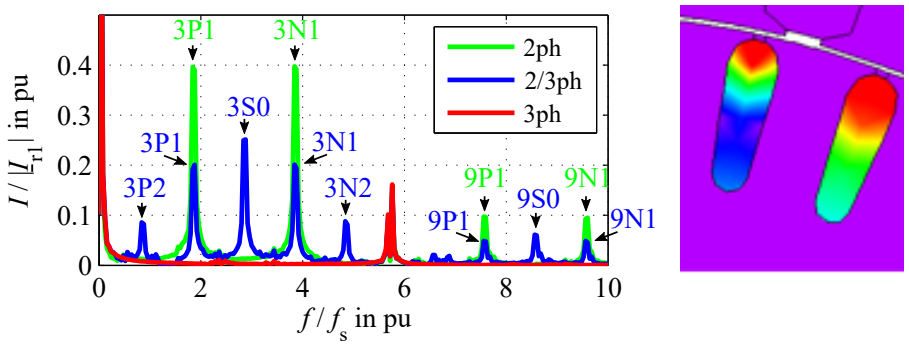

(a) (b)

Fig. 5.5: (a) Spectrum of the rotor bar current of IM3 during different operation modes, (b) current density in the rotor bars visualized using JMAG® [178]. The labels of the harmonics in (a) indicate the following: The first number indicates the order of the involved space harmonic, the letter indicates the direction of rotation of this space harmonic (P: positive, N: negative, S: static), and the second number indicates the frequency of the exciting zero-sequence stator current (0: $f = 0$, 1: $f = f_s$, 2: $f = 2f_s$).

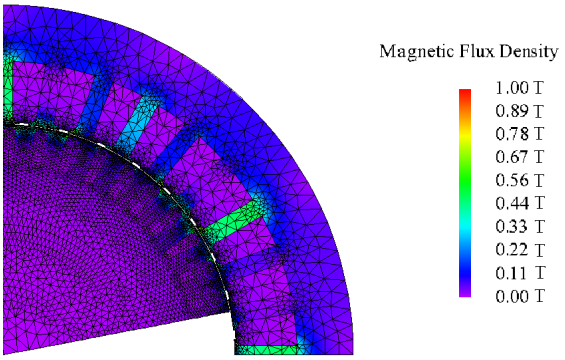

Fig. 5.6: Section of the finite element mesh of IM3 and the flux density when a zero-sequence stator current is applied, visualized using JMAG® [178].

operation (Fig. 5.2) are distinguished from one another. Due to the high frequencies of the bar currents introduced by the zero-sequence system, these currents experience a skin effect, as can be seen in Fig. 5.5b). The interaction of the space harmonics and the corresponding currents of the zero-sequence system leads to a torque that comprises a steady component and alternating components (cf., Chapter 9). For the determination of the steady torques from the FEA below, the torque was averaged over one fundamental period to neutralize the alternating torque components. The parameters of the equivalent circuit of the zero-sequence-system were determined from the FEA by ap-

plying a sinusoidal zero-sequence stator current. Fig. 5.6 shows the finite element mesh and the flux density for such a case. The input parameters of the FEA were chosen to obtain representative conditions that resemble the conditions of a rotor flux-oriented variable speed drive:

- The amplitude of the zero-sequence stator current was chosen equal to the machine's nominal current.
- The stator frequency was varied from zero to the nominal frequency.
- The rotational speed was chosen equal to the synchronous speed of the positive-sequence system (i.e., the speed is proportional to the stator frequency to obtain no-load operating points for the fundamental wave). The relative speeds between the space harmonics and the rotor are within the speed range that occurs during the post-fault operation in this case (cf., discussion of the speed of the third space harmonics in Appendix C).

Fig. 5.7 compares the results of the FEA for the parametrization and the equivalent circuit of the zero-sequence system. The results show a rapid increase of the rotor losses P_{Al0} at low speed and a moderate increase at higher speeds that is related to the skin effect. This effect causes the parameters R_{r0p}, R_{r0n}, $L_{\sigma\mathrm{r0p}}$, and $L_{\sigma\mathrm{r0n}}$ to depend on the relative speeds between the space harmonics and the rotor. Furthermore, an extremum of the steady breaking torque of the zero-sequence system at low speed can be observed.

Table 5.1 shows FEA results of load operating points with the different operation modes. The non-zero zero-sequence stator current during the post-fault operations clearly increases the stator winding losses P_{Cu} and the rotor winding losses P_{Al}. During the two-phase operation, both winding losses are increased approximately by a factor of 2, whereas during the switched two-three-phase operation, both winding losses are increased approximately by a factor of 1.5. A significant change of the iron losses P_{Fe} for the different operation modes was not observed. In Table 5.2, the results obtained from the equivalent circuits are presented. The computed winding losses correspond well with each other. However, the iron losses are underestimated by the mathematical model for lower flux linkages.

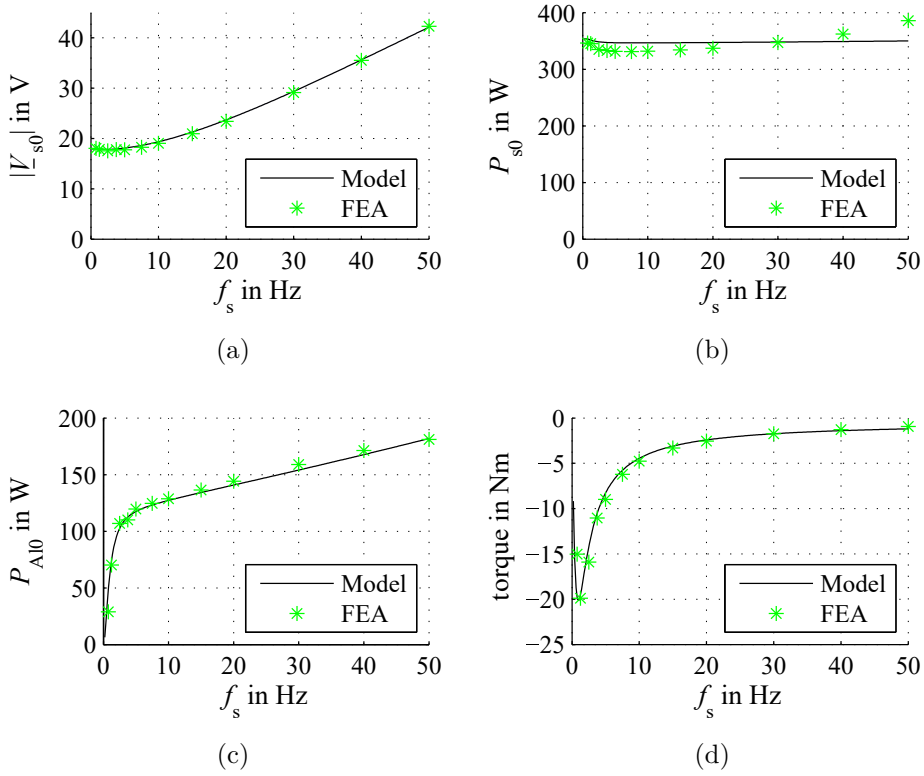

Fig. 5.7: Comparison of the results obtained by a 2D-FEA of IM3 and by the equivalent circuit of the zero-sequence system with sinusoidal zero-sequence current: (a) RMS value of the zero-system stator voltage, (b) stator power due to the zero-sequence system, (c) rotor losses due to the zero-sequence system and (d) steady breaking torque.

Table 5.1: Results of the FEA with IM3 at different operating points and modes.

Mode	Speed in r/min	$\lvert\underline{I}_{s1}\rvert$ in A	f_s in Hz	P_{Cu} in W	P_{Al} in W	P_{Fe} in W	Torque in Nm
3ph	1430	6.4	50	353	240	100	29.34
2ph	1430	6.4	50	705	424	106	27.98
2/3ph	1430	6.4	50	529	333	104	28.96
3ph	1430	3.2	50	83	56	31	7.45
2ph	1430	3.2	50	165	104	37	7.14
2/3ph	1430	3.2	50	124	82	34	7.30
3ph	1480	6.4	50	353	75	210	21.69
2ph	1480	6.4	50	705	166	207	20.60
2/3ph	1480	6.4	50	529	119	207	21.11
3ph	1480	3.2	50	83	37	131	13.18
2ph	1480	3.2	50	165	74	131	12.71
2/3ph	1480	3.2	50	124	55	130	12.93

Table 5.2: Results obtained with the analytic models at different operating points and modes.

Mode	Speed in r/min	$\lvert\underline{I}_{s1}\rvert$ in A	f_s in Hz	P_{Cu} in W	P_{Al} in W	P_{Fe} in W	Torque in Nm
3ph	1430	6.4	50	353	216	77	29.26
2ph	1430	6.4	50	705	395	77	28.01
2/3ph	1430	6.4	50	529	306	77	28.64
3ph	1430	3.2	50	83	53	16	6.79
2ph	1430	3.2	50	165	96	16	6.49
2/3ph	1430	3.2	50	124	75	16	6.64
3ph	1480	6.4	50	353	50	208	22.19
2ph	1480	6.4	50	705	210	208	20.99
2/3ph	1480	6.4	50	529	130	208	21.59
3ph	1480	3.2	50	83	32	132	14.11
2ph	1480	3.2	50	165	74	132	13.81
2/3ph	1480	3.2	50	124	53	132	13.96

5.3.2 Investigations with IM2

Further experiments have been performed with IM2. An overview of the measurement setups is provided in Appendix F. The parameters of the positive-sequence system were determined by standard tests (no-load, locked-rotor and load tests). Fig. 5.8 illustrates the magnetization curve and iron losses determined from the no-load tests and the model curves. The modeled curves are in good alignment with the measurement results, however, the iron losses are underestimated at high flux linkages. The friction and windage losses (Fig. 5.9) were determined as a function of the speed. These losses were calculated from the measured torque and speed when IM2 was disconnected from the power supply and rotated with the speed controlled driving machine. Since the air gap fluid friction after (5.32) is negligible in the nominal speed range of IM2, it is assumed that the measured losses correspond mainly with the bearing friction losses.

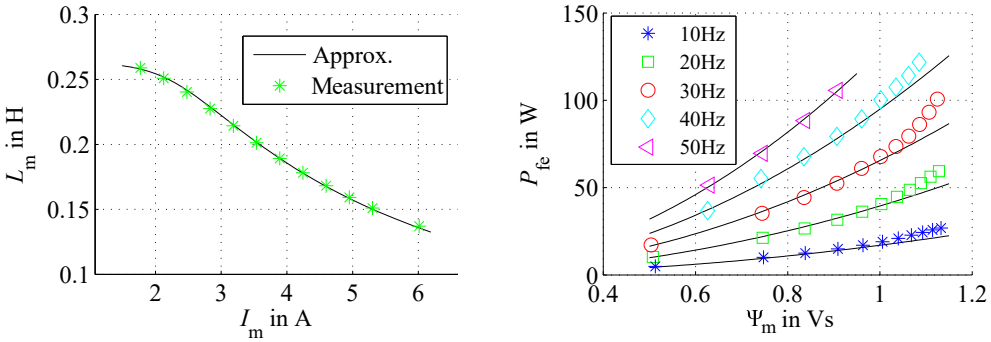

(a) (b)

Fig. 5.8: Measurement results from the no-load tests with IM2: (a) magnetization inductance as a function of the magnetizing current and analytic approximations based on (4.14), and (b) iron losses as a function of the magnetization flux linkage at different stator frequencies as well as analytical approximations by means of (5.27).

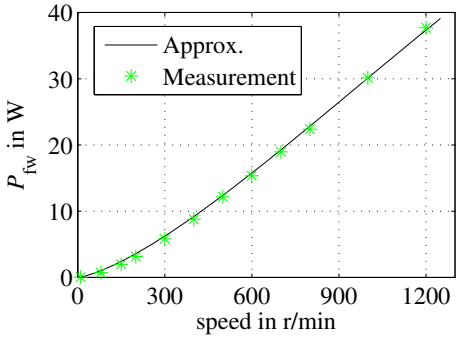

Fig. 5.9: Friction and windage losses of IM2 as well as an empirical approximation.

Further experimental investigations were performed to determine the parameters of the zero-sequence system. As during the aforementioned friction experiments, the driving machine was controlled to obtain different speeds. These experiments were conducted with series-connected windings and sinusoidal zero-sequence stator voltages with constant amplitudes and frequencies. The experimental results of Fig. 5.10 were obtained with a stator voltage of 38 V with a frequency of 40Hz (further experimental results for different frequencies are provided in Appendix D.) The electrical power, the stator current and voltage, the torque, and the speed were measured. Fig. 5.10a) illustrates the electrical power P_{s0} and the mechanical power P_{mech0}, where positive values correspond to power flow into the machine. The mechanical power and the torque (Fig. 5.10b) are corrected by the friction and windage losses P_{fw} to obtain the quanti-

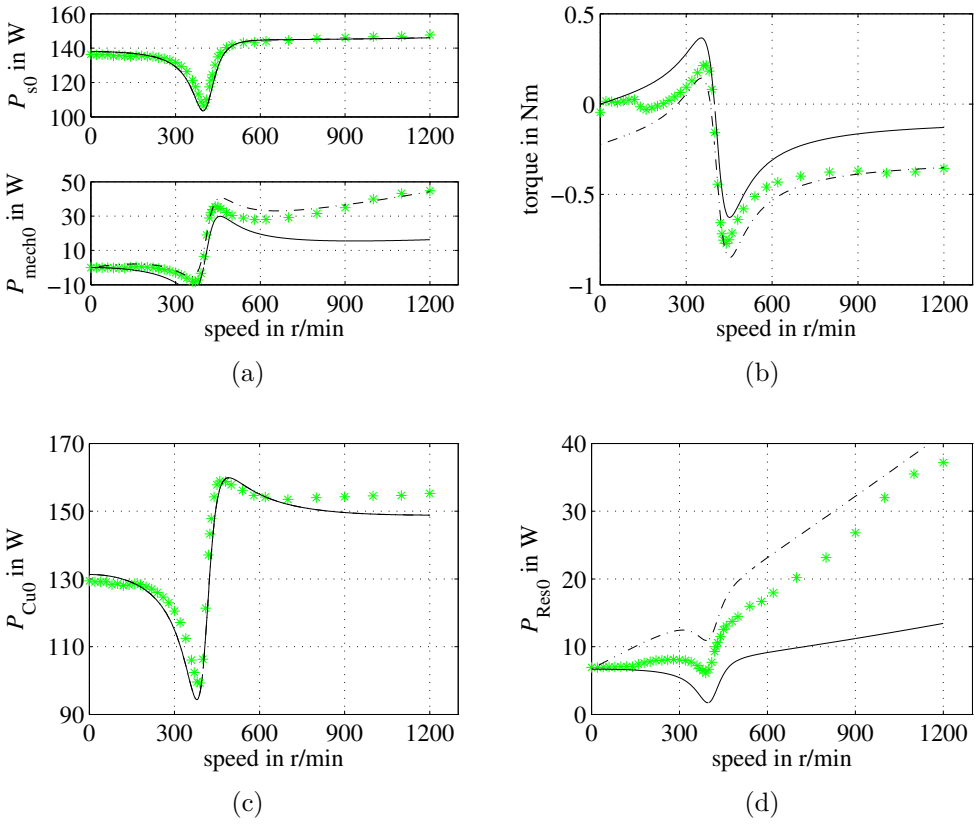

Fig. 5.10: Comparison of the experimental results with IM2 and the equivalent circuit of the zero-sequence system with sinusoidal zero-sequence voltage: (a) electrical and mechanical power, (b) torque, (c) stator winding losses, (d) residual losses. The green stars indicate the measurement results, whereas the solid and dashed lines represent the results of the equivalent circuit without and with additional rotor power, respectively.

ties related to the zero-sequence system. The stator winding losses P_{Cu0} in Fig. 5.10c) are calculated from the stator resistance and the measured stator currents. Furthermore, the rotor power losses are estimated by subtracting stator copper losses from the sum of the electrical and mechanical power (the residual losses P_{Res0} in Fig. 5.10d). The experiments with IM2 again confirm the dominance of the third space harmonic of the zero-sequence system. However, IM2 shows a lower zero-sequence breaking torque when compared to similar tests performed with the other two example case induction machines IM1 and IM3. This is likely related to the lower amplitude of the third space harmonic of the stator MMF for IM2 (cf., Fig. 4.4). IM2 also shows rotor losses increase with the speed, which was also observed in the numerical investigations with IM3 above.

Fig. 5.10 also illustrates the results obtained with the parameterized equivalent circuit of the zero-sequence system. Inputs of the equivalent circuit are the stator voltage, the frequency, and the speed. The comparison with the experiments shows a good agreement of the stator power and stator winding losses, however, there are deviations in the mechanical power and rotor losses. The amount of the rotor losses' increase with speed cannot be modeled with rotor frequency dependent rotor parameters in the equivalent circuit alone. A better agreement can be achieved by including an additional power in the mechanical power and rotor loss that increases linearly with speed with a slope of 0.0110 W/min as shown in Figs. 5.10a), b) and d). Possible reasons for the deviation (beyond the measurement uncertainty, the application of an equivalent circuit and the simplified consideration of the skin effect) include a force dependence of the bearing frictional losses, iron losses, inter-bar currents, and breaking torques of further zero-sequence system space harmonics (the torque of a ninth space harmonic with a synchronous speed at 133 r/min is indicated in Fig. 5.10b).

Further experimental results that show the performance of IM2 during the different operation modes as well as the results of the model are provided in Chapter 8. The results illustrate that at the considered operating points, the stator losses dominate the torque capability of IM2 and the rotor losses of the zero-sequence system play a minor role.

5.4 Conclusion

This chapter discusses the power losses of SCIMs during the three-phase, the two-phase, and the switched two-three-phase operation. The losses were investigated by means of analytical, numerical and experimental methods. The investigations showed significant increases of the stator and rotor winding losses during the post-fault operations. For similar torque, these increases were in the range of a factor of 2 for the two-phase operation, and in a range of a factor of 1.5 for the switched two-three-phase operation. These factors illustrate, that the operation at full torque is only possible for a short time, since such large loss increases lead to overtemperatures in the machine. The resulting reduced continuous torques for the post-fault operations are obtained in Chapter 8 by considering the winding temperatures.

The aforementioned factors obtained for similar torque must be seen as guide values, since the influence of increased temperatures on the losses has not been considered. Furthermore, the rotor losses potentially increase with speed.

The parameters for the analytic models are obtained by numerical (IM3), and experimental results (IM2). For the description of the electromagnetic losses and the torque during the different operating modes, equivalent circuits are applied. Despite the harmonic content of the zero-sequence stator current during the switched two-three-phase operation, the zero-sequence system related losses are approximated indirectly from a single equivalent circuit.

Chapter 6

Temperature Modeling of SCIMs

As discussed in the previous chapter, increased power losses and an asymmetric loss distribution in the stator of the machine occur during the post-fault operations with a zero-sequence stator current. These losses lead to elevated temperatures in the machine components that potentially exceed temperature limits. This chapter discusses the temperature limits in SCIMs in Section 6.1. Section 6.2 discusses analytic and numerical steady-state temperature modeling approaches and reviews temperature models for SCIMs with balanced losses. The heat transfer mechanisms occurring in SCIMs are summarized in Section 6.3.

6.1 Temperature Limits of SCIMs

The power losses discussed in the previous chapter are converted into heat that flows through different paths to the heat sinks of the machine. The heat flow increases the temperature of the machine components. The maximum permissible temperatures of the different components depend on the materials and are also defined in the machine design specification. The most important ones, those of the stator winding, of the rotor winding and of the bearings, are discussed below.

6.1.1 Stator Winding Temperature

The maximum temperature of the stator winding depends on the electric insulation system. Elevated temperatures reduce the mechanical and electrical strength of the winding insulation and may lead to a fault [103]. The maximum temperatures of different insulation system classes are shown in Table 6.1. The stator winding temperature can be determined experimentally by means of the measurement of the stator

resistance. The hot spot temperature is typically higher than the measured temperature, and the difference can be considered by adding a supplement [103]. Montsinger's rule [119] indicates that the lifetime of the insulation halves with every 10 K increasing temperature. [120] describes the thermal aging by a different approach (Arrhenius chemical rate equation). A discussion of different aging models is presented in [121].

Table 6.1: Temperature classes for electrical insulating systems and corresponding maximum permissible temperatures [95, 122–125].

Class	-	A	E	B	F	H	N
$T_{\max}$	°C	105	120	130	155	180	200

6.1.2 Rotor Winding Temperature

The rotor bars in squirrel cage induction machines are typically made of aluminum and are usually not electrically insulated from the rotor iron. The rotor winding temperature limit is defined by a mechanical problem [126]: the end rings of the rotor have a different expansion coefficient than the rotor iron, and therefore the temperature rise leads to mechanical stress. For the rotor bars, higher temperature limits are applied than for the end rings since they can expand with low stress [126]. The maximum temperatures stated by machine manufacturers for normal operation vary in the range of 200 °C - 280 °C for the bars and 40 °C - 200 °C for the end rings [126, 127]. The survey in [127] indicates that for the thermal expansion, the relative increase in temperature is more significant than the absolute temperature. On the other hand, absolute temperature limits can be given due to the decrease in yield strength of the cage material with increasing temperature (at approximately 400 °C, the aluminum turns plastic, the melting point is at 660 °C), see discussion in [127].

6.1.3 Bearing Temperature

The maximum temperature of the bearing is limited by the maximum temperature of the materials used for the bearing components and of the lubricant [128]. For a common steel bearing with mineral oil based lubrication, the maximum temperature is approximately 125 °C [128]. The bearing operation reduces the oil content in the grease. If the bearing is operated over 70 °C, the grease's lifetime decreases approximately by a factor of 1.5 for each 10 K increase in temperature [129]. It is important to choose a grease that provides viscosity for the desired temperature range.

6.1.4 Temperatures of Explosionproof Machines

Induction machines are also used in hazardous locations with a flammable atmosphere. Machines for these locations must be designed in a way that the inner and outer surface temperatures are below the autoignition temperature of the flammable materials [130]. The autoignition temperature depends on the material. Materials with low autoignition temperature inflame at a temperature of 160 °C [131].

6.2 Temperature Modeling Approaches

6.2.1 Lumped Parameter Thermal Networks (LPTNs)

A common approach to calculate the temperatures in SCIMs is the utilization of Lumped Parameter Thermal Networks (LPTNs) [132–141]. In the LPTNs, the complex heat paths of the machine are approximated by a circuit of thermal resistances. The thermal resistance of a component is defined as [154]:

$$R_{\mathrm{th}} = \frac{\Delta T}{\dot{Q}}, \tag{6.1}$$

where ΔT is the temperature rise across and $\dot{Q}$ is the heat flow through the component. The thermal resistance depends on the heat transfer mechanism to be modeled (conduction, convection, or radiation) as well as on the geometry and material parameters, see Section 6.3. To describe a thermal problem with an LPTN, several thermal resistances are connected to an equivalent circuit, as illustrated for a thermal problem in Fig. 6.1. The definition of the nodes of the equivalent circuit depends on the consideration of components with internal heat generation, the presence of parallel heat paths, the temperatures of interest, but also on the desired fineness. The inputs of the LPTNs are the power losses (the internal heat generations) which occur within the machine components, and the outputs are the component temperatures. The steady-state temperatures can be calculated by means of the following matrix product [136]:

$$\Delta\vec{T} = \boldsymbol{G}_{\mathrm{th}}^{-1}\vec{P}, \tag{6.2}$$

where $\Delta\vec{T}$ is the vector of nodal steady-state temperature rises with respect to the reference temperature, $\boldsymbol{G}_{\mathrm{th}}$ is the thermal conductance matrix and $\vec{P}$ is the vector of the nodal power losses. The matrix $\boldsymbol{G}_{\mathrm{th}}$ is obtained from a nodal analysis of the equivalent circuit.

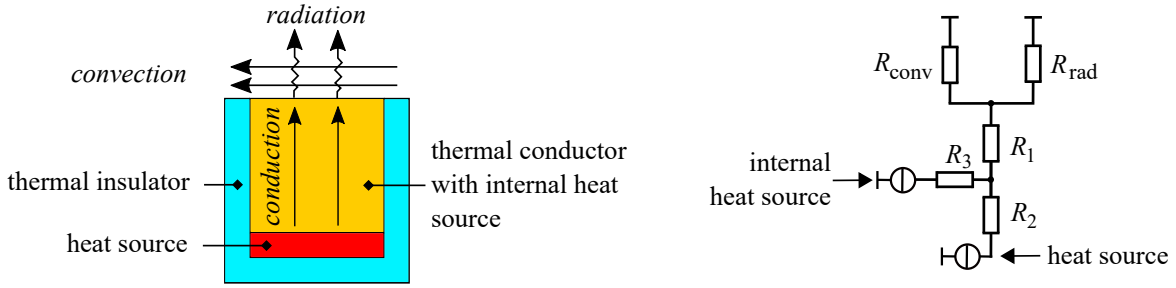

Fig. 6.1: Thermal problem with different heat transfer mechanisms and representation with a LPTN including thermal resistances to describe the conduction (R_1, R_2, R_3), convection (R_{conv}), and radiation (R_{rad}).

Several LPTNs for SCIM for balanced electric conditions and losses have been developed [132–141]. The proposed LPTNs differ significantly in the number of nodes. Higher order LPTNs (e.g., [136,141] 18 - 107 nodes) typically consider more axial layers or differences of the drive side and non-drive side. Such differences are usually neglected in the medium order LPTNs (e.g., [135, 137, 138] 6 - 13 nodes). Low order LPTNs as presented in [139, 140] (2 nodes) and are considered to be more suitable for the online calculation. However, the applicability of the analytical thermal resistance calculation methods discussed below, including the approximation of the three-dimensional heat flow, decreases with the reduction of the number of nodes. Further distinction can be made in the modeling of the heat paths of the stator winding and stator iron, as illustrated in Fig. 6.2. Fig. 6.2a) shows a sector model for a single layer winding with separate heat paths from the slot to the stator teeth and yoke [135]. To investigate the axial temperature distribution [136] proposed a sector model with multiple axial layers, shown in Fig. 6.2b). The slot model shown in Fig. 6.2c) has conductor and insulation layers and distributed heat sources and was proposed in [164].

6.2.2 Numerical Methods

Numerical methods are widely used to solve problems in many engineering discplines. In these methods, the calculation domain is subdivided into a large number of small volumes or elements and the describing partial differential equations are solved numerically. Common numerical methods are the Finite Difference Method (FDM), the Finite Volume Method (FVM), and the Finite Element Method (FEM) [142,143]. The methods differ in the mathematical formulation, the accuracy and flexibility with regard to the shape and the distortions of the mesh [142, 143].

The analysis with FEM - the Finite Element Analysis (FEA) - is widely used for

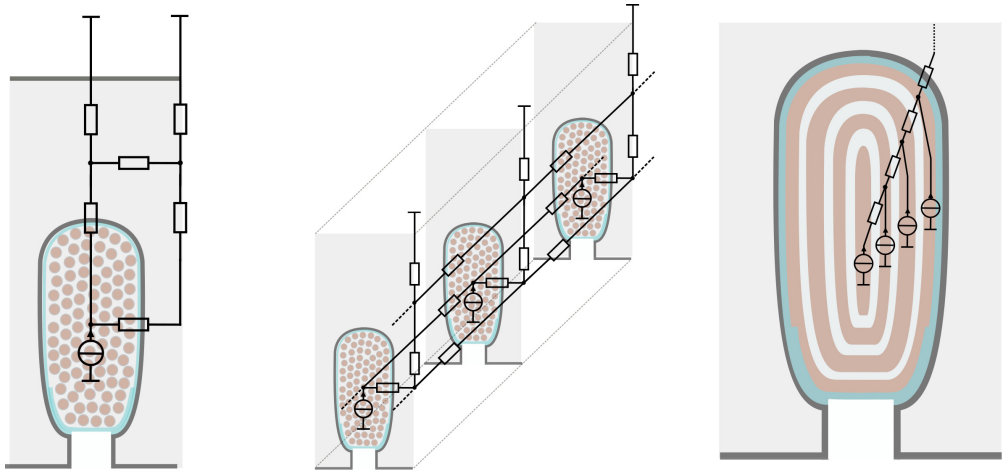

Fig. 6.2: Stator slot representations in LPTNs for random wound single layer windings: (a) sector model with separate heat paths to the stator teeth and back iron [135], (b) model with multiple axial layers [136], (c) conductor and insulation layers model with distributed heat sources [164].

the electromagnetic calculations of electric machines and also has been applied to thermal conduction problems in SCIMs by applying fourier's differential equation. The method has been used to calculate the steady state and transient stator and rotor temperatures [144–149]. In the conduction based FEAs, the convection is considered by analytical approaches. To also consider the convection numerically, the application of Computational Fluid Dynamics CFD has been proposed. CFD uses conservation laws, turbulence models and numerical methods (FDM, FVM, more and more frequently also FEM) [142, 143]. CFD has been applied for the analysis of the convection in the end winding region and the convection in liquid cooling systems [150–153, 172].

The strengths of the numerical methods are a high resolution and the representation of complex geometries. However, the computation time is usually high when compared to LPTNs.

6.3 Heat Transfer in SCIMs

This section summarizes the heat transfer mechanisms in SCIMs. Furthermore, it illustrates the calculation of thermal conductivities, heat transfer coefficients and thermal resistances. These properties can be applied in LPTNs, but also as component conductivities and boundary conditions in FEAs.

6.3.1 Conductive Heat Transfer

Conduction occurs in solids and fluids due to vibrations of atoms or molecules without macroscopic motion and can be described by Fourier's differential equation [154]:

$$div(k \cdot grad(T)) + \dot{\omega} = dc_{\mathrm{p}} \frac{\delta T}{\delta t}, \tag{6.3}$$

where k is the material dependent thermal conductivity, T is the temperature distribution, $\dot{\omega}$ is the internal heat density per volume, d is the density, and c_{p} is the specific heat capacity. If the thermal conductivity is constant, the internal heat generation is zero, and during steady state (energy storage neglected) (6.3) simplifies to:

$$k \cdot div(grad(T)) = 0. \tag{6.4}$$

Conduction Thermal Resistance

The geometries of the machine components are typically approximated by rods and (hollow) cylinders, as illustrated in Fig. 6.3. From (6.4), the one-dimensional solutions of the thermal resistances for these geometries can be derived [133–135].

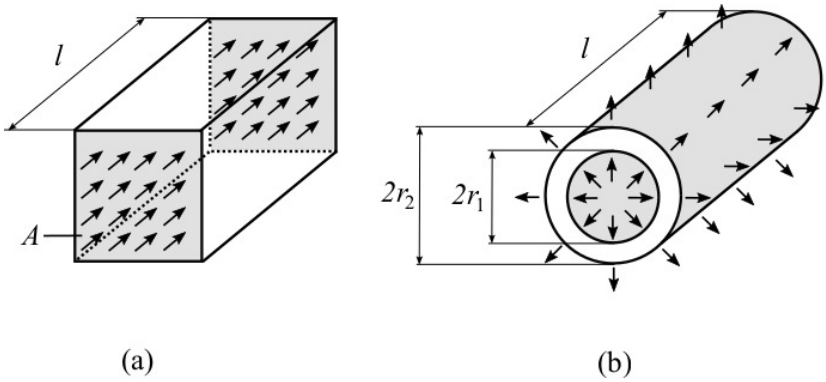

Fig. 6.3: Longitudinal heat flow in a rod (a) and radial heat flow in a hollow cylinder (b).

The one-dimensional resistance of a rod can be calculated from [154]:

$$R_{\mathrm{Ro}} = \frac{l}{kA}, \tag{6.5}$$

where l is the length, k is the thermal conductivity and A is the cross-sectional area. (6.5) can also be used to compute the resistance of hollow cylinders in axial direction with $A = \pi(r_2^2 - r_1^2)$ [137], where r_2 is the outer and r_1 is the inner radius. The resistance of a hollow cylinder in radial direction can be calculated from [154]:

$$R_{\mathrm{Zr}} = \frac{1}{2\pi kl} \ln\left(\frac{r_2}{r_1}\right). \tag{6.6}$$

Typically, the average temperature of a certain component is of interest. The corresponding node is the reference for the connection of the one-dimensional thermal resistances and the node where the internal heat generation is injected. The average temperature rise without internal heat generation can be calculated for the rod and the cylinder as follows [135]:

$$\Delta T_{\mathrm{m}} = \frac{R_2}{R_1 + R_2} \Delta T = R_2 \dot{Q}, \tag{6.7}$$

where $R_1 + R_2$ equals R_{Ro} and R_{Zr}, respectively. In the case of a rod, the average temperature occurs in the middle of the rod, therefore $R_1 = R_2 = \frac{R_{\mathrm{Ro}}}{2}$. In the case of a hollow cylinder, the cross sectional area increases with the radial position and the internal temperature decreases nonlinearely. The average temperature can be calculated with [135, 137, 138]:

$$R_1 = \frac{1}{4\pi kl}\left(\frac{2r_2^2}{r_2^2 - r_1^2} \ln\left(\frac{r_2}{r_1}\right) - 1\right), \tag{6.8}$$

$$R_2 = \frac{1}{4\pi kl}\left(1 - \frac{2r_1^2}{r_2^2 - r_1^2} \ln\left(\frac{r_2}{r_1}\right)\right). \tag{6.9}$$

In the equations above, internal heat generation was neglected. The average temperature rise including internal heat generation ($\dot{\omega} \neq 0$) can be calculated from [135]:

$$\Delta T_{\mathrm{m}} = R_2 \dot{Q} + (R_2 + R_3) \dot{Q}_{\mathrm{int}}, \tag{6.10}$$

where

$$R_3 = -\frac{R_{\mathrm{Ro}}}{6}, \tag{6.11}$$

in the case of a rod, and

$$R_3 = \frac{1}{8\pi kl(r_2^2 - r_1^2)}\left(r_1^2 + r_2^2 - \frac{4r_1^2 r_2^2 ln(r_2/r_1)}{r_2^2 - r_1^2}\right), \tag{6.12}$$

in the case of a cylinder. The corresponding equivalent circuit including the internal heat generation is provided in Fig 6.4. The connection of such circuits for different directions at the node M allows for the approximation of the multidimensional heat flow in the components [133–138].

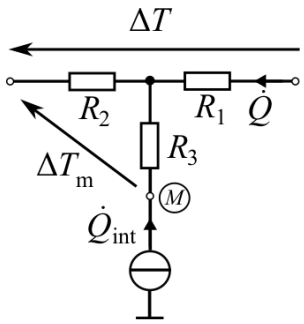

Fig. 6.4: General T-network for the description on a one-dimensional steady state conductive heat flow with internal heat generation [133–138].

Thermal Conductivity of Composites

The thermal resistances above depend on the thermal conductivity and it is assumed, that this conductivity is constant. However, some of the machine components are inhomogeneous multi-material composites, e.g., the laminated cores and the stator winding. Furthermore, the composites exhibit an anisotropy. Approaches for the averaging of the conductivities and the homogenization of composites are discussed in [135, 156–161]. A simple analytic approach to calculate the average conductivity of an inhomogeneous anisotropic material is to assume an equivalent laminated composite, as shown in Fig. 6.5a). In the case of a two-material composite, the average conductivity perpendicular to the lamination direction can be calculated using network theory [156–160]:

$$k_\mathrm{s} = \frac{1}{y_1 \frac{1}{k_1} + (1 - y_1)\frac{1}{k_2}}, \tag{6.13}$$

where k_1 and k_2 are the conductivities and y_1 is the fractional volume of material 1 in the composite. The average conductivity in the lamination direction can be calculated from:

$$k_\mathrm{p} = y_1 k_1 + (1 - y_1) k_2. \tag{6.14}$$

If material 1 is a conductor and material 2 is an isolator ($k_1 \gg k_2$):

$$k_\mathrm{s} \approx \frac{k_2}{(1 - y_1)}, \tag{6.15}$$

$$k_\mathrm{p} \approx y_1 k_1. \tag{6.16}$$

The average conductivity in the lamination direction (6.16) is mainly defined by the

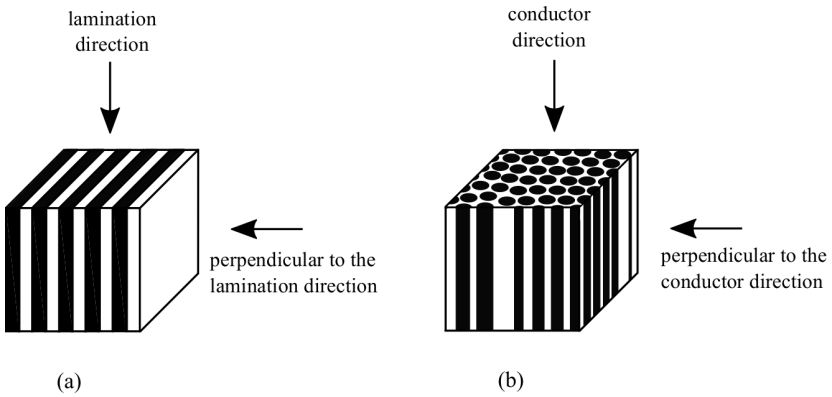

Fig. 6.5: A laminated two-material composite (a) and two-material composite with cylindric conductors (b).

fractional volume and conductivity of the thermal conductive material. This is the case for the steel lamination in radial direction and for the stator winding in direction of the conductors. However, the thermal conductivity is significantly lower perpendicular to the laminations and the conductors, and is mainly defined by the fractional volume and conductivity of the thermal insulating material. Therefore, the conductivity of the insulating material strongly affects the heat dissipation from the stator winding to the stator core.

6.3.2 Convective Heat Transfer

Convective heat transfer occurs at interfaces between solids and streaming fluids in connection with a temperature gradient. It can be described by Newton's law of cooling [162]:

$$\dot{q}_{\mathrm{conv}} = h_{\mathrm{l}}(T - T_{\infty}), \tag{6.17}$$

where $\dot{q}_{\mathrm{conv}}$ is the convective heat flow density, h_{l} is the local heat transfer coefficient, T is the temperature of the solid, and T_{∞} is the (free stream) temperature of the fluid. By integration, the average heat transfer coefficient h is obtained. The integration of convective heat flow density and the definition of the average heat transfer coefficient leads to [162]:

$$\dot{Q}_{\mathrm{conv}} = hA_{\mathrm{c}}(T - T_{\infty}), \tag{6.18}$$

where $\dot{Q}_{\mathrm{conv}}$ is the convective heat flow, h is the (average) heat transfer coefficient, and A_{c} is the area of the convection surface. The heat transfer coefficient strongly depends on the streaming in the boundary layer and therefore on the speed, viscosity, and

thermal diffusivity of the fluid as well as on the characteristic length and the geometry.

Natural and forced convection are distinguished from one another. During natural convection, the motion of the fluid particles is caused by pressure gradients, whereas during forced convection, the motion is caused by technical devices such a pumps and fans. Further, two different flow types are differentiated between, namely laminar and turbulent flow [163]: Laminar flow is characterized by the fluid particles that move in layers that do not mix, whereas during turbulent flow, the fluid particles perform irregular transverse movements. Turbulent flow is locally unstable but well correlated, which enables the mathematical description with empiric expressions [163]. The theory of similarity allows the flow and heat transfer to be described by means of dimensionless numbers (so-called similarity parameters) [162]. For example, laminar and turbulent flow can be distinguished from each other by means of the Reynolds number [163]:

$$Re = \frac{v l_\mathrm{c} d}{\eta}, \tag{6.19}$$

where v is the velocity, l_c is the characteristic length, d is the density of the fluid, and η is the dynamic viscosity of the fluid. If the Reynolds number is greater than a critical value, turbulent flow occurs. The critical value has to be determined experimentally for every flow configuration [163]. The transition from the flow field to the temperature field can be expressed by means of the Prandtl number [162]:

$$Pr = \frac{c_\mathrm{p} \eta}{k}, \tag{6.20}$$

where c_p is the specific heat capacity and k is thermal conductivity of the fluid. The Nusselt number is a dimensionless heat transfer coefficient [162]:

$$Nu = \frac{h l_\mathrm{c}}{k}. \tag{6.21}$$

In practice, for a given flow configuration, empirical expressions can be applied for the calculation of the Nusselt number which allows the calculation of the average heat transfer coefficient:

$$h = \frac{k}{l_\mathrm{c}} Nu. \tag{6.22}$$

Convective Thermal Resistance

By combining (6.18) and (6.1), the convective thermal resistance can then be calculated from [162]:

$$R_{\text{conv}} = \frac{1}{hA_{\text{c}}}. \tag{6.23}$$

6.3.3 Thermal Radiation

Radiation occurs in a vacuum or through solids and fluids, however, it does not require a material medium. The emissive power density of a gray radiator can be calculated by means of the Stefan-Boltzmann law [154]:

$$\dot{q}_{\text{e}} = \epsilon\sigma T^4, \tag{6.24}$$

where ϵ is the material dependent emissivity, σ is the Stefan-Boltzmann constant and T is the absolute temperature. The net radiant power transmitted between two diffuse-gray radiators can be calculated from [154]:

$$\dot{Q}_{12} = A_1\Sigma_{12}(T_1^4 - T_2^4), \tag{6.25}$$

where A_1 is the area of radiator 1, Σ_{12} is the transfer coefficient and T_1 and T_2 are the absolute temperatures of the radiators. The transfer coefficient can be calculated from the geometric configuration. For a general configuration of two diffuse-gray radiators, the coefficient can be calculated from [154]:

$$\Sigma_{12} = \frac{\sigma}{\frac{1-\epsilon_1}{\epsilon_1} + \frac{1-\epsilon_2}{\epsilon_2}\frac{A_1}{A_2} + \frac{1}{F_{12}}}, \tag{6.26}$$

where A_2 is the area of radiator 2, ϵ_1 and ϵ_2 are the emissivities of the radiators, and F_{12} is the view factor.

Radiation Thermal Resistance

By combining (6.1) and (6.25), the thermal resistance due to radiation can be calculated from:

$$R_{\text{rad}} = \frac{(T_1 - T_2)}{A_1\Sigma_{12}(T_1^4 - T_2^4)}. \tag{6.27}$$

The thermal resistance directly depends on the radiator temperatures and quickly decreases with the temperature difference. However, the radiation thermal resistances are typically high in comparison to resistances due to conduction and forced convection.

6.3.4 Thermal Properties of Selected Components and Heat Paths

This section summarizes selected thermal properties of SCIMs.

Thermal Conductivities

Table 6.2 summarizes the thermal conductivities of selected materials. As discussed in Section 6.3.1, the thermal conductivities of composites are associated with the conductivities of the composing materials.

[160] estimates the thermal conductivity of impregnated windings. Different homogenization approaches are compared to the measurements on artificial winding samples. The approaches exhibit good congruence with the measurements and consider the insulation of the wires and the impregnation material, however, air is not taken into consideration. The authors in [164, 165] emphasize that random wound windings in electric machines are never perfectly impregnated, and that a residual air remains within the impregnation. This residual air is of interest from a thermal point of view, since air has a significantly lower conductivity than the impregnation materials and will affect the average conductivity of the insulation system. Based on the measurements on standard machines, a parallel structure (6.14) for the calculation of average conductivity of the insulation material is proposed, with $y_1 = 0.4$ for low cost machines and $y_1 = 0.8$ for vacuum impregnated machines, where k_1 is the conductivity of the impregnation material and k_2 the conductivity of air [164, 165].

Table 6.2: Typical thermal conductivities of selected materials [155, 156].

Thermally conductive materials	k	Thermally isolating materials	k
-	$\frac{W}{mK}$	-	$\frac{W}{mK}$
Aluminium	236	Air	0.026
Carbon steel	43	Epoxy	0.6
Copper	399	Insulation Paper	0.1
Iron	77	Varnish	0.3
Silicon steel	42	Water	0.597

Heat Transfer in a Cooling Jacket

The convective heat transfer from the wall of a cooling jacket to the coolant can be described by empirical expressions for the heat transfer in circular pipes. The critical Reynolds number for this flow configuration is $Re_{\mathrm{crit}} = 2300$. The Nusselt number can be calculated from [162]:

$$Nu = \begin{cases} 4.36 & Re < Re_{\mathrm{crit}} \\ 0.023 Re^{\frac{4}{5}} Pr^{\frac{1}{3}} & Re \geq Re_{\mathrm{crit}}, \end{cases} \tag{6.28}$$

where Re and Pr are given by (6.19) and (6.20), respectively. The characteristic length equals the tube diameter. The fluid properties equal the properties of the coolant.

Air Gap Heat Transfer

The description of the convection between the rotor and the stator is based on the work by Taylor [104–107]. Further investigation, including the effects of stator and rotor slots, as well as a superimposed axial flow, are provided in [110, 166]. Empirical expressions for no axial flow can be found in [166] which, in the case of a low ratio between the gap length and the radius, can be defined as follows:

$$Nu = \begin{cases} 2 & Ta < 1700 \\ 0.128 Ta^{0.367} & 1700 \geq Ta < 10000 \\ 0.409 Ta^{0.241} & Ta \geq 10000, \end{cases} \tag{6.29}$$

where Ta is given by (5.31), respectively. The fluid properties equals the properties of air.

Heat Transfer in the End Space Region

The convective heat transfer in the end space region (this region includes the surfaces of the stator end windings, rotor end rings, and the frame) strongly depends on the air flow. The heat transfer at the stator and rotor surfaces are traditionally described in totally enclosed induction machines by heat transfer coefficients that depend on the air velocity [137, 167–170]:

$$h = h_0 \left(1 + u_{\mathrm{c}} v^{o_{\mathrm{c}}}\right), \tag{6.30}$$

where h_0, u_{c}, and o_{c} are fitting parameters, and v is the air velocity, that is estimated

as half of the velocity of the outer rotor surface. The constant h_0 is the heat transfer coefficient at zero rotational speed that mainly corresponds to the natural convection but partially also to thermal radiation [168] (see also the following Section). In many models, the heat transfer coefficient increases almost linearly with the air velocity (n_c is close to 1) [137,164,168,169]. The reported values for the other two parameters exhibit a wider dispersion. The reported zero-speed heat transfer coefficients h_0 are in the range of 15 $\frac{W}{m^2K}$ - 42 $\frac{W}{m^2K}$ and the speed coefficients u_c are in the range of 2.5 $\frac{W}{m^2K}\frac{s}{m}$ - 7$\frac{W}{m^2K}\frac{s}{m}$. A possible explanation for the differences is the influence of the airflow on the geometry [168,171,172]. Higher heat transfer values are possible with more free space around the end windings [168, 172]. On the contrary, the results [164, 169, 172] indicate a drastic reduction of u_c if the fins on the rotor end rings are absent.

Radiation Heat Transfers

An experimental study performed with a heated machine in a vacuum chamber indicated the outer and inner radiation heat transfer coefficients $h_{rad} = (R_{rad}A)^{-1}$ to be in a range of 6$\frac{W}{m^2K}$ - 8$\frac{W}{m^2K}$ [173]. These findings are also in agreement with the theoretical considerations in [156].

Heat Transfer over Joints

Due to the non-ideal surfaces of the adjacent machine components, constrictions of the heat paths occur [174]. These increase the temperature rise over the joints. Joints in SCIMs occur between the frame and the stator iron, the stator iron and the stator winding, the rotor winding and the rotor iron, but also at the shaft and bearings. The prediction of the thermal contact resistance of a joint is challenging since it depends on the materials, the contact pressure, the surface roughness, the manufacturing process, and the temperature [136,137,164,174,175]. Experimental investigations on the contact resistances of the joint between the stator frame and the stator iron at a set of induction motors revealed a high variance (approximately 350 $\frac{W}{m^2K} - 2500\frac{W}{m^2K}$) and large deviations from the values provided in handbooks [164,165]. Lamination related contacts are a special case since the non-ideal stacking of the sheets causes air pockets [136, 164]. There is also a lack of the systematical prediction of resistances of bearings. Some investigations of bearing contact resistances were performed in [136, 164, 165].

6.4 Conclusion

This chapter reviews the temperature limits of SCIMs. Furthermore, it illustrates the modeling by LPTNs and numerical approaches as well as the heat transfer mechanisms in totally enclosed water cooled SCIMs. The majority of the developed LPTNs assume balanced power losses in the stator winding [132, 133, 135–141]. The following chapter develops LPTNs and numerical models to consider the unbalanced conditions.

Chapter 7

Temperature Models for Unbalanced Losses

This chapter discusses lumped parameter thermal networks (LPTNs) and finite element temperature models that take the unbalanced stator winding power loss distribution during the post-fault operations into account. Furthermore, it shows the results of experimental thermal investigations of an example drive. The LPTNs from this chapter are applied in Chapter 8 for the calculation of the continuous torque during the post-fault operations.

7.1 Heat Paths with Unbalanced Losses

Temperature models such as shown in Fig. 6.2a) assume balanced power losses and utilize the single slot periodicity along the perimeter in such a case. However, if the stator currents and losses are not balanced, as is the case during the zero-sequence stator current based post-fault operations, the single slot periodicity turns into a pole periodicity, and more slots must be considered for the calculation of the stator temperatures, as illustrated in Fig. 7.1a). If the losses in two phases are equal, the symmetry allows merging those two phases, as illustrated in Fig. 7.1b). The assumption of a single slot periodicity also applies to a dual layer winding if the losses are balanced. However, in the case of unbalanced losses, the temperature distribution of a dual layer winding is more complex, especially when the winding is pitched. In this case, several coils of a particular phase share slots with coils of the other phases, as illustrated in Fig. 7.2. This sharing occurs partially in the upper and partially in the lower layer, and it leads to heat paths between different phases in the slot region.

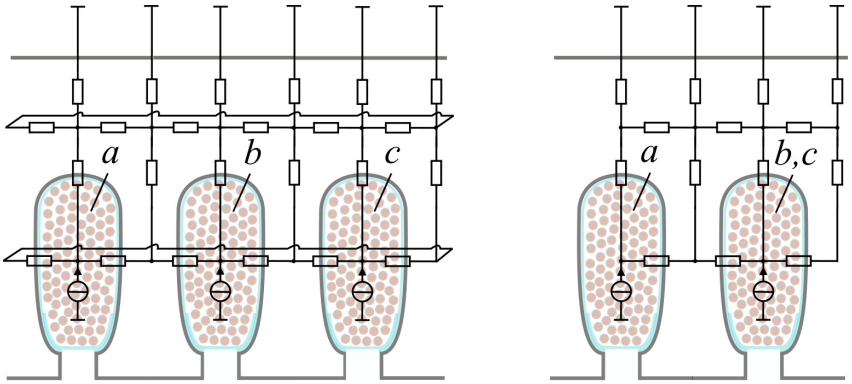

(a) (b)

Fig. 7.1: Stator representations of a three-phase single layer winding for unbalanced losses: (a) three slot model with one slot per pole and phase, (b) simplified model for equal losses in phases b and c.

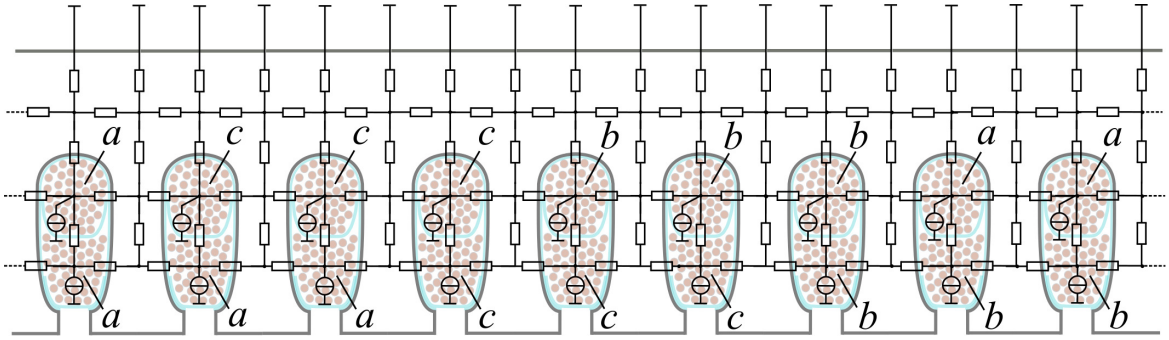

Fig. 7.2: Stator representation for unbalanced losses and a three-phase dual layer winding with three slots per pole and phase and a pitching by 7/9.

Heat paths in the end winding region are illustrated for the cases of a single and a dual layer winding in Figs. 7.3 and 7.4, respectively. They comprise heat paths within the coils and heat paths between different coils. End winding heat paths between different coils have been previously modeled in the context of the voltage unbalance and moderate stator winding loss unbalance of grid operated SCIMs [134] (simple low order LPTNs that include heat paths between the stator phases have been applied in the same context in [176, 177].) If the coils are in contact in the end winding region, conductive heat paths occur between the coils [134]. This is normally the case for random wound low voltage machines, where the coils are bound together and impregnated. Differences of these heat paths can occur between the coils, depending on the coils concerned, since the coils of the same phase and group touch each other, whereas the coils of different phases are usually separated by insulation paper.

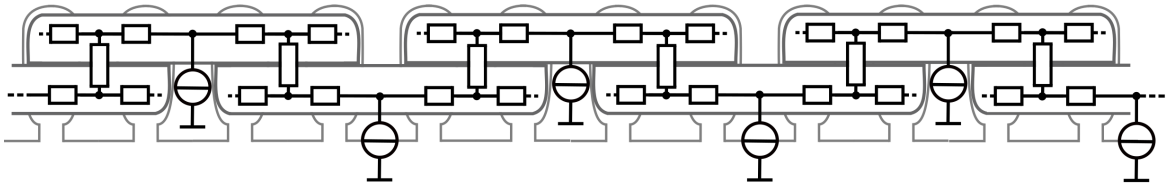

Fig. 7.3: Illustration of conductive end winding heat paths in a single layer winding.

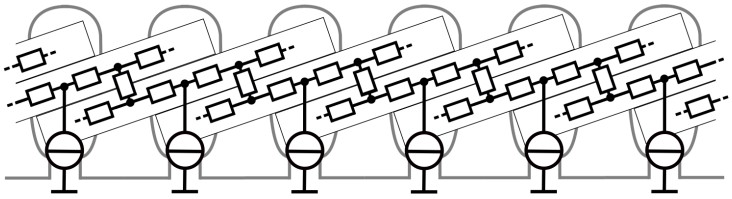

Fig. 7.4: Illustration of conductive end winding heat paths in a dual layer winding.

7.2 Purpose of the Developed Models

At the beginning of the development of a temperature model, several demands such as the purpose, the temperatures of interest and the fineness of the model should be considered. Furthermore, application-specific characteristics affect the development, such as the representative heat paths, boundary conditions or the availability and the uncertainty of parameters.

The purpose of the models discussed here is the application for the temperature calculation in the context of the computation of the continuous torque during the post-fault operations (see Chapter 8) as well as the analysis and discussion of the heat paths with unbalanced stator winding losses. Therefore, two different modeling approaches are chosen. For the torque calculation, a Lumped Parameter Thermal Network (LPTN) with low computational time is developed. It enables the compliance of the winding and bearing temperatures so as to verify they are within the thermal limits (Section 7.3). For the detailed thermal representation, a high order finite element model of the stator of the machine is developed (Section 7.4). Both models consider the unbalanced loss distribution in the stator winding. Since this thesis focuses on the steady state behavior, i.e., continuous torque development, steady state temperature models are developed in which thermal capacitances can be neglected.

7.3 Lumped Parameter Thermal Networks (LPTNs) for Unbalanced Losses

7.3.1 Model for an SCIM with a Single Layer Winding

Fig. 7.5 shows the LPTN developed for the calculation of the temperatures during the post-fault operations of a totally enclosed water cooled machine with a single layer winding (IM3 in Appendix G). The model consists of 14 nodes and assumes symmetry between the drive side and the non-drive side. To consider the unbalanced losses in the stator winding during the post-fault operations, the model includes separate nodes for the stator teeth and winding for both the faulty phase a as well as the healthy phases b and c. The thermal resistances of the healthy phases b and c are merged (cf., Fig. 7.1b), therefore, these resistances in the LPTN have half the value of the corresponding resistances of the faulty phase a. The meaning of the nodes is as follows: 0: coolant, 1: frame in the middle of the axial length, 2: frame at the beginning of the axial length, 3: stator back iron, 4: stator teeth of phase a, 5: embedded stator winding of phase a, 6: end winding of phase a, 7: stator teeth of phases b and c, 8: embedded stator winding of phases b and c, 9: end winding of phases b and c, 10: air gap, 11: rotor teeth, 12: embedded rotor winding, 13: rotor end winding, 14: end cap air, and 15: bearing. For reasons of clarity for Fig. 7.5 the heat sources are not drawn. The heat flow injections are as follows: 3: $\frac{1}{2}$ of the total iron losses, 4: $\frac{1}{6}$ of the total iron losses, 7: $\frac{2}{6}$ of the total iron losses, 5 and 6: copper losses of phase a, 8 and 9: sum of the copper losses of phases b and c, 12 and 13: rotor losses, 15: bearing friction losses.

When identical stator copper losses are applied to all three phases, the temperatures of the corresponding stator winding nodes of the phases a, b, and c are equal. However, due to the unbalanced losses during the post-fault operations, the temperatures of phases b and c exceed the temperature of phase a. Heat paths between the different phases reduce this temperature asymmetry. As discussed above, such heat paths potentially occur in the case of a single layer winding in the end winding region. The heat exchange between the healthy phases b, and c and the faulty phase a in this region is described in the LPTN by means of a single thermal resistance R_{69}. If this heat exchange is low (high R_{69}), the thermal resistance of the effective heat path for the total copper losses from the stator winding to the back iron is increased in comparison to the symmetrical three-phase operation (by a factor of 1.5 in the case of the two-phase operation). In this case, the nominal local copper losses lead to approximately a nominal local temperature rise as during the three-phase operation. The real temper-

ature rise is lower since the heat flow across the joint between the back iron and the frame as well as from the frame to the coolant (R_{01} and R_{13}) leads to a temperature rise that potentially correlates with the total copper losses. (In air-cooled machines the thermal resistance to the coolant is higher, thus, this effect is potentially higher.) A increased heat exchange between the phases (low R_{69}) leads to a better cooling of the healthy phases and to a more symmetrical temperature distribution. The stator temperatures are influenced by the rotor losses as well, since these losses are dissipated along the main heat path via the stator iron to the coolant. This leads to an additional temperature rise in the stator. The additional rise of the rotor temperatures caused by the stator losses correlates with the total stator losses, since the rotor is moving and the main heat path is not constricted.

7.3.2 Model for an SCIM with a Dual Layer Winding

The LPTN for an SCIM with a dual layer winding (IM2 in Appendix G) shown in Fig. 7.6 consists of 20 nodes, assumes symmetry between the drive side and the non-drive side and also includes separate nodes for both the faulty phase a and the healthy phases b and c (includes nodes for the stator yoke and teeth, the end windings, and the embedded upper and lower layers). The thermal resistances of the healthy phases b and c are merged and have half the value of the corresponding resistances of the faulty phase a. The meaning of the nodes is as follows: 0: coolant, 1: frame in the middle of the axial length, 2: frame at the beginning of the axial length, 3: stator back iron of the phase a, 4: stator back iron of phase a, 5: stator teeth of phase a, 6: embedded stator winding of phase a lower layer, 7: end winding of phase a, 8: stator teeth of phase a, 9: embedded stator winding of phase a upper layer, 10: stator teeth of phases b and c, 11: embedded stator winding of phases b and c lower layer, 12: end winding of phases b and c, 13: stator teeth of phases b and c, 14: embedded stator winding of phases b and c upper layer, 15: air gap, 16: rotor teeth, 17: embedded rotor winding, 18: rotor end winding, 19: end cap air, and 20: bearing.

The LPTN has similar characteristics to the single layer winding LPTN. Differences occur in the heat exchange between the coils in the slot and end winding regions that are described by the thermal resistances R_{69}, R_{1114} and R_{712}, R_{911}, R_{614}, respectively. As discussed above, the heat exchange between the phases of a pitched dual layer winding with unbalanced losses is complex, and many heat paths in the slot and end winding regions occur. The LPTN in Fig. 7.6 considers only one slot per phase, as an approximation. However, as shown below, it is suitable to describe the temperatures of such a winding with sufficient accuracy.

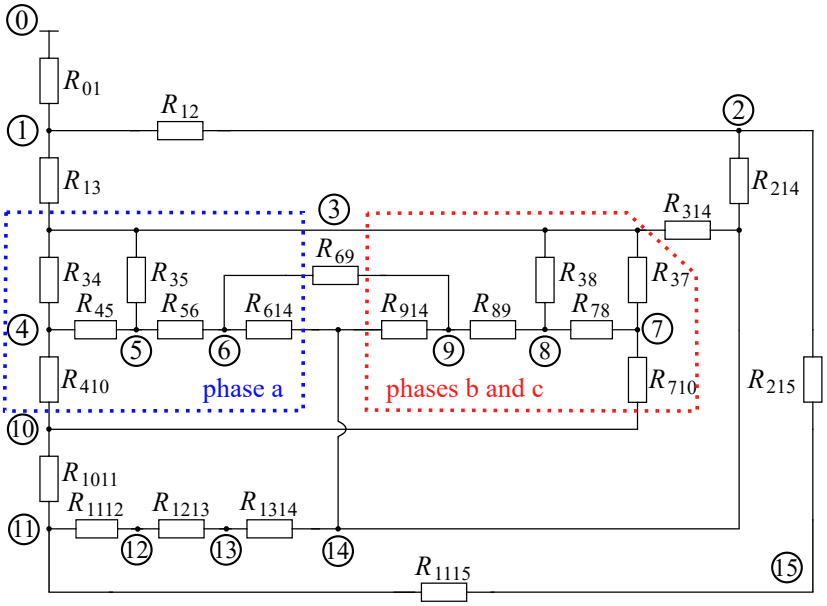

Fig. 7.5: LPTN of a water cooled three-phase induction machine with a single layer winding including separate modeling of the healthy phases b and c and the faulty phase a.

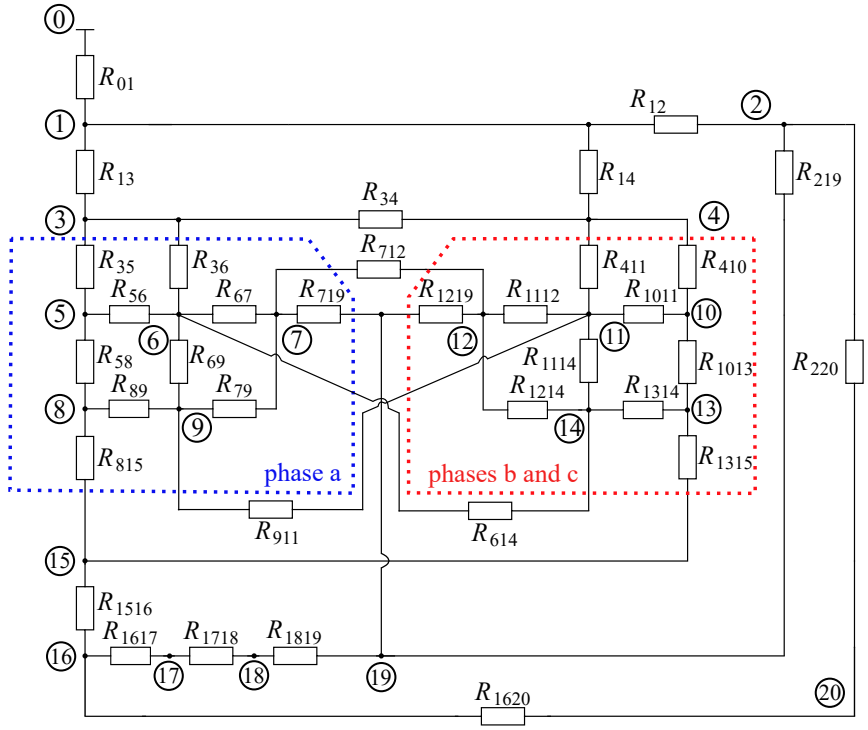

Fig. 7.6: LPTN of a water cooled three-phase induction machine with a pitched dual layer winding including separate modeling of the healthy phases b and c and the faulty phase a.

7.4 Thermal Finite Element Models

A three dimensional thermal FEA with a high number of elements allows a more detailed consideration of the geometry, the three dimensional heat conduction, the loss distribution, and the position of the thermal contacts. The thermal FEA is used for the description of the stator of the machines IM3 and IM2 which corresponds to the nodes 3 - 10 of the single layer LPTN in Fig. 7.5 and the nodes 3 - 14 of the dual layer LPTN in Fig. 7.6. Fig. 7.7 shows the thermal finite element models of machine stators for single and dual layer winding as well as details of the finite element mesh. The utilization of the periodicity along the perimeter and the symmetry of the drive side and the non-drive side drastically reduces the number of elements. As discussed in Section 7.1, the periodicity for unbalanced losses is one pole pitch. This leads, together with drive end symmetry, to a minimum model size of a $\frac{1}{8}$-model for a 4-pole machine. The number of elements of the $\frac{1}{4}$ and $\frac{1}{8}$-models shown in Fig. 7.7 is, for both models, in the range of $3 \cdot 10^6$ elements.

The stator winding and the stator iron are modeled by the homogenized counterparts (cf., Section 6.3.1). The stator coil geometry is replaced by straight rods that can be interpreted as the cut and bend open version of the coils, as illustrated in Fig. 7.8. This enables the consideration of the anisotropy of the thermal conductivity (cf., Section 6.3.1) with the cartesian coordinate system in finite element software. The obtained end faces of the coils are connected virtually in the software by a low thermal resistance. The same technique is used for the consideration of the slot liner and for the contacts between adjacent coils in the slot and in the end winding region. The insulation layers in the slot also have been modeled explicitly. However, to avoid distortions in the mesh due to the thin insulation layers, the use of virtual resistances was preferred. The number of slots per pole and phase is three for both considered machines, which is also the number of coils per group. To consider the end winding contacts of the coils that belong to the same group, the side surfaces of the corresponding rods are connected by a low resistance in the case of the single layer winding. The end winding coil group contacts in the case of the dual layer winding as well as the heat paths between the coils of different phases are considered by resistances between the top and the bottom surfaces of the corresponding rods, as illustrated Fig. 7.3 for a single layer winding and in Fig. 7.4 for a dual layer winding, respectively. In the case of the dual layer winding, the further defined heat path is the one over the slot separator between the upper and lower layer, see Fig. 7.2.

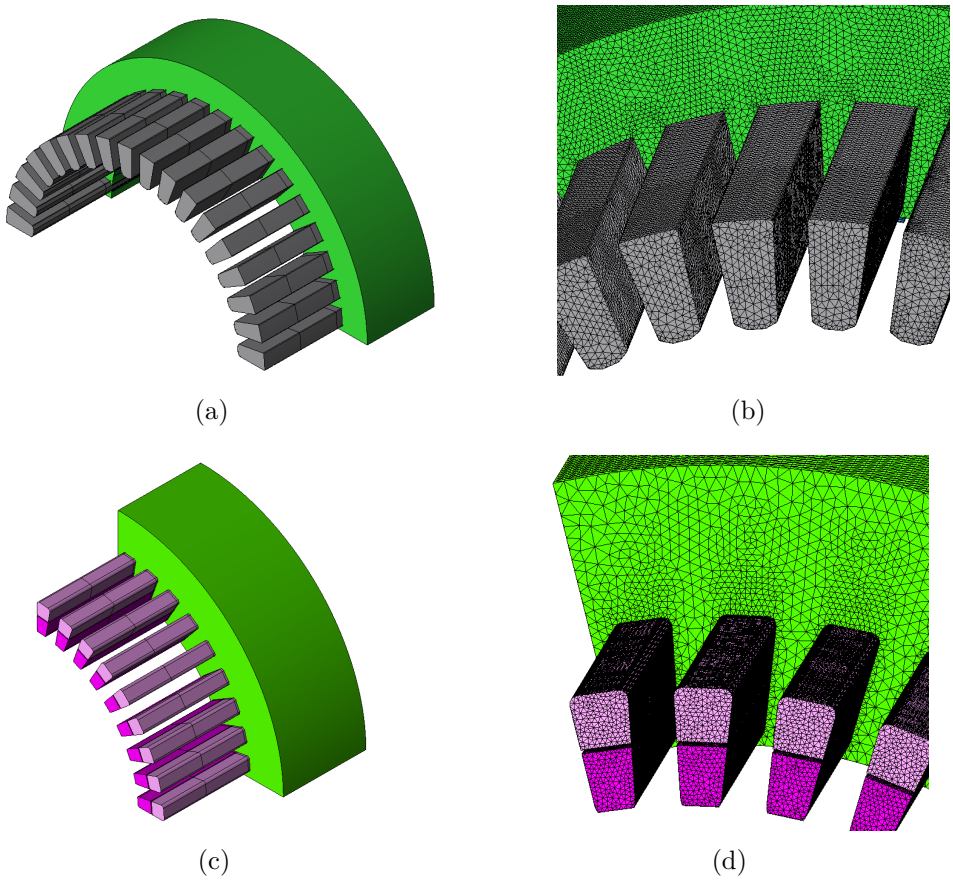

Fig. 7.7: Thermal finite element models: $\frac{1}{4}$-model for a 4-pole machine with a single layer winding (IM3) (a) and detailed view of the finite element mesh (b). $\frac{1}{8}$-model for a 4-pole machine with a dual layer winding (IM2) (c) and detailed view of the finite element mesh for this model (d). The models are visualized by using JMAG® [178].

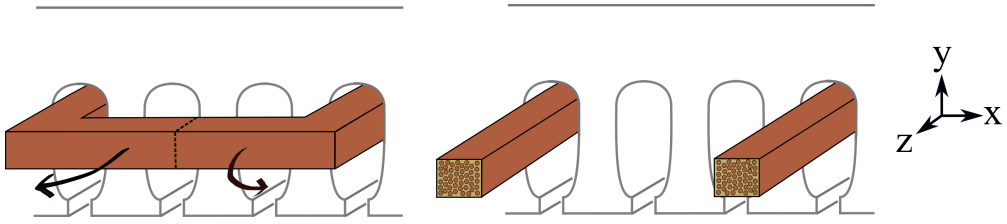

Fig. 7.8: Imaginary cutting and bending of the stator coils that allows the definition of an anisotropic thermal conductivity in the FEA software. The low conductivity for the coils is defined in the FEM software in the x- and y-direction, whereas the low conductivity for the stator iron is defined in the z-direction.

7.5 Thermal Investigations

The temperatures are analyzed both, for the standard three-phase operation and the asymmetric case during the post-fault operations. The investigations are performed for a machine with a single layer winding (IM3) in Section 7.5.1 and for a machine with a dual layer winding (IM2) in Section 7.5.2. The investigations apply LPTNs and FEA as well as experiments with IM2. The thermal resistances and the equivalent conductivities for the models were calculated based on the analytical and empirical approaches discussed in Section 6.3. However, as discussed in Section 6.3.4, the prediction of many thermal resistances is difficult, due to the uncertainties associated with the residual air, the contact resistances, and the convection. For the single layer winding models, the thermal resistances of the joints and the conductivity of the stator winding were chosen based on the literature values (Section 6.3.4). For the dual layer winding model, the values are derived from experimental results.

7.5.1 SCIM with a Single Layer Winding

The models for an SCIM with a single layer winding were used for the initial investigation. The local copper losses in the stator phases determine the temperature asymmetry, thus, these losses are applied for the investigation of the asymmetry during the different operation modes in the FEA using the model shown in Fig. 7.7a) and the LPTN shown in Fig. 7.5. The copper losses are determined with the assumption of a constant stator current space vector magnitude with the corresponding loss increases (Section 5.2.1).

Table 7.1 shows the results of the FEA for the different operation modes. In Table 7.2, the node temperatures of the LPTN are presented. The results show the symmetric temperatures with the copper losses during the three-phase operation and the increased and asymmetric temperatures with the copper losses for the post-fault operations. During the switched two-three-phase operation, the temperature distribution is slightly more symmetrical in comparison to the two-phase operation, since $\frac{1}{9}$ of the total copper losses occur in the faulty phase a.

A further distinction is made with regard to the conductive heat exchanges of the stator phases:

- The first three rows of the tables show the results without conductive heat exchanges of the phases in the end winding region. In this case, the temperatures of the stator phases and the local losses behave approximately proportionally, this

also applies to the case with the unbalanced losses.

- The second three rows of the tables depicts the results including conductive heat exchanges of the phases in the end winding region. These results show the cooling effect of the healthy phases via the end winding and a more symmetrical temperature distribution.

The temperatures of the FEA and the LPTN are in good agreement with one another. The results confirm the sufficient description of the end winding heat paths during the high loss asymmetry with a single thermal resistance (R_{69}) in the LPTN as an approximation. An exemplary temperature distribution of an FEA with heat flow applied in two phases is shown in Fig. 7.9.

Table 7.1: Overtemperatures computed by the thermal FEA of the stator with a single layer winding for different operating conditions and conductive heat exchanges between the stator phases.

	Nodes	4 in K	5 in K	6 in K	7 in K	8 in K	9 in K	10 in K
Without conductive heat exchanges between the phases	3ph	17.8	21.2	26.0	17.8	21.2	26.0	18.0
	2ph	13.4	12.3	12.3	50.3	54.9	68.8	37.2
	2/3ph	15.9	19.0	19.0	33.7	47.0	51.5	27.6
With conductive heat exchanges between the phases	3ph	17.8	21.2	26.0	17.8	21.2	26.0	18.0
	2ph	23.6	31.4	31.4	41.6	48.8	50.8	33.7
	2/3ph	20.8	20.7	27.4	26.6	29.8	35.9	25.8

Table 7.2: Overtemperatures computed by the LPTN of the stator with a single layer winding for different operating conditions and conductive heat exchanges between the stator phases.

	Nodes	4 in K	5 in K	6 in K	7 in K	8 in K	9 in K	10 in K
Without conductive heat exchanges between the phases	3ph	17.1	21.6	24.7	17.1	21.6	24.7	17.1
	2ph	9.6	9.5	9.5	46.6	60.2	69.3	34.3
	2/3ph	13.4	15.6	16.9	31.9	40.9	47.0	25.7
With conductive heat exchanges between the phases	3ph	17.1	21.6	24.7	17.1	21.6	24.7	17.1
	2ph	27.4	33.8	42.6	37.7	48.0	52.7	34.3
	2/3ph	22.2	27.7	33.6	27.4	34.8	38.7	25.7

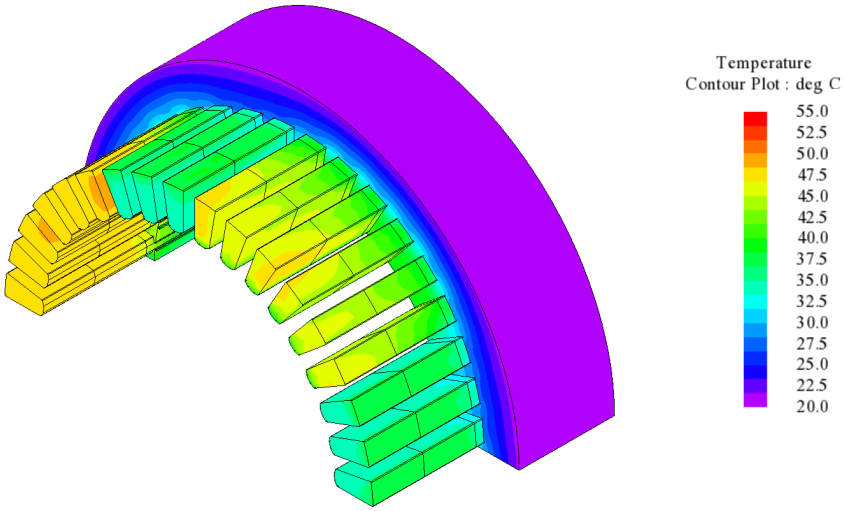

Fig. 7.9: Computed temperature distribution of the stator with a single layer winding of IM3 with heat flow applied in two phases and with heat exchanges between the end windings, visualized using JMAG® [178].

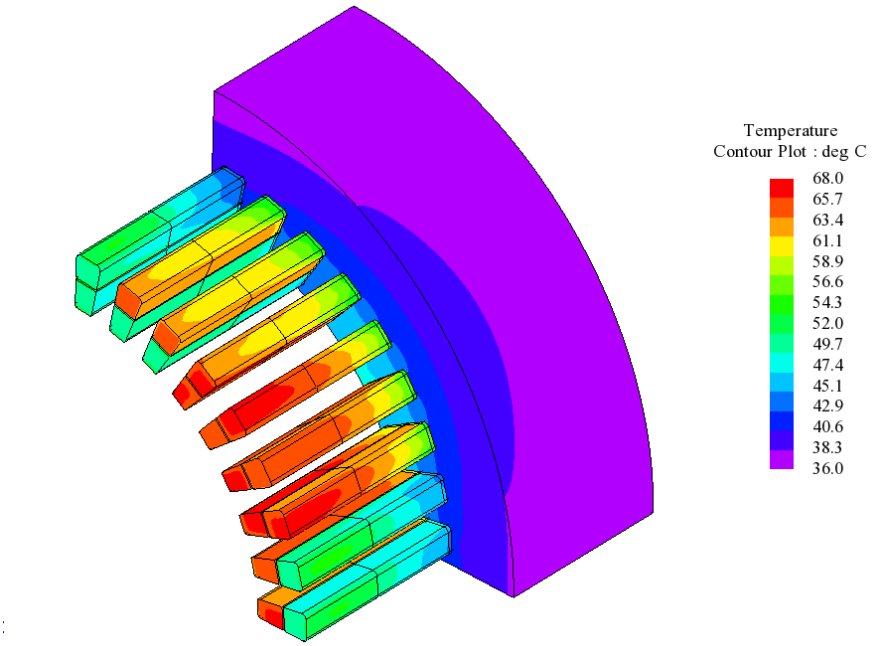

Fig. 7.10: Computed temperature distribution of the stator of IM2 with a dual layer winding with heat flow applied in two phases and with heat exchanges between the phases, visualized using JMAG® [178].

7.5.2 SCIM with a Dual Layer Winding

The investigation and the modeling of the SCIM with a dual layer winding is performed by experiments with IM2, the FEA model shown in Fig. 7.7c) and the LPTN shown in Fig. 7.6. Uncertain stator parameters for the FEA and the LPTN are estimated based on established experiments with balanced DC-currents applied in the stator winding [136,138,140,164,165]. The separation of the steady state temperature rises by the heat flows during these experiments allows the thermal resistances to be calculated (6.1). This approach can be applied to determine the total thermal resistance from the stator winding to the coolant [140], or to estimate further uncertain parameters such as the contact resistances and the conductivity of the stator winding [138]. Furthermore, the application of the temperature rises calculated by means of the increase of the electric resistance of the stator winding (5.19) and the application of temperatures measured by sensors can be distinguished from one another. Here, the measured temperatures from the temperature sensors located in the stator winding, iron and the cooling jacket of IM2 (see Appendix H for further information about the temperature measurement systems) were used to estimate the resistances of the joints between the stator winding and iron as well as between the stator iron and the cooling jacket (cf., Section 6.3.4). For the investigation of the temperature asymmetry and the determination of the heat exchange between the stator phases of the epoxy impregnated stator winding of IM2, modified DC-experiments were performed. In these modified experiments, DC-currents were applied only in two of three phases (phases b and c).

Stator Winding Temperatures

Table 7.3 shows the temperatures of a DC-experiment and a modified DC-experiment that illustrates the cooling effects of the stator winding of IM2 with unbalanced stator winding losses. The corresponding total input power was 339 W (113 W per phase) with three phase currents and 276 W (138 W per phase) with two phase currents. The experimental results show similar end winding temperatures in the phases b and c although the local losses in these phases are 1.22 pu during the two phase experiment. Approximately half of the temperature rise is measured in phase a when two phase currents are applied in phases b and c. From the temperatures and local losses in phases a, b, and c, it is estimated that approximately 18 % of the total input power is dissipated via phase a, whereas the rest is dissipated via phases b and c during the two phase experiment. Furthermore, the unbalanced losses also lead to an asymmetric

temperature distribution in the stator iron. Table 7.3 also shows the results of the FEA and LPTN calculation. Both show a good agreement with the measurements after the calibration of the contact resistances. For a good alignment with the FEA results the axial conductivity of the winding was adjusted as well. An exemplary temperature distribution of an FEA with two phase currents is shown in Fig. 7.10. For comparison, Table 7.4 shows the FEA and LPTN results with neglected heat exchanges between the stator phases and the same input power as for the results in Table 7.3.

Table 7.3: Steady state results obtained for the stator with a dual layer winding with different loss distributions.

	Nodes	5 in K	6 in K	7 in K	8 in K	10 in K	11 in K	12 in K	13 in K
Experiment	3ph	4.6	26.4	34.8	7.1	4.6	25.8	35.0	6.8
	2ph	2.9	15.4	17.9	4.2	4.0	25.3	34.4	6.7
FEM	3ph	6.6	26.5	34.6	8.0	6.6	26.5	34.6	8.0
	2ph	4.2	14.3	16.8	5.2	7.3	28.6	35.9	8.3
LPTN	3ph	6.7	24.5	34.9	7.1	6.7	24.5	34.9	7.1
	2ph	3.9	12.9	17.3	4.1	6.4	23.9	34.7	6.7

Table 7.4: Steady state results obtained for the stator with a dual layer winding with different loss distributions and neglected heat exchanges between the stator phases.

	Nodes	5 in K	6 in K	7 in K	8 in K	10 in K	11 in K	12 in K	13 in K
FEM	3ph	6.6	26.5	34.6	8.0	6.6	26.5	34.6	8.0
	2ph	3.3	7.6	7.6	5.7	7.5	32.2	41.0	9.1
LPTN	3ph	6.7	24.5	34.9	7.1	6.7	24.5	34.9	7.1
	2ph	2.8	3.7	4.8	2.9	7.0	28.3	41.1	7.4

Coupling of the Stator and the Rotor

Further investigations were performed to investigate and to calibrate the convective thermal resistances of the stator and the rotor. During the three-phase DC-experiment illustrated in Table 7.3, the temperature rise in the rotor winding was approximately 9 K which corresponds to 0.25 pu with respect to the stator end winding temperatures. Further experiments were performed with DC currents at standstill and low speed

rotations controlled with the driving machine were conducted. In these experiments, the effects of rotor losses on the stator temperatures were investigated. These losses are calulated from the measured torque and the rotational speed. Table 7.5 shows the results of a DC-experiment with 0 r/min (DC) and with 70 r/min (DC+rot) which leads to 100 W rotor losses. The experiments showed that at low speed, the rotor losses have a minor effect on the stator winding temperatures. The range of the speed dependence of the convective resistances in the heat path between the stator and the rotor was investigated by steps of the coolant temperature at different speeds. The evaluation of the slope and time constants of the transient rotor temperature rises revealed that the total thermal resistance between the stator and the rotor decreases at the nominal speed to approximately 0.62 pu of the value at standstill.

Table 7.5: Steady state results obtained for the stator with a dual layer winding without (DC) and with rotor losses (DC + rot).

	Nodes	5 in K	6 in K	7 in K	8 in K	10 in K	11 in K	12 in K	13 in K	16 in K
Experiment	DC	3.9	23.3	35.7	6.3	2.9	15.2	21.9	3.9	5.9
	DC + rot	5.1	24.6	37.5	8.0	4.3	16.1	24.3	5.9	32.1
LPTN	DC	6.3	25.4	37.0	6.6	4.6	15.0	20.8	4.8	5.5
	DC + rot	8.3	27.4	39.5	8.9	6.5	16.9	23.3	6.9	32.7

7.6 Conclusion

This chapter discusses the temperature modeling of SCIMs with unbalanced stator winding losses. Lumped parameter and finite element models are developed as well as experimental investigations are performed to consider the asymmetric heat flow and temperature distribution during the post-fault operations. The heat exchange of the stator phases and the substantial stator copper loss asymmetry during the post-fault operations leads to a significant heat flow from the healthy phases to the faulty phase. Thereby, the additional cooling for the healthy phases is provided. This gives room for increased local power losses when compared to the three-phase operation. The heat paths potentially occur in the end winding region and, in the case of a dual layer winding, also in the stator slots.

Chapter 8

Continuous Torque of an SCIM during the Post-Fault Operations

Increased power losses during the post-fault operations result in increased temperatures when compared to the standard three-phase operation. Therefore, the continuous torque must be reduced in order to stay within the temperature limits of the individual components. This chapter investigates the continuous torque during the post-fault operations based on experiments as well as the influence on the power loss and temperature models discussed in Chapters 5 and 7. In contrast to the generally assumed reduction down to 0.33 pu during the two-phase operation, the continuous torque can be increased by 0.15 pu (i.e., reduction down to 0.48 pu) and 0.32 pu (i.e., reduction down to 0.65 pu), respectively, for the two-phase and the switched two-three-phase operation, if the thermal and magnetic reserves are exploited.

8.1 Theoretical Consideration

The continuous torques during the different operation modes are compared using the continuous running duty (duty type S1) [95, 125]. The continuous torque is identified assuming a constant stator end winding temperature as this temperature limits the load of the example case machine IM2. Theoretical considerations for the two-phase post-fault operation [69] suggest that the continuous torque of an SCIM is limited down to $\frac{1}{3} \approx 0.33$ pu of the continuous torque during the three-phase operation. This estimate assumes the same local copper losses in the healthy two stator phases as during the three-phase operation, and a reduction of the torque with the square of the corresponding current space vector magnitude of 0.58 pu. However, the calculation and experimental results presented in Section 8.3, show that higher current space vector

magnitudes and significantly more torque are possible during the post-fault operations.

With an inverter operated and rotor flux-oriented SCIM any given torque, at a given speed, can be obtained from different combinations of the direct and quadrature component of the stator current space vector I_{sd} and I_{sq}, respectively. Because of this degree of freedom and the coupling of the electromagnetic and thermal systems, the identification of the continuous torque is a complex task. It entails the determination of the torque maximum on the steady state isotherms in the plane of I_{sd} and I_{sq}. In this work, this torque is determined both experimentally and by a computer based identification program.

8.2 Maximum Continuous Torque Identification Program

A full search of the continuous torque with numerical computation methods, including the electromagnetic and thermal coupling, is hardly realizable due to the significant calculation time. Therefore, an analytic maximum continuous torque identification program is proposed which allows finding the torque in a resonable amount of time. It is based on the electromagnetic and the power loss models discussed in Chapter 5 and the LPTNs discussed in Chapter 7. Fig. 8.1 depicts a flow chart of the identification program that includes the different routines and loops. The routines, the loops and the calculation time of the identification program are explained below.

8.2.1 Routines of the Identification Program

Grid Generator

Defines a grid of equidistant I_{sd} and I_{sq} values in the range of the user defined minimum values $\min(I_{\mathrm{sd}})$, $\min(I_{\mathrm{sq}})$, the maximum values $\max(I_{\mathrm{sd}})$, $\max(I_{\mathrm{sq}})$ and the grid steps dI_{sd}, dI_{sq}. In the second run of the *For Loop Refinement*, the minimum values, maximum values and grid steps are adjusted so as to search over a refined grid in the region of the operating point with the maximum continuous torque. This is derived from $I_{\mathrm{sd,MCT}}$ and $I_{\mathrm{sq,MCT}}$, identified in the first run of the *For Loop Refinement*, and stored in the routine *Find Torque Maximum*.

Vector Control

Calculates the stator voltage and frequency based on the desired values of I_{sd}, I_{sq}

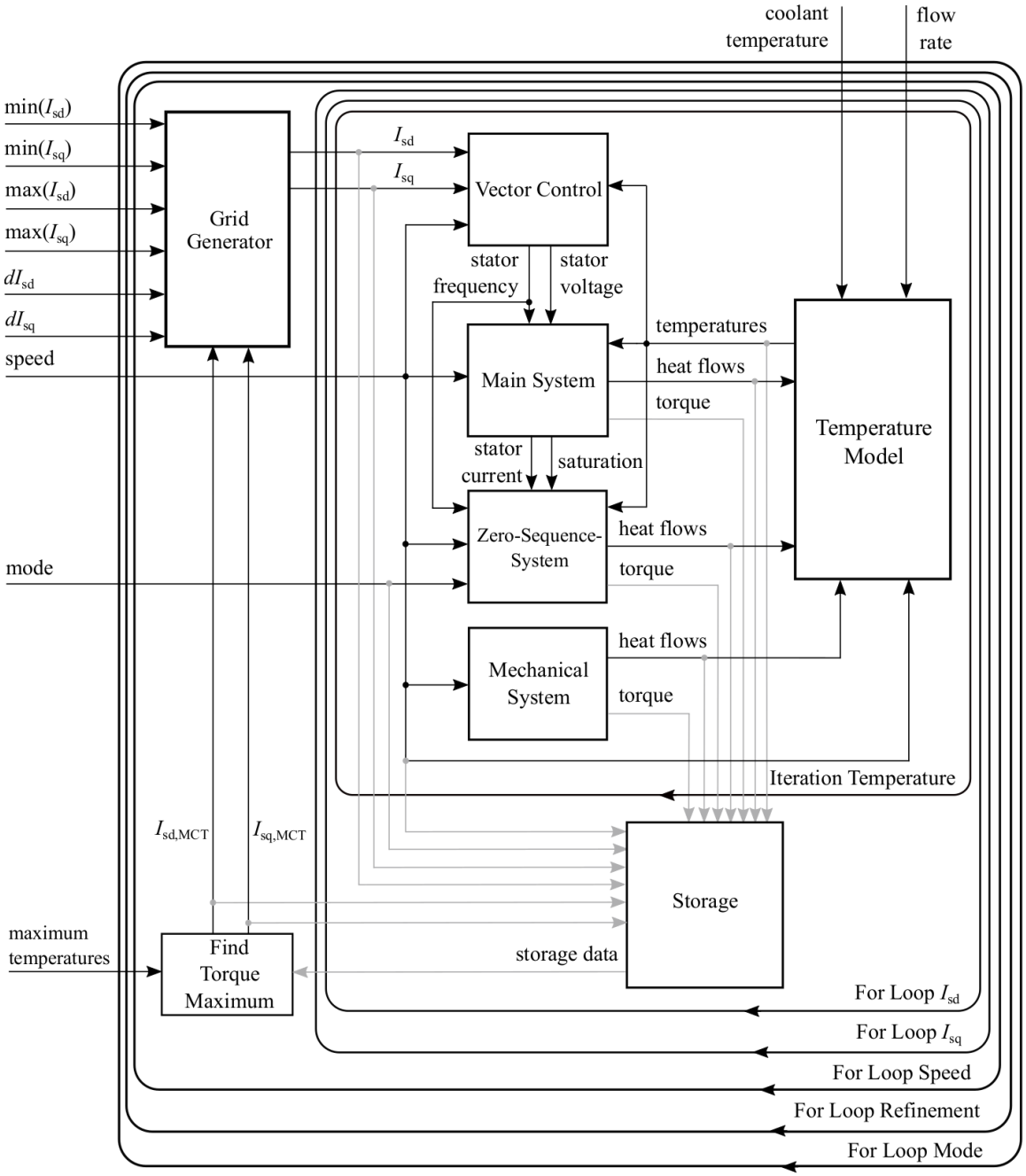

Fig. 8.1: Flowchart of the maximum continuous torque identification program. The figure illustrates the inputs and outputs of the different routines and the loops.

and the speed. The calculation is based on the single-phase equivalent circuit of an SCIM (cf., Section 5.1.2) including the iron losses (cf., Section 5.2.2). It considers the temperature dependence of the stator and rotor resistances (cf., Section 5.2.1). The nonlinear magnetization curve of the main system (4.14) is considered and the magnetization flux linkage is calculated by means of the Newton−Raphson Method. As per Section 4.5, the effect of the zero-sequence current on the magnetization of the main system (cf., Section 4.4) appears mainly during the start-up and is rather small at higher speeds, therefore this effect is not considered.

Main System

Calculates the stator current, heat flows and torque of the main system based on the single-phase equivalent circuit of an SCIM (cf., Section 5.1.2). The routine considers the temperature dependence of the stator and rotor resistances (cf., Section 5.2.1) and the iron losses (cf., Section 5.2.2). As in the case of the routine *Vector Control*, this routine considers the nonlinear magnetization curve of the main system and reflects the effect of the zero-sequence current.

Zero-Sequence System

Calculates the heat flows and the average torque of the zero-sequence system based on the zero-sequence system's equivalent circuit (cf., Section 5.1.2). The output depends on the operation mode (3ph, 2ph or 2/3ph). This routine, too, considers the temperature dependence on the resistances (cf., Section 5.2.1). Furthermore, the magnetization flux linkage calculated by the routine *Main System* is applied to consider the effect of this current on the magnetization of the zero-sequence system (cf., Section 4.4).

Mechanical System

Calculates the friction and windage losses (cf., Sections 5.2.3 and 5.3.2) as well as the corresponding breaking torque based on the speed.

Temperature Calculation

This routine calculates the temperatures based on the LPM provided in Fig. 7.6. Inputs are the heat flows determined by the routines *Main System*, *Zero-Sequence System*, and *Mechanical System*. The coolant temperature, i.e., the reference temperature of the temperature model is also an input of this routine and potentially the flow rate, too. Since the flow rate is constant, also the convective heat transfer coefficient of the cooling jacket is assumed to be constant.

Storage

Stores several quantities for the analysis such as the temperatures, the heat flows, the torques, the values of I_{sd}, I_{sq}, and the speed.

Find Torque Maximum

Within every run of the *For Loop Speed*, this routine identifies the operating point ($I_{\mathrm{sd,MCT}}$, $I_{\mathrm{sq,MCT}}$) with the largest continuous torque while remaining within the user defined temperature limits.

8.2.2 Loops of the Identification Program

Iteration Temperature

The stator and rotor resistances in the routines are initialized with the coolant temperature values. By this loop, the temperature dependence of these resistances is considered.

For Loop Isd

This loop is executed for every value of I_{sd} defined by the *Grid Generator*.

For Loop Isq

This loop is executed for every value of I_{sq} defined by the *Grid Generator*.

For Loop Speed

This loop is executed for every value of the speed defined by the user.

For Loop Refinement

This loop is executed for every execution of the *For Loop Speed*. It enables a first run with large grid steps dI_{sd}, dI_{sq} to identify the region where the maximum continuous torque is located, and a second run with small grid steps in the identified region to reduce the discretization effects on the identification of the maximum continuous torque and the corresponding operating point $I_{\mathrm{sd,MCT}}$ and $I_{\mathrm{sq,MCT}}$. The loop decreases the calculation time in comparison to a single run small grid steps.

For Loop Mode

This loop is executed for every operation mode (3ph, 2ph, and 2/3ph) defined by the user.

8.2.3 Remarks on the Calculation Time

The calculation time with the analytical identification program is short when compared to numerical computation methods. The calculation time increases approximately linearly with the number of calculated operating points. If the direct and quadrature component of the minimum values $\min(I_{\mathrm{sd}})$, $\min(I_{\mathrm{sq}})$, maximum values $\max(I_{\mathrm{sd}})$, $\max(I_{\mathrm{sq}})$ and the grid steps dI_{sd}, dI_{sq} are chosen equally, it can be assumed that the calculation time approximately increases with the square of the resolution $dI = dI_{\mathrm{sd}} = dI_{\mathrm{sq}}$. The grid steps should not be chosen to be too large to avoid deviations due to the discretization. The discretization uncertainty of the power at the nominal operating point with $dI = 0.1\,\mathrm{A}$ (6 400 calculated operating points) is approximately 0.03 pu. To reduce this uncertainty, the calculations were performed with $dI = 0.01\,\mathrm{A}$. The calculation of the corresponding 640 000 operating points took approximately 30 minutes per speed on a personal computer of today with a single core computation. The calculation time can be further reduced to a few minutes if only the maximum torque is of interest and the *For Loop Refinement* is used. Of course, the short calculation time of the calculation program comes at the price of a significant parametrization expense.

8.3 Experimental Approach

For the experimental investigation, IM2 was operated in three-phase, two-phase, and switched two-three-phase operation at constant speed and with a speed controlled load machine (SM2). The measurement setups for these operation modes are discussed in Appendix F. For each operating point investigated, IM2 was operated until steady state behavior of the measured stator and rotor temperatures were reached.

As mentioned earlier, any given torque can be obtained from different combinations of the direct and quadrature component of the stator current space vector I_{sd} and I_{sq}. The combinations of I_{sd} and I_{sq} were chosen depending on the operation mode investigated:

- During the three-phase operation, the reference temperatures for the post-fault operations were determined by identifying the combinations of I_{sd} and I_{sq} that result in the lowest stator winding temperatures but give nominal torque.

- For the two-phase and switched two-three-phase operation, the combinations of I_{sd} and I_{sq} were chosen in the region where the highest torque was expected. This

allows to estimate the torque maxima during the post-fault operations that are limited by the reference temperatures obtained from the three-phase operation.

The temperatures developed by the machine under three-phase operation and the continuous torque were taken as a reference. These temperatures do not reach the thermal limits of the machine components (cf., Section 6.1). This, however, does not compromise the identification of the effects that potentially increase the *ratio* of the continuous torque.

8.3.1 Discussion of the Experimental Results

Fig. 8.2a) depicts the experimentally investigated operating points for the three-phase (3ph), two-phase (2ph), and switched two-three-phase operation (2/3ph) in the I_{sd}-I_{sq} plane. Further illustrations of the measured temperatures, torque and losses for these operating points during the different operation modes are shown in Figs. 8.2b)-d). Figs. 8.2a) and b) indicate the operating points at the isoline of the nominal torque (24.6 Nm) during the three-phase operation. The stator end winding temperature T_{EW} in Fig. 8.2b) also shows a minimum, whereas the rotor winding temperature T_{RW} decreases with I_{sq}. Furthermore, the chosen reference operating point located at the isoline of the nominal torque is visible. This operating point has the highest efficiency and the lowest stator end winding temperature of the measured operating points on this isoline (80 °C, due to a slightly reduced inlet temperature of the coolant during these measurements, the actual temperature would be approximately 5 K higher).

Figs. 8.2a), c) and d) show the operating points with the post-fault operation modes located at the reference stator end winding temperature curve. The stator end winding temperature T_{EW} (here, the average temperature of the healthy phases) reached its reference temperature of 80 °C in the experiments, whereas the rotor winding temperature T_{RW} stayed below its reference temperature of 72 °C. The stator current space vector magnitudes for the compliance of these temperatures has to be reduced when compared to the three-phase operation. The operating points with the maxima of the measured torques are located in the I_{sd}-I_{sq} region where the maxima are expected for the three-phase operation with these reduced current space vector magnitudes. The comparison of Figs. 8.2b), c) and d) reveals that operating points with high torque and low stator winding temperatures are shifted to higher ratios $I_{\mathrm{sd}}/I_{\mathrm{sq}}$ with decreasing stator current space vector magnitudes.

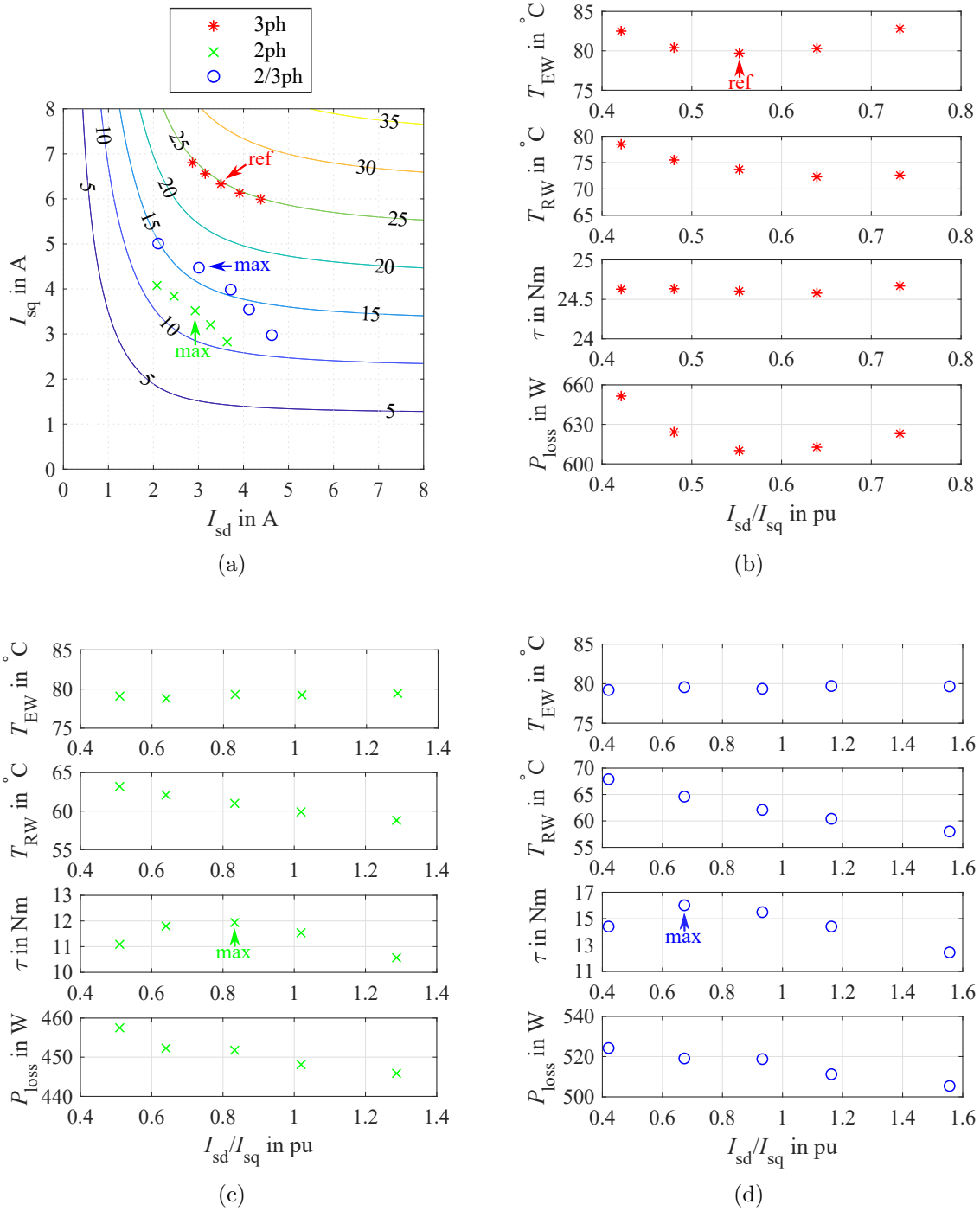

Fig. 8.2: Measurement results at a constant speed of 600 r/min: (a) Location of the operating points during the 3ph, 2ph, and 2/3ph operation in the I_{sd}-I_{sq} plane, and calculated torque isolines during the 3ph operation. (b)-(d) Temperatures, torque and total power losses during the 3ph, 2ph, and 2/3ph operation, respectively. The reference operating point (ref) and the operating points with the maximal measured torque (max) are indicated with arrows; IM2.

The measurement results allow for the determination of the per-unit torques and stator current space vector magnitudes during the post-fault operations. 1 pu corresponds with the values of the reference operating point during the three-phase operation. The maximum of the measured torques during the two-phase operation is 0.48 pu, whereas a higher torque of 0.65 pu is possible due to the reduced losses with the switched two-three-phase operation mode. The corresponding stator current space vector magnitudes are 0.63 pu and 0.75 pu, respectively.

8.3.2 Interpretation of the Experimental Results

The measured torques are significantly higher than the values that can be yielded by assuming the same local copper losses in the healthy stator phases as during the three-phase operation and a reduction of the torque with the square of the stator current space vector magnitude (torques of 0.33 pu and 0.50 pu for the two-phase and switched two-three-phase operation, respectively). The per-unit current space vector magnitudes applied for these estimations can be obtained from the square roots of the reciprocals of the increase factors for the local losses discussed in Section 5.2.1 ($\frac{1}{\sqrt{3}}$ and $\frac{1}{\sqrt{2}}$, respectively).

The estimated torque calculated from the squares of the measured per-unit current space vector magnitudes are 0.40 pu and 0.56 pu, respectively. The torque increases are enabled by utilizing the thermal reserves of the stator with unbalanced losses (cf., Section 7.5.2) that allow the copper losses and currents to be increased. The comparison of these values with the measured torques (Table 8.1) indicates that the utilization of

Table 8.1: Measured stator current space vector magnitudes and torques as well as estimated torques based on the squares of the per-unit stator current space vector magnitudes.

	Mode	$\lvert i_s^s \rvert$	Torque
		pu	pu
Measurement	3ph	1.00	1.00
	2ph	0.63	0.48
	2/3ph	0.75	0.65
Estimation without thermal reserves	2ph	0.58	0.33
	2/3ph	0.71	0.50
Estimation with thermal reserves	2ph	0.63	0.40
	2/3ph	0.75	0.56

these thermal reserves is only partially responsible for the measured torque increases. The differences are explained by the analysis of the torque relations discussed below.

8.3.3 Torque Ratio for a Linear SCIM

If iron losses are neglected, the continuous electromagnetic torque of an SCIM can be calculated from [85]:

$$\tau = \frac{3}{2} p \frac{L_{\mathrm{m}}^2}{L_{\mathrm{m}} + L_{\sigma\mathrm{r}}} i_{\mathrm{sd}} i_{\mathrm{sq}} = 3p \frac{L_{\mathrm{m}}^2}{L_{\mathrm{m}} + L_{\sigma\mathrm{r}}} I_{\mathrm{sd}} I_{\mathrm{sq}}. \tag{8.1}$$

The ratio of the torques of two different operating points (indices 1 and 2) is given by:

$$\frac{\tau_2}{\tau_1} = \frac{3p \dfrac{L_{\mathrm{m},2}^2}{L_{\mathrm{m},2} + L_{\sigma\mathrm{r},2}} I_{\mathrm{sd},2} I_{\mathrm{sq},2}}{3p \dfrac{L_{\mathrm{m},1}^2}{L_{\mathrm{m},1} + L_{\sigma\mathrm{r},1}} I_{\mathrm{sd},1} I_{\mathrm{sq},1}}. \tag{8.2}$$

Assuming a linear SCIM with constant inductances and operating points at the torque maximum ($I_{\mathrm{sd}} = I_{\mathrm{sq}}$, see Appendix E) yields the approximation:

$$\frac{\tau_2}{\tau_1} \approx \left(\frac{I_{\mathrm{s},2}}{I_{\mathrm{s},1}} \right)^2, \tag{8.3}$$

where $I_{\mathrm{s},1}$ and $I_{\mathrm{s},2}$ are the stator currents of the two operating points, respectively.

8.3.4 Torque Ratio for a Saturable SCIM

The application of (8.3) leads to estimated torque ratios that are too low. The further development of (8.2) (see derivation in Appendix E) yields the following torque ratio for a saturable SCIM:

$$\frac{\tau_2}{\tau_1} \approx \underbrace{\overbrace{\frac{L_{\mathrm{m},2}}{L_{\mathrm{m},1}}}^{c_{\mathrm{L}}} \frac{\overbrace{\dfrac{\frac{I_{\mathrm{sd},2}}{I_{\mathrm{sq},2}}}{1 + \left(\frac{I_{\mathrm{sd},2}}{I_{\mathrm{sq},2}}\right)^2}}^{c_{\mathrm{I}}}}{\dfrac{\frac{I_{\mathrm{sd},1}}{I_{\mathrm{sq},1}}}{1 + \left(\frac{I_{\mathrm{sd},1}}{I_{\mathrm{sq},1}}\right)^2}}}_{c_\tau} \left(\frac{I_{\mathrm{s},2}}{I_{\mathrm{s},1}} \right)^2. \tag{8.4}$$

(8.4) shows (8.3) neglects the factor $c_\tau = c_{\mathrm{L}} c_{\mathrm{I}}$. The numerator and denominator of c_{I} have mathematically the same structure and depend on the ratios $\frac{I_{\mathrm{sd}}}{I_{\mathrm{sq}}}$ of the

two operating points. Fig. 8.3 illustrates the decrease of the numerator/denominator of c_I with $\frac{I_\mathrm{sd}}{I_\mathrm{sq}}$. However, if the operating point 2 features a greater ratio $\frac{I_\mathrm{sd}}{I_\mathrm{sq}}$ than operating point 1, c_I is greater than one. Furthermore, the factor c_L is greater than 1 if the magnetization inductance of operating point 2 is greater than the inductance in operating point 1. Both facts apply to the post-fault operating points with high torque which increases the calculated torque ratios compared to the ratios calculated with the approximation (8.3).

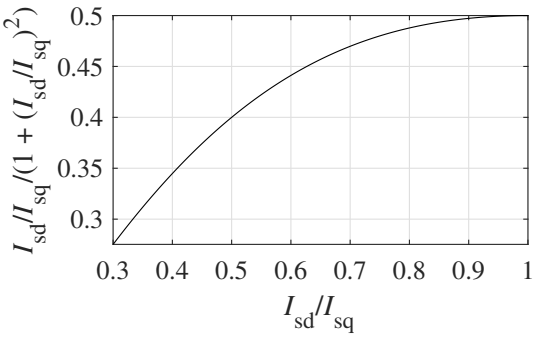

Fig. 8.3: $\frac{\frac{I_\mathrm{sd}}{I_\mathrm{sq}}}{1+\left(\frac{I_\mathrm{sd}}{I_\mathrm{sq}}\right)^2}$, i.e, numerator and denominator of c_I, as a function of the ratio $\frac{I_\mathrm{sd}}{I_\mathrm{sq}}$.

8.3.5 Quantification of the Torque including Saturation

Using the ratios $\frac{I_\mathrm{sd}}{I_\mathrm{sq}}$ of the measured operating points (see Fig. 8.2) and considering the increase of the magnetization inductance by approximately 5 % in c_L (due to the decrease of I_sd), leads to calculated torque ratios of 0.49 pu and 0.67 pu, respectively. This corresponds well with the measured ratios, with slight overestimations. The results for the saturable SCIM are summarized along with the measurement results in Table 8.2.

Note: The torque relations above are derived based on the fundamental wave and the zero-sequence braking torque has not been considered. However, in the performed experiments with IM2 above, this braking torque plays a minor but not inconsiderable role. The results of the investigation of the zero-sequence system in Section 5.3.2, indicate an expectable value for the zero-sequence breaking torques in these experiments of 0.02 pu.

The analysis above shows, that utilization of the thermal reserves and the nonlinear characteristic of the magnetic circuit increase the torque during the post-fault oper-

Table 8.2: Measured stator current space vector magnitudes and torques along with comparison with the estimated torques based on the squares of the per-unit stator current space vector magnitudes for a saturable SCIM.

	Mode	$\lvert i_s^s \rvert$ pu	Torque pu
Measurement	3ph	1.00	1.00
	2ph	0.63	0.48
	2/3ph	0.75	0.65
Estimation for a saturable SCIM with thermal reserves	2ph	0.63	0.49
	2/3ph	0.75	0.67

ations when compared to previous assumptions [69]. The simplified linear approach which builds on the reduction of the torque with the square of the stator current space vector magnitude potentially significantly underestimates the possible torque during the post-fault operations.

After the experimental determination and the semi-experimental determination of the torque ratios based on the stator current ratios, the computation results from the identification program are discussed below.

8.4 Results of the Identification Program

Fig. 8.4a) shows the calculated maximum continuous torque operating points for the different operation modes in the I_{sd}-I_{sq} plane. The calculated operating points are in a similar region as the maxima of the measurement results. The calculated ratios of the continuous torque are 0.52 pu and 0.68 pu for the two-phase and switched two-three-phase operation, respectively. Thereby, the computed ratios are slightly higher than the measured ones. Figs. 8.4b)-d) show the calculated temperatures, torque, and losses at the same values of i_{sd} and i_{sq} as the measured operating points shown in Fig. 8.2a) so as to further compare these quantities with the measurement results from Figs. 8.2b)-d). The comparison shows that the temperature model underestimates the stator end winding temperatures T_{EW} during the post-fault operations. This indicates that the modified DC experiment (cf., Section 7.5.2) overestimates the cooling effect. Furthermore, the rotor winding temperatures T_{RW} and the total losses P_{loss} are underestimated. Such an underestimation was expected, since additional load and high frequency losses (Sections 5.2.4 and 5.2.5) are not considered in the identification program and due to

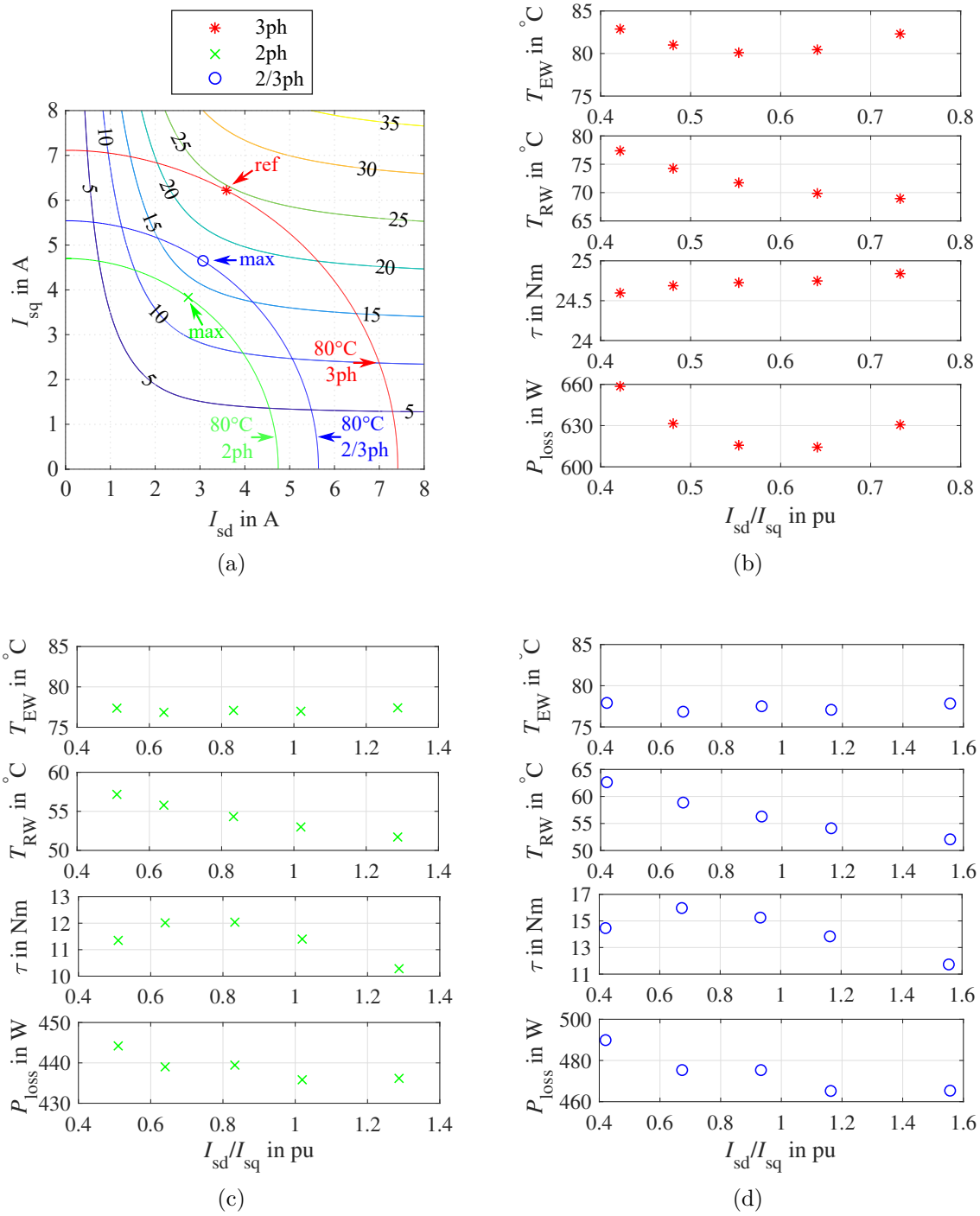

Fig. 8.4: Calculation results at a constant speed of 600 r/min. (a) Location of the calculated reference point (ref) during 3ph operation and the maximum torque operating points (max) during the 2ph and 2/3ph operation in the I_{sd}-I_{sq} plane and calculated isolines of the torque and the constant stator end winding temperature (80°C). (b)-(c) Calculated temperatures, torque and losses during the 3ph, 2ph, and 2/3ph operation, at the same operating point as illustrated in Fig. 8.2(a); IM2.

the underestimation of the zero-sequence system's rotor losses (Section 5.3.2).

To analyze the impact of these deviations on the calculation of the maximum continuous torque, the results were recalculated under consideration of the reduced cooling effect (approximately 15 % instead of 18 %) and the injection of residual losses into the rotor winding. The results are shown in Fig. 8.5 and correspond better with the measured results. The calculated torques with this modified calculation are 0.51 pu and 0.66 pu for the two-phase and switched two-three-phase operation, respectively. If it is assumed that the residual losses are provided by the mechanical power, the calculated torques must be further reduced by 0.01 pu − 0.02 pu.

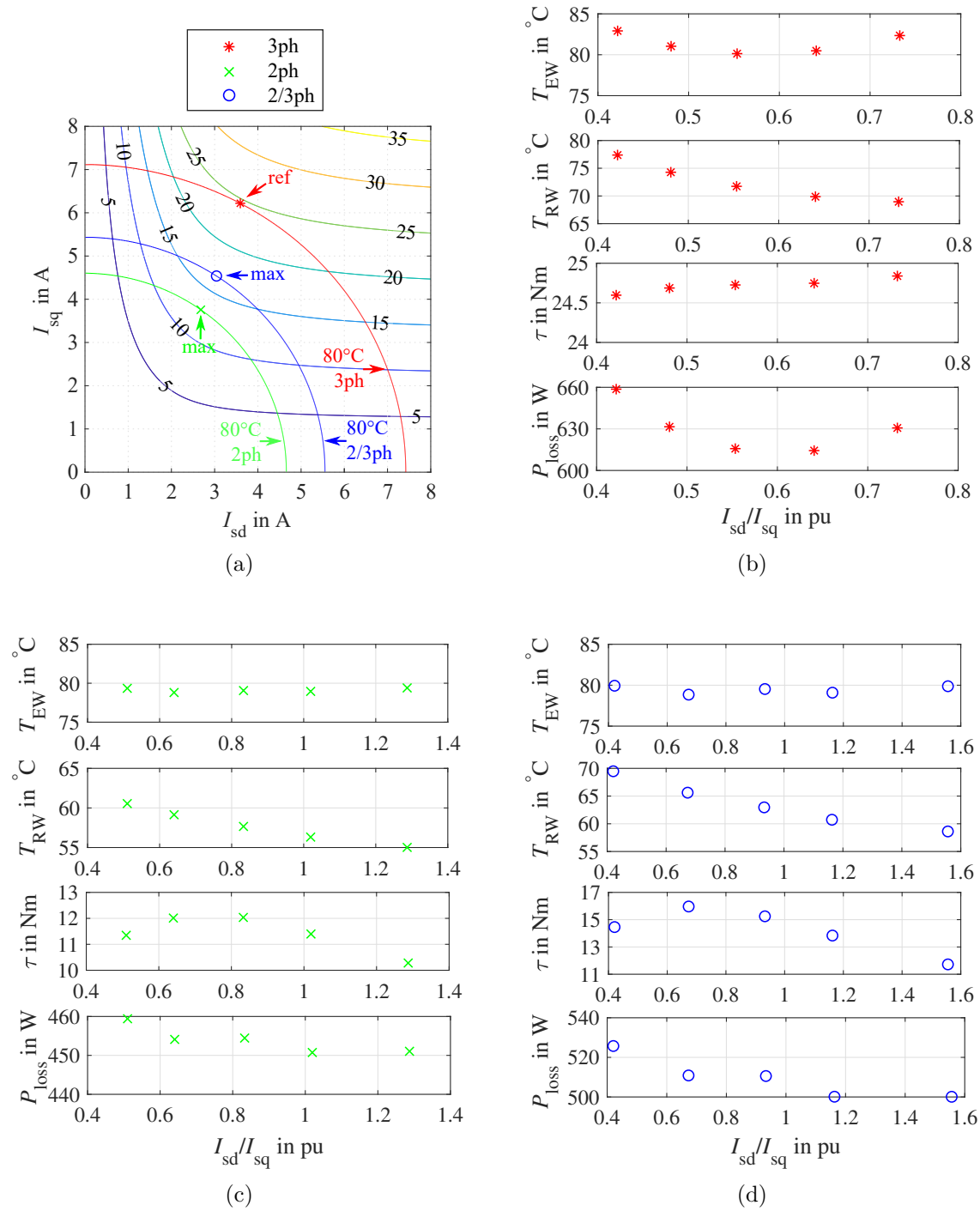

Fig. 8.5: Calculation results obtained with the modified calculation program at a constant speed of 600 r/min. (a) Location of the calculated reference point (ref) during 3ph operation and the maximum torque operating points (max) during the 2ph and 2/3ph operation in the I_{sd}-I_{sq} plane and calculated isolines of the torque and the constant stator end winding temperature (80°C). (b)-(c) Calculated temperatures, torque and losses during the 3ph, 2ph, and 2/3ph operation, at the same operating point as illustrated in Fig. 8.2(a); IM2.

8.5 Conclusion

Due to the increased power losses and asymmetric loss distribution during the post-fault operations, the continuous torque is reduced when compared to three-phase operation. However, in contrast to the initial expectation of 0.33 pu with respect to the three-phase operation [69], potentially significantly higher torques are possible during the post-fault operations, because:

- The operation in the I_{sd}-I_{sq} region where the maximum torque is located is the basis of a high torque.
- Thermal reserves of the stator (cf., Section 7.5.2) additionally cool the healthy phases which allows the local copper losses to be increased when compared to the three-phase operation.
- The application of the switched two-three-phase operation (cf., Section 3.3.2) reduces the power losses when compared to the two-phase operation.
- If the nonlinear characteristic of the machine significantly increases the ratio $\frac{i_{\mathrm{sd}}}{i_{\mathrm{sq}}}$ and the magnetization inductance during the post-fault operations, a further torque reserve can be exploited.

For the example case machine IM2, the utilization of thermal and magnetic reserves lead to a continuous torque of 0.48 pu during the experiments with two-phase operation. The reduced losses during the switched two-three-phase operation lead to a continuous torque of 0.65 pu. Similar results could be obtained by a proposed continuous torque identification program.

Chapter 9

Alternating Torques of an SCIM during the Post-Fault Operations

The post-fault operation strategies that apply a zero-sequence stator current feature a reduced torque quality as a side effect, especially during the start-up and low-speed operation of the SCIM drive. Section 9.1 provides an overview of the development of the zero-sequence torque. In Section 9.2, a method for the reduction of the high alternating torques that occur at low speed is proposed. Section 9.3 shows an experimental study of the alternating torques and the performance of the proposed reduction method.

9.1 Theoretical Consideration

9.1.1 Development of the Alternating Torques

Due to the high number of short-circuited conductors at the circumference of the rotor, the rotor winding of SCIMs responds to the change of the excited harmonic flux waves caused by the zero-sequence stator current with corresponding rotor currents. During the two-phase post-fault operation, the current i_{s0} is sinusoidal with the stator frequency f_s (cf., Section 1.3). In this case, each space harmonic of the zero-sequence system can be interpreted as two rotating waves [89]. One of these waves rotates in the positive direction with $\frac{1}{\nu}$ of the fundamental wave's speed, whereas the other rotates in the negative direction with $-\frac{1}{\nu}$ of the fundamental wave's speed, where ν is the order of the harmonic ($\nu = 3(2\mu - 1), \mu \in \mathbb{N}$). The relative speed between the positive and the negative rotating harmonic flux waves and the occurring rotor currents lead to a steady torque and a main alternating torque that occurs at $2f_s$ during the two-phase operation.

During the switched two-three-phase operation, i_{s0} has the shape of a sinusoidal half-wave (cf., Section 3.1.1) and consists of various harmonic components (Fig. 5.2). The corresponding space harmonics rotate with $\pm\frac{1}{\nu}f/f_s$ of the speed of the fundamental wave. The relative speeds of these space harmonics lead to an alternating torque with the lowest frequency occurring at f_s during the switched two-three-phase operation.

At low speed, the relative speed between the zero-sequence space harmonics and the rotor is low (see also Appendix C). Therefore, both the steady and the alternating zero-sequence torque components develop significantly during both post-fault operation modes at low speed. Hence, it is desirable to reduce the alternating torques, especially in this speed region.

9.2 Method for the Reduction of the Alternating Torques

9.2.1 Mathematical Description

In this section, a method to reduce the alternating torques during the post-fault operations at low speed is presented. It is based on the compensation of the zero-sequence system's torque by means of the main system's torque. The torque of the zero-sequence system is estimated by means of the zero-sequence system model (3.9), (3.11) and (3.12). The equations are discretized with the Backward Euler Scheme. Then, the rotor flux of the zero-sequence system at period k can be calculated from:

$$\underline{\psi}^{s}_{r3,k} = \frac{a + jt_d 3\dot{\phi}_k}{a^2 + (t_d 3\dot{\phi}_k)^2}\left(\underline{\psi}^{s}_{r3,k\text{-}1} + t_d \frac{R_{r3}L_{m3}}{L_{\sigma r3} + L_{m3}} i_{s0,k}\right), \tag{9.1}$$

where $a = 1 + t_d\frac{R_{r3}}{L_{\sigma r3}+L_{m3}}$. The main flux of the zero-sequence system is computed by:

$$\underline{\psi}^{s}_{m3,k} = \frac{L_{m3}}{L_{\sigma r3} + L_{m3}}\underline{\psi}^{s}_{r3,k} + \left(L_{m3} - \frac{L^2_{m3}}{L_{\sigma r3} + L_{m3}}\right) i_{s0,k}. \tag{9.2}$$

The torque of the zero-sequence system is calculated from:

$$\tau_{0,k} = -9\mathrm{Im}\{\underline{\psi}^{s}_{m3,k} i^{*}_{s0,k}\}. \tag{9.3}$$

9.2.2 Implementation in the Torque Control Loop

The discretized zero-sequence system model is applied to the torque control loop of the rotor flux-oriented SCIM drive as shown in Fig. 9.1. The inner current control loop (Fig. 3.4) is extended by a PI-controller and models for the machine torque. The total machine torque is calculated from the sum of the torque of the zero-sequence system and the main system. The latter is calculated by means of:

$$\tau_{\mathrm{f,k}} = \frac{3}{2} p \frac{L_{\mathrm{m}}}{L_{\sigma\mathrm{r}} + L_{\mathrm{m}}} \psi_{\mathrm{rd,k}} i_{\mathrm{sq,k}}. \tag{9.4}$$

The discretized zero-sequence system model provides information about the zero-sequence torque; the PI-controller reduces the alternating torques by adapting the desired quadrature component of the stator current i^*_{sq}. The use of i^*_{sq} is essential to achieve the needed dynamics in the torque control loop. Contrary to when the torque control deviation is calculated with the estimated torque of the main system only, the torque controller must handle continuously alternating torques. Since the closed torque control loop has a low-pass characteristic, the ability of the compensation is limited. However, it is in accordance with the goal of reducing the high alternating torques that occur at low stator frequency and rotational speed.

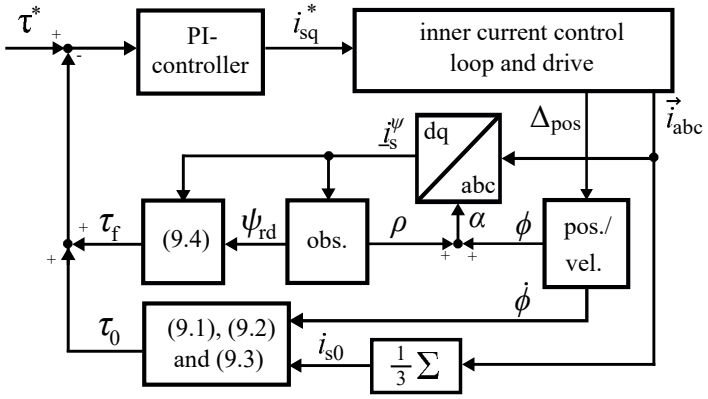

Fig. 9.1: Structure of the torque control loop of the rotor flux-oriented drive including the model for the zero-sequence torque.

The amplitude of the zero-sequence stator current equals the magnitude of the stator current space vector, therefore, it seems reasonable to operate the machine at a maximum torque per ampere operating point, to keep the torque of the zero-sequence system low. However, the proposed compensation shows a higher effectiveness at higher

i_{sd} values. On the one hand, i_{s0} increases less with i_{sq}, on the other hand, τ_f increases more strongly with i_{sq}. This keeps distortions in the phase currents low (see below). In terms of iron losses and the available inverter voltage, the higher rotor flux levels do not represent a difficulty since the stator frequencies are low in the low speed region.

9.3 Experimental Results

The experiments are performed with IM1. The experimental setup is the same as discussed in Section 3.3. For the comparison of the alternating torques and the performance of the alternating torque reduction method, the drive is operated with the three-phase operation (3ph), the two-phase operation (2ph), and the switched two-three-phase operation (2/3ph). To reduce the influence of the inverter nonlinearities, the experiments in Section 9.3.2 were performed with a reduced DC-link voltage (150 V).

9.3.1 Torque Characteristics

Fig. 9.2 shows the frequency spectra of the measured torque at different operating points. As discussed in Section 9.1, the zero-sequence stator current leads to an alternating torque during the two-phase operation, in which the lowest frequency component occurs with twice the stator frequency. However, during the switched two-three-phase operation, the lowest frequency component occurs at the stator frequency. At 1500 r/min and 750 r/min, shown in Figs. 9.2a) and b), the spectra show a component of approximately 0.02 pu - 0.03 pu at twice the stator frequency during the continuous two-phase operation. During the proposed switched two-three-phase operation, the spectrum shows a component at the stator frequency with similar amplitude to that which occurs during continuous two-phase operation and harmonics with lower amplitude. The alternating torques can increase drastically at low stator frequencies, as shown exemplarily at the 120 r/min operating point in Fig. 9.2c). The alternating torques during two-phase and switched two-three-phase operation are approximately 0.2 pu - 0.35 pu at this operating point. Thus, at the low speed range, the alternating torques should be considered in both post-fault operation modes.

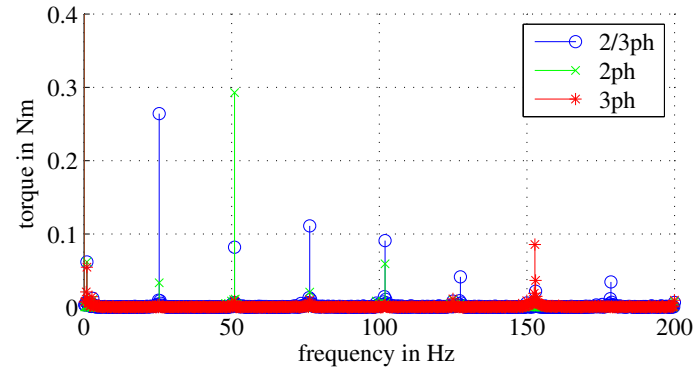

(a)

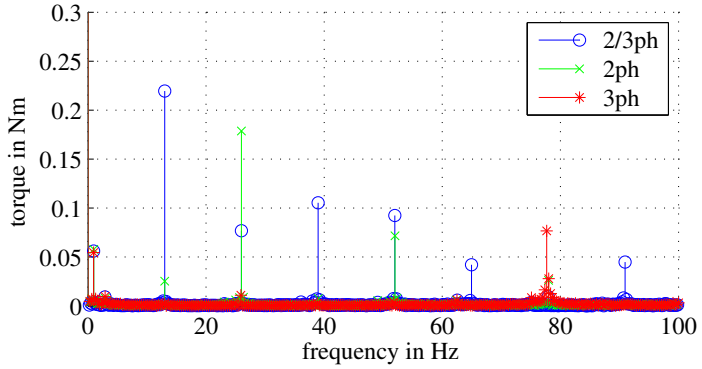

(b)

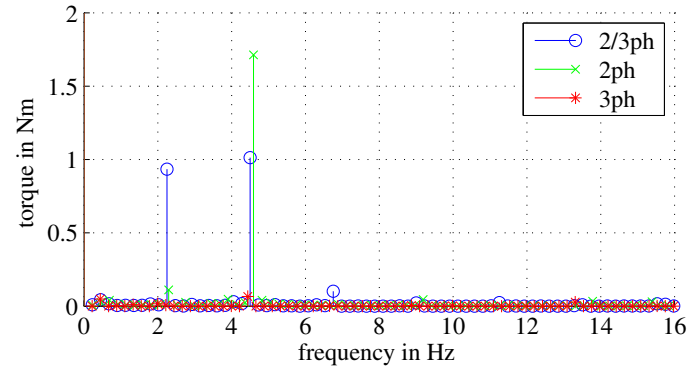

(c)

Fig. 9.2: Fourier spectra of the measured torque of IM1 during the three operation modes at different rotational speeds and average torques of the machine: (a) 1500 r/min, 9.58 Nm, (b) 750 r/min, 9.68 Nm, and (c) 120 r/min, 4,83 Nm. The fundamental stator supply frequencies are: (a) 25.49 Hz during 2/3ph operation, 25.52 Hz during 2ph operation, 25.48 Hz during 3ph operation (b), 12.97 Hz during 2/3ph operation, 13.02 Hz during 2ph operation, 12.95 Hz during 3ph operation, (c), 2.25 Hz during 2/3ph operation, 2.30 Hz during 2ph operation, 2.22 Hz during 3ph operation.

9.3.2 Performance of the Alternating Torque Reduction Method

Fig. 9.3 shows further low-speed operating points, and it illustrates the performance of the proposed alternating torque reduction method. The drive is again operated with the three-phase operation (3ph), the two-phase operation (2ph), the switched two-three-phase operation (2/3ph), and with both post-fault operation modes including the proposed alternating torque reduction method (2ph red and 2/3ph red). Fig. 9.4 illustrates the measured torque, speed and stator currents over time at 150 r/min and 5 Nm during the proposed switched two-three-phase operation mode. The results show a significant reduction of the alternating torques and the rotary oscillations. As per Fig. 9.5, the phase currents show low distortions, when the proposed alternating torque reduction method is applied. These distortions are caused by the adaptation of i_{sq}^{*} and are required to reduce the alternating torques with the proposed method. For the magnetization inductance of the zero-sequence system in (9.1) and (9.2), a reduced value is applied to consider the saturation interaction with the main system discussed in Section 4.4. The experiments were performed with a lower DC-link voltage (150 V) to reduce the influence of the inverter nonlinearies (e.g., voltage drops at the semiconductors, dead time) on the low inverter output voltage during these experiments.

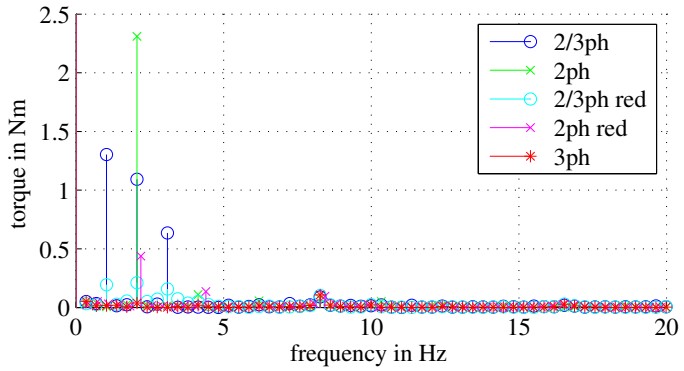

(a)

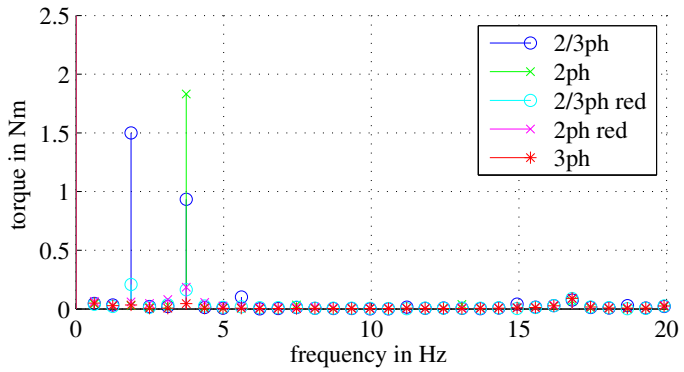

(b)

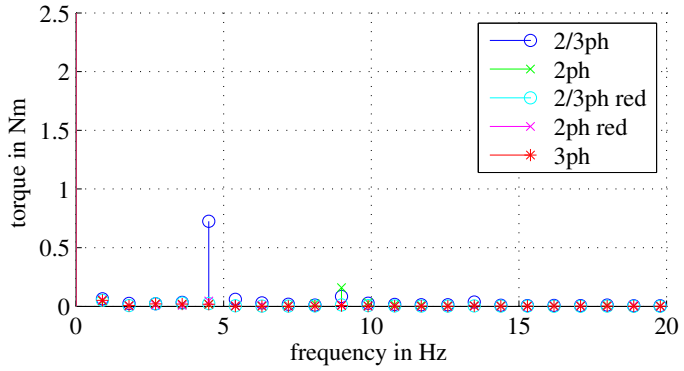

(c)

Fig. 9.3: Fourier spectra of the measured torque of IM1 during the three operation modes at different rotational speed and desired torque without and with the proposed alternating torque reduction method: (a) 50 r/min, 5 Nm, (b) 100 r/min, 5 Nm and (c) 250 r/min, 10 Nm. The relative peak-to-peak values of the alternating rotational speed with respect to the mean value of the rotational speed are as follows: (a) 55% (2/3ph), 58% (2ph), 16% (2/3ph red), 22%, (2ph red), 4% (3ph), (b) 31% (2/3ph), 40% (2ph), 5% (2/3ph red), 5%, (2ph red), 1.2% (3ph) ,(c) 8% (2/3ph), 3% (2ph), 1% (2/3ph red), 0.8%, (2ph red), 0.8% (3ph).

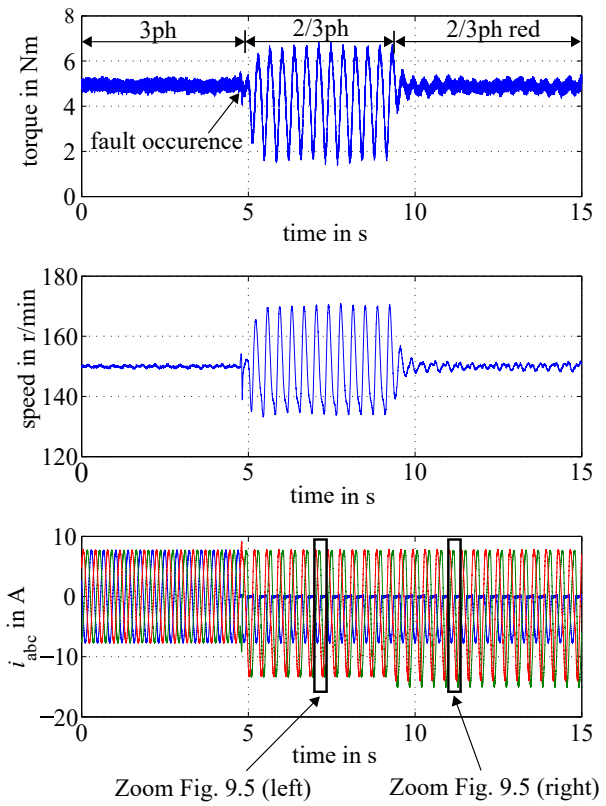

Fig. 9.4: Experimental results with IM1 at 150 r/min and 5 Nm. 1: Measured torque, 2: measured rotational speed, 3: measured phase currents. At the beginning, the drive is operated with standard three-phase operation (3ph). At $t = 4.7$ s, an SSF of switch S_1 occurs. The drive is reconfigured to the switched two-three-phase operation (2/3ph) at $t = 4.9$ s. At $t = 9.3$ s, the proposed alternating torque reduction method is activated (2/3ph red).

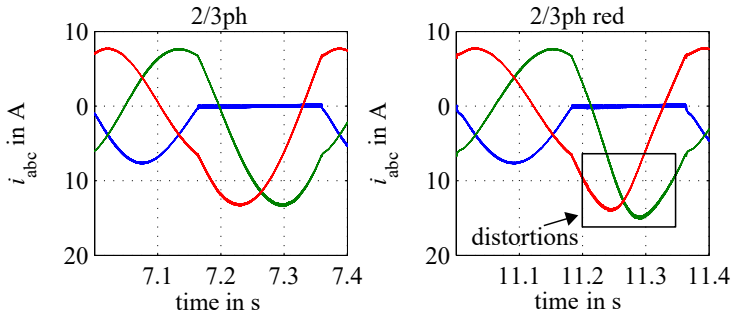

Fig. 9.5: Detailed views of the shapes of the phase currents during the post-fault operation in the experiment shown in Fig. 9.4 without (left) and with (right) the proposed alternating torque reduction method. With the proposed method distortions in the phase currents are introduced.

9.4 Conclusion

Zero-sequence stator current based post-fault operation modes for SCIM drives lead to significant alternating torques, especially during the start-up and in the low-speed region, which has also been illustrated by experiments. In this chapter, a model based method for the reduction of these components is discussed and evaluated. The proposed method applies the torque building component of the stator current space vector i_{sq} for the alternating torque reduction. The method was tested with both, the conventional continuous two-phase post-fault operation mode and with the switched two-three-phase operation strategy discussed in Chapter 3. To keep the harmonics in the phase currents with the alternating torque reduction method low, the operation of the SCIM with higher rotor flux linkages is desirable. In this case, the saturated zero-sequence inductance (cf., Chapter 4) is applied in the method.

Summary and Outlook

The first part of this thesis summarizes the backgrounds of inverter faults as well as the state-of-the-art detection methods and post-fault operation strategies for such faults. The state-of-the-art detection methods, however, lack fast detection time without applying additional hardware. Therefore a novel method for the fast detection of inverter open circuit faults in electric drives is proposed. It features a particularly low detection time of a few switching periods which aims at detecting the fault quickly to avoid any subsequent damage. Moreover, it does not require any additional hardware, and it even allows for detection during transient operation.

Furthermore, this thesis focuses on the torque exploitation of SCIM drives during continuous post-fault operation. The exploitation utilizes the thermal and magnetic reserves and suggests applying a switched post-fault operation strategy with reduced power losses that can be applied in the case of a single switch open circuit fault. Investigations on an example case machine showed that 0.48 pu of the continuous torque, compared to the three-phase operation, are possible with the conventional two-phase post-operation strategy. With the proposed switched two-three-phase post-fault operation strategy, the ratio can be increased to 0.65 pu of the continuous torque. Both values significantly exceed the previously assumed torque limit of 0.33 pu for SCIM drives.

A further part of this thesis is dedicated to the analysis and modeling of the space harmonics related to the zero-sequence system as well as the interaction of these harmonics with the main system. The space harmonics related to the zero-sequence system significantly affect the power losses and torque during the post-fault operations of the example case squirrel cage induction machines. The influence of the stator winding design on these space harmonics and possibilities to reduce these space harmonics have been discussed herein. Moreover, a saturation interaction between these harmonics and the main system has been identified which changes the machine's parameters during the post-fault operation. A modeling approach has been proposed and validated with two example case machines. Moreover, this thesis investigates the torque pulsa-

tions occurring at low speed operation. A reduction method for these pulsations has been proposed and validated for both, the two-phase and the switched two-three-phase post-fault operation.

Although many aspects of the proposed detection method and post-fault operation of squirrel cage induction machines have been investigated, further research may include the following:

- The investigation of the extension of the proposed detection method on multiple inverter open circuit faults.
- The investigation of the thermal behavior of post-fault operated squirrel cage induction machine drives with load transients under consideration of the machine's thermal capacitances.
- The investigation of the influence of the squirrel cage design on the power losses and torque related to the zero-sequence system.
- The further systematic investigation of the relationship between speed, the continuous torque during post-fault operation, and saturation interaction over the total speed range of squirrel cage induction machine drives.

List of Publications

The work in this thesis resulted in two journal and four conference publications. The journal publications [J1] and [J2] are expanded versions of the previously published conference publications [C1] and [C2], respectively.

Journal publications

[**J1**] H. T. Eickhoff, R. Seebacher, A. Muetze and E. G. Strangas, "Enhanced and Fast Detection of Open-Switch Faults in Inverters for Electric Drives," *IEEE Transactions on Industry Applications*, vol. 53, no. 6, pp. 5415-5425, Nov.-Dec. 2017.

[**J2**] H. T. Eickhoff, R. Seebacher, A. Muetze and E. G. Strangas, "Post-Fault Operation Strategy for Single Switch Open-Circuit Faults in Electric Drives," *IEEE Transactions on Industry Applications*, vol. 54, no. 3, pp. 2381-2391, May-June 2018.

Conference publications

[**C1**] H. T. Eickhoff, R. Seebacher, A. Muetze and E. G. Strangas, "Enhanced and fast detection of open circuit faults in inverters for electric drives," *2016 IEEE Transportation Electrification Conference and Expo (ITEC)*, Dearborn, MI, 2016, pp. 1-6.

[**C2**] H. T. Eickhoff, R. Seebacher, A. Muetze and E. G. Strangas, "Post-fault operation strategy for single switch open circuit faults in electric drives," *2016 IEEE Energy Conversion Congress and Exposition (ECCE)*, Milwaukee, WI, 2016, pp. 1-6.

[**C3**] H. T. Eickhoff, E. G. Strangas and A. Muetze, "Electric machine utilization during the post-fault operation after inverter open circuit faults," *2017 IEEE 11th International Symposium on Diagnostics for Electrical Machines, Power Electronics and Drives (SDEMPED)*, Tinos, 2017, pp. 201-207.

[**C4**] H. T. Eickhoff, R. Seebacher and A. Muetze, "Saturation interaction in a fault-tolerant induction machine drive due to a zero-sequence stator current," *2019 IEEE International Electric Machines & Drives Conference (IEMDC)*, San Diego, CA, 2019.

Bibliography

[1] P. Waide and C. U. Brunner, "Energy-Efficiency Policy Opportunities for Electric Motor-Driven Systems," International Energy Agency, 2011.

[2] H. Wang, M. Liserre and F. Blaabjerg, "Toward Reliable Power Electronics: Challenges, Design Tools, and Opportunities," *IEEE Industrial Electronics Magazine*, vol. 7, no. 2, pp. 17-26, June 2013.

[3] Military Handbook MIL HDBK-338B: "Electronic Reliability Design Handbook," Department of Defence USA, Okt. 1, 1998.

[4] P. J. Tavner, "Review of condition monitoring of rotating electrical machines," *IET Electric Power Applications*, vol. 2, no. 4, pp. 215-247, July 2008.

[5] IEEE Std 1415-2006: "IEEE Guide for Induction Machinery Maintenance Testing and Failure Analysis," IEEE, 30 April 2007.

[6] S. Nandi, H. A. Toliyat and X. Li, "Condition Monitoring and Fault Diagnosis of Electrical Motors - A Review," *IEEE Trans. Energy Convers.*, vol. 20, no. 4, pp. 719-729, Dec. 2005.

[7] P. Tavner, L. Ran, J. Penman, H. Sedding, "Condition monitoring of rotating electrical machines," IET, 2008.

[8] H. Wang, K. Ma and F. Blaabjerg, "Design for reliability of power electronic systems," *IECON 2012 - 38th Annual Conference on IEEE Industrial Electronics Society*, Montreal, QC, 2012, pp. 33-44.

[9] S. Eberlin, B. Hock, "Zuverlässigkeit und Verfügbarkeit technischer Systeme," Springer, 2014.

[10] G. A. Klutke, P. C. Kiessler and M. A. Wortman, "A critical look at the bathtub curve," *IEEE Trans. Reliab.*, vol. 52, no. 1, pp. 125-129, March 2003.

[11] IEEE Std 1413.1-2002: "IEEE Guide for Selecting and Using Reliability Predictions Based on IEEE 1413," IEEE, 2003.

[12] H. Wang et al., "Transitioning to Physics-of-Failure as a Reliability Driver in Power Electronics," *IEEE Journal of Emerging and Selected Topics in Power Electronics*, vol. 2, no. 1, pp. 97-114, March 2014.

[13] Military Handbook MIL HDBK-217F: "Reliability prediction of electronic equipment," Department of Defence Washington DC, Dec. 2, 1991.

[14] F. Blaabjerg, "Design for Reliability in Power Electronic Systems," *ECPE Workshop Condition and health monitoring in power electronics*, 4-5 July 2017, Aalborg, Denmark.

[15] G. Vachtsevanos, F. L. Lewis, M. Roemer, A. Hess, B. Wu, "Intelligent fault diagnosis and prognosis for engineering systems," Wiley, 2006.

[16] U. M. Choi, F. Blaabjerg and K. B. Lee, "Study and Handling Methods of Power IGBT Module Failures in Power Electronic Converter Systems," *IEEE Trans. Pow. Electron.*, vol. 30, no. 5, pp. 2517-2533, May 2015.

[17] J. R. Celaya, P. Wysocki, V. Vashchenko, S. Saha and K. Goebel, "Accelerated aging system for prognostics of power semiconductor devices," *2010 IEEE AUTOTESTCON*, Orlando, FL, 2010, pp. 1-6.

[18] D. Astigarraga et al., "Analysis of the Results of Accelerated Aging Tests in Insulated Gate Bipolar Transistors," *IEEE Trans. Power Electron.*, vol. 31, no. 11, pp. 7953-7962, Nov. 2016.

[19] R. Sleik, M. Glavanovics, S. Einspieler, A. Muetze and K. Krischan, "Modular Test System Architecture for Device, Circuit, and System Level Reliability Testing and Condition Monitoring," *IEEE Trans. Ind. Appl.*, vol. 53, no. 6, pp. 5698-5708, Nov.-Dec. 2017.

[20] W. R. Jensen, E. G. Strangas and S. N. Foster, "A Method for Online Stator Insulation Prognosis for Inverter-Driven Machines," *IEEE Trans. Ind. Appl.*, vol. 54, no. 6, pp. 5897-5906, Nov.-Dec. 2018.

[21] W. T. Thomson and M. Fenger, "Current signature analysis to detect induction motor faults," *IEEE Ind. Appl. Mag.*, vol. 7, no. 4, pp. 26-34, July-Aug. 2001.

[22] A. Bellini, F. Filippetti, C. Tassoni and G. Capolino, "Advances in Diagnostic Techniques for Induction Machines," *IEEE Trans. Ind. Electron.*, vol. 55, no. 12, pp. 4109-4126, Dec. 2008.

[23] S. Yang, D. Xiang, A. Bryant, P. Mawby, L. Ran and P. Tavner, "Condition Monitoring for Device Reliability in Power Electronic Converters: A Review," *IEEE Trans. Pow. Electron.*, vol. 25, no. 11, pp. 2734-2752, Nov. 2010.

[24] E. Wolfgang, "Examples for failures in power electronics systems," *Proc. ECPE Tutorial "Reliability of Power Electronic Systems"*, Apr. 2007.

[25] S. Yang, A. Bryant, P. Mawby, D. Xiang, L. Ran and P. Tavner, "An Industry-Based Survey of Reliability in Power Electronic Converters," *IEEE Trans. Ind. Appl.*, vol. 47, no. 3, pp. 1441-1451, May-June 2011.

[26] J. Falck, C. Felgemacher, A. Rojko, M. Liserre and P. Zacharias, "Reliability of Power Electronic Systems: An Industry Perspective," *IEEE Industrial Electronics Magazine*, vol. 12, no. 2, pp. 24-35, June 2018.

[27] P. Beckedahl - Semikron, "Condition monitoring of power semiconductors a critical view," *ECPE Workshop Condition and health monitoring in power electronics*, 4-5 July 2017, Aalborg, Denmark.

[28] R. Wu, F. Blaabjerg, H. Wang, M. Liserre and F. Iannuzzo, "Catastrophic failure and fault-tolerant design of IGBT power electronic converters - an overview," *IECON 2013 - 39th Annual Conference of the IEEE Industrial Electronics Society*, Vienna, pp. 507-513, 2013.

[29] M. Held, P. Jacob, G. Nicoletti, P. Scacco and M. -. Poech, "Fast power cycling test of IGBT modules in traction application," *Proceedings of Second International Conference on Power Electronics and Drive Systems*, Singapore, 1997, pp. 425-430 vol.1.

[30] M. Ciappa and W. Fichtner, "Lifetime prediction of IGBT modules for traction applications," *2000 IEEE International Reliability Physics Symposium Proceedings 38th Annual*, (Cat. No.00CH37059), San Jose, CA, USA, 2000, pp. 210-216.

[31] H. Tseng and M. Wu, "Electro-thermal-mechanical modeling of wire bonding failures in IGBT," *2013 8th International Microsystems, Packaging, Assembly and Circuits Technology Conference (IMPACT)*, Taipei, 2013, pp. 152-157.

[32] M. Ciappa, "Selected failure mechanisms of modern power modules," *Microelectronics Reliability*, 42 (2002), 653-667, 2002.

[33] V. Smet et al., "Ageing and Failure Modes of IGBT Modules in High-Temperature Power Cycling," *IEEE Trans. Ind. Electron.*, vol. 58, no. 10, pp. 4931-4941, Oct. 2011.

[34] Leonrosenbaum, https://de.wikipedia.org/wiki/Datei:Infineon-IGBT-Modul.jpg, Licence: CC BY-SA 3.0, Attribution ShareAlike 3.0 Unported, https://creativecommons.org/licenses/by-sa/3.0/

[35] B. Lu and S. K. Sharma, "A literature review of IGBT fault diagnostic and protection methods for power inverters," *IEEE Trans. Ind. Appl.*, vol. 45, no. 5, pp. 1770-1777, 2009.

[36] D. Kastha and B. K. Bose, "Investigation of fault modes of voltage-fed inverter system for induction motor drive," *IEEE Trans. Ind. Appl.*, vol. 30, no. 4, pp. 1028-1038, 1994.

[37] N. Bianchi, S. Bolognani and M. Zigliotto, "Analysis of PM synchronous motor drive failures during flux weakening operation," *Power Electronics Specialists Conference, PESC '96 Record., 27th Annu. IEEE*, vol. 2, pp. 1542-1548, 1996.

[38] A. M. S. Mendes and A. J. M. Cardoso, "Voltage source inverter fault diagnosis in variable speed AC drives, by the average current Park's vector approach," *IEEE IEMDC '99*, pp. 704-706, 1999.

[39] S. Abramik, W. Sleszynski, J. Nieznanski, and H. Piquet, "A diagnostic method for on-line fault detection and localization in VSI-Fed AC drives," *EPE2003, 10th European Conf. on Power Electronics and Applications*, Toulouse, France, 2003.

[40] K. Rothenhagen and F. W. Fuchs, "Performance of diagnosis methods for IGBT open circuit faults in three phase voltage source inverters for AC variable speed drives," *2005 European Conference on Power Electronics and Applications*, pp. 10 pp.-P.7., 2005.

[41] E. Clarke, "Circuit analysis of A-C power systems," John Wiley & Sons, 1943.

[42] R. H. Park, "Two-reaction theory of synchronous machines generalized method of analysis-part I," *Trans AIEE*, vol. 48, no. 3, pp. 716-727, July 1929.

[43] R. Peuget, S. Courtine and J. P. Rognon, "Fault detection and isolation on a PWM inverter by knowledge-based model," *IEEE Trans. Ind. Appl.*, vol. 34, no. 6, pp. 1318-1326, 1998.

[44] C. Kral and K. Kafka, "Power electronics monitoring for a controlled voltage source inverter drive with induction machines," *Proc. IEEE 31st Power Electron. Spec. Conf.*, pp. 213-217, 2000.

[45] M. R. Mamat, M. Rizon, and M. S. Khanniche, "Fault detection of 3-phase VSI using wavelet-fuzzy algorithm," *Amer. J. Appl. Sci.*, vol. 3, no. 1, pp. 1642-1648, 2006.

[46] F. Charfi, F. Sellami and K. Al-Haddad, "Fault Diagnostic in Power System Using Wavelet Transforms and Neural Networks," *2006 IEEE International Symposium on Industrial Electronics*, Montreal, Que., 2006, pp. 1143-1148.

[47] D. U. Campos-Delgado and D. R. Espinoza-Trejo, "An Observer-Based Diagnosis Scheme for Single and Simultaneous Open-Switch Faults in Induction Motor Drives," *IEEE Trans. Ind. Electron.*, vol. 58, no. 2, pp. 671-679, Feb. 2011.

[48] D. R. Espinoza-Trejo, D. U. Campos-Delgado, E. Barcenas and F. J. Martinez-Lopez, "Robust fault diagnosis scheme for open-circuit faults in voltage source inverters feeding induction motors by using non-linear proportional-integral observers," *IET Power Electronics*, vol. 5, no. 7, pp. 1204-1216, August 2012.

[49] W. Sleszynski, J. Nieznanski and A. Cichowski, "Open-Transistor Fault Diagnostics in Voltage-Source Inverters by Analyzing the Load Currents," *IEEE Trans. Ind. Electron.*, vol. 56, no. 11, pp. 4681-4688, Nov. 2009.

[50] M. Trabelsi, M. Boussak and M. Gossa, "Multiple IGBTs open circuit faults diagnosis in voltage source inverter fed induction motor using modified slope method," *The XIX International Conference on Electrical Machines - ICEM 2010*, Rome, 2010, pp. 1-6.

[51] M. A. Masrur, Z. Chen, B. Zhang and Y. Lu Murphey, "Model-Based Fault Diagnosis in Electric Drive Inverters Using Artificial Neural Network," *2007 IEEE Power Engineering Society General Meeting*, Tampa, FL, 2007, pp. 1-7.

[52] R. L. de Araujo Ribeiro, C. B. Jacobina, E. R. C. da Silva and A. M. N. Lima, "Fault detection of open-switch damage in voltage-fed PWM motor drive systems," *IEEE Trans. Power Electron.*, vol. 18, no. 2, pp. 587-593, 2003.

[53] O. S. Yu, N. J. Park and D. S. Hyun, "A Novel Fault Detection Scheme for Voltage Fed PWM Inverter," *IECON 2006 - 32nd Annual Conference on IEEE Industrial Electronics*, Paris, pp. 2654-2659, 2006.

[54] S. M. Jung, J. S. Park, H. W. Kim, K. Y. Cho and M. J. Youn, "An MRAS-Based Diagnosis of Open-Circuit Fault in PWM Voltage-Source Inverters for PM Synchronous Motor Drive Systems," *IEEE Trans. Power Electron.*, vol. 28, no. 5, pp. 2514-2526, 2013.

[55] J. O. Estima and A. J. Marques Cardoso, "A New Algorithm for Real-Time Multiple Open-Circuit Fault Diagnosis in Voltage-Fed PWM Motor Drives by the Reference Current Errors," *IEEE Trans. Ind. Electron.*, vol. 60, no. 8, pp. 3496-3505, 2013.

[56] M. A. Rodriguez-Blanco et al., "A Failure-Detection Strategy for IGBT Based on Gate-Voltage Behavior Applied to a Motor Drive System," *IEEE Trans. Ind. Electron.*, vol. 58, no. 5, pp. 1625-1633, 2011.

[57] M. A. Rodriguez-Blanco, A. Vazquez-Perez, L. Hernandez-Gonzalez, V. Golikov, J. Aguayo-Alquicira and M. May-Alarcon, "Fault Detection for IGBT Using Adaptive Thresholds During the Turn-on Transient," *IEEE Trans. Ind. Electron.*, vol. 62, no. 3, pp. 1975-1983, 2015.

[58] Q. T. An, L. Sun and L. Z. Sun, "Hardware-circuit-based diagnosis method for open-switch faults in inverters," *Electronics Letters*, vol. 49, no. 17, pp. 1089-1091, 15 August 2013.

[59] C. Bae, D. Lee and T. H. Nguyen, "Detection and identification of multiple IGBT open-circuit faults in PWM inverters for AC machine drives," *IET Power Electronics*, vol. 12, no. 4, pp. 923-931, 10 4 2019.

[60] Z. Jian-Jian, C. Yong, C. Zhang-Yong and Z. Anjian, "Open-Switch Fault Diagnosis Method in Voltage-Source Inverters Based on Phase Currents," *IEEE Access*, vol. 7, pp. 63619-63625, 2019.

[61] Z. Li, Z. Bai, H. Ma and Y. Wang, "Fast open-transistor fault diagnosis based on calculated bridge arm pole-to-pole voltages in voltage-source inverters," *2016 IEEE 2nd Annual Southern Power Electronics Conference (SPEC)*, Auckland, 2016, pp. 1-6.

[62] I. Jlassi, J. O. Estima, S. K. El Khil, N. M. Bellaaj and A. J. M. Cardoso, "A Robust Observer-Based Method for IGBTs and Current Sensors Fault Diagnosis in Voltage-Source Inverters of PMSM Drives," *IEEE Trans. Ind. Appl.*, vol. 53, no. 3, pp. 2894-2905, May-June 2017.

[63] F. Wu and J. Zhao, "A Real-Time Multiple Open-Circuit Fault Diagnosis Method in Voltage-Source-Inverter Fed Vector Controlled Drives," *IEEE Trans. Power Electron.*, vol. 31, no. 2, pp. 1425-1437, Feb. 2016.

[64] E. Levi, R. Bojoi, F. Profumo, H. A. Toliyat and S. Williamson, "Multiphase induction motor drives - a technology status review," *IET Electric Power Applications*, vol. 1, no. 4, pp. 489-516, July 2007.

[65] L. Parsa and H. A. Toliyat, "Fault-Tolerant Interior-Permanent-Magnet Machines for Hybrid Electric Vehicle Applications," *IEEE Trans. Veh. Technol.*, vol. 56, no. 4, pp. 1546-1552, July 2007.

[66] A. M. El-Refaie, "Fault-tolerant permanent magnet machines: a review," *IET Electric Power Applications*, vol. 5, no. 1, pp. 59-74, January 2011.

[67] M. B. d. R. Correa, C. B. Jacobina, E. R. C. da Silva and A. M. N. Lima, "An induction motor drive system with improved fault tolerance," *IEEE Trans. Ind. Appl.*, vol. 37, no. 3, pp. 873-879, 2001.

[68] C. B. Jacobina, M. B. de Rossiter Correa, E. R. Cabral da Silva and A. M. N. Lima, "Induction motor drive system for low-power applications," *IEEE Trans. Ind. Appl.*, vol.35, no.1, pp.52-61, Jan/Feb 1999.

[69] Tian-Hua Liu, Jen-Ren Fu and T. A. Lipo, "A strategy for improving reliability of field-oriented controlled induction motor drives," *IEEE Trans. Ind. Appl.*, vol. 29, no. 5, pp. 910-918, 1993.

[70] A. M. S. Mendes and A. J. Marques Cardoso, "Continuous operation performance of faulty induction motor drives," *IEEE International Electric Machines and Drives Conference, 2003. IEMDC'03.*, Madison, WI, USA, 2003, pp. 547-553 vol.1.

[71] A. M. S. Mendes and A. J. Marques Cardoso, "Fault-Tolerant Operating Strategies Applied to Three-Phase Induction-Motor Drives," *IEEE Trans. Ind. Electron.*, vol. 53, no. 6, pp. 1807-1817, Dec. 2006.

[72] O. Jasim, C. Gerada, M. Sumner and J. Arellano-Padilla, "Operation of an induction motor with an open circuit fault by controlling the zero sequence voltage," *Electric Machines and Drives Conference, 2009. IEMDC '09. IEEE Internat.*, pp.1426-1433, 3-6 May 2009.

[73] O. Jasim, M. Sumner, C. Gerada and J. Arellano-Padilla, "Development of a new fault-tolerant induction motor control strategy using an enhanced equivalent circuit model," *Electric Power Applications*, IET, vol. 5, no. 8, pp. 618-627, 2011.

[74] S. Bolognani, M. Zordan and M. Zigliotto, "Experimental fault-tolerant control of a PMSM drive," *IEEE Trans. Ind. Electron.*, vol. 47, no. 5, pp. 1134-1141, 2000.

[75] N. Bianchi, S. Bolognani, M. Zigliotto and M. Zordan, "Innovative remedial strategies for inverter faults in IPM synchronous motor drives," *IEEE Energy Convers.*, vol. 18, no. 2, pp. 306-314, 2003.

[76] O. Wallmark, L. Harnefors and O. Carlson, "Post-fault operation of fault-tolerant inverters for PMSM drives," *2005 European Conf. on Power Electronics and Applications*, pp. 10 pp.-P.11, 2005.

[77] O. Wallmark, L. Harnefors and O. Carlson, "Control Algorithms for a Fault-Tolerant PMSM Drive," *IEEE Trans. Ind. Electron.*, vol.54, no.4, pp.1973-1980, Aug. 2007.

[78] F. Meinguet, X. Kestelyn, E. Semail and J. Gyselinck, "Fault detection, isolation and control reconfiguration of three-phase PMSM drives," *Industrial Electronics (ISIE), 2011 IEEE Int. Symp. on*, pp. 2091-2096, 2011.

[79] A. Gaeta, G. Scelba and A. Consoli, "Modeling and Control of Three-Phase PMSMs Under Open-Phase Fault," *IEEE Trans. Ind. Appl.*, no. 1, pp. 74-83, 2013.

[80] J. O. Estima and A. J. M. Cardoso, "Fast fault detection, isolation and reconfiguration in fault-tolerant permanent magnet synchronous motor drives," *2012 IEEE Energy Conversion Congress and Exposition (ECCE)*, Raleigh, NC, 2012, pp. 3617-3624.

[81] B. A. Welchko, T. A. Lipo, T. M. Jahns and S. E. Schulz, "Fault tolerant three-phase AC motor drive topologies: a comparison of features, cost, and limitations," *IEEE Trans. Power Electron.*, vol. 19, no. 4, pp. 1108-1116, 2004.

[82] B. Mirafzal, "Survey of Fault-Tolerance Techniques for Three-Phase Voltage Source Inverters," *IEEE Trans. Ind. Electron.*, vol. 61, no. 10, pp. 5192-5202, Oct. 2014.

[83] R. R. Errabelli and P. Mutschler, "Fault-Tolerant Voltage Source Inverter for Permanent Magnet Drive," *IEEE Trans. Pow. Electron.*, vol. 27, no. 2, pp. 500-508, Feb. 2012.

[84] J. O. Estima and A. J. M. Cardoso, "Efficiency evaluation of fault-tolerant operating strategies applied to three-phase permanent magnet synchronous motor drives," *2012 XXth International Conference on Electrical Machines*, Marseille, 2012, pp. 2411-2417.

[85] D. Schroeder, "Elektrische Antriebe - Regelung von Antriebssystemen," Springer-Verlag Berlin Heidelberg, 4. Auflage, 2015.

[86] M. Horn, N. Dourdoumas, "Regelungstechnik: Rechnerunterstützter Entwurf zeitkontinuierlicher und zeitdiskreter Regelkreise," Pearson Studium, 2003.

[87] R. Seebacher, "Modelle für die Asynchronmaschine mit Bezug auf die Feldorientierte Regelung," Dissertation, Technische Universität Graz, 1996.

[88] C. L. Fortescue, "Method of symmetrical co-ordinates applied to the solution of polyphase networks," *34th Annual Convention of the AIEE*, Atlantic City, pp. 1027-1140, 1918.

[89] K. P. Kovacs, "Symmetrische Komponenten in Wechselstrommaschinen," Lehr- und Handbuecher der Ingenieurswissenschaften, Birkhaeuser Verlag Basel, 1962.

[90] IEC Standard 60034-2-1: "Rotating electrical machines - Part 2-1: Standard methods for determining losses and efficiency from tests (excluding machines for traction vehicles)," IEC, 2014.

[91] IEC Standard 60034-28: "Rotating electrical machines - Part 28: Test methods for determining quantities of equivalent circuit diagrams for three-phase low-voltage cage induction motors," IEC, 2013.

[92] W. Nuernberg and Rolf Hanitsch, "Die Prüfung elektrischer Maschinen," Sechste, vollständig überarbeitete Auflage, Springer-Verlag Berlin Heidelberg GmbH, 1987.

[93] IEC Standard 60034-2-3: "Rotating electrical machines - Part 2-3: Specific test methods for determining losses and efficiency of converter-fed AC induction motors," IEC, 2013.

[94] H. J. Bartsch, "Taschenbuch mathematischer Formeln," 21. Auflage, Carl Hanser Verlag, 2007.

[95] IEC Standard 60034-1: "Rotating electrical machines - Part 1: Rating and performance," IEC, 2017.

[96] A. Krings: "Iron Losses in Electrical Machines - Influence of Material Properties, Manufacturing Processes, and Inverter Operation," Doctoral Thesis, KTH Electrical Engineering, Sweden, 2014.

[97] M. C. Levin: "Charakterisierung von weichmagnetischen Pulververbundwerkstoffen für den Einsatz in Traktionsantrieben," Dissertation, Technische Universität München, 2014.

[98] G. Bertotti, "Hysteresis in magnetism: for physicists, material scientists, and engineers," *Academic Press*, San Diego, 1998.

[99] R. Richter, "Elektrische Maschinen IV," 2. Auflage, Verlag Birkhaeuser AG Karlsruhe, 1954.

[100] W. Nuernberg, "Die Asynchronmaschine," Zweite Auflage, Springer-Verlag Berlin Heidelberg New York, 1976.

[101] G. Mueller, K. Vogt and B. Ponick: "Berechnung elektrischer Maschinen," 6., völlig neu bearbeitete Auflage, Wiley-VCH Verlag GmbH & Co KGaA, 2008.

[102] J. Pyrhönen, T. Jokinen, V. Hrabovcova: "Design of Rotating Electrical Machines," John Wiley & Sons Ltd, 2008.

[103] T. A. Lipo, "Introduction to AC machine design," Third Edition, Wisconsin Power Electronics Research Center, University of Wisconsin, 2011.

[104] G. I. Taylor, "Stability of a viscous liquid contained between two rotating cylinders," *Philosophical Transactions of the Royal Society of London. Series A, Containing Papers of a Mathematical or Physical Character*, 223, pp.289343, 1922.

[105] G. I. Taylor, "Distribution of Velocity and Temperature between Concentric Rotating Cylinders," *Proc. R. Soc. Lond. A*, Vol. 151, No. 874, pp. 494-512, 1935.

[106] G. I. Taylor, "Fluid friction between rotating cylinders ITorque measurements," *Proc. R. Soc. Lond. A*, Vol. 157, No. 874, pp. 546-564, 1936.

[107] G. I. Taylor, "Fluid friction between rotating cylinders IIdistribution of velocity between concentric cylinders when outer one is rotating and inner one is at rest," *Proc. R. Soc. Lond. A*, Vol. 157, No. 892, pp. 565-578, 1936.

[108] J. E. Vkzncik, "Prediction of windage power loss in alternators," NASA Technical Note D-4849, 1968.

[109] T. Theodorsen, A. Regier, "Experiments on Drag of Revolving Disks, Cylinders, and Streamline Rods at High Speeds," NASA Technical Report, No. 793, 1944.

[110] C. Gazley, "Heat-Transfer Characteristics of the Rotational and Axial Flow Between Concentric Cylinders", *Trans. ASME*, 80, pp. 79-90, 1958.

[111] Svenska Kullagerfabriken, "The SKF model for calculating the frictional moment," [Online]. Link: https://www.skf.com/binaries/331-299767/0901d1968065e9e7-The-SKF-model-for-calculating-the-frictional-movement.pdf, downloaded April 2020.

[112] Svenska Kullagerfabriken, "Using a friction model as an engineering tool," SKF Evolution, 2006.

[113] P. Narbutovskih, "Power losses in induction machines," *Electrical Engineering*, vol.53, no.11, pp.1466-1471, 1934.

[114] P. L. Alger, G. Angst and E. J. Davies, "Stray-Load Losses in Polyphase Induction Machines," *Trans. AIEE. Part III: Power Apparatus and Systems*, vol. 78, no. 3, pp. 349-355, 1959.

[115] K. K. Schwarz, "Survey of basic stray losses in squirrel-cage induction motors," *Proc. IEE*, vol. 111, no. 9, pp. 1565-1574, September 1964.

[116] A. Schindler, "Betriebsverhalten und Verluste von Asynchron-Käfigläufermotoren beim Betrieb am Transistor-Pulswechselrichter," Dissertation, Technische Universität Darmstadt, 1985.

[117] P. G. Cummings, "Estimating Effect of System Harmonics on Losses and Temperature Rise of Squirrel-Cage Motors," *IEEE Trans. Ind. Appl.*, vol.IA-22, no.6, pp.1121-1126, 1986.

[118] Wenping Cao, K.J. Bradley, J.C. Clare and P.W. Wheeler, "Comparison of Stray Load and Inverter-Induced Harmonic Losses in Induction Motors Using Calorimetric and Harmonic Injection Methods," *IEEE Trans. Ind. Appl.*, vol.46, no.1, pp.249-255, 2010.

[119] V. M. Montsinger, "Loading Transformers By Temperature," *Trans. AIEE*, vol. 49, no. 2, pp. 776-790, April 1930.

[120] T. W. Dakin, "Electrical Insulation Deterioration Treated as a Chemical Rate Phenomenon," *Trans. AIEE*, vol. 67, no. 1, pp. 113-122, Jan. 1948.

[121] E. L. Brancato, "Estimation of lifetime expectancies of motors," *IEEE Electr. Insul. Mag.*, vol. 8, no. 3, pp. 5-13, May-June 1992.

[122] IEC Standard 60085: "Electrical insulation - Thermal evaluation and designation," IEC, 2007.

[123] IEC Standard 60505: "Evaluation and qualification of electrical insulation systems," IEC, 2011.

[124] IEEE Std 1-2000TM (R2005): "IEEE Recommended Practice - General Principles for Temperature Limits in the Rating of Electrical Equipment and for the Evaluation of Electrical Insulation," IEEE, 2005.

[125] IEC Standard 60349-2: "Electric traction - Rotating electrical machines for rail and road vehicles - Part 2: Electronic converter-fed alternating current motors," IEC, 2014.

[126] J. F. Heidbreder, "Induction Motor Temperature Characteristics," *Trans. AIEE. Part III: Power Apparatus and Systems*, vol. 77, no. 3, pp. 800-804, April 1958.

[127] W. T. Martiny, R. M. McCoy and H. B. Margolis, "Thermal Relationships in an Induction Motor under Normal and Abnormal Operation," *Trans. AIEE. Part III: Power Apparatus and Systems*, vol. 80, no. 3, pp. 66-76, April 1961.

[128] M. M. Khonsari and E. R. Booser, "Applied Tribology: Bearing Design and Lubrication," Second Edition, John Wiley and Sons, 2008.

[129] E. R. Booser and M. Khonsari, "Systematically Selecting the Best Grease for Equipment Reliability," *Machinery Lubrication*, pp. 19-25, 2007.

[130] R. J. Buschart, R. L. Doughty, R. A. Epperly and W. J. Martiny, "Safe Application of Totally Enclosed Motors in Hazardous Class I, Division 2 Locations," *IEEE Trans. Ind. Appl.*, vol. 30, no. 6, pp. 1538-, Nov/Dec 1994.

[131] P. S. Hamer et al., "Flammable vapor ignition initiated by hot rotor surfaces within an induction motor: reality or not?," *IEEE Trans. Ind. Appl.*, vol. 35, no. 1, pp. 100-111, Jan/Feb 1999.

[132] R. L. Kotnik, "An Equivalent Thermal Circuit for Nonventilated Induction Motors [includes discussion]," *Trans. AIEE. Part III: Power Apparatus and Systems*, vol. 73, no. 2, pp. 1604-1609, 1954.

[133] P. H. Mellor, "Improvements in the efficiency and thermal ageing of single and parallel machine drives," Doctoral Thesis, University of Liverpool, 1983.

[134] D. Roberts, "The application of an induction motor thermal model to motor protection and other functions," Doctoral Thesis, University of Liverpool, 1986.

[135] A. Bousbaine, "An investigation into the thermal modeling of induction motors," Doctoral Thesis, Department of Electronic and Electrical Engineering, University of Sheffield, 1993.

[136] G. Kylander, "Thermal modelling of small cage induction motors," Doctoral Thesis, School of Electrical and Computer Engineering, Chalmers University of Technology, 1995.

[137] P. H. Mellor, D. Roberts and D. R. Turner, "Lumped parameter thermal model for electrical machines of TEFC design," *IEE Proceedings B - Electric Power Applications*, vol. 138, no. 5, pp. 205-218, 1991.

[138] A. Boglietti, A. Cavagnino, M. Lazzari and M. Pastorelli, "A simplified thermal model for variable-speed self-cooled industrial induction motor," *IEEE Trans. Ind. Appl.*, vol. 39, no. 4, pp. 945-952, 2003.

[139] M. A. Valenzuela, P. V. Verbakel and J. A. Rooks, "Thermal evaluation for applying TEFC induction motors on short-time and intermittent duty cycles," *IEEE Trans. Ind. Appl.*, vol. 39, no. 1, pp. 45-52, 2003.

[140] M. J. Duran and J. Fernandez, "Lumped-parameter thermal model for induction machines," *IEEE Trans. Energy Convers.*, vol. 19, no. 4, pp. 791-792, 2004.

[141] C. Kral, A. Haumer, H. Kapeller, F. Pirker and G. Pascoli, "Comparison of two rotor temperature estimation models of a surface cooled squirrel cage induction machine," *IEEE International Conference on Electric Machines and Drives*, 2005., San Antonio, TX, pp. 207-211, 2005.

[142] K. Ghaib, "Einführung in die numerische Strömungsmechanik," Springer Vieweg, 2019.

[143] E. Laurien, H. Oertel jr. , "Numerische Strömungsmechanik," 5., überarbeitete und erweiterte Auflage, Springer Vieweg, 2013.

[144] C. C. Chan, Lietong Yan, Pizhang Chen, Zezhong Wang and K. T. Chau, "Analysis of electromagnetic and thermal fields for induction motors during starting," *IEEE Trans. Energy Convers.*, vol. 9, no. 1, pp. 53-60, March 1994.

[145] Yangsoo Lee, Hyang-beom Lee, Song-yop Hahn and Ki-sik Lee, "Temperature analysis of induction motor with distributed heat sources by finite element method," *IEEE Trans. Magn.*, vol. 33, no. 2, pp. 1718-1721, March 1997.

[146] M. S. Rajagopal, K. N. Seetharamu and P. A. Ashwathnarayana, "Transient thermal analysis of induction motors," *IEEE Trans. Energy Convers.*, vol. 13, no. 1, pp. 62-69, March 1998.

[147] Chang-Chou Hwang, S. S. Wu and Y. H. Jiang, "Novel approach to the solution of temperature distribution in the stator of an induction motor," *IEEE Trans. Energy Convers.*, vol. 15, no. 4, pp. 401-406, Dec. 2000.

[148] B. Bai, Q. Yu, H. He and X. Wang, "3-D Thermal Analysis and Computation of Flameproof Induction Motor," 2010 Asia-Pacific Power and Energy Engineering Conference, Chengdu, pp. 1-4, 2010.

[149] R. Wrobel, P. H. Mellor and D. Holliday, "Thermal Modeling of a Segmented Stator Winding Design," *IEEE Trans. Ind. Appl.*, vol. 47, no. 5, pp. 2023-2030, Sept.-Oct. 2011.

[150] C. A. Cezario and A. A. M. Oliveira, "Electric motor internal fan system CFD validation," 2008 18th International Conference on Electrical Machines, Vilamoura, pp. 1-6, 2008.

[151] M. Hettegger, B. Streibl, O. Biro and H. Neudorfer, “Measurements and Simulations of the Convective Heat Transfer Coefficients on the End Windings of an Electrical Machine,” *IEEE Trans. Ind. Electron.*, vol. 59, no. 5, pp. 2299-2308, May 2012.

[152] S. Nategh, Z. Huang, A. Krings, O. Wallmark and M. Leksell, "Thermal Modeling of Directly Cooled Electric Machines Using Lumped Parameter and Limited CFD Analysis,“ *IEEE Trans. Energy Convers.*, vol. 28, no. 4, pp. 979-990, Dec. 2013.

[153] M. Schrittwieser, A. Marn, E. Farnleitner and G. Kastner, “Numerical Analysis of Heat Transfer and Flow of Stator Duct Models," *IEEE Trans. Ind. Appl.*, vol. 50, no. 1, pp. 226-233, Jan.-Feb. 2014.

[154] W. Polifke and J. Kopitz, “Wärmeübertragung,” 2. aktualisierte Auflage, Pearson Studium, 2009.

[155] W. S. Janna, “Engineering Heat Transfer,” Third edition, CRC Press, Taylor and Francis Group, 2009.

[156] G. Gotter, “Erwärmung und Kühlung elektrischer Maschinen,” Springer-Verlag Berlin Heidelberg, 1954.

[157] S. K. Pal, “Heat Transfer in Electrical Machines - a critical review,” Electrical Research Assoc., 1971.

[158] R. C. Progelhof, J. L. Throne, R. R. Ruetsch, “Methods of Predicting the Thermal Conductivity of Composite Systems: A Review,” *Polymer Engineering and Science*, Vol. 16, No. 9, Sept. 1976.

[159] B. W. James, G. H. Wostenholm, G. S. Keen and S. D. McIvor, “Prediction and measurement of the thermal conductivity of composite materials,” *J. Phys. D: Appl. Phys.*, 20 (1987) 216-268, 1987.

[160] N. Simpson, R. Wrobel and P. H. Mellor, “Estimation of Equivalent Thermal Parameters of Impregnated Electrical Windings,” *IEEE Trans. Ind. Appl.*, vol. 49, no. 6, pp. 2505-2515, Nov.-Dec. 2013.

[161] L. Idoughi, X. Mininger, F. Bouillault, L. Bernard and E. Hoang, “Thermal Model With Winding Homogenization and FIT Discretization for Stator Slot,” *IEEE Trans. Magn.*, vol. 47, no. 12, pp. 4822-4826, Dec. 2011.

[162] F. P. Incropera, D. P. Dewitt, T. L. Bergman, A. S. Lavine, "Introduction to Heat Transfer," Fifth Edition, John Wilef & Sons, 2007.

[163] H. Sigloch, "Technische Fluidmechanik," 9. ergänzte Auflage, Springer-Verlag Berlin Heidelberg, 2014.

[164] D. Staton, A. Boglietti and A. Cavagnino, "Solving the more difficult aspects of electric motor thermal analysis in small and medium size industrial induction motors," *IEEE Trans. Energy Convers.*, vol. 20, no. 3, pp. 620-628, Sept. 2005.

[165] A. Boglietti, A. Cavagnino and D. Staton, "Determination of Critical Parameters in Electrical Machine Thermal Models," *IEEE Trans. Ind. Appl.*, vol. 44, no. 4, pp. 1150-1159, July-aug. 2008.

[166] K. M. Becker, J. Kaye, "Measurements of diabatic flow in an annulus with an inner rotating cylinder," *Trans. ASME, Journal of Heat Transfer*, pp.97-105, May 1962.

[167] G. E. Luke, "The Cooling of Electric Machines," *Trans. AIEE*, Volume XLII, pp. 636-652, 1923.

[168] A. Boglietti, A. Cavagnino, "Analysis of the Endwinding Cooling Effects in TEFC Induction Motors," *IEEE Trans. Ind. Appl.*, Volume 43, Issue 5, pp.1214 1222, 2007.

[169] A. Boglietti, A. Cavagnino, D. A. Staton, and M. Popescu, "Impact of different end region cooling arrangements on endwinding heat transfer coefficients in electric motors," *Industrial Electronics, 2009. 1ECON '09. 35th Annual Conference of IEEE*, pp. 1168-1173, 2009.

[170] D. A. Staton, M. Popescu, D. Hawkins, A. Boglietti and A. Cavagnino, "Influence of different end region cooling arrangements on end-winding heat transfer coefficients in electrical machines," *2010 IEEE Energy Conversion Congress and Exposition*, Atlanta, GA, pp. 1298-1305, 2010.

[171] K. Takahashi, H. Kuwahara, K. Kajiwara, and T. Obata, "Airflow and thermal conductance in totally enclosed induction motor," *Heat Transfer Asian Research*, vol. 31, no. 1, pp. 7-20, 2002.

[172] G. L. Basso, J. Goss, Y. C. Chong and D. Staton, "Improved thermal model for predicting end-windings heat transfer," *2017 IEEE Energy Conversion Congress and Exposition (ECCE)*, Cincinnati, OH, 2017, pp. 4650-4657.

[173] A. Boglietti, A. Cavagnino, M. Parvis, A. Vallan, "Evaluation of radiation thermal resistances in industrial motors," *IEEE Trans. Ind. Appl.*, Vol. 42, No. 3, pp. 688-693, 2006.

[174] N. D. Weills and E. A. Ryder, "Thermal Resistance Measurements of Joints Formed between stationary metal surfaces," *Trans. ASME*, Vol. 71, No. 3, pp.259-267, 1949.

[175] A. W. Brunot and F. F. Buckland, "Thermal Contact Resistance of Laminated and Machined Joints," *Trans. ASME*, Vol. 71, No. 3, pp. 253-257 1949.

[176] P. Pillay and M. Manyage, "Loss of Life in Induction Machines Operating With Unbalanced Supplies," *IEEE Trans. Energy Convers.*, vol. 21, no. 4, pp. 813-822, Dec. 2006.

[177] P. Gnacinski, "Windings Temperature and Loss of Life of an Induction Machine Under Voltage Unbalance Combined With Over- or Undervoltages," *IEEE Trans. Energy Convers.*, vol. 23, no. 2, pp. 363-371, June 2008.

[178] JMAG-Designer, Versions 15.1 and 18.1, Copyright (c) JSOL Corporation 2016 and 2019. Simulation technology for electromechanical design, [Online]. Available: https://www.jmag-international.com/

Acronyms

AC	Alternating Current
CFD	Computational Fluid Dynamics
DC	Direct Current
EMF	Electromotive Force
FEA	Finite Element Analysis
FEM	Finite Element Method
FDM	Finite Difference Method
FLMS	Flux Linkage Measurement System
FVM	Finite Volume Method
IGBT	Insulated Gate Bipolar Transistor
IM	Induction Machine
IOCF	Inverter Open Circuit Fault
LDM	Load and Driving Machine
LPTN	Lumped Parameter Thermal Network
MMF	Magnetomotive Force
MUT	Machine Under Test
PMSM	Permanent Magnet Synchronous Machine
PI	Proportional-Integral
PT1	Low Pass Filter of Order 1
PWM	Pulse Width Modulation
RMS	Root Mean Square
RRF	Rotor Reference Frame
ΨRF	Rotor Flux-Oriented Reference Frame
SCIM	Squirrel Cage Induction Machine
SM	Synchronous Machine
SSF	Single Switch Fault
SRF	Stator Reference Frame

Symbols

Real Quantities

A	Cross-Sectional Area
A_1	Area of Radiator 1
A_2	Area of Radiator 2
A_c	Area of the Convection Surface
B	Magnetic Flux Density
B_ref	Reference Magnetic Flux Density
C_d	Skin Friction Coefficient
c	Constant
c_1	First Parameter of the Unaffected Magnetizing Current of the Main System
c_2	Second Parameter of the Unaffected Magnetizing Current of the Main System
c_3	Third Parameter of the Unaffected Magnetizing Current of the Main System
c_L	Coefficient of the Torque Ratio due to the Inductance
c_i	Coefficient of the Torque Ratio due to the Current
c_ish	Inlet Shear Heating Reduction Factor
c_p	Specific Heat Capacity
c_rs	Kinematic Replenishment/Starvation Reduction Factor
c_rr	Load Variable of the Rolling Frictional Torque
c_sl	Sliding Friction Coefficient
c_sll	Load Variable of the Sliding frictional Torque
c_w1	First Parameter of the Affected Magnetizing Current of the Main System
c_w2	Second Parameter of the Affected Magnetizing Current of the Main System
c_τ	Coefficient of the Torque Ratio with Saturation
d	Density
d_1	First Parameter of the Unaffected Zero-Sequence Magnetizing Current

d_2	Second Parameter of the Unaffected Zero-Sequence Magnetizing Current
d_{w1}	First Parameter of the Affected Zero-Sequence Magnetizing Current
d_{w2}	Second Parameter of the Affected Zero-Sequence Magnetizing Current
e_f	Fault Specific Current Control Deviation
e_α	Real Part of the Current Control Deviation Space Vector in the SRF
e_β	Imaginary Part of the Current Control Deviation Space Vector in the SRF
e_∞	Permanent Current Control Deviation
F_{12}	View Factor
f	Frequency
f_d	Sampling Frequency
f_ref	Reference Frequency
f_s	Stator Frequency
G	Controller Gain
H	Magnetic Field Strength
h	Heat Transfer Coefficient
h_0	Zero-Speed Heat Transfer Coefficient
h_l	Local Heat Transfer Coefficient
h_rad	Equivalent Radiation Heat Transfer Coefficient
I	RMS Value of the Phase Currents
I_m	Magnitude of the Magnetizing Current Space Vector (Main System)
I_mu	Unaffacted Magnitude of the Magnetizing Current Space Vector (Main System)
I_m3	Amplitude of the Zero-Sequence Magnetizing Current
I_m3u	Unaffacted Amplitude of the Zero-Sequence Magnetizing Current
I_s	Stator Current
I_sd	Real Part of the Stator Current Space Vector in the ΨRF (RMS)
I_sq	Imaginary Part of the Stator Current Space Vector in the ΨRF (RMS)
$I_\mathrm{sd,MCT}$	I_sd for Maximum Continuous Torque (RMS)
$I_\mathrm{sq,MCT}$	I_sq for Maximum Continuous Torque (RMS)
i	Current
i_a	Current in Phase a
i_b	Current in Phase b
i_c	Current in Phase c
i_d	Real Part of the Current Space Vector in the RRF
i_d^*	Real Part of the Reference Current Space Vector in the RRF

i_n	Neutral Current
i_q	Imaginary Part of the Current Space Vector in the RRF
i_q^*	Imaginary Part of the Reference Current Space Vector in the RRF
$\tilde{i}_\mathrm{q}$	Modeled Imaginary Part of the Current Space Vector in the RRF
i_s0	Zero-Sequence Stator Current
i_s0^*	Desired Zero-Sequence Stator Current
$i_\mathrm{s0,k}$	Zero-Sequence Stator Current at Period k
i_α	Real Part of the Current Space Vector in the SRF
i_α^*	Desired Real Part of the Current Space Vector in the SRF
i_β	Imaginary Part of the Current Space Vector in the SRF
i_β^*	Desired Imaginary Part of the Current Space Vector in the SRF
$i_{\mathrm{s}\alpha}$	Real Part of the Stator Current Space Vector in the SRF
$i_{\mathrm{s}\alpha}^*$	Desired Real Part of the Stator Current Space Vector in the SRF
$i_{\mathrm{s}\beta}$	Imaginary Part of the Stator Current Space Vector in the SRF
$i_{\mathrm{s}\beta}^*$	Desired Imaginary Part of the Stator Current Space Vector in the SRF
i_sd	Real Part of the Stator Current Space Vector in the ΨRF
i_sd^*	Desired Real Part of the Stator Current Space Vector in the ΨRF
i_sq	Imaginary Part of the Stator Current Space Vector in the ΨRF
i_sq^*	Desired Imaginary Part of the Stator Current Space Vector in the ΨRF
$i_\mathrm{sq,k}$	Imaginary Part of the Stator Current Space Vector in the ΨRF at Period k
j	Imaginary Unit
k	Thermal Conductivity
k_1	Thermal Conductivity of the First Composite Material
k_2	Thermal Conductivity of the Second Composite Material
k_p	Thermal Conductivity in the Lamination Direction
k_s	Thermal Conductivity Perpendicular to the Lamination Direction
L_d	Stator Inductance in the Direct Axis
L_m	Magnetization Inductance
L_m3	Magnetization Inductance of the Zero-Sequence System
L_q	Stator Inductance in the Quadrature Axis
L_s	Stator Inductance
$L_{\sigma\mathrm{r}}$	Rotor Leakage Inductance
$L_{\sigma\mathrm{r3}}$	Rotor Leakage Inductance of the Zero-Sequence System
$L_{\sigma\mathrm{s}}$	Stator Leakage Inductance

$L_{\sigma s0}$	Stator Leakage Inductance of the Zero-Sequence System
L_0	Zero-Sequence Stator Inductance Parameter for the Control
l	Length
l_g	Gap Length
M_l	Mass of a Segment
m	Modulation Index
N	Number of Turns
Nu	Nusselt Number
n	Rotational Speed
o_c	Speed Exponent of the End Space Heat Transfer
o_h	Hysteresis Loss Exponent
o_{sB}	Flux Density Exponent of the Steinmetz Equation
o_{sf}	Frequency Exponent of the Steinmetz Equation
P_{Al}	Power Losses in the Squirrel Cage
P_{Al0}	Power Losses in the Squirrel Cage caused by the Zero-Sequence System
P_{Cu}	Power Losses in the Stator Winding
P_{Cu0}	Power Losses in the Stator Winding of the Zero-Sequence System
P_{el}	Electrical Power
P_{Fe}	Iron Power Losses
$P_{Fe,l}$	Iron Power Losses of a Segment
P_{fr}	Frictional Power of a Grease Lubricated Bearing
P_{fw}	Friction and Windage Power Losses
P_{loss}	Total Power Losses
P_{mech}	Mechanical Power
P_{mech0}	Mechanical Power of the Zero-Sequence System
P_{Res0}	Residual Power Losses during the Zero-Sequence System Experiments
P_{s0}	Stator Power of the Zero-Sequence System
P_w	Windage Power Losses
Pr	Prandtl number
p	Number Of Pole Pairs
p_{Fe}	Iron Loss Density per Volume
$p_{Fe,l}$	Iron Loss Density of a Segment per Mass
Q	Heat
Q_{int}	Internal Heat

Q_{conv}	Convective Heat
Q_{12}	Transmitted Energy between two diffuse-gray radiators
q	Number of Slots per Pole and Phase
q_{conv}	Convective Heat Density
q_{e}	Emissive Heat Density
R	Resistance
R_{a}	Electrical Resistance of Phase a
R_{b}	Electrical Resistance of Phase b
R_{c}	Electrical Resistance of Phase c
R_{conv}	Convective Thermal Resistance
R_{Fe}	Iron Loss Resistance
R_{Ro}	One Dimensional Thermal Resistance of a rod
R_{r}	Electrical Rotor Resistance
R_{rad}	Thermal Resistance due to Radiation
R_{r0p}	Zero-Sequence Rotor Resistance for the Third Space Harmonic (Positive Direction)
R_{r0n}	Zero-Sequence Rotor Resistance for the Third Space Harmonic (Negative Direction)
R_{r3}	Electrical Rotor Resistance of the Zero-Sequence System
R_{s}	Electrical Stator Resistance
R_{s0}	Stator Resistance of the Zero-Sequence System
R_{th}	Thermal Resistance
R_{Zr}	Thermal Resistance of a Hollow Cylinder in Radial Direction
R_0	Zero-Sequence Stator Resistance Parameter for the Control
$R_{0^\circ\mathrm{C}}$	Electrical Resistance at 0°C
R_1	First Partial Conduction Thermal Resistance
R_2	Second Partial Conduction Thermal Resistance
R_3	Conduction Thermal Resistance for the Internal Heat
Re	Reynolds Number
Re_{crit}	Critical Reynolds Number
r	Specific Resistance / Radius
r_{ref}	Specific Resistance at the Reference Temperature
r_1	Inner Radius of a Hollow Cylinder
r_2	Outer Radius of a Hollow Cylinder
S	Switch
s	Slip

T	(Absolute) Temperature
T_c	Celsius Temperature
T_EW	Stator Endwinding Temperature
T_m	Absolute Temperature of the Conductive Component
T_RW	Rotor Winding Temperature
T_ref	Reference Temperature
T_s	Temperature of the Solid
T_1	Absolute Temperature of the Radiator 1
T_2	Absolute Temperature of the Radiator 2
T_∞	Free Stream Temperature of the Fluid
Ta	Taylor Number
t	Time
t_PT1	Low Pass Filter Time Constant
t_d	Sampling Period
t_f	Fundamental Period
t_r	Reset Time
t_s	Switching Period
t_0	Beginning Time of the Integration Interval
t_1	Ending Time of the Integration Interval
u_a	Anomalous Loss Coefficient
u_c	Speed Coefficient of the End Space Heat Transfer
u_e	Eddy Current Loss Coefficient
$u_\mathrm{e,add}$	Additional Eddy Loss Coefficient
$u_\mathrm{e,ref}$	Reference Eddy Current Loss Coefficient
$u_\mathrm{e,t}$	Eddy Loss Coefficient
u_h	Hysteresis Loss Coefficient
$u_\mathrm{h,add}$	Additional Hysteresis Loss Coefficient
$u_\mathrm{h,ref}$	Reference Hysteresis Loss Coefficient
$u_\mathrm{h,t}$	Hysteresis Loss Coefficient
u_s	Coefficient of the Steinmetz Equation
v	Velocity
v_a	Voltage of Phase a
v_b	Voltage of Phase b
v_c	Voltage of Phase c

v_{dc}	DC-Link Voltage
v_{n}	Voltage of the Neutral Point of the Machine n
v_{s0}	Zero-Sequence Stator Voltage
v_{s0}^{*}	Desired Zero-Sequence Stator Voltage
$v_{\mathrm{s}\alpha}$	Real Part of the Stator Voltage Space Vector in the SRF
$v_{\mathrm{s}\beta}$	Imaginary Part of the Stator Voltage Space Vector in the SRF
v_{ta}	Terminal Voltage of Inverter Leg a
v_{ta}^{*}	Commanded Terminal Voltage of Leg a
v_{tb}	Terminal Voltage of Inverter Leg b
v_{tc}	Terminal Voltage of Inverter Leg c
v_{α}	Real Part of the Voltage Space Vector in the SRF
v_{α}^{*}	Desired Real Part of the Voltage Space Vector in the SRF
$v_{\alpha,\mathrm{res}}$	Voltage Reserve for an SSF of S_1
$\overline{v}_{\alpha}$	Average Real Part of the Voltage Space Vector in the SRF in one switching Period
$v_{\alpha+}$	Real Part of the Additional Voltage Space Vector in the SRF
v_{β}	Imaginary Part of the Voltage Space Vector in the SRF
v_{β}^{*}	Desired Imaginary Part of the Voltage Space Vector in the SRF
$\overline{v}_{\beta}$	Average Imaginary Part of the Voltage Space Vector in the SRF in one switching Period
$v_{\beta+}$	Imaginary Part of the Additional Voltage Space Vector in the SRF
W	Weakening Factor
W_{c}	Coil Width
W_{p}	Pole Pitch
w	Weighting Factor for the Magnetizing Current of the Main System
w_0	Weighting Factor for the Zero-Sequence Magnetizing Current
X_{m}	Magnetization Reactance
X_{m0}	Zero-Sequence Magnetization Reactance
$X_{\sigma\mathrm{r}}$	Rotor Leakage Reactance
$X_{\sigma\mathrm{r0}}$	Zero-Sequence Rotor Leakage Reactance
$X_{\sigma\mathrm{s}}$	Stator Leakage Reactance
$X_{\sigma\mathrm{s0}}$	Zero-Sequence Stator Leakage Reactance
y_1	Fractional Volume of Material 1 of the Composite
α	Thermal Diffusivity
α_{ref}	Linear Temperature Coefficient
α_{s}	Displacement Angle of the Slots

$\alpha_{0°C}$	Linear Temperature Coefficient at 0°C
γ	Angle of the Reference Stator Current Space Vector in the SRF
δ	Transformation Angle for the Rotation of the Reference Frame
ϵ	Emissivity
ϵ_1	Emissivity of the Radiator 1
ϵ_2	Emissivity of the Radiator 2
ζ	Angle of the Rotor Flux Space Vector in the SRF
η	Dynamic Viscosity
$\hat{\Theta}_1$	Magnitude of the Stator MMF Space Vector of the Fundamental Wave
$\hat{\Theta}_\nu$	Magnitude of the Stator MMF Space Vector with the Order ν
$\hat{\Theta}_{\nu,\mathrm{ph}}$	Amplitude of the Stator MMF Harmonic with the Order ν of a Stator Coil
ϑ	Angle of the Current Control Deviation Space Vector in the SRF
ϑ_i	Ideal Angles of the Current Control Deviation Space Vector in the SRF
μ	Natural Number
ν	Order of the Harmonic / Kinematic Viscosity
ξ_gr	Group Factor
ξ_p	Pitching Factor
ξ_1	Winding Factor for fundamental wave
ξ_ν	Winding Factor for the Harmonic ν
π	Archimedes Constant
ρ	Angle of the Rotor Flux Space Vector in the RRF
Σ_{12}	Radiation Transfer Coefficient
σ	Stefan-Boltzmann Constant
τ	Electromagnetic Torque
τ^*	Desired Torque
τ_f	Torque of the Main System
$\tau_{\mathrm{f,k}}$	Torque of the Main System at Period k
τ_fr	Frictional Torque
τ_0	Torque of the Zero-Sequence System
$\tau_{0,\mathrm{k}}$	Torque of the Zero-Sequence System at Period k
τ_rr	Rolling Frictional Torque
τ_sl	Sliding Frictional Torque
τ_seal	Frictional Torque of the Seals
φ	Rotor Angle (Angle of the Direct Axis of the PMSM) in the SRF

ϕ	Rotor Angle (Angle of the Rotor of the SCIM) in the SRF
ϕ_0	Phase Angle
ϕ_k	Rotor Angle (Angle of the Rotor of the SCIM) in the SRF at Period k
Ψ_c	Third Parameter of the Affected Magnetizing Current of the Main System
Ψ_c3	Fourth Parameter of the Affected Magnetizing Current of the Main System
Ψ_m	Magnitude of the Magnetization Flux Linkage Space Vector (Main System)
Ψ_m3	Magnitude of the Magnetization Flux Linkage Space Vector (Zero-Sequence System)
Ψ_PM	Flux Linkage caused by the Permanent Magnets
Ψ_s0	Amplitude of the Stator Flux Linkage of the Zero-Sequence System
ψ	Flux Linkage
$\psi_{\mathrm{m}\alpha}$	Real Part of the Magnetization Flux Linkage Space Vector in the SRF
$\psi_{\mathrm{m}\beta}$	Imaginary Part of the Magnetization Flux Linkage Space Vector in the SRF
ψ_rd	Direct Component of the Rotor Flux Linkage Space Vector
$\psi_\mathrm{rd,k}$	Direct Component of the Rotor Flux Linkage Space Vector at Period k
ψ_sa	Stator Flux Linkage of Phase a
ψ_sb	Stator Flux Linkage of Phase b
ψ_sc	Stator Flux Linkage of Phase c
$\psi_{\mathrm{s}\alpha}$	Real Part of the Stator Flux Linkage Space Vector in the SRF
$\psi_{\mathrm{s}\beta}$	Imaginary Part of the Stator Flux Linkage Space Vector in the SRF
ψ_s0	Stator Flux Linkage of the Zero-Sequence System
ψ_α	Real Part of the Flux Linkage Space Vector in the SRF
ψ_β	Imaginary Part of the Flux Linkage Space Vector in the SRF
ω	Angular Frequency

Complex Quantities

$\underline{C}$	Closed Loop Transfer Function
$\underline{D}$	Disturbance Transfer Function
$\underline{e}^\mathrm{r}$	Current Control Deviation Space Vector in the RRF
$\underline{e}^\mathrm{s}$	Current Control Deviation Space Vector in the SRF
$\underline{I}_\mathrm{a}$	RMS Time Vector of the Fundamental Voltage of Phase a
$\underline{I}_\mathrm{b}$	RMS Time Vector of the Fundamental Voltage of Phase b
$\underline{I}_\mathrm{c}$	RMS Time Vector of the Fundamental Voltage of Phase c

$\underline{I}_{\mathrm{d}}$	Laplace transformed i_{d}
$\underline{I}_{\mathrm{d}}^{*}$	Laplace transformed i_{d}^{*}
$\underline{I}_{\mathrm{q}}$	Laplace transformed i_{q}
$\underline{I}_{\mathrm{q}}^{*}$	Laplace transformed i_{q}^{*}
$\underline{I}_{\mathrm{r0p}}$	RMS Time Vector of the Zero-Sequence Rotor Current (Positive Direction)
$\underline{I}_{\mathrm{r0n}}$	RMS Time Vector of the Zero-Sequence Rotor Current (Negative Direction)
$\underline{I}_{\mathrm{r1}}$	RMS Time Vector of the Positive-Sequence Rotor Current
$\underline{I}_{\mathrm{s1}}$	RMS Time Vector of the Positive-Sequence Stator Current
$\underline{I}_{\mathrm{s2}}$	RMS Time Vector of the Negative-Sequence Stator Current
$\underline{I}_{\mathrm{s0}}$	RMS Time Vector of the Zero-Sequence Stator Current
$\underline{i}_{\mathrm{m}}^{s}$	Magnetizing Current Space Vector uin the SRF
$\underline{i}^{\mathrm{r}}$	Current Space Vector in the RRF
$\underline{i}^{\mathrm{r}*}$	Reference Current Space Vector in the RRF
$\underline{i}_{\mathrm{r}}^{\mathrm{r}}$	Rotor Current Space Vector in the RRF
$\underline{i}_{\mathrm{r}}^{\mathrm{s}}$	Rotor Current Space Vector in the SRF
$\underline{i}_{\mathrm{r3}}^{\mathrm{s}}$	Rotor Current Current Space Vector of the Zero-Sequence System in the SRF
$\underline{i}_{\mathrm{s}}^{\mathrm{r}}$	Stator Current Space Vector in the RRF
$\underline{i}_{\mathrm{s}}^{\mathrm{s}}$	Stator Current Space Vector in the SRF
$\underline{i}_{\mathrm{s}}^{\mathrm{s}*}$	Reference Stator Current Space Vector in the SRF
$\underline{i}^{\mathrm{s}*}$	Reference Current Space Vector in the SRF
$\underline{i}_{\mathrm{s}}^{\Psi}$	Stator Current Space Vector in the ΨRF
$\underline{i}_{\mathrm{s}}^{\Psi*}$	Reference Stator Current Space Vector in the ΨRF
$\underline{O}$	Open Loop Transfer Function
$\underline{Q}_{\mathrm{a}}$	RMS Time Vector of a Quantity of Phase a
$\underline{Q}_{\mathrm{b}}$	RMS Time Vector of a Quantity of Phase b
$\underline{Q}_{\mathrm{c}}$	RMS Time Vector of a Quantity of Phase c
$\underline{Q}_{\mathrm{s0}}$	Zero-Sequence Component of a Quantity
$\underline{Q}_{\mathrm{s1}}$	Positive-Sequence Component of a Quantity
$\underline{Q}_{\mathrm{s2}}$	Negative-Sequence Component of a Quantity
$\underline{q}_{\mathrm{Fe}}$	Iron Loss Factor
$\underline{s}$	Parameter of the Laplace-Transform
$\underline{V}_{\mathrm{a}}$	RMS Time Vector of the Fundamental Voltage of Phase a
$\underline{V}_{\mathrm{b}}$	RMS Time Vector of the Fundamental Voltage of Phase b
$\underline{V}_{\mathrm{c}}$	RMS Time Vector of the Fundamental Voltage of Phase c

$\underline{V}_{\mathrm{s0}}$	RMS Time Vector of the Zero-Sequence Stator Voltage
$\underline{V}_{\mathrm{s1}}$	RMS Time Vector of the Positive-Sequence Stator Voltage
$\underline{V}_{\mathrm{s2}}$	RMS Time Vector of the Negative-Sequence Stator Voltage
$\underline{v}_{\mathrm{c}}^{\Psi}$	Compensation Voltage Space Vector in the RRF
$\underline{v}_{\mathrm{c}}^{\Psi *}$	Compensation Stator Voltage Space Vector in the ΨRF
$\underline{v}_{\mathrm{c}}^{\mathrm{r}*}$	Compensation Voltage Space Vector in the RRF
$\underline{v}^{\mathrm{r}*}$	Reference Voltage Space Vector in the RRF
$\underline{v}_{\mathrm{s}}^{\Psi *}$	Reference Stator Voltage Space Vector in the ΨRF
$\underline{v}_{\mathrm{s}}^{\mathrm{s}}$	Stator Voltage Space Vector in the SRF
$\underline{v}_{+}^{\mathrm{s}}$	Additional Voltage Space Vector in the SRF
$\underline{z}$	Parameter of the Bilinear Transform
$\underline{\Theta}_{\nu}$	Stator MMF Space Vector of the harmonic ν
$\underline{\psi}_{\mathrm{m}}^{\mathrm{s}}$	Magnetization Flux Linkage Space Vector in the SRF
$\underline{\psi}_{\mathrm{m3}}^{\mathrm{s}}$	Zero-Sequence Magnetization Flux Linkage Space Vector in the SRF
$\underline{\psi}_{\mathrm{m3,k}}^{\mathrm{s}}$	Zero-Sequence Magnetization Flux Linkage Space Vector in the SRF at Period k
$\underline{\psi}_{\mathrm{r}}^{\mathrm{s}}$	Rotor Flux Linkage Space Vector in the SRF
$\underline{\psi}_{\mathrm{r3}}^{\mathrm{s}}$	Zero-Sequence Rotor Flux Linkage in the SRF
$\underline{\psi}_{\mathrm{r3,k}}^{\mathrm{s}}$	Zero-Sequence Rotor Flux Linkage in the SRF at Period k
$\underline{\psi}_{\mathrm{s}}^{\mathrm{s}}$	Stator Flux Linkage Space Vector in the SRF

Vectors

$\vec{i}_{\mathrm{abc}}$	Vector of the Phase Currents of Phases a, b and c
$\vec{P}$	Vector of the Nodal Power Losses
$\vec{T}$	Vector of Absolute Temperatures
$\vec{v}_{\mathrm{abc}}$	Vector of the Phase Voltages of Phases a, b and c
$\vec{v}_{\mathrm{abc}}^{*}$	Vector of the Desired Phase Voltages of Phases a, b and c
$\vec{v}_{\mathrm{tabcn}}$	Vector of the Terminal Voltages of Inverter Legs a, b, c and n
$\vec{\Psi}_{\mathrm{abc}}$	Vector of the Phase Flux Linkages of Phases a, b and c

Matrices

$\boldsymbol{E}$	Transformation Matrix of the Clarke Transformation
$\boldsymbol{F}$	Transformation Matrix of the Symmetrical Components
$\boldsymbol{G}_{\mathrm{th}}$	Thermal Conductance Matrix
$\boldsymbol{R}_{\mathrm{abc}}$	Diagonal Matrix of the Stator Resistances of Phases a, b and c

Appendix A

Voltage Disturbance with Sinusoidal Pulse Width Modulation

This Appendix discusses the transformation of a desired average voltage space vector into the average voltage space vector that is realized during an SSF of S_1 and $i_\alpha > 0$ with sinusoidal pulse width modulation with and without third harmonic injection. The transformation for sinusoidal pulse width modulation differs from space vector modulation (Fig. 2.4) due to the different time of the desired passive states 000 and 111 of these modulation methods. Fig. A.1 depicts the transformation for the sinusoidal pulse width modulation with third harmonic injection, whereas A.2 shows the transformation without third harmonic injection. During healthy operation, the components of the average voltage space vector equal the desired values, see Figs. a) and b). If an SSF of switch S_1 occurs, $\overline{v}_\alpha$ is disturbed if $i_\alpha > 0$, whereas the orthogonal component $\overline{v}_\beta$ remains unaffected, see Figs. c) and d). The deviation depends on the position of the desired voltage space vector. Without third harmonic injection, the deviation depends only on the α-component of this space vector.

Fig. f) illustrate the slope $\frac{\delta v_\alpha^*}{\delta v_\alpha}$. With third harmonic injection, the slope varies between 0 and $\frac{1}{2}$, depending on the space vector position. Without third harmonic injection, the slope is, independently of the space vector position, equal to $\frac{1}{3}$.

The degree of the voltage disturbance and the slope $\frac{\delta v_\alpha^*}{\delta v_\alpha}$ depend on the modulation method. However, in all three considered modulation methods, the space vector modulation, as well as the sinusoidal pulse width modulation with and without third harmonic injection, the α-component of the realized voltage space vector is transferred to the negative α-region and the slope is reduced significantly.

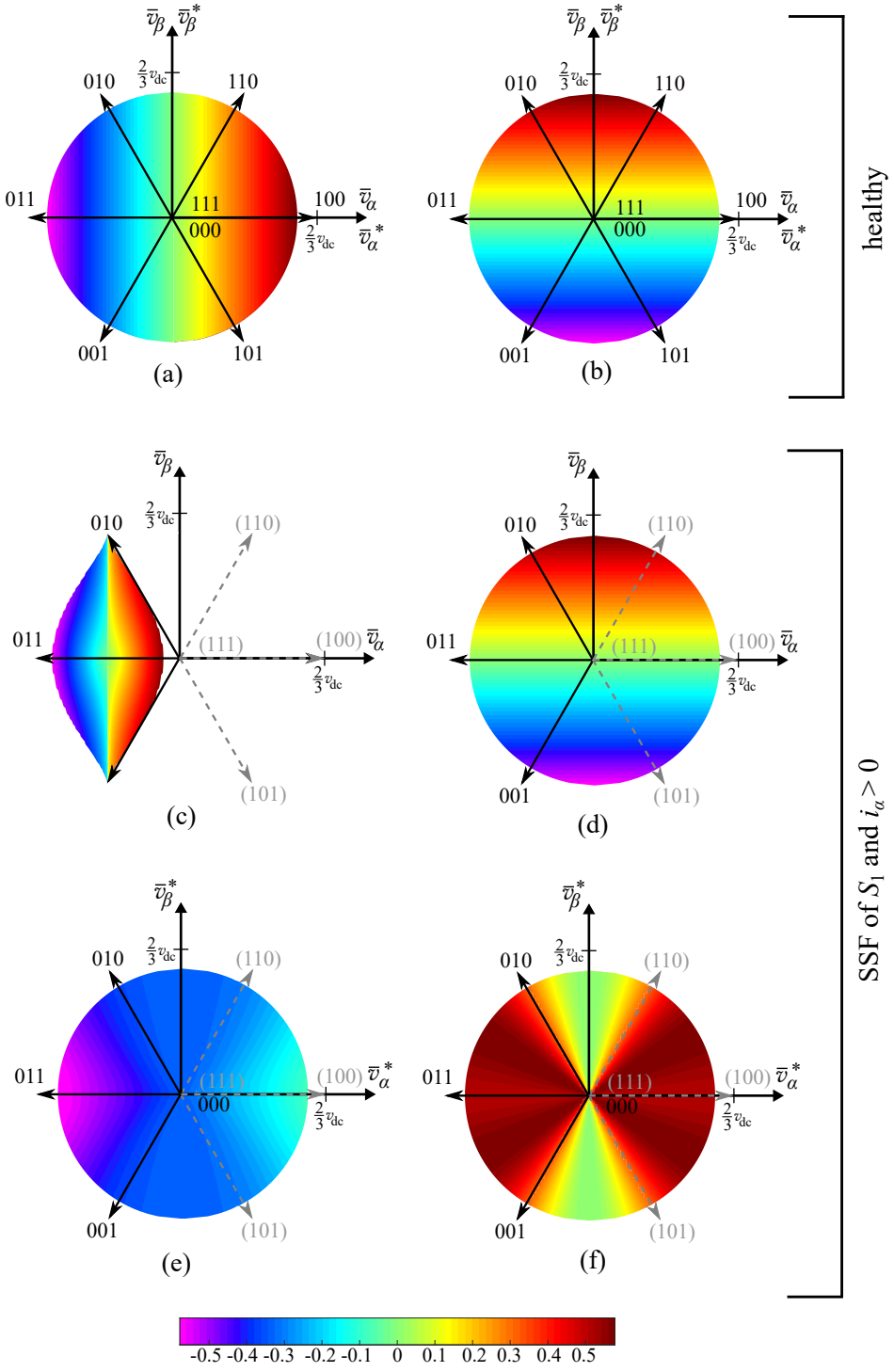

Fig. A.1: Transformation of desired voltage space vectors into realized voltage space vectors during pulse width modulation with third harmonic injection during healthy operation (a) and (b), and under an SSF of switch S_1, if $i_\alpha > 0$ (c)-(f). The switching states that can be realized and that cannot be realized are indicated in black, without parentheses, and in gray, with parentheses, respectively. The colors show the following: The desired average space vector components in one switching period v_α^* in (a) and (c) and v_β^* in (b) and (d). The realized component v_α is shown in (e), whereas (f) illustrates the derivative $\frac{\delta v_\alpha^*}{\delta v_\alpha}$.

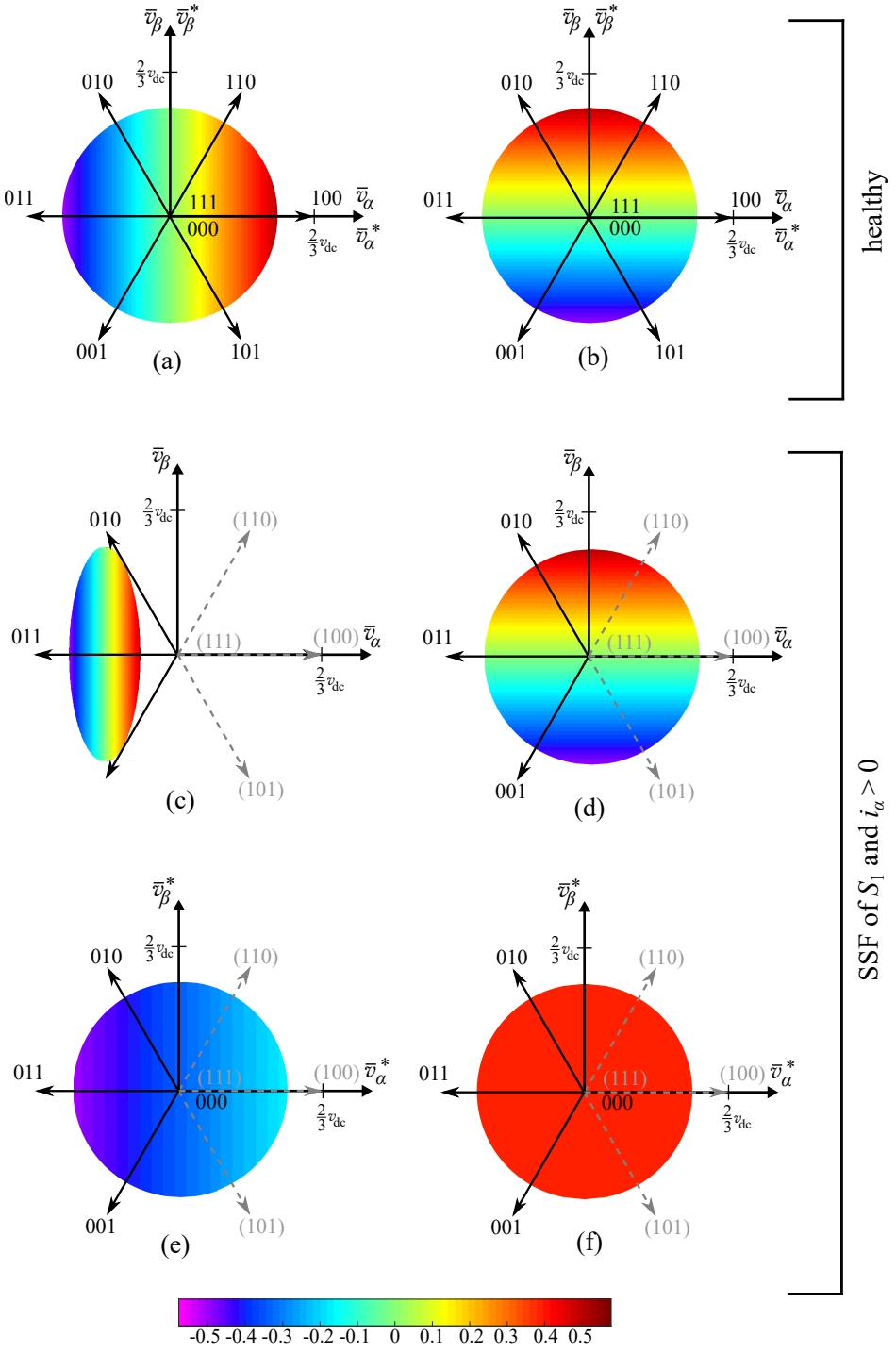

Fig. A.2: Transformation of desired voltage space vectors into realized voltage space vectors during sinusoidal pulse width modulation without third harmonic injection during healthy operation (a) and (b), as well as under an SSF of switch S_1, if $i_\alpha > 0$ (c)-(f). The switching states that can be realized and that cannot be realized are indicated in black, without parentheses, and in gray, with parentheses, respectively. The colors show the following: The desired average space components in one switching period v_α^* in (a) and (c) and v_β^* in (b) and (d). The realized component v_α is shown in (e), whereas (f) illustrates the derivative $\frac{\delta v_\alpha^*}{\delta v_\alpha}$.

Appendix B

Calculation of the Terminal Voltage of the Faulty Inverter Leg

This Appendix shows the calculation of the terminal voltage of phase a of a two-level inverter driven Y-connected three-phase machine with an isolated neutral point at $i_\mathrm{a} = 0$. Voltage drops across the semiconductors are neglected.

The stator voltage equations of the three-phase machine can be described by:

$$\begin{pmatrix} v_\mathrm{a} \\ v_\mathrm{b} \\ v_\mathrm{c} \end{pmatrix} = R_\mathrm{s} \begin{pmatrix} i_\mathrm{a} \\ i_\mathrm{b} \\ i_\mathrm{c} \end{pmatrix} + \begin{pmatrix} \dot{\psi}_\mathrm{sa} \\ \dot{\psi}_\mathrm{sb} \\ \dot{\psi}_\mathrm{sc} \end{pmatrix}, \tag{B.1}$$

where $v_\mathrm{a}, v_\mathrm{b}$, and v_c are the phase voltages, $i_\mathrm{a}, i_\mathrm{b}$, and i_c are the phase currents, $\psi_\mathrm{sa}, \psi_\mathrm{sb}$, and ψ_sc are the phase flux linkages, and R_s is the stator resistance.

B.1 Calculation of the Neutral Point Voltage

See Fig. 1.4 for the definition of the terminal voltages v_ta, v_tb, v_tc, and the neutral point voltage v_n.

B.1.1 Case 1: Terminals b and c have the same Electric Potential

In the case that v_tb - $v_\mathrm{tc} = 0$ (the terminals of the phase b and phase c are connected both to the negative or positive potential of the DC-link), Kirchhoff's voltage law leads to:

$$R_\mathrm{s} i_\mathrm{b} + \dot{\psi}_\mathrm{sb} - R_\mathrm{s} i_\mathrm{c} - \dot{\psi}_\mathrm{sc} = 0. \tag{B.2}$$

By using $i_\mathrm{b} = -i_\mathrm{c}$, (B.2) can be transformed to:

$$R_\mathrm{s} i_\mathrm{b} + \frac{1}{2}(\dot{\psi}_\mathrm{sb} - \dot{\psi}_\mathrm{sc}) = 0. \tag{B.3}$$

The difference between the potential of the terminals and the potential of the neutral point equals the phase voltage b and can be calculated by means of (B.1) and (B.3):

$$\Delta v = R_\mathrm{s} i_\mathrm{b} + \dot{\psi}_\mathrm{sb} = \frac{1}{2}(\dot{\psi}_\mathrm{sb} + \dot{\psi}_\mathrm{sc}). \tag{B.4}$$

In the case that the terminals of phases b and c are connected to the positive potential of the DC-link, the voltage of the neutral point is given by:

$$v_\mathrm{n} = v_\mathrm{tb} - \Delta v = v_\mathrm{dc} - \frac{1}{2}(\dot{\psi}_\mathrm{sb} + \dot{\psi}_\mathrm{sc}). \tag{B.5}$$

In the case that the terminals of phases b and c are connected to the negative potential of the DC-link, the voltage of the neutral point is given by:

$$v_\mathrm{n} = -\frac{1}{2}(\dot{\psi}_\mathrm{sb} + \dot{\psi}_\mathrm{sc}). \tag{B.6}$$

B.1.2 Case 2: Terminals b and c do not have the same Electric Potential

In the case that the terminal of phase b is connected to the positive potential of the DC-link and the terminal of phase c is connected to the negative potential of the DC-link, Kirchhoff's voltage law leads to:

$$v_\mathrm{dc} = R_\mathrm{s} i_\mathrm{b} + \dot{\psi}_\mathrm{sb} - R_\mathrm{s} i_\mathrm{c} - \dot{\psi}_\mathrm{sc}. \tag{B.7}$$

By using $i_\mathrm{b} = -i_\mathrm{c}$, (B.7) can be transformed to:

$$v_\mathrm{dc} = -2R_\mathrm{s} i_\mathrm{c} + \dot{\psi}_\mathrm{sb} - \dot{\psi}_\mathrm{sc}. \tag{B.8}$$

The neutral point voltage equals the negative phase voltage of phase c and can be calculated by means of (B.1) and (B.8):

$$v_\mathrm{n} = -R_\mathrm{s} i_\mathrm{c} - \dot{\psi}_\mathrm{sc} = \frac{1}{2} v_\mathrm{dc} - \frac{1}{2}(\dot{\psi}_\mathrm{sb} + \dot{\psi}_\mathrm{sc}). \tag{B.9}$$

Correspondingly, in the case that the terminal of phase c is connected to the positive potential of the DC-link and the terminal of phase b is connected to the negative potential, the neutral point voltage is:

$$v_{\mathrm{n}} = \frac{1}{2}v_{\mathrm{dc}} - \frac{1}{2}(\dot{\psi}_{\mathrm{sb}} + \dot{\psi}_{\mathrm{sc}}). \tag{B.10}$$

B.1.3 Model of the four Switching States

By combining (B.5), (B.6), (B.9), and (B.10), the neutral voltage in these four switching states can be calculated from:

$$v_{\mathrm{n}} = \frac{1}{2}(v_{\mathrm{tb}} + v_{\mathrm{tc}}) - \frac{1}{2}(\dot{\psi}_{\mathrm{sb}} + \dot{\psi}_{\mathrm{sc}}). \tag{B.11}$$

B.2 Terminal Voltage of Phase a

For $i_{\mathrm{a}} = 0$ and the case that both switches of the inverter leg a are off, the inverter leg shows a high resistance, and the terminal voltage of phase a in this state is defined by the neutral point voltage and the derivative of the phase flux linkage of phase a:

$$v_{\mathrm{ta}} = \dot{\psi}_{\mathrm{sa}} + v_{\mathrm{n}}. \tag{B.12}$$

The derivatives of the phase flux linkages can be calculated by means of the inverse Clarke Transformation:

$$\begin{pmatrix} \dot{\psi}_{\mathrm{sa}} \\ \dot{\psi}_{\mathrm{sb}} \\ \dot{\psi}_{\mathrm{sc}} \end{pmatrix} = \underbrace{\begin{pmatrix} 1 & 0 & 1 \\ -\frac{1}{2} & \frac{\sqrt{3}}{2} & 1 \\ -\frac{1}{2} & -\frac{\sqrt{3}}{2} & 1 \end{pmatrix}}_{\boldsymbol{E}^{-1}} \begin{pmatrix} \dot{\psi}_{\mathrm{s}\alpha} \\ \dot{\psi}_{\mathrm{s}\beta} \\ 0 \end{pmatrix}. \tag{B.13}$$

The terminal voltage of phase a for $i_{\mathrm{a}} = 0$ and the case that both switches of inverter leg a are off can be calculated by means of (B.12), (B.11), and (B.13):

$$v_{\mathrm{ta}} = \frac{3}{2}\dot{\psi}_{\mathrm{s}\alpha} + \frac{1}{2}(v_{\mathrm{tb}} + v_{\mathrm{tc}}). \tag{B.14}$$

In the case of a PMSM, the terminal voltage can also be calculated with the assump-

tion $\dot{i}_\mathrm{a} = 0$ (cf., (2.1)) from:

$$v_\mathrm{ta} = -\frac{3}{2}\dot{\varphi}\Psi_\mathrm{PM}\sin\varphi + \frac{1}{2}(v_\mathrm{tb} + v_\mathrm{tc}). \tag{B.15}$$

Appendix C

Speed of the Third Space Harmonics

This section discusses the relative speed of the third space harmonics of the zero-sequence system. If the positive-sequence system and the zero-sequence system are electrically operated with the same frequency f_s (i.e., sinusoidal currents/voltages with f_s), the following relations apply to the rotational frequencies of the third space harmonics of the zero-sequence system:

$$f_{3+} = \frac{1}{3} f_s, \tag{C.1}$$

$$f_{3-} = -\frac{1}{3} f_s, \tag{C.2}$$

where f_{3+} and f_{3-} are the rotational frequencies of the third space harmonic rotating in the positive and negative direction of rotation, respectively, and f_s equals the rotational speed of the fundamental wave. Fig. C.1 illustrates the dependence of the space harmonics on the rotational speed n in the case that f_s is constant: $f_s = f_{ref}$. For this case, the following synchronous rotational speeds apply:

$$n_{syn} = f_s \frac{60 \frac{s}{min}}{p}, \tag{C.3}$$

$$n_{syn3+} = \frac{1}{3} f_s \frac{60 \frac{s}{min}}{p}, \tag{C.4}$$

$$n_{syn3-} = -\frac{1}{3} f_s \frac{60 \frac{s}{min}}{p}, \tag{C.5}$$

where n_{syn} is the synchronous speed for the fundamental wave, and n_{syn3+} and n_{syn3-} are the synchronous speeds for the third space harmonics rotating in the positive and negative direction of rotation, respectively. The application of a constant frequency

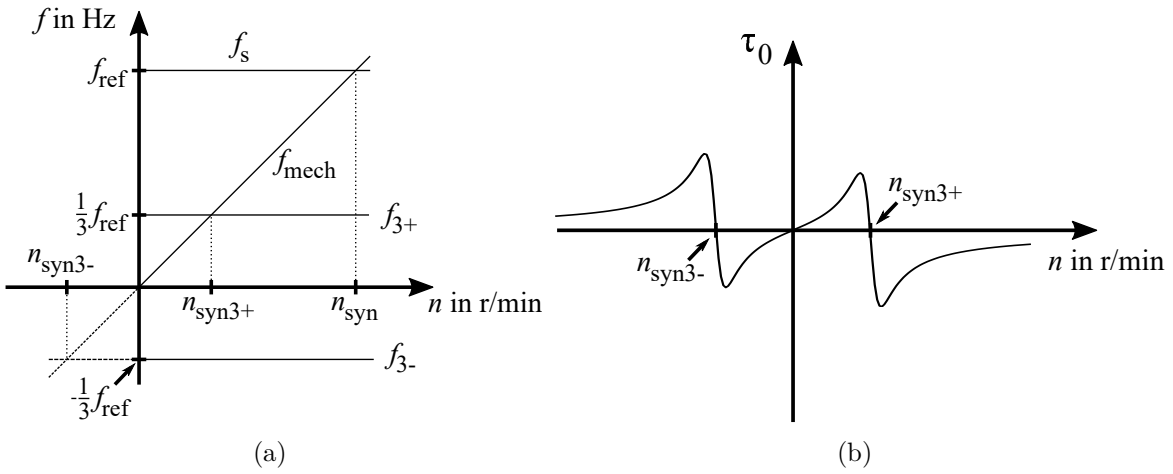

Fig. C.1: Rotational frequencies (a) and exemplary steady zero-sequence torque (b) of the third space harmonics in the case that $f_s = f_{ref}$.

f_s is convenient for the experimental parameter determination of the zero-sequence system (cf., Sections 3.2 and 5.3.2). In a rotor flux-oriented drive, the stator frequency f_s is adjusted to the speed. Fig. C.2 illustrates the dependence of the speed of the third space harmonics in the case of a rotor flux-oriented drive operated with constant rotor flux linkage and torque during motor operation. In such a case, the stator frequency is $f_s = f_{mech} + f_r$, where f_r is a constant and positive rotor frequency. The synchronous speed of the fundamental wave does not exist and the synchronous speeds of the third space harmonics are given by:

$$n_{syn3+} = \frac{1}{2} f_r \frac{60\frac{s}{min}}{p}, \tag{C.6}$$

$$n_{syn3-} = -\frac{1}{4} f_r \frac{60\frac{s}{min}}{p}. \tag{C.7}$$

The rotor frequency f_r is a fraction of the nominal stator frequency. Therefore, the synchronous speeds (and rotational speeds with low relative speed between the third space harmonics and the rotor) are shifted to lower absolute values of the rotational speed, when compared to the operation with a constant nominal frequency. This also shifts operating points with higher zero-sequence flux linkages and torque to the low speed region, as illustrated in Fig. C.2.

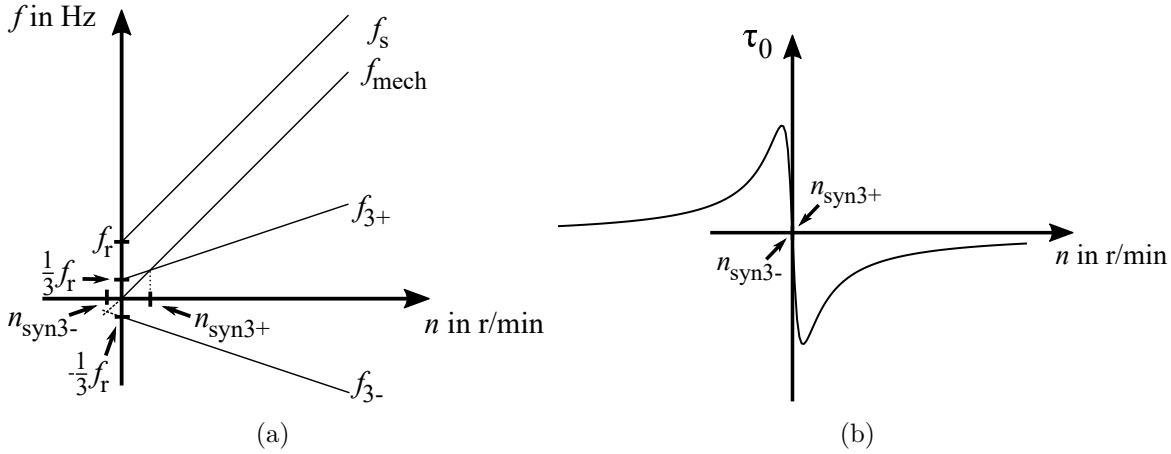

Fig. C.2: Rotational frequencies (a) and exemplary steady zero-sequence torque (b) of the third space harmonics in the case that $f_s = f_{mech} + f_r$.

Appendix D

Additional Results for the Zero-Sequence System of IM2

This Appendix shows further experimental investigations for the zero-sequence system of IM2. The results were obtained with the same methods as described for the 40 Hz results in Section 5.3.2. Figs. D.1 and D.2 shows results for frequencies of 10 Hz and 20 Hz, respectively. Figs. a) illustrate the electrical power P_{s0} and the mechanical power P_{mech0}, where positive values correspond to power flow into the machine. The mechanical power and the torque (Figs. b) are corrected by the friction and windage losses P_{fw} to obtain the quantities related to the zero-sequence system. The stator winding losses P_{Cu0} in Figs. c) are calculated from the stator resistance and the measured stator currents. Furthermore, the rotor power losses are estimated by subtracting stator copper losses from the sum of the electrical and mechanical power (the residual losses P_{Res0} in Figs. d). Figs. D.1 and D.2 also include the results obtained with the parameterized equivalent circuit of the zero-sequence system with and without additional rotor related power of 0.0110 W/min.

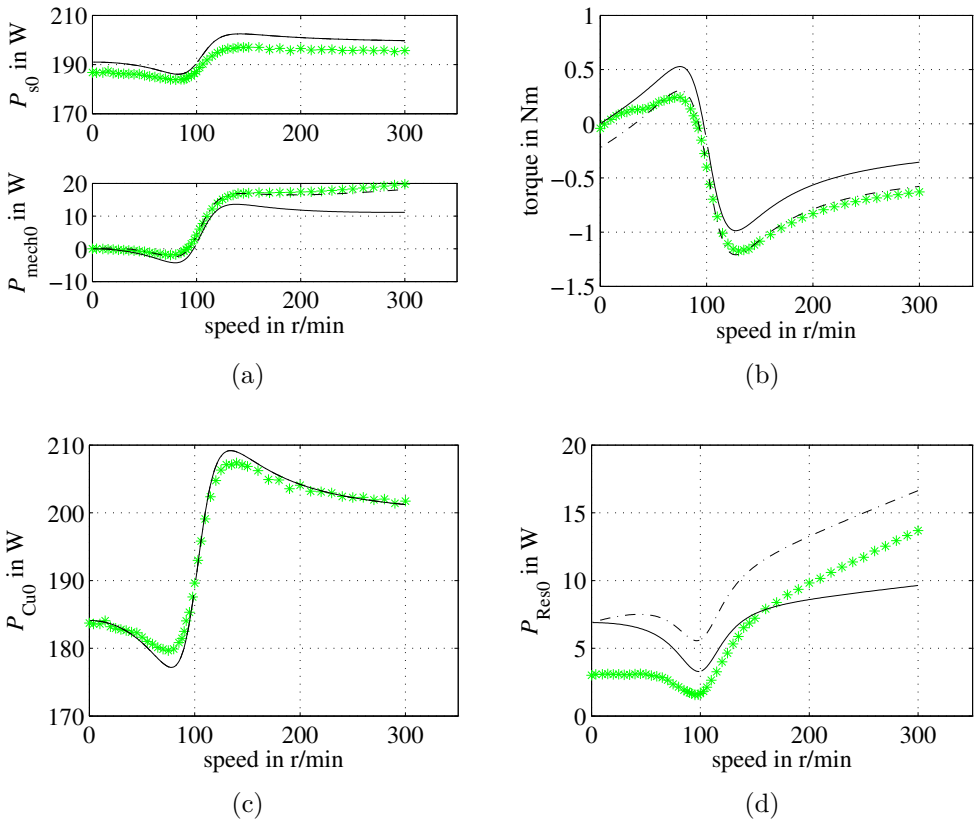

Fig. D.1: Comparison of the experimental results with IM2 and the equivalent circuit of the zero-sequence system with sinusoidal zero-sequence voltage of 38 V and 10 Hz: (a) electrical and mechanical power, (b) torque, (c) stator winding losses, (d) residual losses. The green stars indicate the measurement results, whereas the solid and dashed represent indicate the results of the equivalent circuit without and with additional rotor power, respectively.

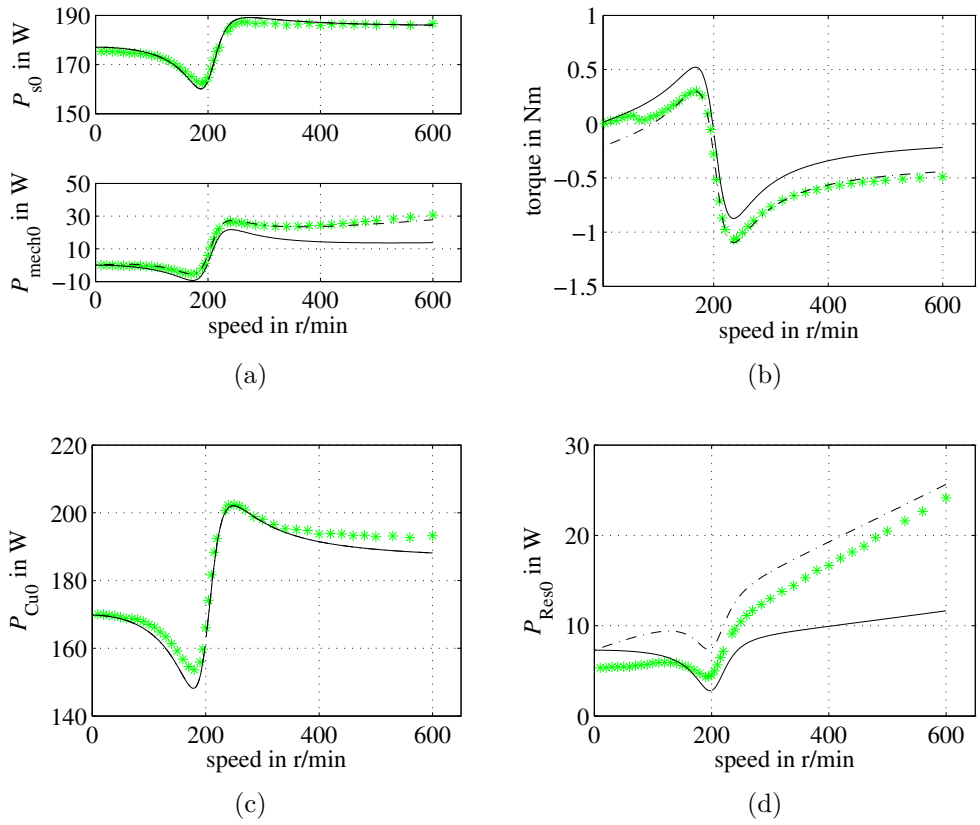

Fig. D.2: Comparison of the experimental results with IM2 and the equivalent circuit of the zero-sequence system with sinusoidal zero-sequence voltage of 38 V and 20 Hz: (a) electrical and mechanical power, (b) torque, (c) stator winding losses, (d) residual losses. The green stars indicate the measurement results, whereas the solid and dashed linies represent the results of the equivalent circuit without and with additional rotor power, respectively.

Appendix E

SCIM Torque Ratio of two Different Operating Points

E.1 Torque as a Function of the Ratio I_{sd} / I_{sq}

If iron losses are neglected, the continuous electromagnetic torque of an SCIM can be calculated from [85]:

$$\tau = \frac{3}{2} p \frac{L_m^2}{L_m + L_{\sigma r}} i_{sd} i_{sq} = 3p \frac{L_m^2}{L_m + L_{\sigma r}} I_{sd} I_{sq}. \tag{E.1}$$

The current space vector components I_{sd} and I_{sq} are the catheti, and the stator current $I_s = \frac{|\underline{i}_s^s|}{\sqrt{2}}$ is the hypotenuse of a right angle triangle. For this triangle, the following trigonometric relations apply:

$$I_{sd} = I_s \sin \gamma, \tag{E.2}$$

$$I_{sq} = I_s \cos \gamma, \tag{E.3}$$

$$\gamma = \arctan \frac{I_{sd}}{I_{sq}}. \tag{E.4}$$

Furthermore, following transformations apply [94]:

$$\sin(\arctan x) = \frac{x}{\sqrt{1+x^2}}, \tag{E.5}$$

$$\cos(\arctan x) = \frac{1}{\sqrt{1+x^2}}. \tag{E.6}$$

The combination of (E.2)-(E.6) allows with $x = \frac{I_{\mathrm{sd}}}{I_{\mathrm{sq}}}$ to rewrite the product of the stator current components:

$$I_{\mathrm{sd}} I_{\mathrm{sq}} = \frac{\frac{I_{\mathrm{sd}}}{I_{\mathrm{sq}}}}{1 + \left(\frac{I_{\mathrm{sd}}}{I_{\mathrm{sq}}}\right)^2} I_{\mathrm{s}}^2. \tag{E.7}$$

The combination of (E.1) and (E.7) yields the following torque equation:

$$\tau = 3p \frac{L_{\mathrm{m}}^2}{L_{\mathrm{m}} + L_{\sigma\mathrm{r}}} \frac{\frac{I_{\mathrm{sd}}}{I_{\mathrm{sq}}}}{1 + \left(\frac{I_{\mathrm{sd}}}{I_{\mathrm{sq}}}\right)^2} I_{\mathrm{s}}^2. \tag{E.8}$$

E.2 Torque Ratio for a Saturable SCIM

The torque ratio of two different operating points (indices 1 and 2) is given by:

$$\frac{\tau_2}{\tau_1} = \frac{\frac{L_{\mathrm{m},2}^2}{L_{\mathrm{m},2} + L_{\sigma\mathrm{r},2}}}{\frac{L_{\mathrm{m},1}^2}{L_{\mathrm{m},1} + L_{\sigma\mathrm{r},1}}} \frac{\frac{\frac{I_{\mathrm{sd},2}}{I_{\mathrm{sq},2}}}{1 + \left(\frac{I_{\mathrm{sd},2}}{I_{\mathrm{sq},2}}\right)^2}}{\frac{\frac{I_{\mathrm{sd},1}}{I_{\mathrm{sq},1}}}{1 + \left(\frac{I_{\mathrm{sd},1}}{I_{\mathrm{sq},1}}\right)^2}} \left(\frac{I_{\mathrm{s},2}}{I_{\mathrm{s},1}}\right)^2. \tag{E.9}$$

(E.9) allows the differences of the operation points to be considered, such as the stator currents, the ratios of the stator current components and the saturation of the current depending inductances. A simplification of (E.9) is possible if the rotor leakage inductance is a few percentages of the saturated magnetization inductance. In this case, the following inductance ratios have a low influence on the torque ratio:

$$\frac{L_{\mathrm{m},1}}{L_{\mathrm{m},1} + L_{\sigma\mathrm{r},1}} \approx \frac{L_{\mathrm{m},2}}{L_{\mathrm{m},2} + L_{\sigma\mathrm{r},2}}, \tag{E.10}$$

and (E.9) can be approximated with the following simplified relation:

$$\frac{\tau_2}{\tau_1} \approx \frac{L_{\mathrm{m},2}}{L_{\mathrm{m},1}} \frac{\frac{\frac{I_{\mathrm{sd},2}}{I_{\mathrm{sq},2}}}{1 + \left(\frac{I_{\mathrm{sd},2}}{I_{\mathrm{sq},2}}\right)^2}}{\frac{\frac{I_{\mathrm{sd},1}}{I_{\mathrm{sq},1}}}{1 + \left(\frac{I_{\mathrm{sd},1}}{I_{\mathrm{sq},1}}\right)^2}} \left(\frac{I_{\mathrm{s},2}}{I_{\mathrm{s},1}}\right)^2. \tag{E.11}$$

E.3 Torque Ratio for a Linear SCIM

For a linear SCIM (constant inductances), the torque ratio is given by:

$$\frac{\tau_2}{\tau_1} = \frac{\frac{\frac{I_{\mathrm{sd},2}}{I_{\mathrm{sq},2}}}{1+\left(\frac{I_{\mathrm{sd},2}}{I_{\mathrm{sq},2}}\right)^2}}{\frac{\frac{I_{\mathrm{sd},1}}{I_{\mathrm{sq},1}}}{1+\left(\frac{I_{\mathrm{sd},1}}{I_{\mathrm{sq},1}}\right)^2}} \left(\frac{I_{\mathrm{s},2}}{I_{\mathrm{s},1}}\right)^2. \tag{E.12}$$

Equation (E.12) can be simplified if the ratios $\frac{I_{\mathrm{sd}}}{I_{\mathrm{sq}}}$ of the two operation points are equal. For a linear SCIM, the $\frac{I_{\mathrm{sd}}}{I_{\mathrm{sq}}}$ ratio for maximum torque can be determined by calculating the first and second derivative of the term x with respect to $\frac{I_{\mathrm{sd}}}{I_{\mathrm{sq}}}$:

$$\begin{aligned} x &= \frac{\frac{I_{\mathrm{sd}}}{I_{\mathrm{sq}}}}{1+\left(\frac{I_{\mathrm{sd}}}{I_{\mathrm{sq}}}\right)^2}, \\ x' &= \frac{1-\left(\frac{I_{\mathrm{sd}}}{I_{\mathrm{sq}}}\right)^2}{\left(1+\left(\frac{I_{\mathrm{sd}}}{I_{\mathrm{sq}}}\right)^2\right)^2}, \\ x'' &= \frac{2\frac{I_{\mathrm{sd}}}{I_{\mathrm{sq}}}\left(\left(\frac{I_{\mathrm{sd}}}{I_{\mathrm{sq}}}\right)^2-3\right)}{\left(1+\left(\frac{I_{\mathrm{sd}}}{I_{\mathrm{sq}}}.\right)^2\right)^3}. \end{aligned} \tag{E.13}$$

Setting $x' \stackrel{!}{=} 0$ yields an extremum of x at $\frac{I_{\mathrm{sd}}}{I_{\mathrm{sq}}} = 1$. The calculation of x'' at $\frac{I_{\mathrm{sd}}}{I_{\mathrm{sq}}} = 1$ shows that this extremum is a maximum. Hence, if the linear SCIM is operated at the torque maximum $\frac{I_{\mathrm{sd}}}{I_{\mathrm{sq}}} = 1$ in both operation points, the torque ratio is given by:

$$\frac{\tau_2}{\tau_1} = \left(\frac{I_{\mathrm{s},2}}{I_{\mathrm{s},1}}\right)^2. \tag{E.14}$$

Appendix F

Measurement Setups

This Appendix illustrates measurement setups applied for the experimental investigations. Fig. F.1 shows a setup for experiments during the three-phase operation. It is applied for no-load, locked-rotor or load-tests with balanced stator currents. The Machine Under Test (MUT) is Y-connected. The MUT's phase currents and phase voltages are measured by a power analyzer. The phase currents are also measured by supplementary ampere meters for the current control with a signal processing system. The MUT is mechanically connected to a Load and Driving Machine (LDM). The torque between the MUT and the LDM is measured by a torque sensor. Rotary encoders are applied to measure rotor positions and the rotational speed. A DC-source is applied to measure the stator resistances or to produce heat in the stator winding in thermal experiments.

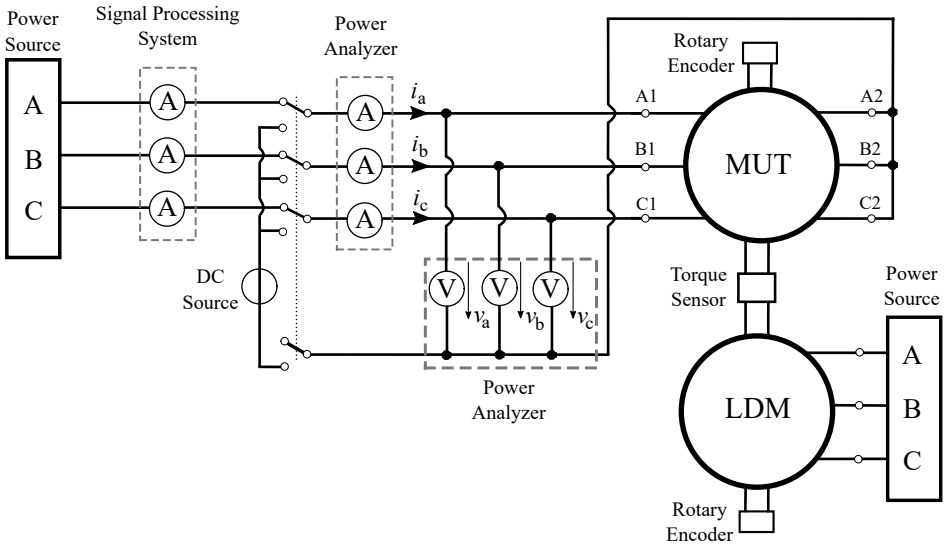

Fig. F.1: Setup for three-phase experiments.

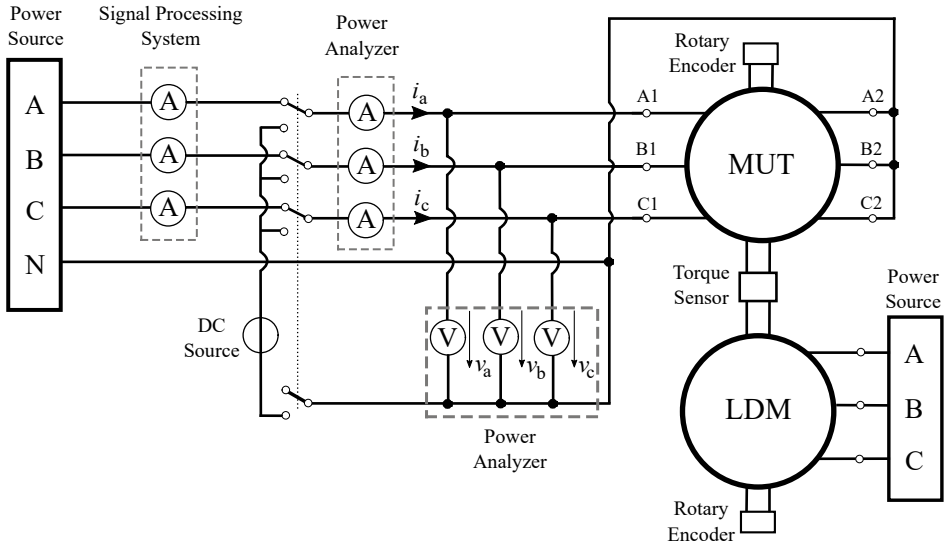

Fig. F.2: Setup for three-phase experiments with a neutral current.

For the two-phase operation and switched two-three-phase operation, the Setup is extended by a connection of the MUT's neutral point to a neutral terminal of the power source, as shown in Fig. F.2.

Note: In the experiments where IM2 is inverter-fed, the stator winding coils of the machine are reconfigured to a parallel connection (cf. Appendix H). The experiments in such a configuration could be performed with the measurement setups shown in Fig. F.1 and Fig. F.2. However, to exclude circulating currents, these setups are extended by three additional ampere and voltmeters of the power analyzer, to measure all six coil currents and voltages.

Fig. F.3 shows a measurement setup for experiments with the zero-sequence system. The MUT's stator windings are series-connected to force a zero-sequence stator current. Single phase power sources are applied (AC or DC). A power analyzer measures the zero-sequence current and the total voltage of the series-connected stator winding. The MUT is mechanically connected to the LDM. The torque between the MUT and the LDM is measured by a torque sensor and rotary encoders are applied to measure rotor positions and the rotational speed.

Fig. F.4 shows a setup for the investigation of the magnetization behavior and the saturation interaction between the main system and the zero-sequence system. A three-phase power source with a neutral terminal is applied. The MUT's phase currents and phase voltages are measured by a power analyzer. The phase currents are also measured by supplementary ampere meters for the current control with a signal processing system. Auxiliary switches enable the offset correction of the current and voltage in-

puts of the power analyzer. These switches are applied to disconnect the MUT from the power source and to short-circuit the voltage inputs for the offset correction. An auxiliary DC-source enables the feeding of the switch positions to the power analyzer and the signal processing system.

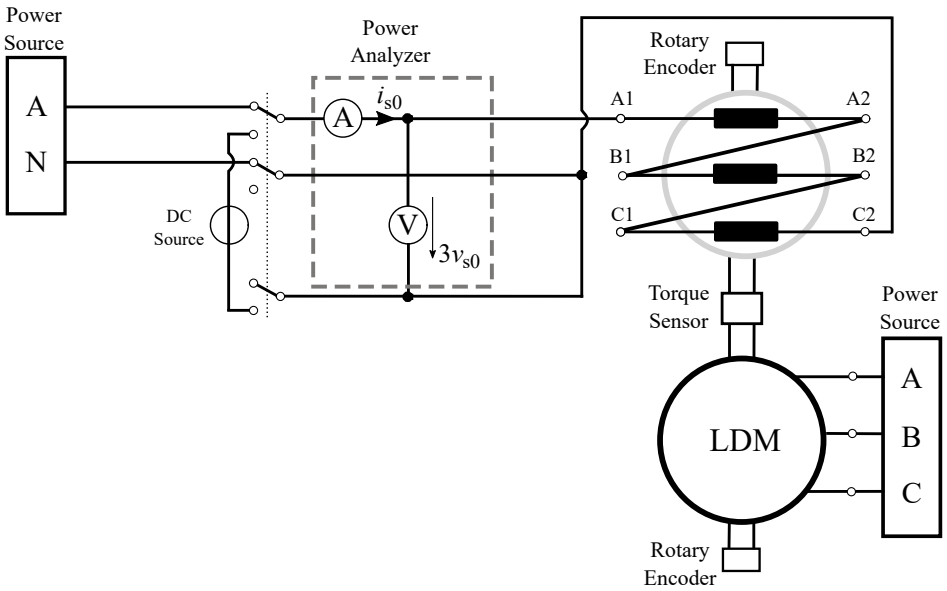

Fig. F.3: Setup for AC and DC zero-sequence system experiments with series-connected stator windings.

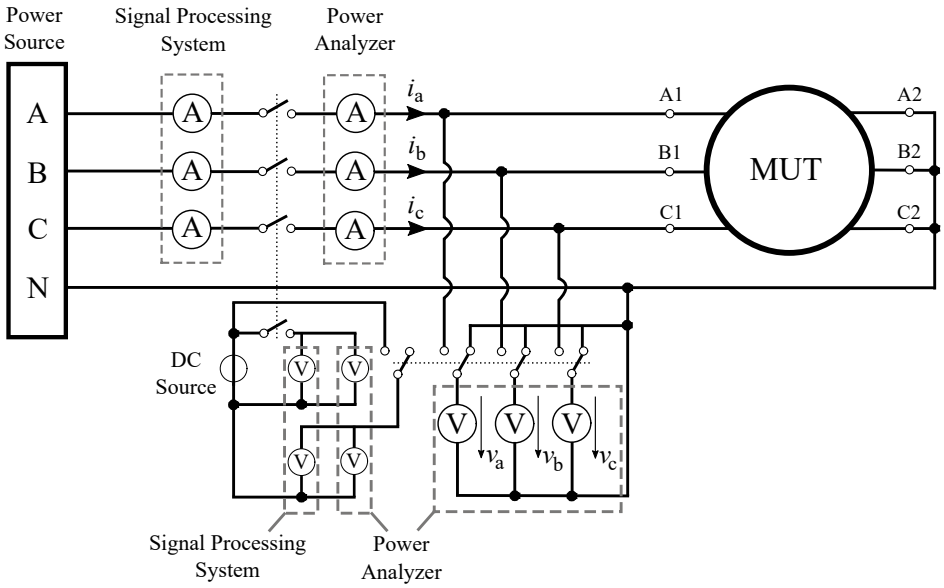

Fig. F.4: Setup for the investigation of the magnetization behavior and the saturation interaction of the main system and the zero-sequence system.

Table F.1 summarizes equipment used in the experiments. Further equipment used for the temperature and flux linkage measurement systems of IM2 is discussed in Appendix H.

Table F.1: Summary of equipment used in the experiments.

Inverter modules	SEMIKRON SKiiP 2
Analog power amplifiers	Spitzenberger+Spiess PAS 5000
DC sources	TTi PL Series and HP 6269B
Signal processing system	dSPACE 1005
Power analyzer	Norma 5000
Torque sensor IM1/SM1	HBM T12
Torque sensor IM2/SM2	HBM T10F

Appendix G

Overview of the Involved Electric Machines

This Appendix provides an overview of the two permanent magnet synchronous machines (SM1 and SM2) and the three squirrel cage induction machines (IM1, IM2, and IM3) involved in this thesis.

G.1 Permanent Magnet Synchronous Machines

Two permanent magnet synchronous machines were involved in this thesis. SM1 was the example machine in the PMSM drive for the analysis and the detection of inverter open circuit faults in Chapter 2. Both machines (SM1 and SM2) were used as speed controlled load and driving machines in the experiments with involved induction machines: SM1 was used in the experiments with IM1 of Chapters 3 and 9, whereas SM2 was used in the experiments with IM2 of Chapters 5, 7, and 8. The nominal data of the two PMSMs is summarized below.

Synchronous Machine 1 (SM1)

Three-phase permanent magnet synchronous machine
Surface mounted magnets
Self-cooling over flange, Class F a.t. 40 deg. C.
IP54

Table G.1: Data of SM1

Nominal torque	17.2 Nm
Nominal current RMS	9.3 A
Flux linkage caused by the PMs	0.184 Vs
Nominal speed	2500 r/min
Number of pole pairs	5
Moment of inertia	0.040 kgm^2
Stator resistance	0.4 Ω
Stator inductance	3.5 mH

Synchronous Machine 2 (SM2)

Three-phase permanent magnet synchronous machine
NdFeB magnets
Self-cooling over flange, Class F a.t. 40 deg. C.
IP64

Table G.2: Data of SM2

Nominal torque	31 Nm
Nominal current RMS	14 A
Flux linkage caused by the PMs	0.347 Vs
Nominal speed	2200 r/min
Number of pole pairs	3
Moment of inertia	0.065 kgm^2
Stator resistance	0.2 Ω
Stator inductance	5 mH

G.2 Squirrel Cage Induction Machines

The three squirrel cage induction machines (IM1, IM2, and IM3) were involved in a variety of different investigations regarding the power losses, torque, temperatures, and the magnetic behavior during the post-fault operations. In this context, these machines were used as example cases in experimental (IM1 and IM2), analytical (IM1, IM2, and IM3), and numerical (IM2 and IM3) investigations. Table G.3 provides an overview of the involved induction machines and the obtained results.

Table G.3: Results of the analytical (A), numerical (N), and experimental (E) investigations with the involved induction machines and the corresponding chapters (Ch).

Results	IM1	IM2	IM3
Power Losses	Ch 3 (E)	Ch 5 (A,E), Ch 8 (A,E)	Ch 5 (A,N)
Torque	Ch 9 (E)	Ch 8 (A,E)	Ch 5 (A,N)
Temperatures	-	Ch 7 (A,N,E), Ch 8 (A,E)	Ch 7 (A,N)
MMF and Saturation	Ch 4 (A,E)	Ch 4 (A,E)	-

In addition to the investigations of induction machines, IM1 was used as a speed controlled load and driving machine in the experiments with SM1 regarding the analysis and detection of inverter open circuit faults discussed in Chapter 2.

The three induction machines differ, e.g., in the stator winding, the output power, and the cooling. The effects of the differences in the stator winding design of IM1 and IM2 on the MMF and the saturation interaction were investigated in Chapter 4. The two water cooled induction machines were used to investigate the difference in the heat flow with asymmetric losses for the case of a single layer winding (IM3) and a dual layer winding (IM2) in Chapter 7. The nominal data of the three induction machines follows below.

Induction Machine 1 (IM1)

Three-phase squirrel cage induction machine
Totally enclosed fan cooled, T. amb. 40 deg. C.
IEC 60034, IE2, IP55
Single layer winding, 6 slots per pole and phase

Table G.4: Data of IM1 for Y-connection

Nominal power	5.5 kW
Nominal voltage RMS	400 V
Nominal current RMS	10.2 A
Nominal speed	2900 r/min
Nominal frequency	50 Hz
Power factor	0.89
Efficiency	87.9 %
Number of pole pairs	1
Moment of inertia	0.0287 kgm^2

Induction Machine 2 (IM2)

Three-phase squirrel cage induction machine
Totally enclosed water cooled, T. amb. 40 deg. C.
Dual layer winding, 3 slots per pole and phase, 7/9 pitching

Table G.5: Data of IM2 for Y-connection

Nominal power	3.7 kW
Nominal voltage RMS	400 V
Nominal current RMS	6.9 A
Nominal speed	1430 r/min
Nominal frequency	50 Hz
Number of pole pairs	2
Moment of inertia	0.0195 kgm^2

Induction Machine 3 (IM3)

Three-phase squirrel cage induction machine
Totally enclosed water cooled
Single layer winding, 3 slots per pole and phase

Table G.6: Data of IM3 for Y-connection

Nominal power	5.5 kW
Nominal voltage RMS	400 V
Nominal current RMS	10.9 A
Nominal speed	1430 r/min
Nominal frequency	50 Hz
Power factor	0.86
Number of pole pairs	2

Appendix H

Special Features of Induction Machine 2

Induction machine 2 (IM2) is a special machine complemented for thermal and magnetic investigations. For this purpose, the machine is equipped with a liquid cooling system, temperature measurement systems, flux finkage measurement systems, and flexible wiring.

H.1 Liquid Cooling System

IM2 is rated with the design principles for an air-cooled machine, however, it is constructed with a cooling jacket. The cooling jacket of IM2 forces a well defined rotational speed independent heat dissipation and enables thermal experiments such as an external heat injection and sensor calibration. The jacket, the end plates, and the stator flange (International Mounting B5) are isolated with thermal insulating materials from the ambient and the connection plate to reduce parasitic heat flows. To monitor the cooling system parameters, this system is equipped with a flow meter and platinum resistance detectors (Pt100) at the inlet and outlet tube of the jacket.

H.2 Temperature Measurement Systems

IM2 is equipped with temperature sensors in the stator and rotor. The stator temperature sensors are platinum resistance thin film detectors (Pt1000) that are electrically isolated and equipped with twisted and shielded wires. The rotor temperature sensors are type-T thermocouples with twisted wires. The stator winding temperature sensors are located in the stator slots and end windings of all three phases. The stator iron

temperature sensors are located in holes in the middle of the axial length of the stator back iron and the stator teeth. Further stator temperature sensors are located at the inside and outside of the end shields and the outside of the cooling jacket. The rotor temperature sensors of IM2 are located in the shaft close to the bearings, the middle of the axial length of the shaft and the rotor winding end rings. The wires of the rotor sensors are kept inside the hollow shaft of IM2 and the ends of these wires are connected to the telemetry that is located at the non-drive side of the shaft.

The test stand is equipped with further sensors to measure the temperature of the ambient, the supply, and the terminal box.

H.3 Flux Linkage Measurement Systems

Each of IM2's Flux Linkage Measurement System (FLMS) is a three-phase full-pitch coil system that allows for the decomposition of the linked flux into the main and the zero-sequence flux linkage (Clarke Transformation). The coils are located in the stator slots of one pole pair of the machine between the stator winding and the slot wedges. Fig. H.3 illustrates the alignment of the coils in the stator of IM2. FLMS-α is aligned according to the stator winding. As the stator winding, this system is sensitive to the α-component of the zero-sequence flux linkage. FLMS-β is shifted by 30 electrical degrees with respect to the stator winding to measure the β-component of the zero-sequence flux linkage. The β-component is not linked with the stator winding, therefore this component cannot be measured with this winding. Since a coil with a shift of 30 electrical degrees cannot be realized within the stator of IM2 (36 stator slots, 4 poles), each coil is composed of two series-connected coils shifted by 20 and 40 electrical degrees with respect to the stator winding. The partial linkages of these coils with the α-component of the zero-sequence flux linkage have the same amplitude and opposite signs. Therefore, the α-component cancel out electrically by the series connection. The flux linkage space vector of an FLMS can be converted to the flux linkage space vector of a stator winding as follows:

$$\underline{\Psi}_s = \frac{N_\mathrm{s}\xi_{\mathrm{s},1}}{N_\mathrm{FLMS}\xi_{\mathrm{FLMS},1}}\underline{\Psi}_\mathrm{FLMS}, \tag{H.1}$$

where $\underline{\Psi}_\mathrm{FLMS}$ is the flux linkage space vector measured with the FLMS, N_s is the number of the series-connected turns of the stator winding, N_FLMS is the number of turns of the FLMS, $\xi_{\mathrm{s},1}$ and $\xi_{\mathrm{FLMS},1}$ are the winding factors of the stator winding, and

the FLMS for the dominating fundamental wave, respectively. The zero-sequence flux linkage can be converted analogously:

$$\Psi_{s0} = \frac{N_s \xi_{s,3}}{N_{FLMS} \xi_{FLMS,3}} \Psi_{0,FLMS}, \tag{H.2}$$

where $\Psi_{0,FLMS}$ is zero-sequence flux linkage measured with the FLMS, $\xi_{s,3}$ and $\xi_{FLMS,3}$ are the winding factors of the stator winding, and the FLMS for the dominating third harmonic, respectively. The conversion of FLMS-α leads, due to the appropriate alignment, to the flux linkage of the stator winding of IM2. The conversion of FLMS-β leads to the flux linkage of a hypothetical 30 electrical degrees shifted stator winding and the β-component of the zero-sequence flux linkage. Potential sources for deviations in the conversion are the different linkage of the leakage flux of the FLMS and the stator winding or space harmonics.

H.4 Flexible Wiring

All coil group ends of IM2 are accessible, which allows the machine to be rewired. The nominal machine data in Table G.5 is valid for a series connection of all four coil groups per phase. To reduce the risk of a breakdown of the temperature sensor insulation during inverter operation, the machine was rewired to a serial/parallel connection of two coil groups each, as illustrated in Fig. H.2. This rewiring halves the voltages, doubles the line currents and changes the resistances and inductances to a quarter. The measured quantities in this thesis are mathematically converted to a series connection of all coil groups with these conversion factors. The rewiring is also considered at the inverter, the supply cables, and the control of the drive.

H.5 Recording of the Sensor Outputs

The output signals of the discussed temperature sensors and the flow meter are recorded with multiplexed Keithley 2700 multimeters, whereby the rotor temperature sensor signals are priorly transmitted and adjusted by a Datatel telemetry. The voltages of the flux linkage measurement systems are measured by an HBM Gen3i Data Recorder.

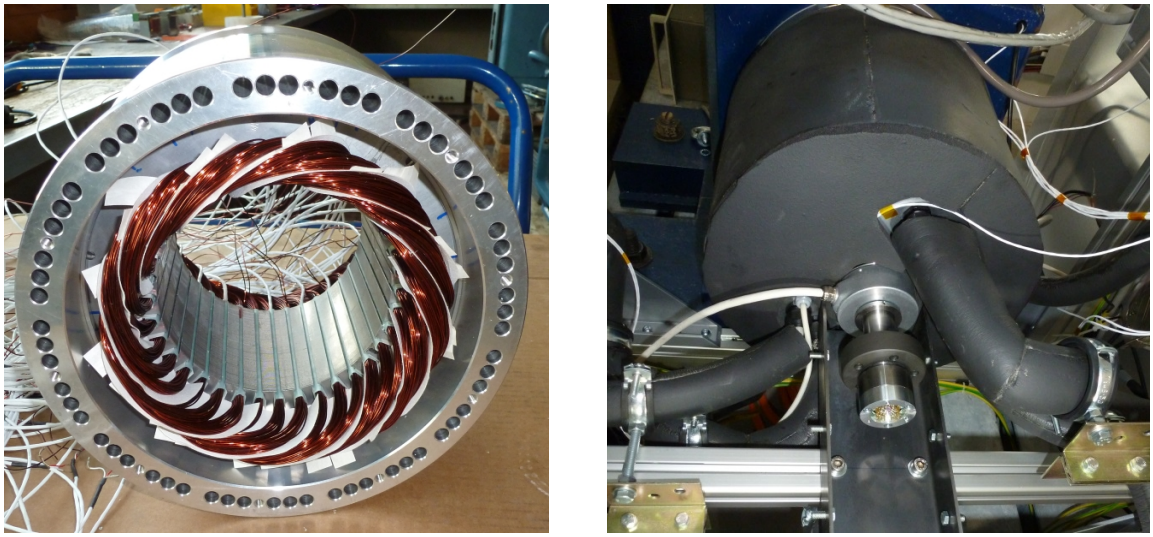

(a) (b)

Fig. H.1: (a) Cooling jacket and stator of IM2 with inserted stator winding coils during the manufacturing. (b) Thermally isolated IM2 at the test stand. The figure shows the non-drive side with mounted rotary encoder and the shaft end rotor telemetry.

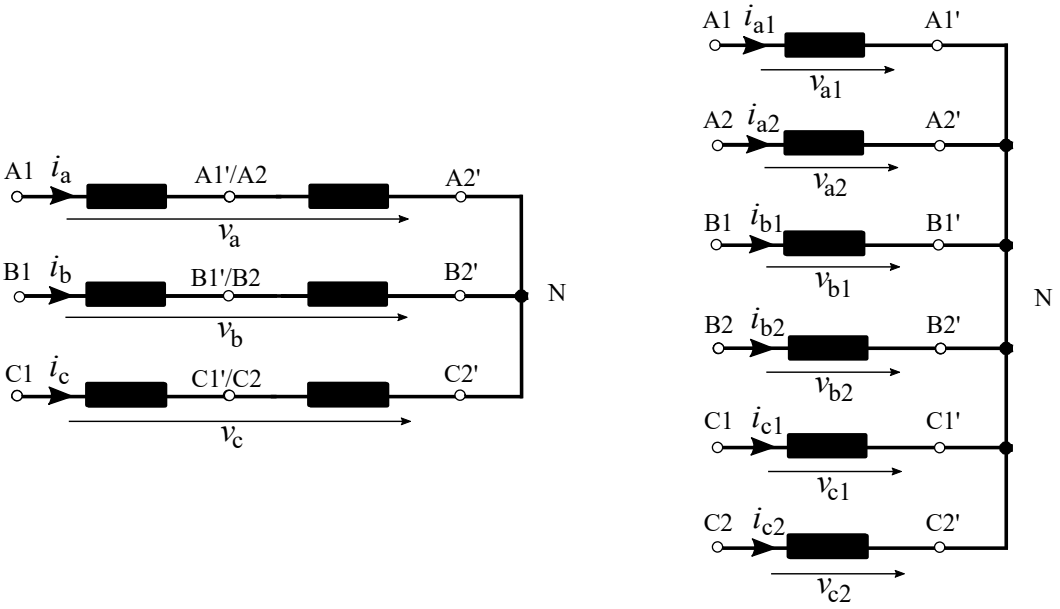

Fig. H.2: Rewiring of IM2 from a series connection (left) to a series/parallel connection (right). One inductance in this figure corresponds to a series connection of two coil groups.

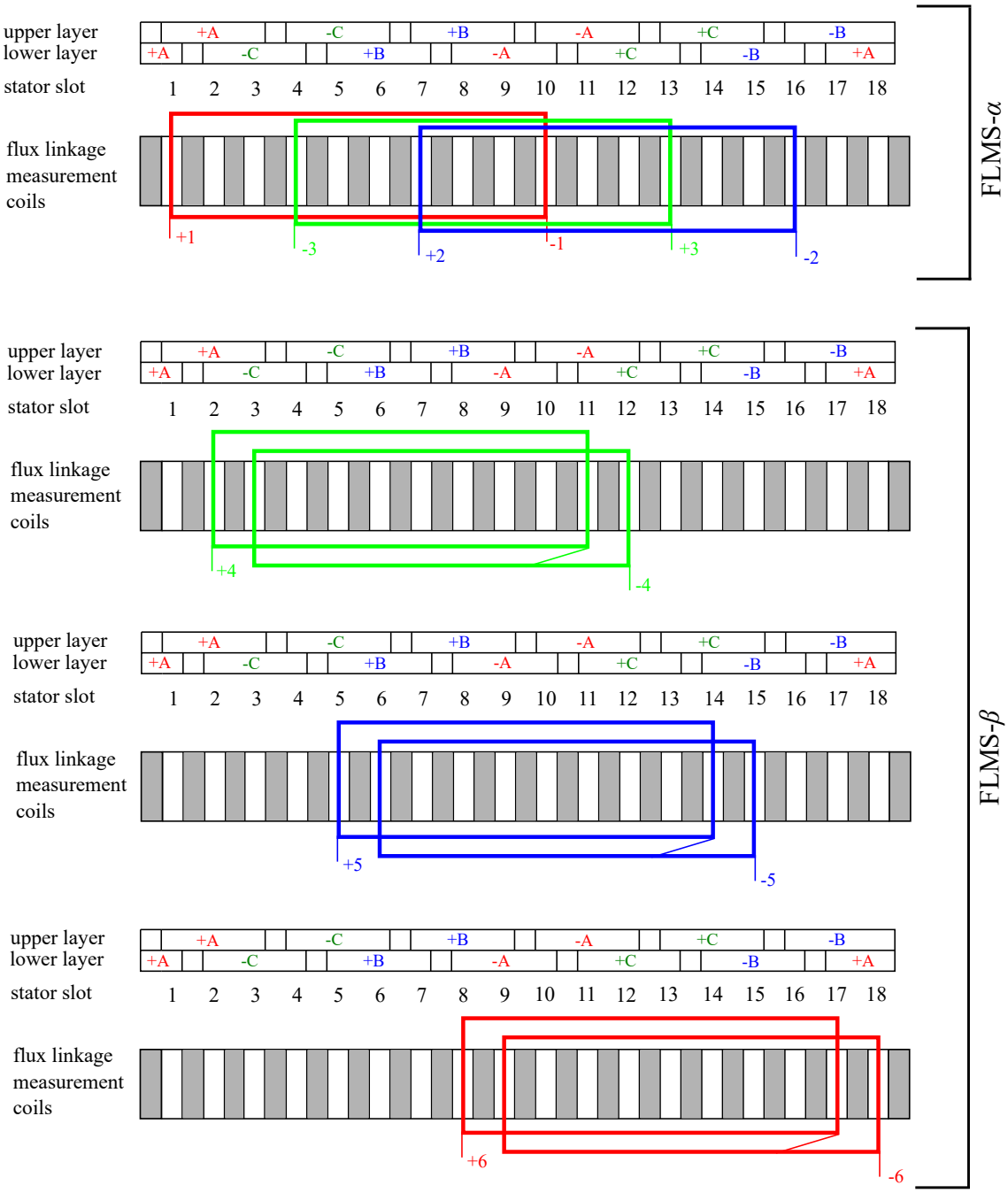

Fig. H.3: Stator winding phases A, B, and C and flux linkage measurement coils 1, 2, 3, 4, 5, and 6 in the first pole pair of IM2. FLMS-α comprises of coils 1, 2, and 3, whereas FLMS-β comprises of coils 4, 5, and 6.

Appendix I

Space Vector Definitions

The instantaneous space vector components in the stator reference frame q_α and q_β as well as the instantaneous zero-sequence component q_0 are obtained from the instantaneous phase quantities q_a, q_b, and q_c by means of the amplitude conserving Clarke Transformation [41]:

$$\begin{pmatrix} q_\alpha \\ q_\beta \\ q_0 \end{pmatrix} = \underbrace{\frac{2}{3}\begin{pmatrix} 1 & -\frac{1}{2} & -\frac{1}{2} \\ 0 & \frac{\sqrt{3}}{2} & -\frac{\sqrt{3}}{2} \\ \frac{1}{2} & \frac{1}{2} & \frac{1}{2} \end{pmatrix}}_{\boldsymbol{E}} \begin{pmatrix} q_\mathrm{a} \\ q_\mathrm{b} \\ q_\mathrm{c} \end{pmatrix}. \tag{I.1}$$

The complex space vector in the stator reference frame is defined by:

$$\underline{q}^\mathrm{s} = q_\alpha + jq_\beta. \tag{I.2}$$

The complex space vector in the rotor-oriented reference frame is defined by:

$$\underline{q}^\mathrm{r} = q_\mathrm{d} + jq_\mathrm{q}, \tag{I.3}$$

where q_d and q_q are the direct and quadrature components of the space vector in the rotor-oriented reference frame, respectively. The complex space vector in the rotor flux-oriented reference frame is defined by:

$$\underline{q}^\Psi = q_\mathrm{d} + jq_\mathrm{q}, \tag{I.4}$$

where q_d and q_q are the direct and quadrature components of the space vector in the rotor flux-oriented reference frame, respectively.

The space vectors can be transformed from the stator reference frame to the other reference frames (and vice versa) by means of the Park Transformation [42]:

$$\underline{q}^{\mathrm{r}} = e^{j\varphi}\underline{q}^{\mathrm{s}}, \tag{I.5}$$

$$\underline{q}^{\Psi} = e^{j\zeta}\underline{q}^{\mathrm{s}}. \tag{I.6}$$